Development and Performance Characterisation of High Concentrating Multi-Junction PV/Thermal Technology

By

Abdulrahman S. Aldossary

B.Eng. (Mechanical Engineering), MSc. (Thermal Power and Fluid Engineering)

Thesis submitted in partial fulfilment of the requirements for the Degree of Doctor of Philosophy

Department of Mechanical Engineering

College of Engineering and Physical Sciences

University of Birmingham

JANUARY, 2017

ABSTRACT

Multi-junction (MJ) solar cells are new generation of solar Photovoltaic (PV) technology with high efficiency, better response to high solar concentration and lower temperature coefficients. These cells are integrated with high concentrating optical systems to maximise their power output. However, high concentration of solar radiation can lead to a significant increase in the cell temperature, thus cooling is essential which offers potential for heat recovery leading to the development of High Concentrator PV/Thermal (HCPV/T) systems. HCPV/T is an emerging technology where more research needs to be carried out to evaluate its performance and the related challenges. This thesis presents a detailed investigation of the optical, electrical and thermal performance of a MJ based HCPV/T system in a harsh environment like Saudi Arabia where ambient temperatures can reach 50 ^{o}C in the summer.

Outdoor examination revealed that non-uniform illumination on the solar cell can reduce the MJ electrical output by more than 40%. Using ray tracing method, the irradiation uniformity was improved by increasing the distance between the concentrator and the receiver (l) and placing a 0.06m high secondary optical element (SOE) with surface reflectivity of 90% above the PV assembly. The outdoor measurement of the electrical efficiency under high non-uniformity (>692) was about 22% and after reducing the non-uniformity (<2) the electrical efficiency increased to about 36% with an increment of 64%. The hot spot initiated by the non-uniform illumination was also assessed outdoor by measuring the centre, side and corner surface temperature of the PV cell. A difference of about 13 K between the centre and the side (0.005m distance) of the PV cell surface was reduced to 1 K after enhancing the illumination uniformity. A parametric study on a developed Fresnel lens with different aperture areas including focal length, thickness, groove pitch and transmissivity was undertaken to enhance the performance of the HCPV/T optical system. The optical efficiency of the system was enhanced with a maximum and average increase of 24% and 21% respectively.

The developed MJ based HCPV/T system was tested thermally under a concentration ratio of 500X and at different ambient temperatures using Finite Element Analysis (FEA) and Computational Fluid Dynamics (CFD). It was found that the HCPV/T system performs better at higher ambient temperatures due to the increase in the generated thermal energy and the low electrical sensitivity of the MJ solar cell to the elevated temperature. The total efficiency of the HCPV/T system at 25 ^{o}C and 50 ^{o}C ambient temperatures are about 78% and 87% respectively with an increase of about 12%.

The performance analysis of HCPV/T integrating a 0.25x0.25 m^2 Fresnel lens under concentration ratios of 425X based on Saudi Arabia solar irradiation and ambient conditions was carried out to estimate the maximum and average power output that can be collected in one year. It was found that the yearly total power yield can be up to 191.3 kWh. Therefore, 184 units of HCPV/T, which occupy only 11.5 m^2, can provide more than the annual electrical energy demand of a typical house in Saudi Arabia. Also, in comparison to the flat plate silicon PV module with electrical efficiency of 20% and 1.2x0.8 m^2 area, the HCPV/T system can save about 76% of the area needed to meet this demand. In terms of carbon savings, these units can displace approximately 23 tons of CO_2 every year.

ACKNOWLEDGEMENT

All praise is due to Allah for his guidance, blessing and assistance to me to complete my thesis. May his prayers and peace be upon our role model and leader Prophet Muhammad.

My sincere appreciation goes to my supervisor **Dr Raya Al-Dadah**, for her kindness, patience, guidance and continuous support throughout this work. I am deeply indebted to her for invaluable ideas, encouragement and revising my work.

I am grateful to **Dr Saad Mahmoud** for his various invaluable suggestions and guidance through the entire period of my PhD study. I would like to thank **Mr Simon Rowan** for helping me to construct my indoor and outdoor test rig. Also, I would like to thank all staff members of the school of Mechanical Engineering, University of Birmingham who have supported me during my study.

My deep appreciations go to my mother, wife, daughter (**Dana**), brothers, sisters and friends back home and here for their patience, support and prayers during my study.

I am thankful to all my colleagues in Birmingham Dr Ahmed Elsayed, Abdulmajeed, Adel, Suliman, Ali, Bala and Wisam, etc.

Finally, I would like to acknowledge the government of Saudi Arabia represented by Royal Commission for Jubail and Yanbu for sponsoring my PhD project. Also, i am thankful to the embassy of Saudi Arabia in London and the Cultural Bureau for the continuous encouragement and honouring my colleagues and me in the National day (2016) as ‘‘High achieving students’’.

TABLE OF CONTENTS

LIST OF FIGURES

LIST OF TABLES

ABBREVIATIONS

AFHS	Angular Fins Heat Sink
AM	Air Mass
a-Si	Amorphous silicon
BIPV	Building Integrated PV
BPC	Back Point Contact
CCA	Concentrator Cell Assembly
CdTe	Cadmium Telluride
CFD	Computational Fluid Dynamics
CIGS	Copper Indium Gallium Selenide
CO_2	Carbon dioxide
CPC	Compound Parabolic Concentrator
CPV	Concentrator PV
CPV/T	Concentrator Photovoltaic and Thermal
CR	Concentration Ratio
c-Si	Crystalline silicon
CSP	Concentrating Solar Power
CST	Concentrating Solar Thermal
CSTC	Concentrator Standard Test Conditions
DHI	Diffuse Horizontal Irradiance
DiACPC	Dielectric Asymmetric Compound Parabolic Concentrator
DNI	Direct Normal Irradiance
DSSC	Dye-Sensitized Solar Cell
DTIR	Double Total Internal Reflection
EES	Engineering Equation Solver
ERH	Electrical Resistance Heater
ERI	Energy Research Institute
ESFHS	Extended Straight Fins Heat Sink
FEA	Finite Element Analysis
GaAs	Gallium Arsenide
GCR	Geometric Concentration Ratio
Ge	Germanium
GHI	Global Horizontal Irradiance
GWP	Global Warming Potential
HCPV	High Concentrator Photovoltaic
HCPV/T	High Concentrator Photovoltaic and Thermal
HITPR	Hollow Inverted Truncated Pyramid Reflector
InGaAs	Indium Gallium Arsenide
InGaP	Indium Gallium Phosphide
KACARE	King Abdullah City for Atomic and Renewable Energy
KACST	King Abdulaziz City for Science and Technology

LCPV	Low Concentrator Photovoltaic
LGBC	Laser Grooved Buried Contact
MCPV	Medium Concentrator Photovoltaic
MJ	Multi-Junction
MPP	Maximum Power Point
NREL	National Renewable Energy Laboratory
PMMA	Polymethyl Methacrylate
POE	Primary Optical Element
PV	Photovoltaic
PV/T	PV/Thermal
R&D	Research and Development
RPHS	Round Pins Heat Sink
RTD	Resistance Temperature Detector
SFHS	Straight Fins Heat Sink
SLA	Stretched Lens Array
SOE	Secondary Optical Element
STC	Standard Test Conditions
TJ	Triple-junction
UAE	United Arab Emirates
UHCPV	Ultra-High Concentrator Photovoltaic
UV	Ultraviolet
WEO	World Energy Outlook

NOMENCLATURE

Symbols	***Description***	***Unit***
A	Area	m^2
A_a	Area of the aperture	m^2
A_r	Area of the receiver	m^2
c	Speed of light	-
C_{max}	Maximum concentration	-
C_p	Specific heat capacity	J/ kg.K
D	Diameter	m
E_0	Total internal energy	W
E_g	Width of the semiconductor bandgap	eV
f	Focal length	m
FF	Fill Factor	-
G	Incident ray	W/m^2
h	Planck constant	J/s
h	Heat transfer coefficient	$W/m^2.K$
I	Electrical current	A
I_D	Diode current	A
I_L	Light generated current	A
I_m	Current at maximum power	A
I_{SC}	Short circuit current	A
I_{scr}	Short circuit current at reference temperature	A
k	Boltzmann’s constant	J/K
I_0	Saturation current	A
k	Thermal conductivity of the material	W/m.K
K_i	Short circuit current temperature coefficient	mA/K
$\dot{m}$	Mass flow rate	kg/s
n	Refractive index	-
P_{in}	Electrical power input	W
P_m	Maximum electrical power	W
P_{out}	Electrical power output	W
q	Electron charge	C
q_{in}	Input solar irradiation flux	W/m^2
q_{heat}	Input energy converted to heat	W/m^2
q_{irra}	Solar irradiation flux	W/m^2
Q_{cond}	Conduction heat transfer rate	W
Q_{conv}	Convection heat transfer rate	W
Q_{conv}	Natural/forced convection heat transfer	W
Q_{cool}	Thermal energy absorbed by the coolant	W

Q_{elec}	Electrical energy	W
Q_{in}	input power	W
Q_{rad}	Radiation heat transfer rate	W
Q_{radi}	Radiation energy	W
Q_{therm}	Thermal energy	W
Q_{water}	Water volume flow rate	m^3/s
R	Distance between incident ray and the centre axis of the Fresnel lens	m
Re	Reynolds number	-
R_s	Series resistance	Ω
S	Solar irradiation	mW/cm^2
t	Time	s
T	PV temperature	K
T_{amb}	Ambient temperature	K
T_C	Cell reference temperature	K
T_{in}	Inlet temperature	K
T_{out}	Outlet temperature	K
T_{PV}	Average PV temperature	K
T_{ref}	Reference temperature	K
T_s	Surface temperature	K
T_{surf}	Surface temperature	K
U	Mean velocity	m/s
V	Electrical voltage	V
V_D	Diode voltage	V
V_m	Voltage at maximum power	V
V_{OC}	Open circuit voltage	V
ΔT	Temperature difference	K

Greek Symbols	***Description***	***Unit***
2θ	Acceptance angle	degree
ε	Emissivity of the material	-
e_{tot}	Total energy flux	W
α	Slope angle	degree
β	Angle between the normal direction of the Fresnel lens's facet and the refractive ray	degree
$\beta_{thermal}$	Thermal coefficient	%/K
γ	Temperature dependence of the saturation current	-
η_{elect}	Electrical efficiency	-
η_{opt}	Optical efficiency	-

η_{therm}	Thermal efficiency	-
η_{tot}	Total efficiency	-
η_{Tref}	Efficiency at reference temperature	-
θ	Half acceptance angle	degree
θ_i	Angle of incidence	degree
λ	Wavelength of light	nm
ρ	Density	kg/m^3
σ	Stefan Boltzmann constant	Kg/ s^3 .K^4
σu	Convective stress energy	W
ω	Angle between the normal of the receiver and the refractive ray	degree

Subscript	***Description***
a	Aperture
amb	Ambient
cond	Conduction
conv	Convection
cool	Coolant
D	Diode
elec	Electrical
in	Input
irra	Irradiation
L	Light
max	Maximum
out	Output
r	Receiver
rad	Radiation
ref	Reference
SC	Short Circuit
surf	Surface
therm	Thermal

LIST OF PUBLICATIONS

1. A. Aldossary, S. Mahmoud, R. AL-Dadah. **Technical feasibility study of passive and active cooling for concentrator PV in harsh environment**. Applied Thermal Engineering 2016; 100:490-500.

2. A. Aldossary, S. Mahmoud, R. AL-Dadah. **Outdoor investigation of High Concentrator PV/Thermal integrating multi-junction solar cell under uniform and non-uniform illumination**. Applied Energy 2017 (Under preparation).

3. A. Aldossary, S. Mahmoud, R. AL-Dadah. **Electrical performance of high Concentrating Photovoltaic in harsh environment under passive cooling**. The 9th Saudi Students Conference, University of Birmingham, February 2016.

4. A. Aldossary, A. Algareu, A. Aldihani, R. AL-Dadah, S. Mahmoud. **Improving illumination and temperature distribution uniformity in high concentrating solar cells**. The 14th International Conference on Sustainable Energy Technologies (SET2015), University of Nottingham, August 2015.

5. A. Aldihani, A. Aldossary, R. AL-Dadah, S. Mahmoud, A. Alqattan. **Effect of Dusty Environment on the Electrical Performance of Different Photovoltaic Modules**. The 14th International Conference on Sustainable Energy Technologies (SET2015), University of Nottingham, August 2015.

6. A. Algareu, A. Aldossary, S. Mahmoud, R. AL-Dadah. **Optical Analysis of Flux Uniformity and Efficiency in Low Concentrating PV Systems.** The 14th International Conference on Sustainable Energy Technologies (SET2015), University of Nottingham, August 2015.

7. A. Aldossary, S. Mahmoud, R. AL-Dadah. **Alleviating non-uniform illumination of high concentration Fresnel lens**. The 8th Saudi Students Conference, Imperial College London, February 2015**.**

8. A. Aldossary, A. Algareu, S. Mahmoud, R. AL-Dadah. **Performance of multi-junction PV cells with high concentration ratio in Saudi Arabia**. International Conference on Applied Energy (ICAE), Taiwan, June 2014.

9. A. Aldihani, A. Aldossary, S. Mahmoud, R. AL-Dadah. **The effect of cooling on the performance of Photovoltaic cells under dusty environmental conditions**. International Conference on Applied Energy (ICAE), Taiwan, June 2014.

10. A. Aldossary, A. Algareu, A. Aldihani, S. Mahmoud, R. AL-Dadah. **Effect of Concentrator Geometry and sand on the Efficiency of Concentrated PV System**, University of Birmingham 2nd Mechanical Engineering Symposium, May 2013.

CHAPTER 1

Introduction

1.1. Background

Energy is certainly needed by all human societies for sustainability and development. Energy consumption is increasing day by day due to the rapid growth in the developed countries population and advances in technology. According to the World Energy Outlook (WEO), by 2040 the global energy demand is expected to grow by 37% [1]. Conventional sources of energy specifically fossil fuel have been consumed for many decades to fulfil the energy demand. Figure 1.1 shows the amount of carbon dioxide (CO_2) emission into the atmosphere due to the burning of coal, natural gas and liquids. CO_2 emission is projected to increase from 30.2 billion metric tons in the year 2008 to 43.2 billion metric tons by 2035 with increment of 43% [2].

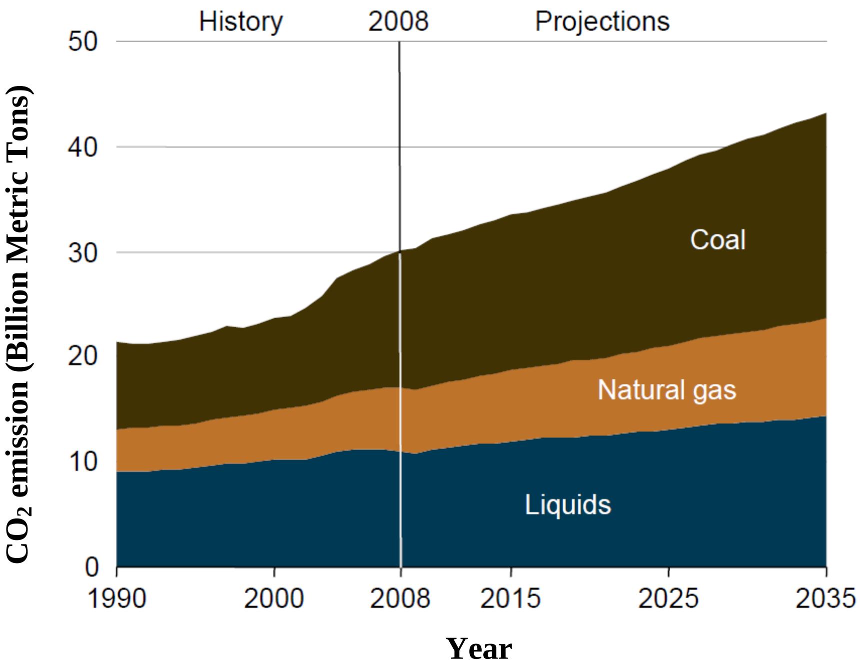

Figure 1.1: World energy CO2 emission contribution [2].

The emission of CO_2 is one of the main causes of air pollution, environmental disasters and global warming. Global warming leads to environmental degradation such as water shortage, floods, storms and extinction of some species [3]. Also, due to the current consumption rate of the conventional energy there has been a growing concern about the amount of fossil fuels remaining. Therefore, energy security has become an important aspect to ensure the uninterrupted supply of energy at an acceptable price. Any disruption of electricity, oil and gas supply can cause huge economic and social costs [4].

In this energy scenario, renewable energy sources such as solar, thermal, hydropower, geothermal, wind and marine attracted significant attention globally and became important over recent years as one of the solutions to the world energy issues [5,6]. Figure 1.2 shows the potential of a dramatic growth in the use of renewable energy over the next 20 years [2].

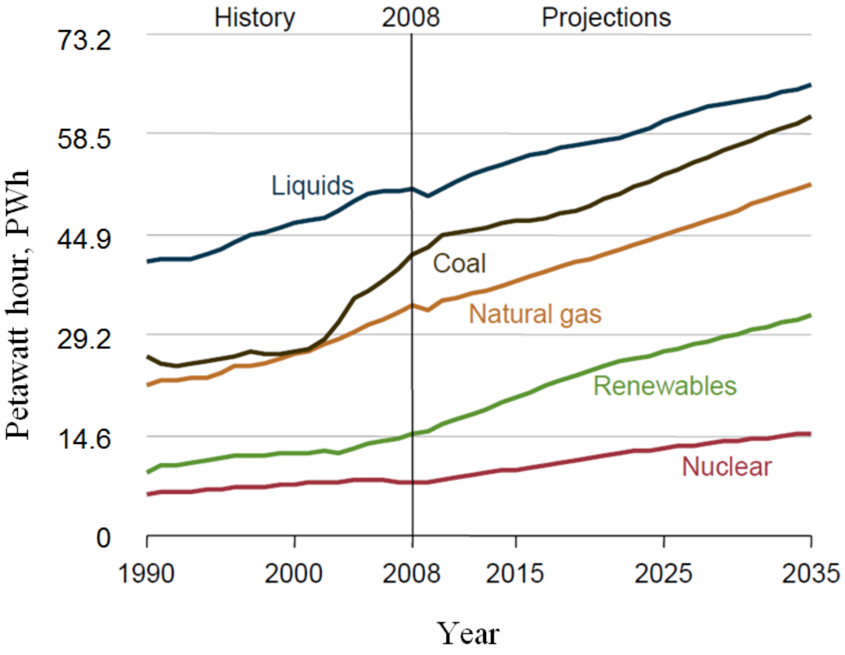

Figure 1.2: Forecast of world energy consumption [2].

Currently, solar and wind are the most utilised renewable energies around the world compared to others like hydro, geothermal and biomass due to their availability, flexibility in installation of the system and zero pollution [7]. Solar energy emitted by the sun and received by earth is one of the most abundant energy resources on the planet. Everyday, over 1.5 x 10^{22} J of solar energy reaches earth compared to daily energy consumption by human activity of about 1.3 x

10^{18} J [8]. But, the main challenge of promoting the solar energy is the low conversion efficiency which leads to a high initial cost when compared to electricity generated from conventional sources [9].

1.2. Energy issues in Saudi Arabia

Saudi Arabia is located in the heart of the Middle East between the Arabian Gulf and Red Sea. It occupies about 80% of the Arabian Peninsula lying between latitudes 16°and 33° N and longitudes 34° and 56° E. The country is divided into 13 provinces and it is composed primarily of desert. With the exception of south-western province of Asir, Saudi Arabia has a desert climate with extremely high day-time temperatures that may reach to 50°C during the summer time and drop in temperature at night [10]. Moreover, the annual mean rainfall is very low and mostly falls during winter time when temperatures are moderate in general. Saudi Arabia has an area of more than 2 million km^2 (2,149,690 km^2) and total population of 29.37 million [11].

According to BP, 2015, Saudi Arabia holds the world's second largest conventional crude oil reserves with 267 billion barrels of proved oil reserves (15.7% of world total) and the second largest petroleum liquids producer after the United States with a daily production of 11.5 million barrels in 2014 [12]. Also, Saudi Arabia’s proved natural gas reserves are estimated at 8.2 trillion cubic meters, ranking fifth in the world (4.4% of world total) behind Russia, Iran, Qatar and the United Arab Emirates (UAE) with a yearly production of 108 billion cubic meters [12,13].

On the other hand, Saudi Arabia faces serious energy issues related to rapid increase in domestic energy demand. The local daily oil consumption increased from about 1 million barrel in 1993 to more than 3 million barrel in 2014 with increase of more than 200% in only 20 years [12]. It is ranked the 7th largest oil consumer in the world after the US, China, Japan, India, Brazil and Russia. Moreover, the domestic consumption of natural gas increased from

40 billion cubic meters in 1993 to about 110 in 2014 with increment rate of 175%. Figures 1.3 and 1.4 show the oil and gas production and consumption in Saudi Arabia for the last 2 decades respectively. As can be seen in Figure 1.4, all the produced natural gas is consumed locally for domestic demand [12,14].

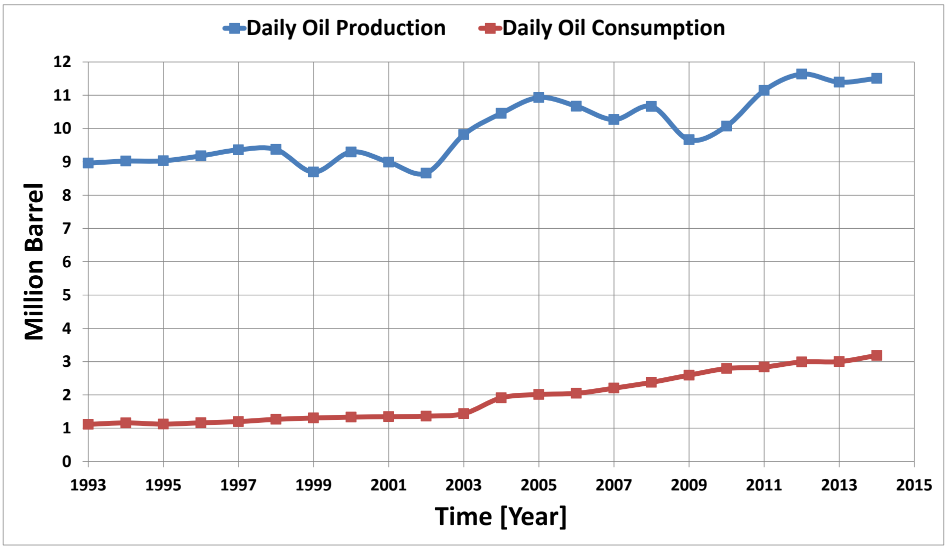

Figure 1.3: Daily oil production and consumption in Saud Arabia [12,14].

The local high demand in energy (fossil fuel) is driven by population growth with 1.9% yearly for the last three years, industrial development, growing production of electricity and drinkable water and a subsidy regime that encourage wasteful consumption [11]. According to IEA 2010, Saudi Arabia is the second highest energy subsidizers with an average subsidization rate of 77.3% [15,16].

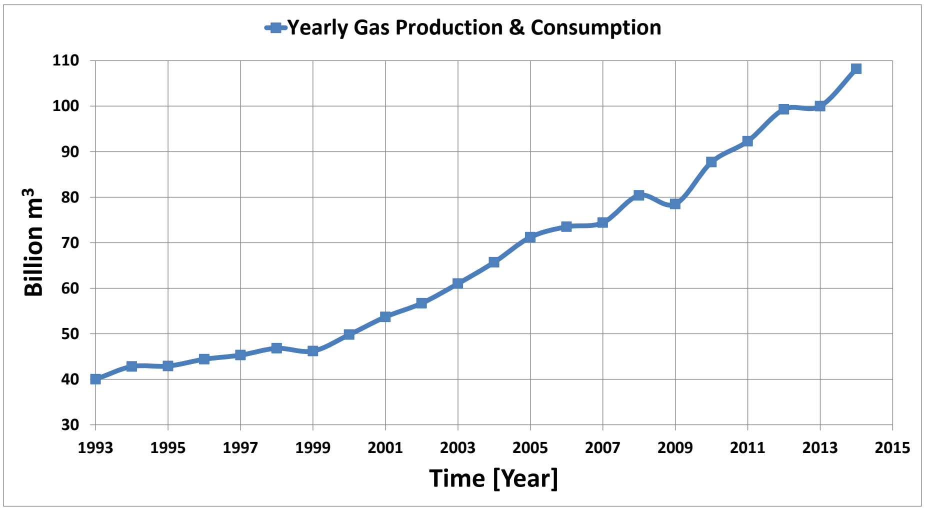

Figure 1.4: Yearly gas production and consumption In Saudi Arabia [12,14].

The domestic rapid consumption of fossil fuel is mainly due to the high demand in electricity as its generation in Saudi Arabia is heavily dependant on burning hydrocarbons with 44% natural gas, 32% crude oil, 13% diesel and 11% heavy fuel oil as shown in Figure 1.5 [16,17].

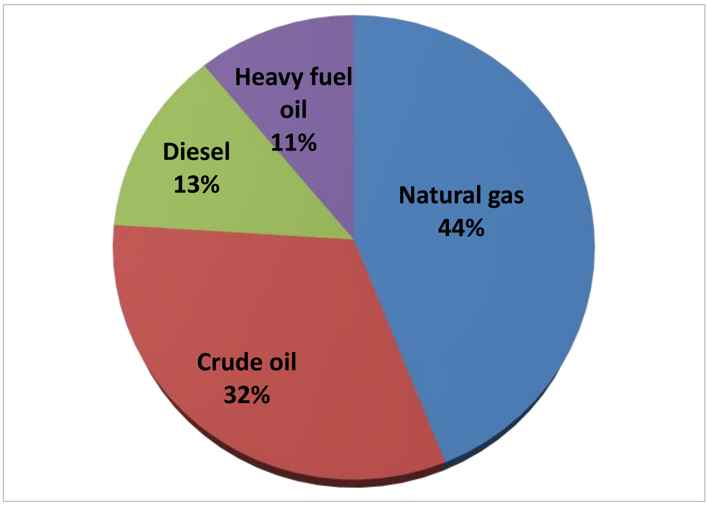

Figure 1.5: Hydrocarbons used for electricity generation [17].

The average electricity use in Saudi Arabia increased by about 10% annually over the last decade. In 2005, the electricity consumption was about 140 thousand GWh and it reached doubled to 280 thousand GWh in 2014 as illustrated in Figure 1.6. Also, due to the climate factor the summer peak demand increased by 90% between 2005 and 2014 from 30 to 57 GW [17].

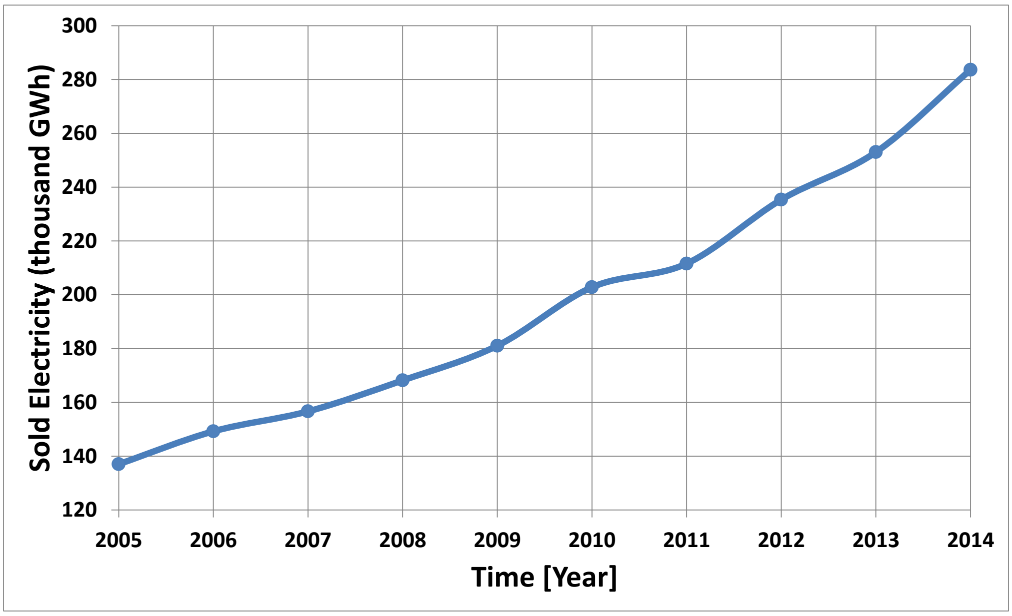

Figure 1.6: Yearly sold electricity In Saudi Arabia [17].

The growth of electricity demand in the residential sector has high degree of seasonality due to the need for air conditioning in the hot summer months and nearly 70% of the residential electricity is sold for this purpose [16]. Figure 1.7 shows the electricity consumption share for each sector with strong demand in residential sector consuming about half of the kingdom's total electricity production [17].

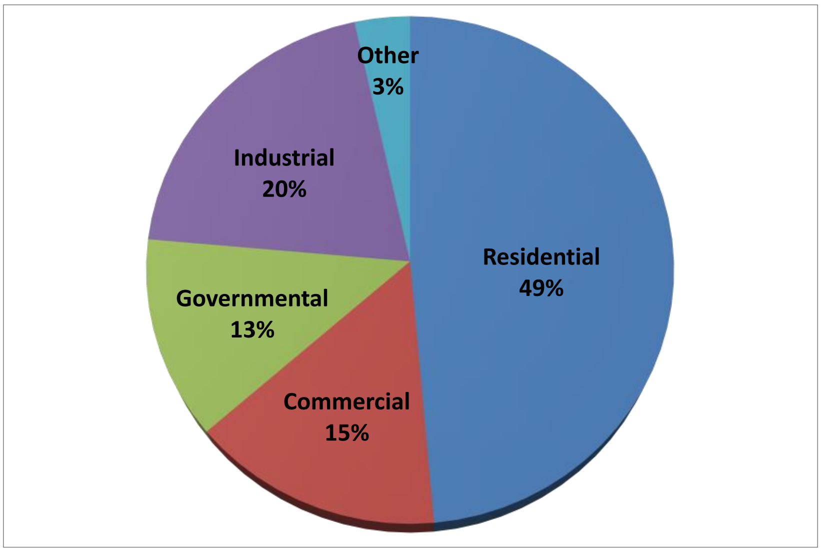

Figure 1.7: Electricity consumption share by sector in Saudi Arabia [17].

Electricity tariff in Saudi Arabia is one of the lowest globally due to the subsidy regime of fossil fuel. Figure1.8 shows that the average electricity tariff in Saudi Arabia is 0.04 $/kWh whereas in Denmark 0.4 $/kWh and the average of the listed 28 countries is about 0.21 $/kWh [18].

Due to the strong population growth, the development boom and overly generous subsidy regime the water sector is another growing energy consumer. Saudi Arabia lacks natural water resources and, therefore, mostly depends on seawater desalination (60%) with the remaining coming from water wells to meet its water demands [16]. As can be seen in Figure 1.9, the drinkable water demand increased from about 2.4 million m^3 in 2010 to 3.1 million m^3 in 2014 with an increment of about 30% in only 4 years [17].

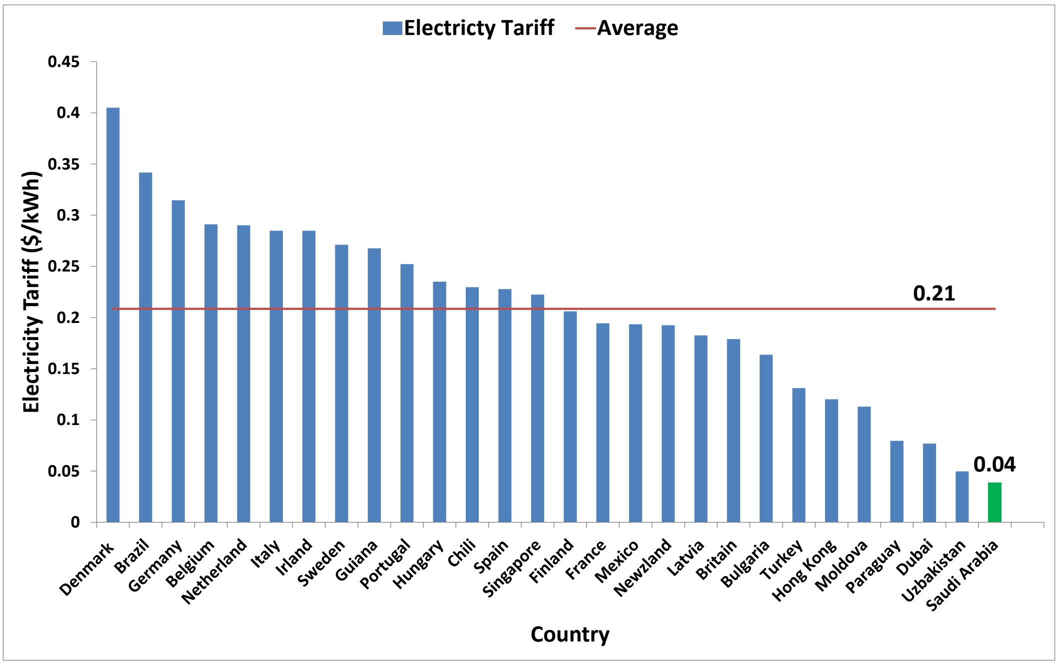

Figure 1.8: Average electricity tariff comparison [18].

To meet this consumption growth in drinkable water, Saudi Arabia has built 30 desalination plants as the largest producer of desalinated water in the world with about 26% of global production [16]. Desalination processes consume significant quantities of energy to achieve separation of salts from seawater. The water cost paid by the end users is equivalent to only 5-10% of the actual production cost. Nowadays, water desalination in Saudi Arabia accounts for 10-20% local energy consumption [16].

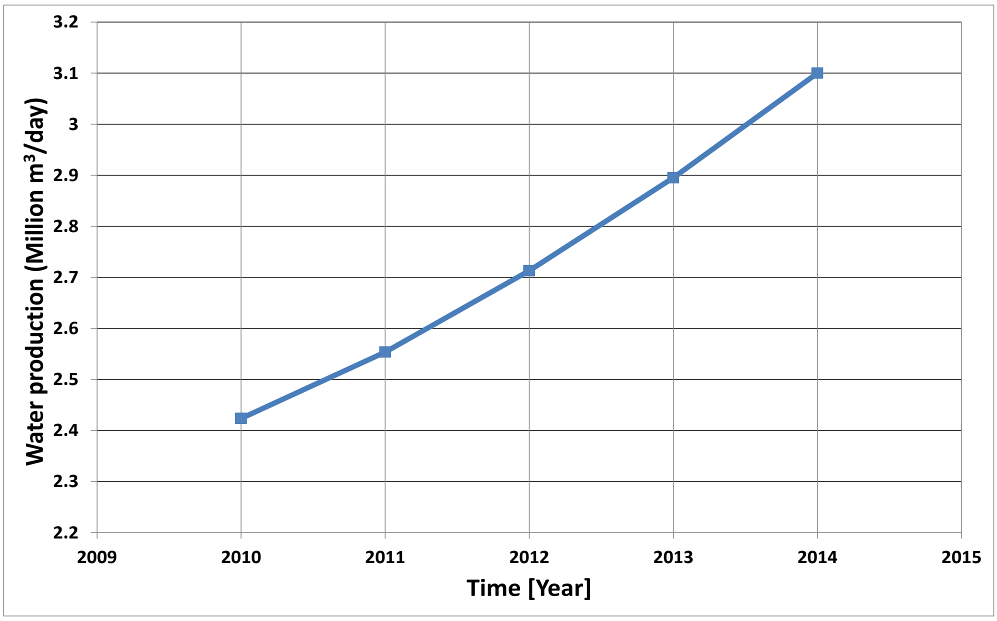

Figure 1.9: Average daily production of desalinated water in Saudi Arabia [17].

The Saudi Arabian government estimates the anticipated demand for electricity in the kingdom to exceed 120 GW in 2032 [19]. This rate of energy consumption is not sustainable in the long run and without taking serious steps toward reviewing the fossil fuel subsidies, using alternative energy and implementing energy conservation measures, the overall demand for energy will increase from about 3 million barrels of oil equivalent per day in 2010 to 8.3 million of oil equivalent per day in 2028 for power, industry, transportation and water desalination [19]. According to Lahn and Stevens 2008, by 2038 Saudi Arabia will become a net oil importer if the domestic consumption is not curbed significantly [20]. Moreover, in terms of pollution due to this rapid consumption in fossil fuel, Saudi Arabia's annual CO_2 emission per capita is one of the highest globally with 18.7 metric tons per capita higher than United Kingdom (7.1) and United States (17) [21].

Saudi Arabia's government realised the importance of diversifying the power mix towards renewable energy to reduce the CO_2 emission, meet the growing domestic energy demand, extend the lifetime of oil reserves and release additional domestic oil and gas resources to export and towards higher added value sectors such as petrochemicals [16].

King Abdullah City for Atomic and Renewable Energy (KACARE) was established in 2010 to build Saudi Arabia's renewable and atomic energy program that can meet a considerable portion of the growing electricity demand. KACARE launched in 2012 an ambitious plan to introduce renewable and atomic energy gradually such that more than 50% of all electricity generated will be from non-fossil fuel by 2032. The plan is to install 41 GW of solar energy (16 GW will be generated through the use of Photovoltaic (PV) cells and the balance of 25 GW by Concentrated Solar Power), 9 GW of wind, 3 GW of waste-to-energy and 1 GW of geothermal corresponding to 41% of total electricity generation [19].

1.3. Research and applications of solar energy in Saudi Arabia

Saudi Arabia has abundant freely available solar energy as its location lies within the Sunbelt region with average annual global solar radiation of about 2270 kWh/m^2 and area of more than 2 million km^2 [22,23]. The utilization of solar energy may cover a considerable part of the local energy demand. Also, due to the geographical location of the country, its widespread desert land and high clearance index Saudi Arabia can be a successful candidate to export solar energy in the form of electricity [23].

Applications of solar energy in Saudi Arabia have been developing since 1960. Research activities started with small-scale university projects during 1969, and systemised major Research and Development (R&D) work to develop solar energy technologies was initiated by King Abdulaziz City for Science and Technology (KACST) in 1977. The Energy Research Institute (ERI) at KACST has conducted major R&D work in this field. The ERI had a number of international joint research programs in the field of solar energy including SOLERAS with the United States of America which was signed in late 1977 and HYSOLAR with the Federal Republic of Germany initiated in 1991. These joint programs were focused on projects that were of mutual interest to the participating countries such as electricity generation, water desalination, agricultural applications and cooling systems.

Table 1.1 lists major solar energy R&D projects conducted by the ERI along with their location, type, capacity and applications [13,23]. By 2000, the cumulative installed capacity of solar PV cells reached 4 MW in Saudi Arabia [13].

Table 1.1: List of solar energy projects executed by the ERI, KACST [13,23].

Year conducted	Location	Description of projects		Application purposes
		Type	Capacity	
1981–1987	Solar Village	PV system	350 kW (2155 MWh)	AC/DC electricity for remote areas
1981–1987	Saudi universities	Solar cooling		Developing of solar cooling laboratory
1986–1991	KAU, Jeddah	Solar hydrogen	2 kW (50 kWh)	Testing of different electrode materials for solar hydrogen plant
1986–1994	Solar Village	Solar-thermal dishes	2 pieces, 50 kW	Advanced solar stirling engine
1987–1990	Solar Village	PV test system	3 kW	Demonstration of climatic effects
1987–1993	Solar Village	PV hydrogen production	350 kW (1.6 MWh)	Demonstration plant for solar plant hydrogen production
1988–1993	Dammam	Energy management in buildings		Energy conservation
1988–1993	Al-Hassa, Qatif	Solar dryers		Food dryers (dates, vegetables, etc.)
1989–1993	Solar Village	Solar hydrogen generator	1 kW (20–30 kWh)	Hydrogen production, testing and measurement (laboratory scale)
Since 1990	Solar Village	Long-term performance of PV	3 kW	Performance evaluation
1993–1995	Solar Village	Internal combustion engine		Hydrogen utilization
1993–1997	Solar Village	Solar collectors development		Domestic, industrial, agricultural
1993–2000	Solar Village	Fuel cell development	100–1000 W	Hydrogen utilization
1994–1999	Sadous Village	PV water desalination	0.6 m^3	PV/RO interface per hour
1994–2000	12 stations	Solar radiation measurement		Saudi solar atlas
1994–2000	5 stations	Wind energy measurement		Saudi solar atlas
1996	Southern regions	PV system	4 kW	AC/DC electricity for remote areas
1996	Muzahmia	PV in agriculture	4 kWp	AC/DC grid connected
1996–1997	Solar Village	Solar-thermal desalination		Solar distillation of brackish water
1996–1998	Solar Village	PV system	6 kW	PV grid connection
1999–2000	Solar Village	Solar refrigeration		Desert application

Figure 1.10 shows the solar village PV system installed in 1981 which was the largest in the world at that time with peak output of 350 kW and the only large concentrator PV (CPV) power system in operation [24,25]. The objective of this project was to exploit solar energy to provide power to three remote villages (Al-Jubailah, Al-Uyaynah and Al-Higera) 50 km north-west of Riyadh which were not served by an electric power grid [13]. This computerised 350 kW Fresnel lens concentrator PV comprising of 160 silicon PV arrays and occupying an area of 4000 m^2 was working in two modes of operation: stand-alone and co-generation. This PV system remains one of the most successful R&D projects implemented as the experience acquired through the execution and after the operation of this project is rich. Also, it was the start for many following renewable energy projects as can be seen in Table 1.1 [13]. Research and development activities in Saudi Arabia have confirmed that solar energy has a wide range of practical uses [26].

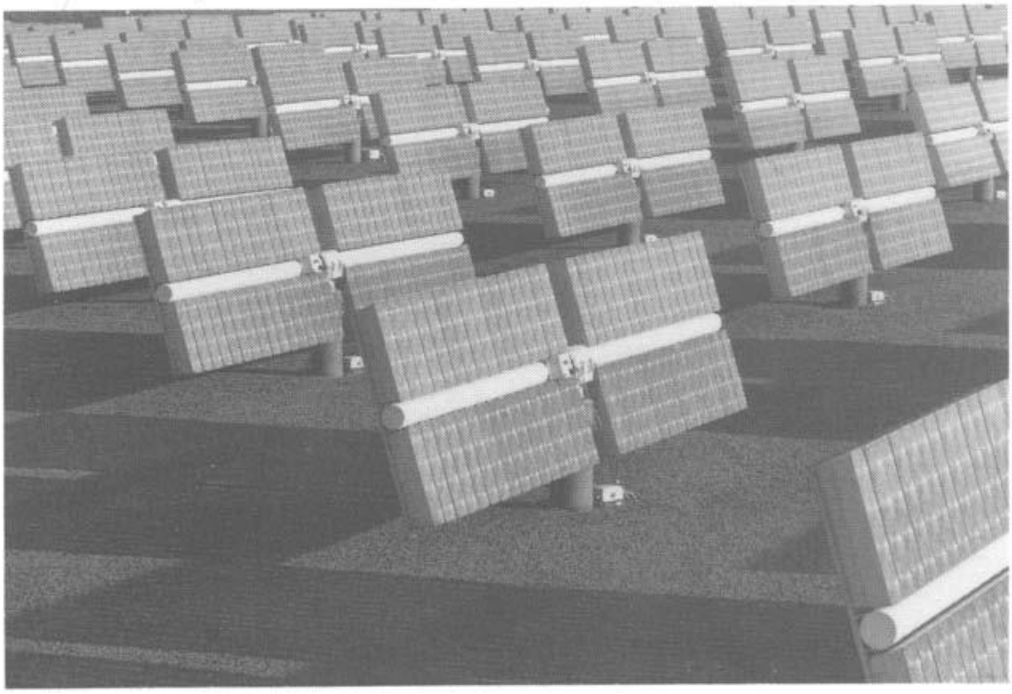

Figure 1.10: Solar Village concentrator PV system in Saudi Arabia [24].

Despite the early and successful implementation of renewable energy projects and gaining wide experience in different applications, progress in utilisation of solar energy in Saudi Arabia slowed down in the last few decades due to several reasons such as:

i. The end of oil crisis.

ii. The wide availability of oil at low cost compared to solar energy.

iii. The governmental substantial subsidies for oil and electricity generation and non-availability of such subsidies for solar energy programs.

iv. The dust accumulation effect; about 50% and more decrease in power output can be experienced if no cleaning is performed on PV modules for a long period of time [13,27,28].

v. High ambient temperature; outdoor experimental study on silicon PV modules reveals that more than 30% decrease in power generation can occur during summer time [29].

In recent years, the interest in renewable energy options has risen as the country’s oil and gas consumption has dramatically increased. Figure 1.11 indicates the annual addition and cumulative PV installed capacity between 2002 and 2008 in Saudi Arabia. According to BP Solar Company in Riyadh, Saudi Arabia, the total PV installed capacity reached about 4 MW in 6 years i.e. from 2002 to 2008 [30].

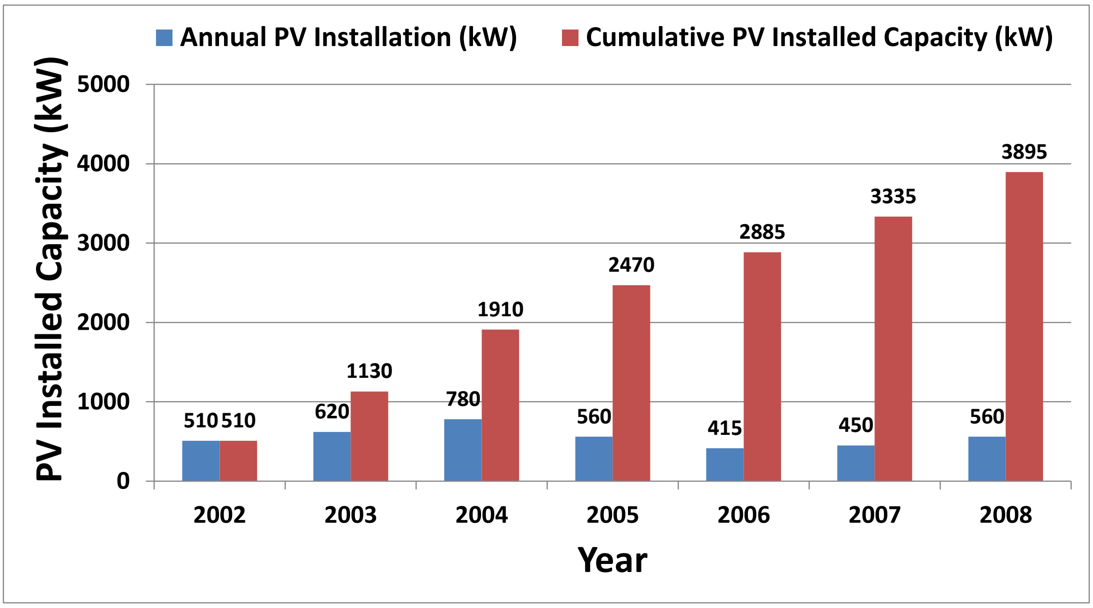

Figure 1.11: Annual addition and cumulative PV installed capacity between 2002 and 2008 in Saudi Arabia [30].

The country has to use its current wealth to reduce the dependence on fossil fuel by developing alternative energy sources. In this regards, researchers have welcomed the establishment of KACARE in 2010 to serve as a centre for renewables research and for coordinating national and international energy policy. Also, some universities established research centres focusing on sustainable and renewable energy. All these recent institutions are expected to play a major role in utilizing and developing renewable sources of energy besides reconstructing energy policies in the Kingdom [23]. Moreover, the Kingdom of Saudi Arabia has started building the first solar powered seawater desalination plant on the Arabian Gulf as a new research collaboration project between KACST and IBM initiated in 2010 which could substantially reduce water and energy costs [25]. This is the first step in a three-part program to introduce solar energy into the Kingdom [31,32]. The expected production capacity of this energy efficient desalination plant is 30,000 cubic meters per day to serve

100,000 people located in Al Khafji city. KACST plans to power the desalination plant using the Ultra-High Concentrator Photovoltaic (UHCPV) technology with a concertation ratio greater than 1500 suns, which is jointly developed by IBM and KACST. This is besides working on improving polymeric membranes through nanoscale modification of polymer properties to make seawater desalination using reverse osmosis, which is most commonly used in Saudi Arabia besides multi-stage flashing system, more efficient and less costly. The goal of this project is to reduce the cost of desalinating seawater which is ranging from 2.5 to 5.5 Saudi Riyals per cubic meter by combining solar power and the new nano-membrane [31,32].

1.4. Future trends of solar energy applications in Saudi Arabia

A new solar monitoring network in Saudi Arabia was established by KACARE in 2013 to assess the solar radiation resources. The solar monitoring network has 30 stations distributed across the country based on one-minute measurements of Global Horizontal Irradiance (GHI), Diffuse Horizontal Irradiance (DHI), Direct Normal Irradiance (DNI) and related meteorological parameters. The most important component of the sun light for CPV systems to be feasible is the DNI. The first year set of measurement (October 2013 - September 2014) was collected from those stations and analysed [22]. It was found that the total daily average DNI in Saudi Arabia is 6047 Wh/m^2 i.e. about 2207 kWh/m^2/year. According to more than one study [22,33,34], the DNI levels needed to be appropriate for concentrating solar technologies at current prices is >1800 kWh/m^2/year where all regions of the country have exceeded this number [22].

One of the lessons learned from the 350kW solar village CPV system project is that large-scale CPV may not be economically viable when operated as stand-alone systems due to the high cost of electrical energy storage [13]. However, these systems can be more cost-effective if they are connected directly to the electrical grid [13]. Moreover, since year 2000 interest globally shifted towards small scale, grid connected and building integrated PV (BIPV) applications [25,35]. Almost no CPV projects for residential applications have been investigated in Saudi Arabia which can be a promising technology to provide an alternative source of electrical energy. Research on CPV systems in Saudi Arabia is needed to help in boosting the solar applications in the region, which is one of the aims of this study.

1.5. High Concentrator Photovoltaic/Thermal (HCPV/T) system

Solar PV power has been one of the fastest growing renewable energy technologies, and it is anticipated that this technology will play a major role in the future of global electricity generation [35]. However, PV technology is more expensive than the energy generated from conventional sources. CPV system has the potential to replace the expensive PV material with cheaper optical elements such as lenses and mirrors [36]. Point-focus Fresnel lens concentrator has been widely used in HCPV systems with many advantages over any other concentrators such as small volume, light-weight, mass production with low cost and effectively increasing the energy density. Integrating Fresnel lenses in CPV systems can lead to achieving high concentration ratios exceeding 100 suns, hence called high concentrator PV (HCPV). The new PV technology, generation III-V multi-junction (MJ) solar cells with efficiencies exceeding 40% at high concentration are normally integrated in HCPV systems since they are more efficient, have a better response to high concentration and lower temperature coefficient [37]. HCPV technology has attracted more attention especially after introducing these solar cells for terrestrial applications as they keep hitting new conversion efficiency records. However, point-focus concentration will cause high and non-uniform PV cell surface temperature which reduces the output power from the cell and ultimately degrades its life [25]. Therefore, effective cooling is necessary to dissipate the heat load from the solar cell surface and maintain the peak performance at all conditions [38]. High concentrator Photovoltaic/Thermal (HCPV/T) principle using water as a coolant can enhance the overall efficiency of the system by utilising the absorbed thermal energy in different applications [39].

1.6. Aims and Objectives

Unlike crystalline-silicon technology, high concentrator Photovoltaic/Thermal (HCPV/T) integrating multi-junction solar cell is an emerging technology and research in this area is at its early stages. Although there are many issues related to the operation of the HCPV system, there are only few reports characterising its performance outdoors and even less on point-focus Fresnel systems where the concentration ratio can reach up to 1000X [40]. HCPV/T systems consist of four main components: solar concentrator, solar cell, cooling mechanism and tracking system. In this study, a comprehensive investigation including optical, electrical and thermal analysis of a developed single HCPV/T will be carried out for the Fresnel lens, triple-junction solar cell and cooling system respectively by simulation and experimental testing. The HCPV/T system will be tested under United Kingdom climate conditions but the study will be extended to predict its performance in the harsh environment of Saudi Arabia where ambient temperature can reach up to 50°C in the summer time [41].

This research project aims to develop and characterise a HCPV/T system for electricity and heat energy generation with the following objectives:

- Develop an optical model using ray tracing method able to evaluate and optimise the optical efficiency of the concentrator system.
- Evaluate and optimise the incident irradiation uniformity on the solar cell surface.
- Develop an electrical model capable of examining the performance of the multi-junction solar cell under different concentration ratios and surface temperatures.

- Develop a thermal model using Finite Element Analysis (FEA) technique able to predict the solar cell surface temperature under different solar irradiations and ambient temperatures.
- Study the performance of the HCPV/T cooling system to maintain the PV surface temperature and to utilise the output thermal energy carried by the coolant for different thermal applications such as solar thermal water desalination, solar cooling and air-conditioning using Computational Fluid Dynamics (CFD).
- Develop a single, small scale and light weight HCPV/T system including point-focus Fresnel lens, multi-junction solar cell and cooling mechanism for outdoor optical, electrical and thermal performance investigation.
- Conduct outdoor and indoor experimental work to validate the developed optical, electrical and thermal models.
- Study the feasibility of passive and active cooling in harsh environment like Saudi Arabia to maintain the multi-junction HCPV surface temperature below the operating temperature limit recommended by the manufacturer using CFD/FEA.
- Predict the annual electrical and thermal power yield of a single and multi HCPV/T systems in Saudi Arabia.

1.7. Thesis Outline

This thesis presents a comprehensive analysis of the performance of a high concentration multi-junction photovoltaic thermal system (HCPV/T). Optical, electrical and thermal modelling was conducted under a variety of concentration ratios and ambient temperatures. Technical issues related to HCPV/T systems including high surface temperature, non-uniform irradiation and small acceptance angle will be described as well. Hence, the contents of this thesis can be summarized as follows:

Chapter One contains brief discussion of the world's energy issues, Saudi Arabia's energy issues and the solar energy research implemented in Saudi Arabia. It also contains brief introduction of the HCPV/T and the general thesis overview.

Chapter Two reviews the research reported on the HCPV/T in terms of history and future trends, HCPV/T components design approach, performance enhancement techniques and applications, HCPV/T related challenges and experimental as well as numerical studies.

Chapter Three presents a detailed procedure for developing an outdoor single HCPV set-up and details of all measuring devices used for optical, electrical and thermal investigations.

Chapter Four describes an investigation of the performance of a HCPV optical system in terms of optical efficiency and incident irradiation uniformity with and without secondary optical element using ray tracing software. Moreover, it describes the validation of the developed optical simulation using outdoor experimental set-up.

Chapter Five presents the optimisation process of the HCPV optical system and performance evaluation in terms of optical efficiency and incident rays uniformity with and without secondary optical element. In addition, it shows the simulation results investigating the effect of increasing the incident ray angle on the HCPV optical efficiency and the evaluation of the acceptance angle with and without secondary optical element. Moreover, different assembly configurations of more than one HCPV system will be investigated to examine the possibility of saving space and cost.

Chapter Six presents the development of an electrical model using Engineering Equation Solver (EES) to evaluate the performance of multi-junction solar cell. The model was calibrated against the solar cell manufacturer indoor experimental data. Also, it describes the comparison of electrical model results with the outdoor experimental outputs.

Chapter Seven describes the development of a HCPV/T thermal model and cooling system using FEA and CFD. Also, it presents a technical feasibility study results of passive and active cooling for HCPV in harsh environment of Saudi Arabia.

Chapter Eight describes the conclusions drawn from the research work conducted and proposed future work.

CHAPTER 2

Literature review

2.1. Introduction

This chapter presents a detailed literature review of research work regarding concentrator Photovoltaic systems in general and more specifically on High Concentrator PV/Thermal (HCPV/T) systems. It begins with a brief introduction to concentrating solar thermal and PV. Then, it presents a brief history and progress in CPV technology and the future trends. Also, a detailed literature review on each component of HCPV/T i.e. concentrator solar cells, solar concentrators, tracking systems and cooling mechanisms will be reported. Moreover, the experimental and numerical performance studies of HCPV/T with the associated challenges are reviewed as well.

2.2. Solar Energy Technologies

Solar technology is generally divided into two categories: thermal and photovoltaic. Solar thermal refers to the process of converting solar radiation into heat by the use of a solar thermal collector, while Photovoltaic involves conversion of the solar radiation directly into electricity by the use of a solar cell. Concentrating Solar Thermal (CST) and Concentrating PV (CPV) systems, use either mirrors or lenses to concentrate solar radiation to produce forms of useful energy such as heat or electricity. Unlike flat plate Photovoltaics (PV), CSP systems are not able to use solar radiation that has been diffused but only capture the direct beam component. Therefore, this technology is more suited in sites with high beam radiation and clearness index. The CSP technologies that are currently used commercially in order of deployment level are [33]:

- Parabolic trough
- Central receiver tower

- Linear Fresnel reflectors
- Fresnel lenses with CPV
- Parabolic dishes

Figure 2.1 shows four CSP technologies: parabolic trough, central receiver tower, linear Fresnel and parabolic dish. Each technology has particular advantages and therefore project and technology developers are actively pursuing all types of CSP technologies.

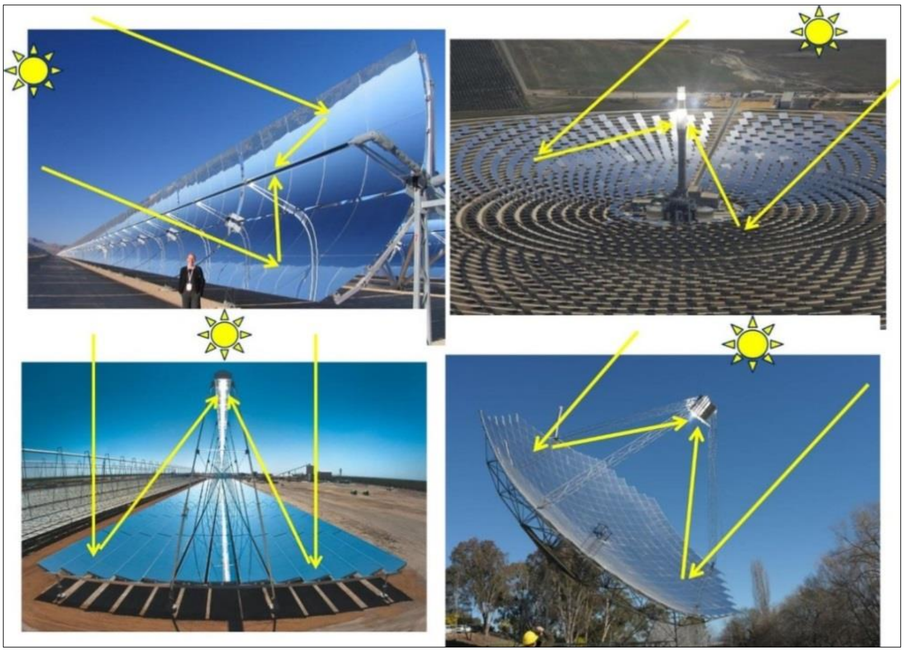

Figure 2.1: From left to right; Parabolic trough, Central receiver tower, Linear Fresnel and Parabolic dishes [42].

Figure 2.2 shows Fresnel lenses for CPV technology with the sun’s radiation concentrated on semiconductor material i.e. PV to generate electricity. A detailed review on CPV technology will be introduced in the following sections.

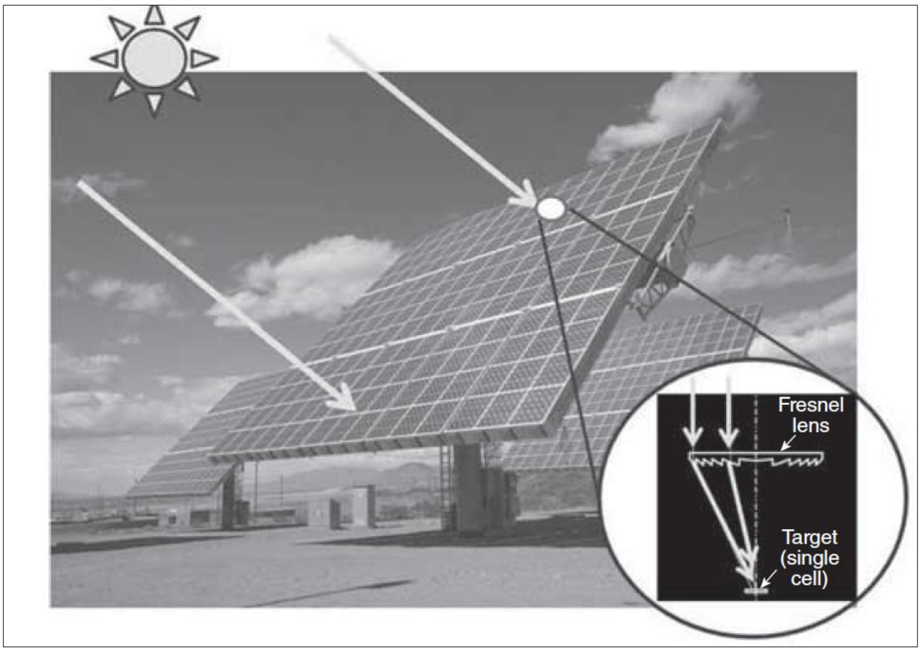

Figure 2.2: Fresnel lens-based CPV array [33].

2.3. Concentrator Photovoltaic (CPV) technology

2.3.1. Introduction

The main challenge of using PV is the high initial cost when compared to electricity generated from conventional sources. In order to increase the efficiency of solar power generation and make it more cost effective, different methods have been considered in the past and several approaches have been introduced and investigated. Sun tracking is one of these methods which can enhance the total collected energy from the sun [43]. Other approach for cost reduction in solar power generation is using mirrors, reflectors or lenses to concentrate the incoming solar irradiation on the PV cell [36,44]. CPV systems replace the expensive semiconductor PV material with cheaper material such as glass, mirror and plastic to focus a large area of sunlight onto the small area of solar cell. CPV are categorised based on the amount of solar concentration into three groups including low (LCPV), medium (MCPV) and high concentration (HCPV).

CPV systems operate efficiently in areas with a high direct solar irradiation since diffuse light, which falls on earth after being scattered by haze, clouds, etc., cannot be concentrated. As the concentration level goes higher, the need for using accurate tracking and appropriate cooling systems becomes more important. Although concentration of direct solar irradiation can increase the power output, PV surface temperature increase is an issue as PV efficiency is inversely proportional to the PV surface temperature [25]. Several studies have been carried out to determine the most efficient method for PV cooling including passive and active cooling methods. Active cooling is in general more effective in reducing PV surface temperature but at the same time more costly. However, using Photovoltaic-Thermal collectors principle (PV/T) where water or air passing through channels at the back side of the PV panel can be more economically feasible if the removed heat by the cooling fluid is utilised in different thermal applications as this can add to the overall efficiency of the PV/T system [39].

Multi-junction (MJ) solar cells are recently favoured over single junction cells to be integrated in CPV systems as they are more efficient, have a better response to high concentration and lower temperature coefficient. The new technology, generation III-V multi-junction solar cells, offer high efficiencies exceeding 43% at high concentration compared to traditional solar cells made of a single layer of semiconductor material [37].

In this thesis, optical, electrical and thermal modelling are undertaken to develop HCPV/T system and characterise its performance. Tracking system performance analysis is not a part of this thesis but it will be reviewed in this chapter.

2.3.2. Brief history and progress in CPV technology

In the 70s, the idea of substituting the expensive PV cells with cheaper optical elements became an attractive option. The research and development of CPV technology effectively started at the Sandia National Laboratories in 1975 when a national program launched in the

USA to develop ideas and concentration photovoltaic prototypes was encouraged by the oil crisis in 1973 [25,45,46]. Almost all types of concentrating technologies were explored during this period including reflective dishes (Boeing), reflective troughs (Acurex), point-focus Fresnel lenses (RCA, Varian, Motorola, Martin Marietta), linear Fresnel lenses (E-Systems) and compound parabolic concentrators (Sun Trac, University of Chicago) [45]. At that time, system efficiencies for these developed prototypes ranged from 5% for the reflective trough systems to 10% for point-focus Fresnel lens systems [45,47]. Despite the rapid progress of CPV technologies in the 80s, the research and development in this area slowed down in the next few decades due to several reasons: the end of the oil crisis which was the initial motivation for developing CPV technologies, the absence of any significant breakthrough, the market was not prepared to build the large facilities that CPV systems require like tracking systems and the need to economically compete at this scale with the energy produced by conventional power stations [25,45,48,49].

At the present time, CPV technology is back into business and more companies are coming forward to introduce CPV systems for two reasons: PV production and application have grown to a size where larger systems are desirable and significant increase in the solar cells performance with efficiencies of more than 40%, which in the future may reach 50% [25,45,50]. On the other hand, there is also interest in smaller scale applications as many CPV systems were developed for building integration (BIPV) like façade applications, sky lighting, wall curtains and few other applications still under development [25,51]. BIPV and power generation remain the most important applications employing CPV systems [25].

2.3.3. Current and future status of CPV technology

The key principle of CPV technology is the use of cost-efficient optical elements that significantly reduce the solar cell area facilitating the use of high efficiency more expensive cells. This key principle allows CPV to be cost competitive compared to CST and standard flat-plate PV technology in certain sunny regions where Direct Normal Irradiance (DNI) is high [50]. HCPV systems were mostly integrated with crystalline silicon (c-Si) concentrator cells before 2008, but III-V multi-junction solar cells have since become standard [50]. Concentrating the sun light by a factor of more than 100X onto a small area enables the use of highly efficient but relatively expensive multi-junction solar cell based on 3-4 layers of different semiconductor materials. Those with concentration ratio below 100X i.e. medium and low concentration systems are also being deployed mainly with c-Si solar cells and single-axis tracking although dual axis tracking can also be used. The popularity of the HCPV is due to the significant increase in the efficiency of individual modules which ultimately leads to a reduction of area-related system costs. A CPV module efficiency of 38.9% at Concentrator Standard Test Conditions (CSTC) was demonstrated by Soitec [52] in 2015 and efficiencies of commercially available CPV modules exceed 30% [50]. Moreover, CPV system efficiencies have also increased reaching 25-29% and CPV companies anticipate further increases in efficiency for CPV system to more than 30% in the near future driven mainly by improvements in cell efficiency and the optical efficiency of the concentrators [50,53]. Figure 2.3 demonstrates the CPV cell, CPV module and CPV system efficiency roadmap from 2007 to 2020. It is anticipated that the cell, module and system efficiencies of CPV reach to 50%, 40% and 35% respectively in 2020.

A typical CPV system consists of the following main components: solar PV, solar concentrator, tracking mechanism and a cooling system. A detailed review on CPV components will be introduced in the following sections. The overall performance of the CPV system depends on how efficiently each of these components performs independently and collectively.

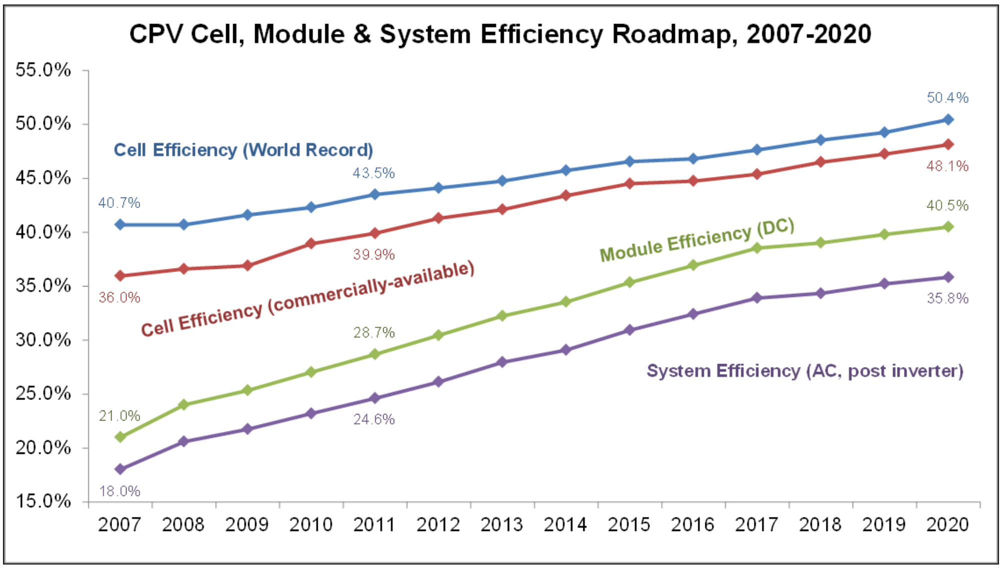

Figure 2.3: CPV cell, module and system efficiency roadmap, 2007-2020 [54].

2.4. Solar Photovoltaics for CPV

2.4.1. Introduction

Significant progress has been made towards the development of solar cells in the last few decades. Researchers have made efforts not only to improve the existing solar cell efficiency but also to develop solar cells from different semiconductor materials. Today, the highest efficiency of silicon solar cells is more than four times the 6% in 1954 i.e. ~25.0% as demonstrated in Figure 2.4 [55,56]. Various solar technologies and their progress in the last 40 years have been summarised in a single graph plotted by the National Renewable Energy Laboratory (NREL) as shown in Figure 2.4. These technologies including crystalline silicon (c-Si) such as mono and multi crystalline, Gallium Arsenide (GaAs), Thin-Film such as Copper Indium Gallium Selenide (CIGS), Cadmium Telluride (CdTe) and Amorphous silicon (a-Si), multi-junction cells and new emerging PV such as dye-sensitized and organic solar cells.

Generation III-V four-junction solar cells based on four different semiconducting materials currently hold the world record efficiency of 46% under concentrated sunlight of 508 suns by Fraunhofer Institute for Solar Energy Systems (Fraunhofer ISE) [50,55–57]. Moreover, the maximum efficiency of a triple junction InGaP/GaAs/InGaAs (Indium Gallium Phosphide/Gallium Arsenide/ Indium Gallium Arsenide) solar cell has been reported to be 44.4% for intensity of 302 suns [56,58].

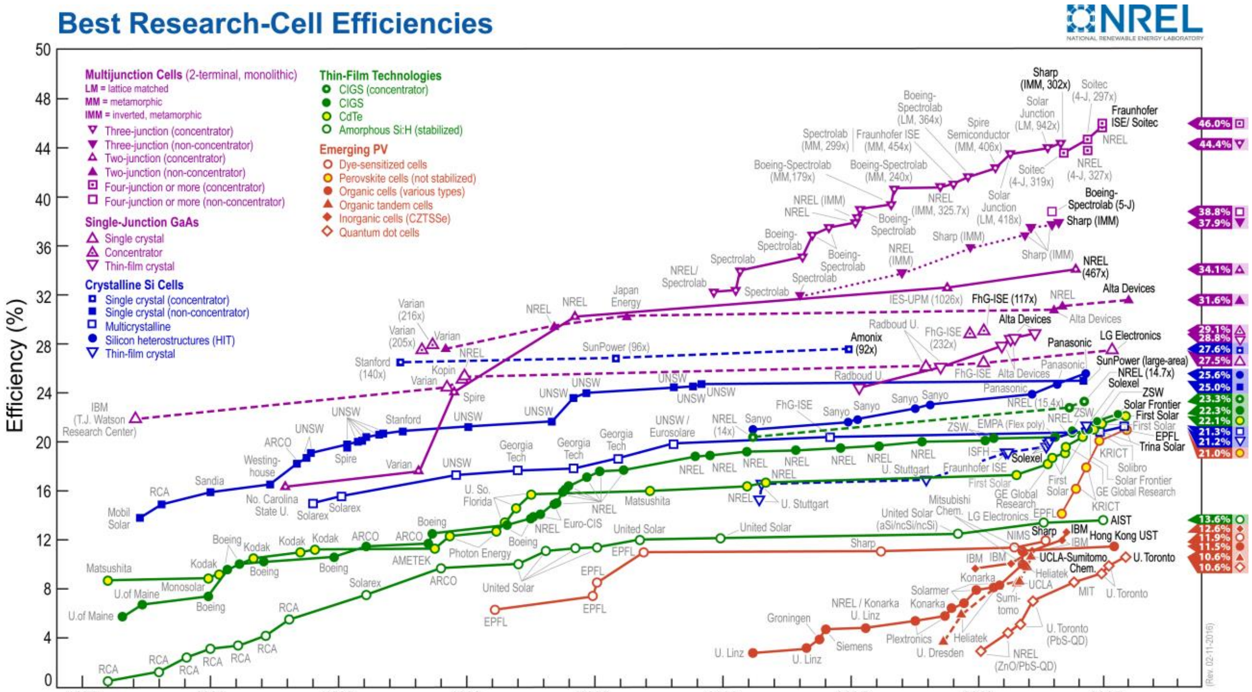

Figure 2.4: Best research-cell efficiencies through end of 2015 [55].

2.4.2. The sun spectrum

The intensity of solar radiation reaching the earth surface is dependent on the latitude of the observer and varies with the time throughout the day and the year; this is defined by the air mass (AM). When the sun is at zenith (i.e. $\theta = 0^o$), the spectrum is termed as AM1 at sea level. With the change in sun position from zenith, depending on the angle (θ) the air mass is given by [59]:

$$Air\ mass = \frac{1}{\cos\theta} \tag{2.1}$$

The solar industry uses AM1.5 (i.e. $\theta = 48.2^o$) and radiation intensity of 1 kW/m^2 for all standardized testing or rating of terrestrial solar cells or modules including those used in concentrating systems.

The solar radiation received by the earth is in two forms: direct (beam) and diffuse; the sum of those two values on plane is called global radiation:

$$Global\ radiation = Direct\ radiation + Diffuse\ radiation \tag{2.2}$$

CPV systems are more feasible in areas of the world where the direct component of the light is high like Middle East and North Africa (Sunbelt region). Spectral distribution of the sun light is also important for the photovoltaic power generation. The global radiation has a different spectrum than the direct radiation as shown in Figure 2.5.

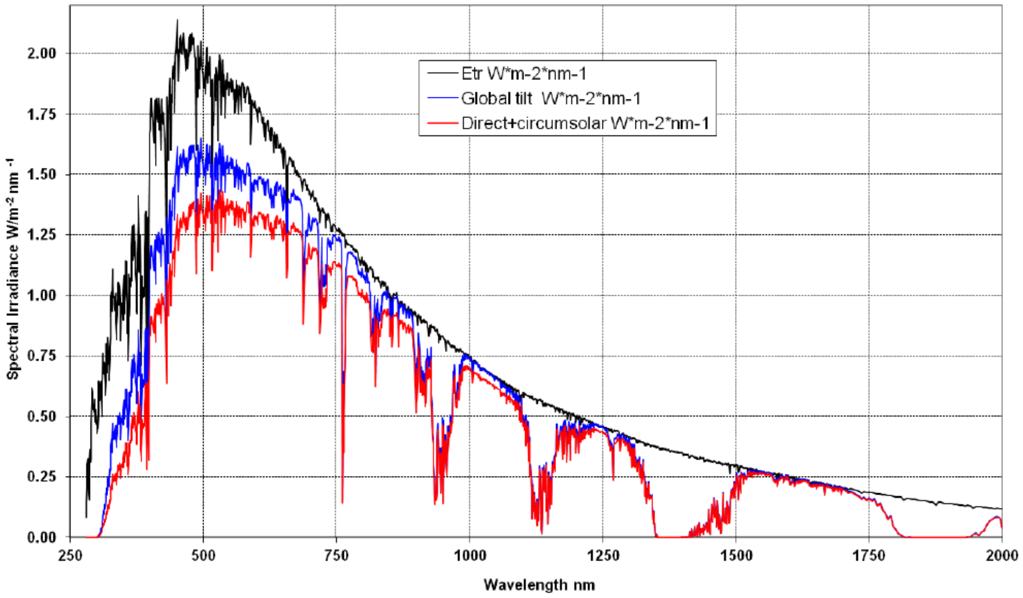

Figure 2.5: Extra-terrestrial and terrestrial global and direct solar spectrum [60].

The highest spectrum in the Figure above is for the extra-terrestrial radiation which reaches outside the earth atmosphere. The internationally accepted extra-terrestrial intensity of solar radiation is 1.353 kW/m^2 [59]. The spectrum of the sun outside the atmosphere is called AM0.

2.4.3. Fundamentals of solar cells

The solar cell operation is based on the ability of semiconductors to convert the incident sunlight energy directly into electricity by taking advantage of the photovoltaic effect [61]. Photovoltaic energy conversion depends on the quantum nature of light whereby light is identified as a flux of particles called ‘‘photons’’ which carry energy as given by the following equation [61]:

$$E_{ph}(\lambda) = \frac{hc}{\lambda} \tag{2.3}$$

The energy of a photon is a function of the wavelength of light λ (and thus also of the frequency), h the Planck constant $6.6256\times10^{-34}\mathrm{Js}^{-1}$ and c the speed of light. On a clear day, about 4.4×10^{17} photons are received every second by a square centimetre of the earth's surface [61]. The solar cell only gets advantage of photons with energy in excess of the semiconductor material band gap to generate electricity [61]. The energy band gap can be defined as the energy needed to produce electron excitation and to activate the PV process [62]. The nature of this absorption process indicates that a part of the photon energy is lost; it is seen that practically all the generated electron-hole pairs have energy in excess of the material bandgap [61]. After the creation of electron-hole pairs, the electron and hole decay to states near the edges of their respective bands; therefore the excess energy is lost in the form of heat and cannot be utilised into useful power. Moreover, this heat negatively affects the performance of the solar cell which represents one of the fundamental loss mechanisms in a solar cell [61].

For practical purposes, a pure semiconductor (which is called intrinsic) is considered to be an insulator as it contains just the right number of electrons to fill the valence band and therefore the conduction band is empty. One way to enable the semiconductor to conduct electricity is by alloying the semiconductor with an impurity; this process is called doping [61]. Doping makes it possible to control the electronic properties of a semiconductor which is the heart of the manufacturing process of all semiconductor devices [61]. If phosphorous atoms (group 5 impurity atoms) are added to the silicon melt from which the crystal is grown, four of the five outer electrons are used to fill the valence band and the extra electron from each impurity atom is promoted to the conduction band. Therefore, these impurity atoms are called donors. The electrons in the conduction band are mobile and hence the crystal becomes a conductor.

This type of semiconductor is named n-type. A similar concept occurs when silicon is doped with Boron atoms (group 3 impurity atoms) which are called acceptors. Since four electrons per atom are needed to fill the valence band completely, this doping creates a hole for each impurity atom which behaves as positively charged mobile particle. This type of semiconductor is named p-type [61]. The mobile charges within the semiconductor generated by the incident light can be separated by device structure or in the junction to produce an electric current [59,63–66]. The operation of a solar cell is basically based on the formation of two junctions i.e. p-type and n-type junctions of the semiconductor (Figure 2.6) [59,61]; the p-n junction can be defined as an interface between the n and p regions of one semiconductor. When p-type and n-type semiconductor are in contact, few surplus electrons near the junction in n-type will diffuse into p-type leaving behind positive charge in n-type [59,61]. Likewise, in p-type few holes diffuse from p-type to n-type leaving behind negative charges in the p-type. This will create a strong electric field at the junction; this field is generated in the opposite direction to the electron-hole flow and balances further flow of the electron and holes [59,61]. When light is incident on the PV, electron-hole pair is generated on both sides of the junction. The generated minority carriers of both sides diffuse to the junction and then swept away by the electric field at junction which produces a current [59].

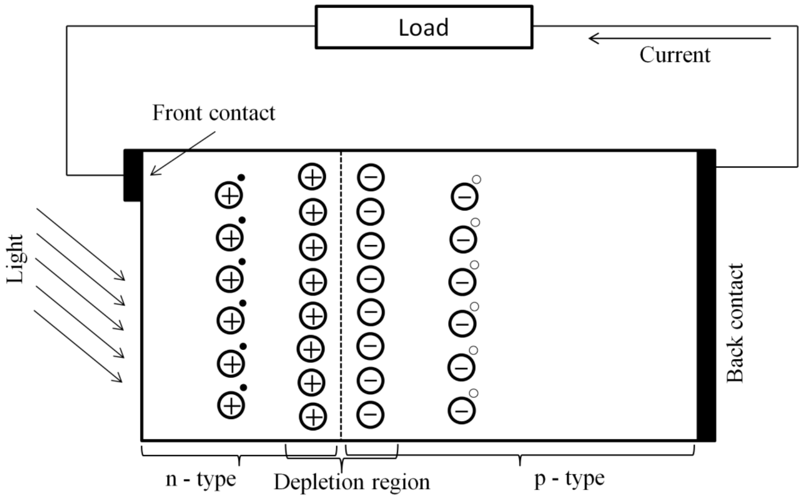

Figure 2.6: Schematic diagram of the solar cell circuit [59].

2.4.4. Classifications of the PV technologies

At the present time, there are a wide range of PV cell technologies available on the market using different types of materials and different manufacturing processes employed to make these solar cells. Depending on the technology, the conversion efficiency and life time also varies from cell to cell. PV cell technologies are usually categorised into three generations depending on the basic material used and the level of commercial maturity [62]:

- **First generation PV systems:** these systems are fully commercialised and use the wafer-based crystalline silicon (c-Si) technology.
- **Second generation PV systems:** these systems are at early market deployment and are based on thin film PV technologies.
- **Third generation PV systems:** these systems are emerging PV technologies which are either under demonstration or have not been widely commercialised. The most mature third generation PV technologies are [61]: Dye-sensitized solar cells (DSSC), organic solar cells and concentrating PV (CPV).

In CPV systems special kinds of solar cells are necessary since they are operated at high concentration and elevated temperatures. These concentrator cells differ from one-sun cells in many ways including the method of manufacture, the overall cell design and their performance. The bus bars in concentrator solar cells are generally around the perimeter of the cell as they can be accommodated without blocking any of the incoming light [25,67]. Due to the high concentration received, a concentrator cell is designed to generate higher output current. This output current can be transferred well if the series resistance of the cell allows its flow [68]. Low series resistance cell needs proper metallisation. Screen printed silicon solar cells may reduce the output power at higher illuminations due to the high series resistance for this kind of metallisation [60,69]. Depending on the concentration ratio, the type of solar cells to be used in CPV can be a single junction cell [70–76] or a multi-junction solar cell [77–79].

Single junction solar cells can be integrated with line focused concentrator. Moreover, low and medium concentration systems are employing high quality single junction silicon cells which are cost effective as their manufacturing are not much different from those used in conventional PV panels. These solar cells can be manufactured by making improvements in material quality to have longer minority carrier lifetime, proper grid design, light trapping and improved surface passivation [25,75]. There are three different silicon based solar cell types applicable to use with concentrators: Laser Grooved Buried Contact (LGBC), Back Point Contact (BPC) and Silver solar cells [60].

Multi-junction solar cells III-V are needed for applications demanding high concentrations such as point-focused systems which can perform under high concentration and extreme temperatures for a long period of time. Power generation is the main application of these types of systems where the high investment gets paid off [25]. Multi-junction solar cells have been studied since 1960 [80,81]. The first multi-junction device was demonstrated for space applications in late 1980s with electrical conversion efficiency of 18.5% [82]. In 1994, US NREL broke the 30% efficiency barrier in the concentration range of 115-260 suns [47,81,83]. These cells are made by semiconductor compounds from group III and V of the periodic Table such as Gallium Arsenide which offer the highest PV conversion efficiency [8,57,58,62]. Multi-junction solar cells consists of a stack of layered p-n junctions each made from different set of semiconductors with different band gap and spectral absorption to capture as much of the solar spectrum as possible. Stacked configuration is the generally preferable approach to arrange the semiconductor cells in a way that the sunlight strikes the highest band gap first and then goes to the lower band gap junctions [84].

Figure 2.7 shows the difference between single junction silicon and triple-junction solar cell in utilising the solar spectrum. Ge (0.67 eV), GaAs or GaInAs (1.18 eV) and GaInP (1.70 eV) are the most commonly employed semiconductors in a triple junction solar cell due to their high optical absorption coefficients and good values of minority carrier lifetimes and mobilities [62,84,85]. The first layer (GaInP) converts the short wavelength portion of the spectrum while the second layer (GaAs or GaInAs) captures the near-infrared light and the third layer (Ge) absorbs the lower photon energies of the infrared radiation.

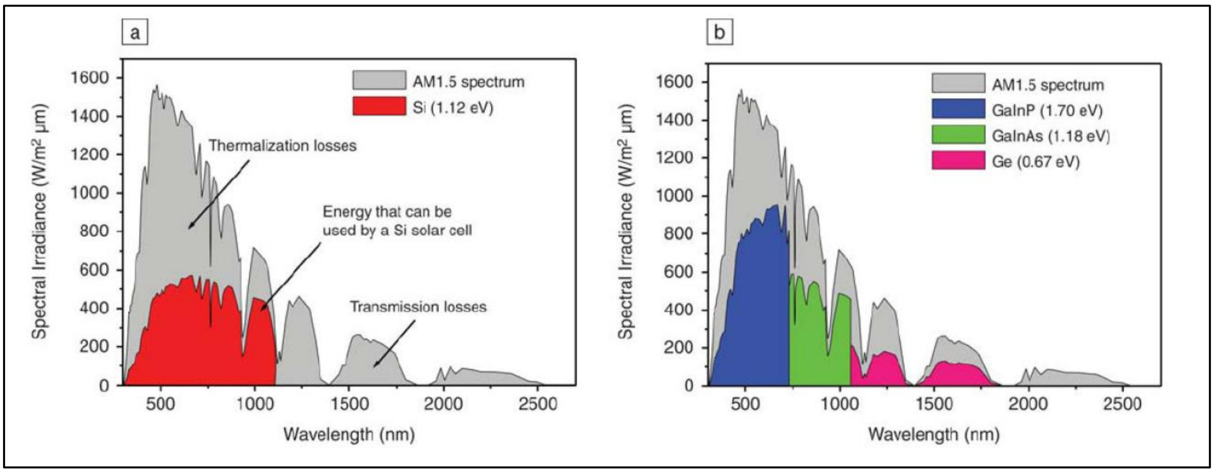

Figure 2.7: The solar spectrum and the parts of the spectrum that can, in theory, be used by: (a) Si solar cells; (b) $Ga_{0.35}In_{0.65}P/Ga_{0.83}In_{0.17}As/Ge$ solar cells [81].

Figure 2.8 shows the physical schematic of triple junction solar cell and the electrical circuit equivalent diagram showing top, middle and bottom junction diodes and interconnecting upper and lower tunnel junctions [86].

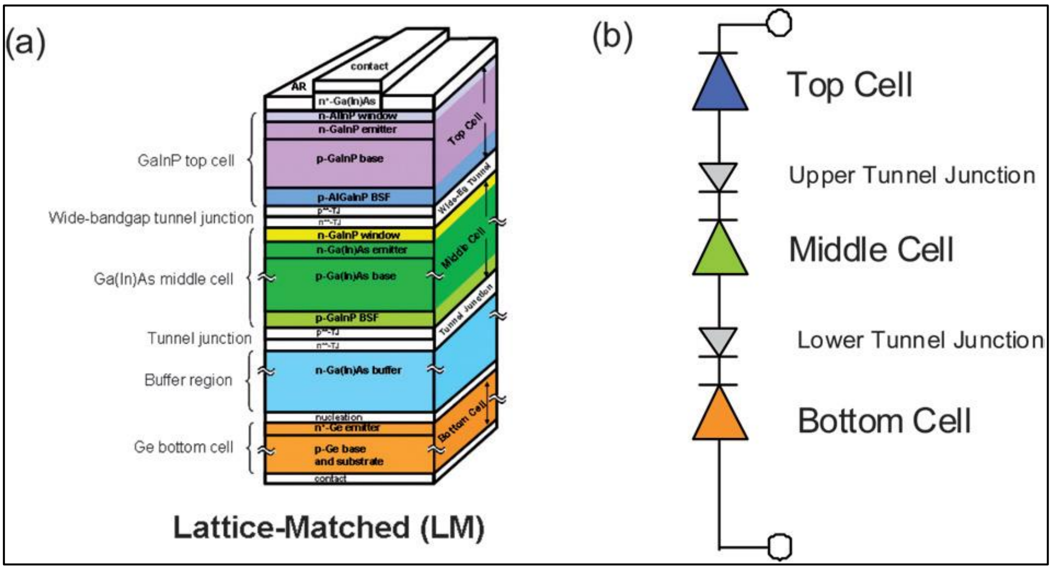

Figure 2.8: (a) Structure of a triple-junction PV cell. (b) The electrical circuit equivalent diagram [86].

Henry [87] calculated the terrestrial multi-junction solar cell limiting theoretical conversion efficiency under 1000 suns concentration and with the solar cell held at room temperature with 1, 2,3 and 36 band gaps; the respective efficiencies were 37, 50, 56 and 72%. Therefore, this technology can be considered to be the most promising one among other PV technologies.

2.5. Electrical performance characterisation of a multi-junction solar cell

2.5.1. Solar cell I-V curve characterisation

I-V curve, as shown in Figure 2.9, is an important tool to characterise the electrical performance of a typical solar cell. This curve includes many important electrical parameters of the solar cell. These electrical parameters are V_{OC} (open circuit voltage), I_{SC} (short circuit current), I_m (current at maximum power), V_m (voltage at maximum power), P_m (maximum power), P_T (theoretical maximum power) and FF (Fill Factor).

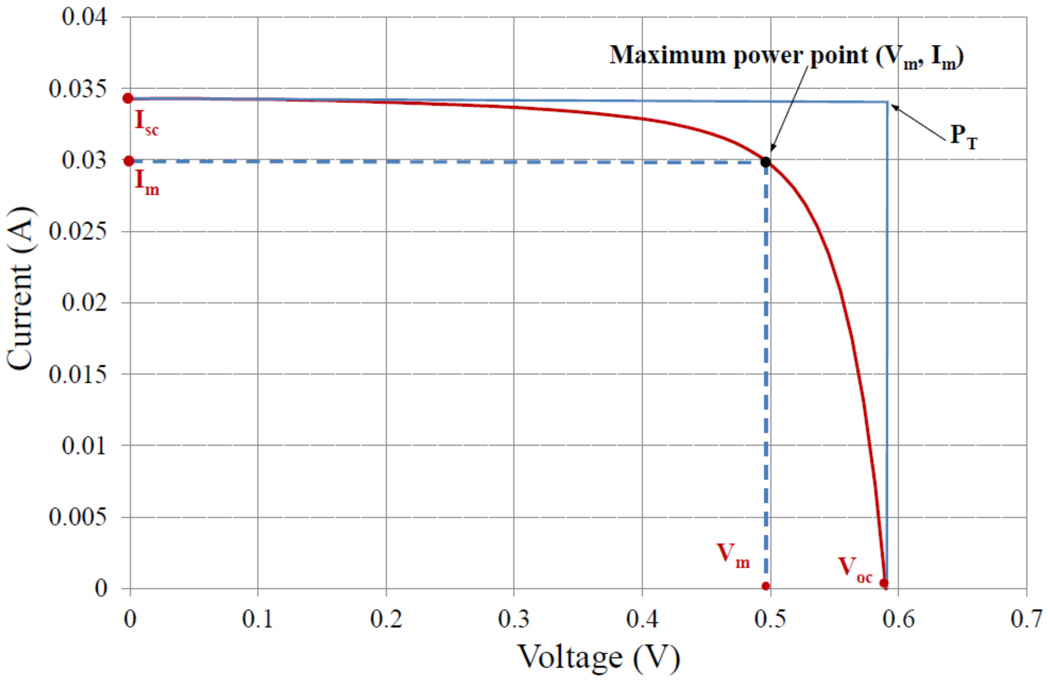

Figure 2.9: Typical I-V curve of a solar cell connected to variable resistive load [88].

2.5.1.1. Short Circuit Current (I_{SC})

Short Circuit Current (I_{SC}) is the maximum amperage generated by a solar cell exposed to sunlight with the output shorted i.e. I at $V= 0 = I_{SC}$. The short circuit current is corresponding to the short circuit condition when the resistance is low and the voltage is equal to zero. Figure 2.9 shows the short circuit current on the y-axis.

2.5.1.2. Open Circuit Voltage (V_{OC})

Open Circuit Voltage (V_{OC}) is the maximum voltage generated by a solar cell exposed to sunlight with no load connected. It occurs when the current passing through the cell is zero i.e. V at $I = 0 = V_{OC}$. Figure 2.9 shows the open circuit voltage on the x-axis.

2.5.1.3. Maximum Power (P_m), Current at P_m (I_m), Voltage at P_m (V_m)

The maximum power produced by the solar cell exposed to sunlight in Watts is called the maximum power (P_m) determined by the product of I_m and V_m as:

$$P_m = I_m \times V_m \tag{2.4}$$

In order to achieve the maximum efficiency from the system, the PV solar cells must be operated at their Maximum Power Point (MPP). But, the MPP is directly influenced by the illumination spectrum, radiation and temperature of the solar cell [89]. Therefore, to maintain the maximum output from the PV system a control of P_m is needed [88].

2.5.1.4. Fill Factor (FF)

The Fill Factor, FF, is the ratio of the actual rated maximum power (P_m) to the theoretical maximum power (P_T) as shown in Figure 2.9. It is a measure of the quality of the solar cell which mainly depends on the device’s series and shunt resistances. P_T can be calculated using the following equation which is a product of V_{OC} and I_{SC}:

$$P_T = V_{OC} \times I_{SC} \tag{2.5}$$

The *FF* can be calculated from the following equation:

$$FF = \frac{I_m \times V_m}{I_{SC} \times V_{OC}} \tag{2.6}$$

The *FF* is a key parameter to evaluate the performance of solar cells and panels. Typical commercial multi-junction solar cell have a *FF* >0.8 [90,91].

2.5.1.5. Electrical Efficiency (η_{elec})

Electrical efficiency of the solar cell is the ratio of the power output (P_{out}) to the solar power input i.e. (P_{in}) into the PV cell. P_{out} in this case will be P_m while P_{in} is the product of the irradiance of the incident light measured in W/m^2 with the surface area of the solar cell in m^2 as shown in the following equation:

$$\eta_{elec} = \frac{P_{out}}{P_{in}} = \frac{P_m}{Irradiance \times Area} \tag{2.7}$$

The efficiency of the solar cell is directly affected by the temperature variation of the solar cell surface, intensity and spectrum of the incident light. Therefore, it is recommended to test and compare solar cells using similar lighting and temperature conditions called Standard Test Conditions (STC) [88].

2.5.2. Irradiation effect on solar cells

Both voltage and current are functions of the light falling on the cell and the relationship between irradiance and output power can be illustrated in Figure 2.10a. It can be observed that the short circuit current (I_{SC}) on the vertical axis is decreased by the reduction of the light intensity. This can be referred to the number of photons absorbed by the semiconductor material as it falls down at lower concentration. The improved efficiency under concentrated sunlight is related to the current and output voltage of a solar cell. The short circuit current (I_{SC}) is considered to have a linear relationship with concentration ratio [92–94]. Moreover, the open circuit voltage (V_{OC}) on the horizontal axis increases with the light intensity [95]. The variation of the *Voc* as a function of the radiation is low compared to the variation of the *Isc* [88].

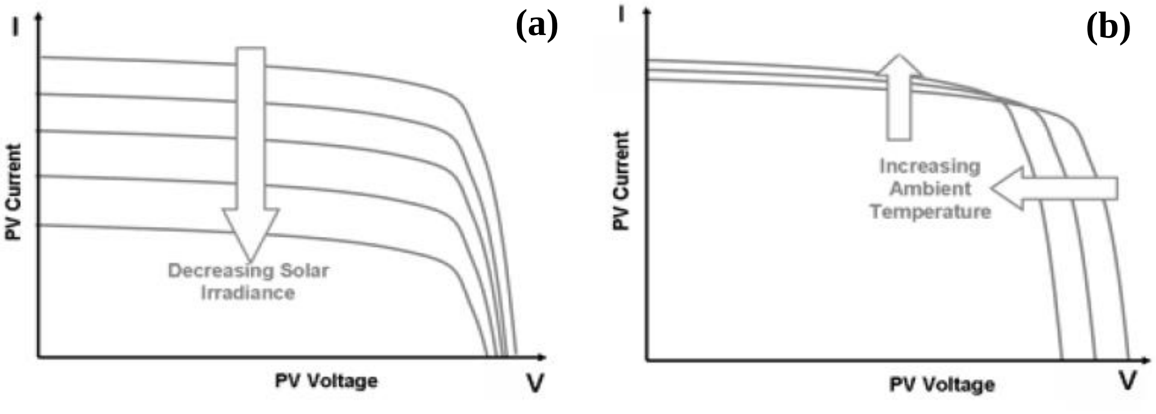

Figure 2.10: Dependence of the I-V curve from irradiance (a) and temperature (b) [95].

2.5.3. Temperature effect on solar cells

Solar cell surface temperature increases with the increment of the concentration ratio (CR). High and non-uniform PV surface temperature causes short-term and long-term cell degradation. The increase in operating temperature of the solar cell causes decrease in cell efficiency [25,29,38,41]. Although the current increases with the temperature as shown in Figure 2.10b, the output voltage decreases leading ultimately to reducing the electrical conversion efficiency. At open circuit voltage (*I*=0) the light generated current will be flowing through the diode and the equation for open circuit voltage can be written as [59,96,97]:

$$V_{oc} = \frac{kT}{q} \ln \frac{I_{sc} + I_0}{I_0} \tag{2.8}$$

Since $I_{sc} >> I_o$, this equation can be rewritten as:

$$V_{oc} \approx \frac{kT}{q} \ln \frac{I_{sc}}{I_0} \tag{2.9}$$

Where k is the Boltzmann’s constant, T is the PV temperature and q is the electron charge. The equation of open circuit voltage indicates that the V_{OC} is logarithmically related to the reciprocal of the saturation current (I_0). With the increase in temperature, the intrinsic carrier concentration increases and this leads to an increase in reverse saturation current and eventually increases recombination current. Due to the increase in recombination current, the open circuit voltage of the solar cell decreases. The elevation in temperature has another effect on the semiconductor as it decreases the band gap of the material which decreases the output voltage. By decreasing the band gap, photons with lower energy can be absorbed which leads to increasing the photocurrent or called light generated current. But, the gain in I_{SC} cannot compensate for the loss in V_{OC}, which results in overall decrease in electrical output of the solar cell [59].

If the HCPV solar cell temperature exceeds certain limit set by the manufacturer, it may cause also long-term degradation [38]. For instance, overheating can break the electrical connections and uneven temperature distribution can distort the module structure because of thermal expansion which leads to optical misalignments [60].

2.6. Solar Concentrators for CPV

2.6.1. Introduction

Solar concentrators are devices which focus incoming solar radiation onto a designated target area (PV) using light beam reflection or refraction for gaining higher solar concentration; this concept is known as CPV technology. Solar concentration using an optical concentrator such as a Fresnel lens [79,98–113], parabolic troughs [114], dishes [115,116] and compound parabolic concentrator [71,117–121] is one of the most effective methods of reducing overall energy generation costs [25]. PV under concentration operates at an irradiation level many times greater than that of direct un-concentrated sunlight. The solar cell electrical efficiency improves with increasing irradiation levels which ultimately delivers more power than a solar cell operated under direct sunlight [84,122]. Moreover, concentrating solar radiation on PV has the potential to replace the expensive PV material with cheaper optical elements which consequently reduce the total cost of the CPV system [46,49,122,123]. In the following sections, important concepts and terminologies related to the solar concentrators will be introduced.

2.6.2. CPV configurations

There are many different CPV system configurations. They can be classified based on the concentration level i.e. low, medium and high concentration. Also, CPV systems can be categorised based on the optics, solar cells, cooling mechanism and tracking system utilised as shown in Figure 2.11.

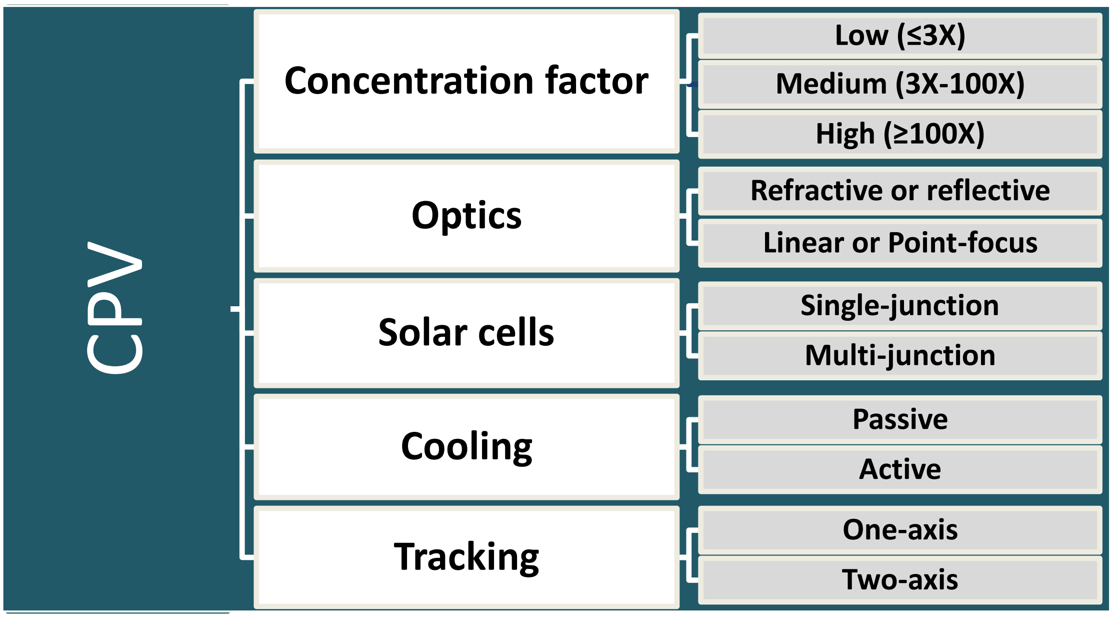

Figure 2.11: Criteria used in CPV classification [124].

2.6.3. Concentration ratio

There are several definitions of concentration ratio or factor in use. The most common is ‘geometric concentration ratio’ , GCR , which can be defined as the area of the aperture (A_a) divided by the absorber or receiver area (A_r) [125]. The absorber area is the region of the cell that is designed to be illuminated.

$$GCR = \frac{A_a}{A_r} \tag{2.10}$$

Another definition of the concentration ratio is termed as ‘flux concentration ratio’ (CR) which can be defined as the ratio of average energy flux on the absorber i.e. receiver to that at the aperture of the system [126]. The second definition takes into account the optical losses where the *GCR* is multiplied by the optical efficiency (η_{opt}) as shown in equation 2.11. Since the energy flux may not be homogeneous on the receiver surface, the flux average on the receiver is considered.

$$CR = \frac{A_a}{A_r} \times \eta_{opt} \tag{2.11}$$

Optical concentration ratio is also called ‘suns’; one sun can be defined as the flux on aperture. For example, if the flux on the receiver is 10 times the flux on the aperture, then the concentration ratio is termed as 10 suns or 10X. Furthermore, one sun can be defined as 1000 W/m^2 which is the case in the current study.

The CPV systems are divided into three classes based on the geometric concentration ratio [127]:

- **Low Concentration Photovoltaic (LCPV):** the typical concentration ratio is below 3X. Single-junction silicon solar cells are mostly associated with this type of concentration**.**
- **Medium Concentration Photovoltaic (MCPV):** the typical concentration ratio of this type lies between 3X and 100X. Silicon or other cells such as thin-films can be integrated in this type of concentration.
- **High Concentration Photovoltaic (HCPV):** the typical concentration ratio of this type is above 100X. Multi-junction solar cells are classically integrated with this type.

The range of the concentration ratio for each category may vary depending on the author or the publication date. The HCPV systems developed by the CPV companies have a share of 44% of the market [124,127].

2.6.4. Acceptance angle

Acceptance angle (2θ) can be defined as the incidence angle corresponding to 90% of the maximum optical efficiency at normal incidence [33,108,128]. Concentration limit (C_{max}) is a function of refractive index of the material (n) and half acceptance angle (θ) as shown in the equations below [129,130]:

$$C_{\max} = \frac{\mathrm{n}}{\sin\theta} \quad \text{(for 2-D concentrators)} \tag{2.12}$$

$$C_{\max} = \frac{\mathrm{n}^2}{\sin^2\theta} \quad \text{(for 3-D concentrators)} \tag{2.13}$$

3-D concentrators have a better potential for higher concentrations than the 2-D concentrators with the increase of the acceptance angle as the concentration ratio decrease gradually and the effect of the refractive index is squared [129,130]. If the concentration is set too high (C_{max}), the acceptance angle (2θ) will be very small i.e. more precise and expensive sun tracking system to maintain the CPV module facing sun with an error within the acceptance angle limit is needed. Also, narrower angles of acceptance may lead the optical system to suffer more from misalignment and therefore the whole HCPV system performance is reduced. Therefore, an additional optical element can be integrated to increase the acceptance angle and maintain the optical performance as described below.

2.6.5. Secondary Optical Element (SOE)

Besides the Primary Optical Element (POE) some HCPV systems include a SOE which is mainly used to increase acceptance angle or instead to increase concentration [126]. Moreover, SOE is integrated as a classical method to improve the irradiation uniformity on the receiver surface as shown in Figure 2.12 which ultimately prevent the degradation of the solar cell’s life and improves the electrical conversion efficiency [25,109,131]. They are applicable to be used with reflective or refractive CPV systems. However, they are most often integrated in high concentration PV systems typically point-focus Fresnel lenses in which concentration ratios is more than 100 suns [126]. Figure 2.12a shows that any misalignment of the incident light on the POE may shift the focused light which reduces the optical efficiency of the system. To accommodate this misalignment, SOE is used as shown in Figure 2.12b. There are many different types of SOE which can be either refractive, reflective or both. For example, V-trough, refractive CPCs, refractive silos and hollow inverted pyramid reflector [126,132]. The only drawback of using SOE is that the optical efficiency is reduced by the increasing number of optical components in the optical system.

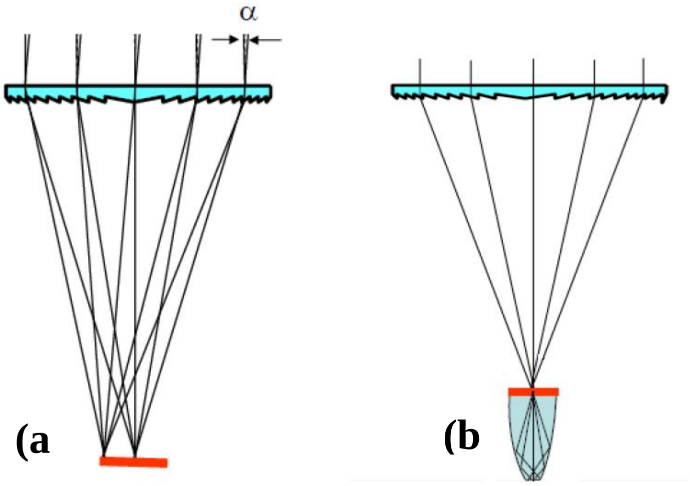

Figure 2.12: (a) System without secondary optics; (b) System with secondary optics [60].

2.6.6. Types of Concentrator optics

Most concentrator optics found in the literature can be either refractive such as lenses or reflective like mirrors or a combination of both [126]. Figure 2.13 shows the principle of CPV optics using lenses and mirrors. The reflector or refractor concentrator directs the radiation to the receiver. Different concentrator profiles and designs for various applications are developed over the years to achieve high optical efficiency [100,103,133]. The reflector and refractor optics can be divided into two types: imaging and non-imaging concentrators [59,134,135]. The concentrators with imaging optics make an image of the sun on the receiver such as convex lens; whereas concentrators with non-imaging optics do not form an image of the sun but only concentrate the solar irradiation into the receiver like Compound Parabolic Concentrator (CPC) [59,134].

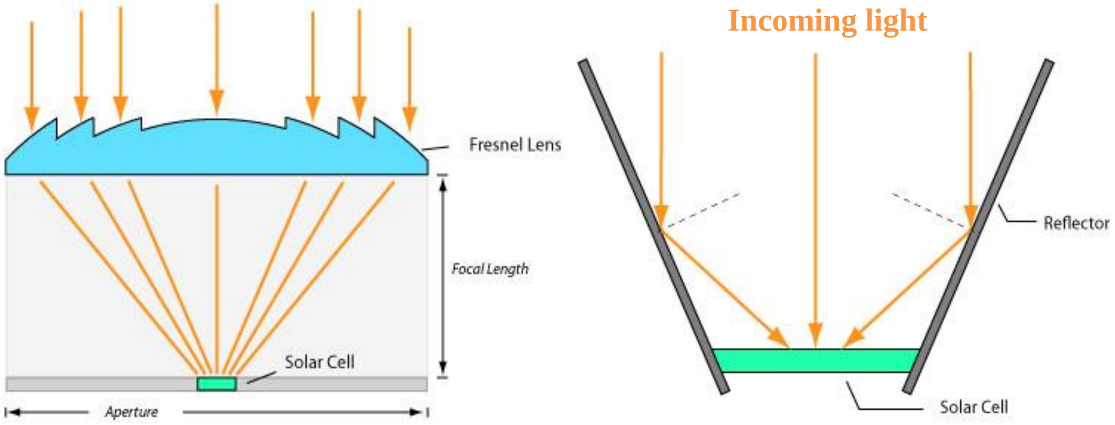

Figure 2.13: The principle of CPV optics: lens (on the left); mirrors (on the right) [136].

2.6.6.1. Refractive optics

Lenses of any size over 5 cm in diameter is too thick and costly to be practical; hence, Fresnel lenses are usually used [126]. A Fresnel lens is essentially chains of prisms and can be thought of as a standard Plano-Convex lens that has been collapsed at a number of locations into a thinner profile. Fresnel lenses may be divided into: point and linear focus. Point-focus Fresnel lens has a circular symmetry about their axis (Figure 2.14a); this configuration usually uses one cell behind each lens. Whereas, linear focus Fresnel lens has a constant cross section along a transverse axis and focus the light into a line as shown in Figure 2.14b [126]. Domed Fresnel lens is one type of linear configuration of the Fresnel lens as illustrated in Figure 2.14c [126]. Also, Fresnel lenses are divided into two categories: imaging and non-imaging. Non-imaging design Fresnel lenses are generally of convex shape to get high concentration ratio and flux distribution with short focal length [100]. Fresnel lenses are generally used for a high concentration ratio system and as such require a tracking system. The common material of Fresnel lens is Acrylic plastic (Polymethyl methacrylate or PMMA), which molds well and when combined with ultraviolet (UV) stabiliser has shown good weatherability [24,124,126].

In order to increase the durability of such lenses, there are attempts to make these lenses from glass or to mold the lens material to the underside of a glass substrate. Fresnel lenses are usually incorporated into modules that contain a lens or multiple lenses, a housing to protect the back side of the lens from dust and dirt deposits and a solar cell.

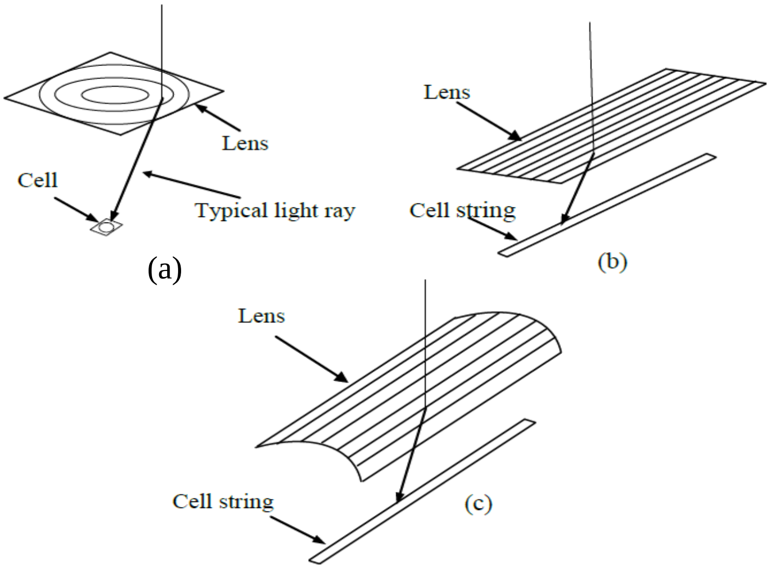

Figure 2.14: Fresnel lens configurations. (a) Point-focus Fresnel lens showing a typical ray hitting the circular active area of the solar cell. (b) Linear, or one-axis, Fresnel lens focusing on a line of solar cells in a string. (c) Domed linear Fresnel lens [126].

Refraction is characterised by Snell's law, which was initially stated in 1621 by the Dutch astronomer and mathematician Willebrord Snell [134]. Referring to Figure 2.15b for the definitions of the symbols [88]:

$$\frac{\sin\theta_i}{\sin\theta_t} = \frac{n_t}{n_i} \tag{2.14}$$

$$n_i \sin\theta_i = n_t \sin\theta_t \tag{2.15}$$

Where n_i and n_t are the two different refractive indices of the materials, θ_i and θ_t are the angle of incidence and refraction of the ray with respect to the surface normal respectively.

Simple geometric shapes are analysed analytically using these relations, however modern practice is to utilise advanced ray-tracing softwares to solve these equations numerically which will be used in the current study. The refraction usually happens between two different mediums or materials, the angle of the incident ray with the normal in the first medium and the angle of the refracted ray with the normal in the second medium [126,134,88].

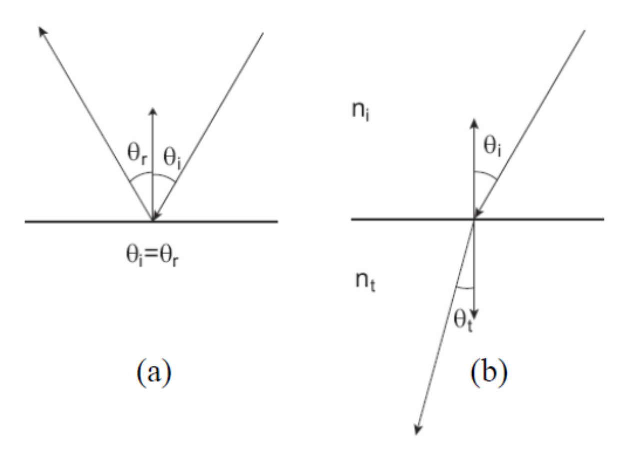

Figure 2.15: Representation of the laws of reflection (a) and refraction (b) [88].

2.6.6.2. Reflective optics

Reflective lenses or mirrors can be used as an alternative to refractive lenses. A reflective surface with the shape of a parabola will focus all light parallel to the axis of the parabola to a point located at the parabola's focus [126]. Like lenses, parabolas can be a point-focus configuration, which is made by rotating the parabola around its axis and creating a paraboloid, and line-focus configuration, which is formed by translating the parabola perpendicular to its axis. These configurations are shown in Figure 2.16 [126].

Generally, parabolic concentrators are used for thermal applications where a high temperature is needed and irradiation uniformity is not a big issue. However, there are some projects where parabolic dish concentrators are used for PV applications which are more expensive compared to other designs [88,137]. Referring to the law of reflection, the incident ray and the direction of the reflected ray make the same angle with respect to surface normal as shown in Figure 2.15a i.e. :

$$\text{Angle of incidence } (\theta_i) = \text{angle of reflection } (\theta_r) \qquad (2.16)$$

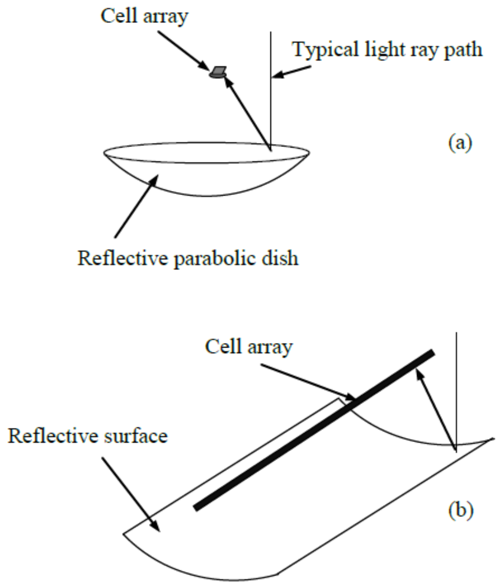

Figure 2.16: Reflective concentrator configurations. (a) Reflective paraboloid, or dish, focusing on a cell array. (b) Linear parabolic trough focusing on a line of cells [126].

2.6.7. Literature review on Fresnel lens High Concentrator PV (HCPV)

In the field of concentrated solar energy applications, Fresnel lenses have been one of the best choices recently; they have many advantages when compared to other concentrators such as: small volume, light-weight, mass production with low cost and effectively increase the energy density [100]. In 1961, research on Fresnel lens for concentrated Photovoltaic power generation started when Oshida investigated the Photovoltaic applications with Fresnel lenses based on spectral distribution considerations [100,138]. The efficiency and intensity variations of a 3 M company circular Fresnel lens as a solar concentrator was determined through experimental and analytical methods by Harmon [139]. The conclusion of that study is that the lens was an inefficient concentrator with losses ranging from 20-80% as the focal distance decreased. However, the lens was adequate for low concentration applications with Photovoltaic systems.

James et al. discussed the economic feasibility of concentrator Photovoltaic systems based on maintaining high cell conversion efficiency, a high optics transmission efficiency and a low structure cost per unit area [140]. It was found by both theoretical and experimental methods that the conversion efficiency of concentrator solar cells is reduced by illuminating the solar cells with a non-uniform flux density. Moreover, the structure cost was reduced by increasing the allowable tracking error. Therefore, flux density uniformity, optical transmission, allowable tracking error, cost per unit area and lifetime are some important criteria for Fresnel lens Photovoltaic concentrating optics.

Many concentrated Photovoltaic products came out during 1980s. New research was focused on tracking system, cooling techniques for solar cell, high concentration system and other shapes of imaging Fresnel lens [100]. Nakata et al. fabricated a 300 W polar axis tracking concentrator with 36 circular Fresnel lenses (40 cm x 40cm) to obtain a uniform light distribution [141]. It was shown that the optical efficiency of the lens was 83% and the output power was about 50% higher than that of the commercial lens. The output power from a typical concentrator cell is 9.13 W with 12% cell efficiency under 4.7 W/cm^2 sunlight at 38 ^{o}C and the output power from five concentrator units was 253.7 W with 10.2% total cell efficiency.

The distribution of the received flux on the absorber is a key problem especially at high concentration ratios as Photovoltaic cells require uniform flux and direct radiation for optimum performance [101,142,143]. Jebens et al. presented a specially designed Fresnel lens where a solar cell located on the axis of the lens at its focal plane [144]. The lens was designed so that its central facets direct the light from the sun towards the outer boundary of the cell. Similarly, the facets at the boundary of the lens project light progressively toward the centre of the cell to obtain a uniform distribution of light on the cell. Lastly, the adjacent groups of facets of the lens direct the light alternately in front and beyond the cell to maintain a constant light intensity for a certain depth of focus of the lens.

Since 1990s, and due to the previous work concentrated Photovoltaic systems based on imaging Fresnel lenses became more mature [100]. The research and development works covered many fields such as bifocal Fresnel lens for multi-junction solar cells [145], space concentrator Photovoltaic modules [146,147] and field test of concentrator Photovoltaic system [148]. Moreover, more concentrated photovoltaic projects based on imaging Fresnel lenses were initiated in several countries [100]. Davies studied a design with two-stage concentrator where a single-surface refractive spherical lens used as a secondary optical element with the primary Fresnel lens concentrator to increase the concentration ratio further and reduce the non-uniform illumination negative effect on the performance of the solar cell [149]. Figure 2.17 shows a cross section view of the two-stage axially-symmetric concentrator. In the design, Fresnel lens with maximum concentration ratio of about 100 times at F-number =1.37 has been enhanced using the two-stage concentrator system to maximum concentration of 530 times at optimum F-number = 2.84.

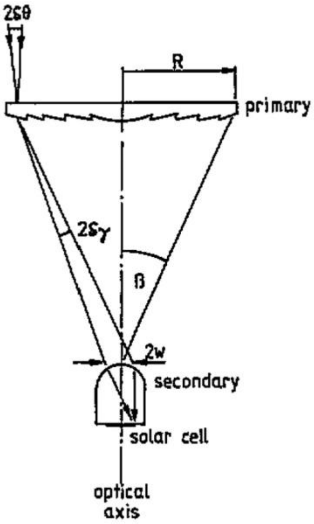

Figure 2.17: Sketch showing a cross section through a two-stage, axially-symmetric concentrator with Fresnel lens as primary and single-surface spherical lens as secondary [103].

Whitfield et al. compared some 90 possible small PV concentrator designs in terms of performance and volume production costs that might be suitable for use at remote sites including point-focus Fresnel lens with two-axis tracking and linear Fresnel lens with solid Compound Parabolic Concentrator (CPC) secondary optical element and two-axis tracking [150]. The advantages of this prototype are maximum beam insolation collection, potential for simple mass-produced optics and the use of CPV housing as heat sink. But, the high cost is the main disadvantage of this prototype due to the need for two-axis tracking system. Also, flat Fresnel lenses are found less efficient than domed ones at F-numbers below about 1.1 due to the reflection losses at the second surface where incidence angle is large.

Andreev et al. used a composite (glass–silicone) panel secondary lens between the primary Fresnel lens and the solar cells to increase the system concentration ratio to more than 1000X [151] and to improve environmental protection of the solar cell. Although after introducing the secondary lens the optical efficiency of the system reduced by 6.25%, the secondary lens increased the off-normal angular acceptance.

Recently, attempts to enhance the solar flux uniformity on the receiver by developing unique Fresnel lens designs without the need to include secondary optical element have been reported. Ryu et al. proposed a new configuration of solar concentration optics utilising modularly faceted Fresnel lenses to achieve a uniform intensity on the receiver surface with a moderate concentration ratio [152]. In the design, a modular Fresnel lens composed of a number of lens units, refract the normally incident solar radiation onto the absorber as shown in Figure 2.18. The distribution of the solar flux at the receiver was simulated using ray-tracing technique for 9, 25, 49, 81 and 121 suns concentration ratios. The predicted uniformity of irradiance distribution at the solar cell plane was reported to be within 20% with an optical efficiency larger than 70% at concentration ratio of less than 50 suns.

Pan et al. designed a Fresnel lens where each pitch focused to a different position on the receiver to improve the solar flux uniformity without the need to a secondary optical element [108,153]. However, the acceptance angle of the design was low i.e. only about 0.3^{o}.

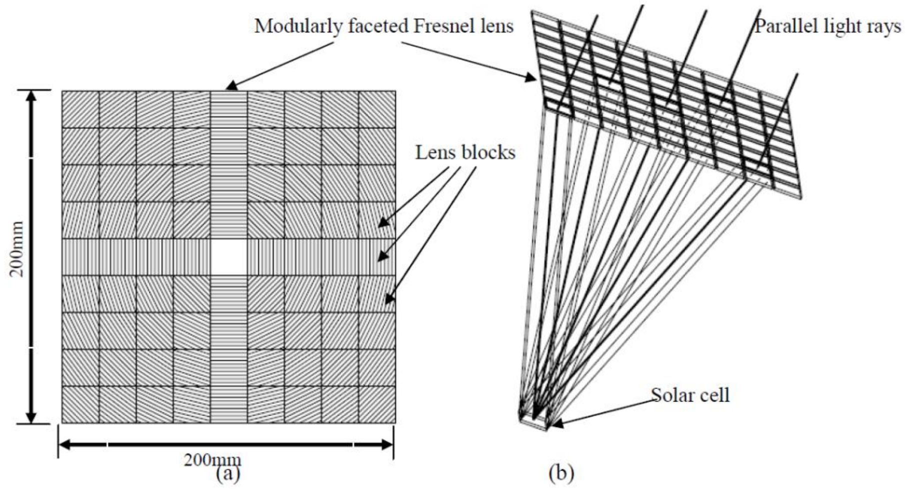

Figure 2.18: (a) Facet directions of the modularly faceted Fresnel lens (b) a 3D view of the concentration optic [144,145].

In 2014, Zhuang et al. also redesigned the ring structure of a hybrid Fresnel-based concentrator which consists of two parts the inner and the outer part [153,154]. The inner part is the conventional Fresnel lens, while the outer part is double the total internal reflection (DTIR) lens. Rearrangement of the rings resulted in a significantly improved irradiance uniformity i.e. less than 16.2% as shown in Figure 2.19.

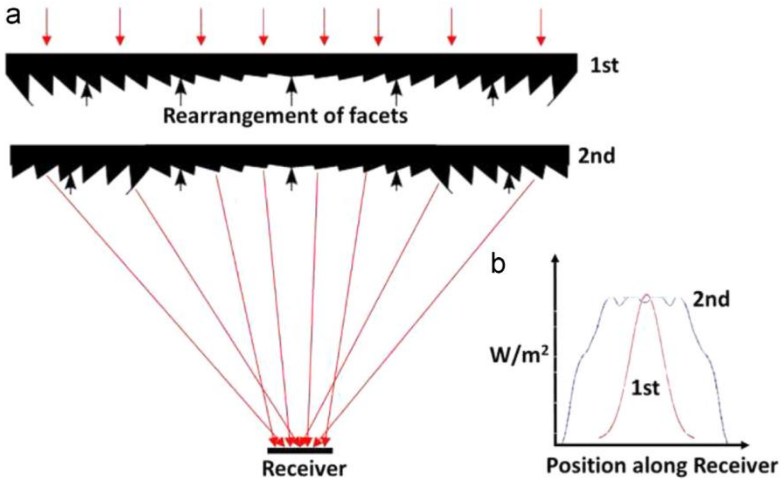

Figure 2.19: Improved irradiance distribution of Fresnel lens. By rearranging, or horizontally ‘flipping’ the Fresnel lens rings (a) an improved, more uniform irradiance distribution is obtained as shown in (b) [153].

Fresnel lens design has been through improvement processes since the official invention in 1822, especially Polymethyl methacrylate (PMMA). From the review above, it can be concluded that Fresnel lenses are able to raise the concentration ratio to a high level using cheap Acrylic material. Moreover, the total CPV system cost can be reduced by using less semiconductor material when integrated with Fresnel lens. On the other hand, non-uniform illumination, high surface temperature and small acceptance angle are the main challenges when point-focus Fresnel lens is utilised. Recently, multi-junction solar cells have been integrated with Fresnel lens based HCPV systems and therefore more numerical and outdoor experimental investigations are needed to evaluate the effect of these challenges on the HCPV performance. Ray tracing methodology is an important tool that will be used to investigate the optical efficiency of the imaging Fresnel lenses, the incident rays uniformity on the receiver and the maximum acceptance angle.

2.7. Tracking systems for High Concentrator PV (HCPV)

Concentrator PV systems only makes use of the Direct Normal Irradiation (DNI) of solar radiation; they don’t collect diffuse or scattered radiation [122]. Therefore, they require a continuous and precise tracking system to ensure the sun light enters the aperture of the module within the acceptance angle throughout the day and the year. The tracking precision required is imposed by the acceptance angle of the optical system and a secondary concentrator is added to the optical system in order to relax the demand. Sun tracking systems are usually grouped into two types: one and two axis trackers. The tracking requirement in a CPV system is dependent on the concentration ratio of the system; generally, one-axis tracking is sufficient for low concentration levels. Two-axis tracking system is more applicable at high concentration ratios where the acceptance angle is smaller. In case of point-focus optics, the optical components are generally required to track the sun along two axes rather than one axis [126]. From a mechanical point of view, two-axis tracking systems are more complex than one axis-tracking. However, point-focus systems can reach higher concentration ratios and hence lower cell size and cost. Line-focus reflective troughs need only to track along one axis such that the image falls along the focus line. On the other hand, linear Fresnel concentrators suffer severe optical aberrations when the sun is not perpendicular to the lens' translation axis. Therefore, linear Fresnel systems are generally limited to two-axis tracking [126].

2.7.1. Two-axis tracking system

A tracking system with two axes allows the CPV to be pointed exactly toward the sun position during all day through the year. Depending on location, this type of tracker may lead to an increase of about 35% in the yearly energy yield [124]. There are three types of two-axis systems illustrated in Figure 2.20 [126]:

- **Pedestal form:** uses a central pedestal supporting a flat tracking array structure. Tracking is usually performed by a gearbox, which tracks the array along vertical axis (the azimuth rotation) and along a horizontal axis (the elevation rotation). The advantage of this configuration is the simplicity of installation while the disadvantage is the wind loads which are transmitted to the central gear drive in the form of very large torque, requiring large capacity gears (Figure 2.20a).
- **Roll-tilt structure:** here wind loads on drive components are considerably reduced; however more rotating bearings and linkages are required which make the installation of the system more complicated. The roll axis is usually placed in a north-south direction to minimise shadowing by adjacent modules along the roll axis. It is also necessary to have a tilt axes that moves according to the height of the sun (Figure 2.20b and c).
- **TurnTable:** this configuration provides for the lowest profile and lowest wind loading, and can use rather small drive components and support members (Figure 2.20d). However, it presents the most complex installation scenario.

The selection of tracker type listed above is dependent on many factors such as land constraints, latitude, wind loads, ease of installation and installation size [126].

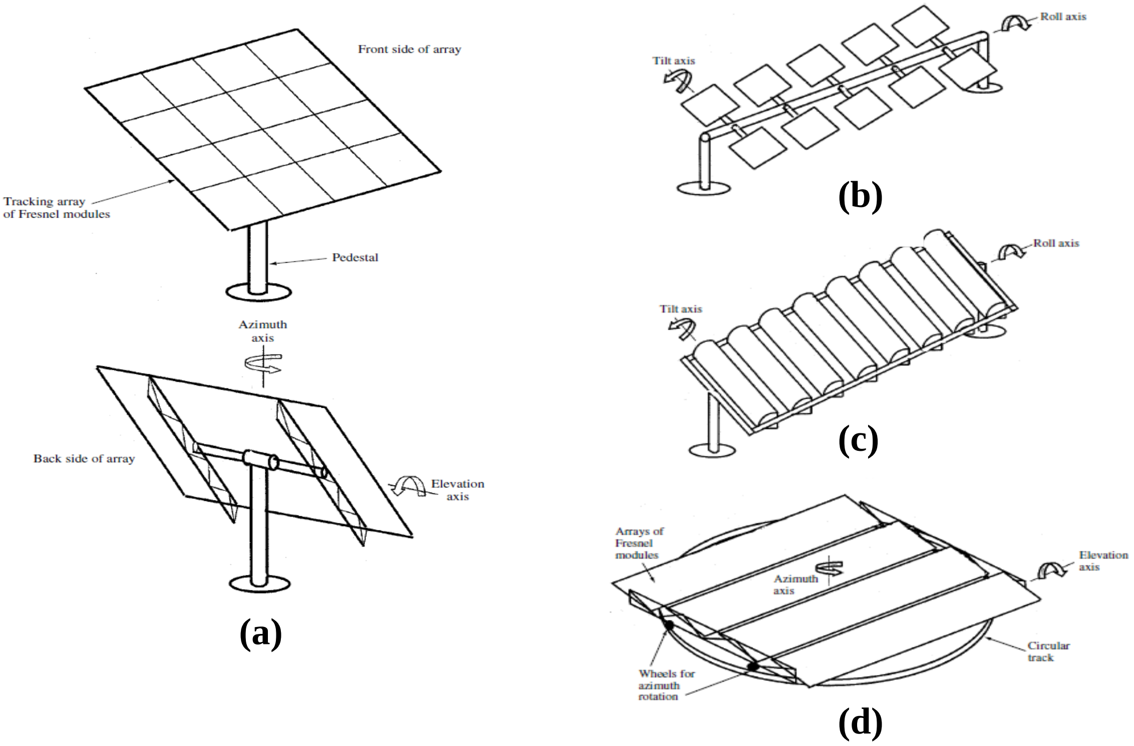

Figure 2.20: Two-axis tracking configurations: (a) Two-axis tracker with elevation and azimuth tracking mounted on a pedestal. (b) Roll-tilt tracking arrangement using central torque tube. (c) Roll-tilt arrangement using box frame. (d) TurnTable two-axis tracker [126].

2.7.2. Single-axis tracking system

Single-axis tracking systems provide lower yield than dual-axis but are cheaper to produce with less technical faults [124]. One of its main advantages is the minor wind sensitivity since the installation height is lower besides the less space requirements. The most common one-axis structure designs are horizontal axis and polar-axis as shown in Figure 2.21 [126]. Horizontal-axis configuration is more common choice due to the simplicity and low profile when compared to polar-axis tracker.

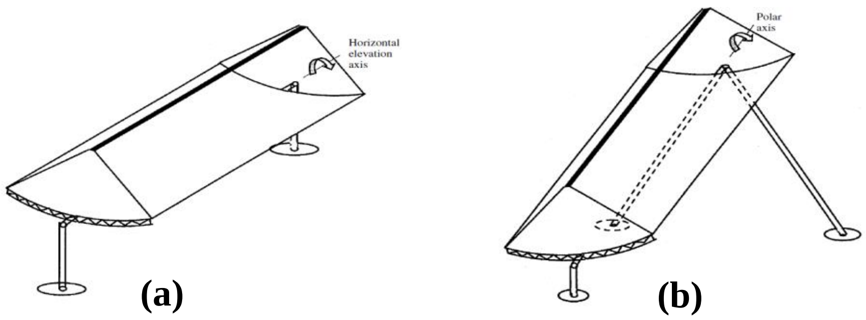

Figure 2.21: One-axis tracking configurations. (a) One-axis horizontal tracker with reflective trough (b) One-axis polar axis tracker with reflective trough [126].

2.8. Cooling systems for CPV

2.8.1. Introduction

One of the main concerns when developing concentrating Photovoltaic systems is cooling the solar cell. Cells under excess temperature may suffer both short-term (efficiency loss) and long-term (irreversible damage) degradation [38,155]. The cooling system design challenges that have to be considered include low and uniform cell temperatures, system reliability, sufficient capacity to deal with ‘worst case scenario’ and minimal power consumption by the system [38]. Depending on the electrical efficiency of the solar cell, only a fraction of incoming sunlight striking the cell is converted into electrical energy. The remainder of the absorbed energy will be converted into heat which may cause the solar cell surface temperature to rise unless the heat is efficiently dissipated to the environment. In the following section, major cooling system development aspects are described.

2.8.2. Major development considerations for cooling PV cells

Cell temperature: the photovoltaic cell efficiency decreases with increasing its temperature [25,29,41]. If the temperature exceeds the operating range (up to 100^{o}C in case of MJ solar cell) then the life of the cell will also exhibit long-term degradation [156]. The manufacturer of the solar cell will generally specify a given temperature degradation coefficient, normal operating temperature and the maximum operating temperature of the cell [90].

Uniformity of temperature: the cell efficiency decreases due to non-uniform temperatures across the solar cell surface [38,157]. Non-uniform temperature is more serious in a photovoltaic module where solar cells are connected in series and the output current will be limited by the solar cell that gives the smallest output. This is known as the ‘current mismatch’. Since the cell efficiency decreases with increasing temperature, the cell at the highest temperature will limit the efficiency of the whole module. This problem can be avoided by introducing bypass diodes to the module which bypass cells when they reach a certain temperature or by maintaining a uniform temperature across each series connection [38].

Reliability and simplicity: reliability of the cooling system is important as any failure may lead to the destruction of the solar cell. The cooling system should be developed to tolerate the 'worst case scenarios' such as power outages, tracking inconsistencies and electrical faults within modules. To maintain costs to a minimum, the cooling system should be simple and reliable.

Usability of thermal energy: to make HCPV system more economically feasible, the extracted thermal energy can be used in different thermal applications [39,158]. This hybrid system described as high concentrator PV thermal (HCPV/T) where the output is not only electrical but also thermal energy [40,116,155,158–161]. Thermal energy when utilised can lead to a significant increase in the total conversion efficiency of the receiver [40,161]. Therefore, it is desirable to have an open-loop cooling system that delivers water as high temperature as possible.

Pumping power: the power required of any active component of the cooling circuit is needed to be minimised. Although turbulent flow dissipates heat more effectively than laminar flow, it causes pressure drop in the cooling channel which ultimately leads to a higher power consumption to run the pump [155]. This aspect is crucial during designing and selecting the cooling system.

Material efficiency: cost and weight of the cooling system have to be considered during the selection of materials' type and quantity.

2.8.3. Cooling for various concentrator geometries

Since the requirements for cell cooling differ significantly between the various types of concentrator geometries, cooling of concentrator PV can be grouped based on the concentrator PV configuration. The issue of shading has to be considered in designing the cooling system for mirror concentrators. If lenses are used, the cells are generally placed underneath the light source so there is no problem of shading by the cooling system. However, in mirror systems the cells are normally illuminated from below, such as parabolic dish, which makes shading an important issue in the cooling system development. In the following sub-sections, three types of concentrator PV configurations i.e. single cells, linear geometry and densely packed modules are described with particular attention to the cooling requirements [38].

2.8.3.1. Single cells

In small point-focus concentrators, sunlight is focused onto each cell separately. This means that each cell has an area equal to the concentrator available for heat sinking as shown in Figure 2.22. For example, a cell under 50X concentration should have 50 times its area available to dissipate the heat i.e. 50 times the cell area heat sink geometry can be attached for passive cooling. This method is effective to remove the excess heat from the solar cell but the extracted thermal energy will be wasted to the atmosphere. Therefore, active cooling has an advantage of collecting the thermal energy and using it in different thermal applications which ultimately increase the total conversion efficiency.

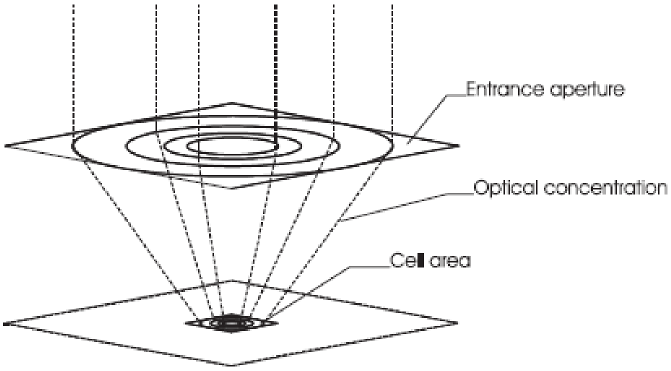

Figure 2.22: Single-cell concentrator: area below the cell is available for heat sinking [38].

2.8.3.2. Linear geometry

To focus light onto a row of cells, line focus systems are typically used including parabolic troughs or linear Fresnel lenses. In this configuration, since two of the cell sides are in close contact with the adjacent cells, the cells have less area available for heat sinking. The areas available for heat sinking extend from two of the sides and the back of the cell as shown in Figure 2.23.

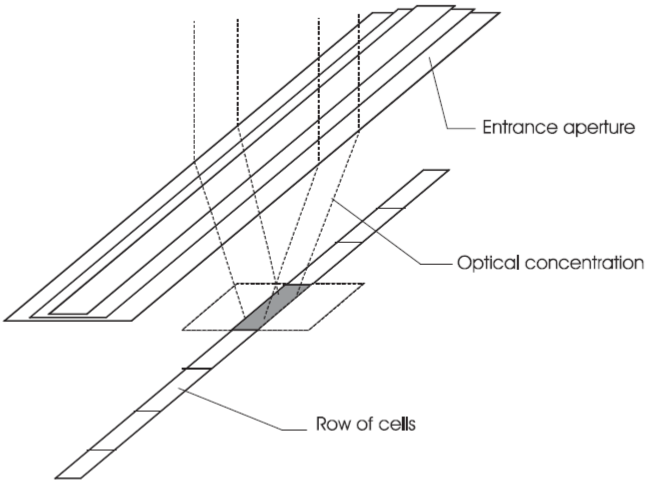

Figure 2.23: Linear concentrator: sides and back areas are available for heat sinking [38].

2.8.3.3. Densely packed modules

In large point-focus systems, like paraboloidal dish and heliostat field, the receiver generally consists of an assembly of densely packed cells. To increase the illumination uniformity, the receiver is usually located slightly away from the focal plane and the secondary optical element is used. This configuration is more challenging to cool than the two previous configurations since except for the edge cells each of the cells only has its back side available for heat sinking as shown in Figure 2.24b. So, the cooling mechanism has to dissipate the entire heat load in a direction normal to the module surface. Therefore, active cooling in this configuration at their typical concentration levels may be considered better than passive cooling choice [38].

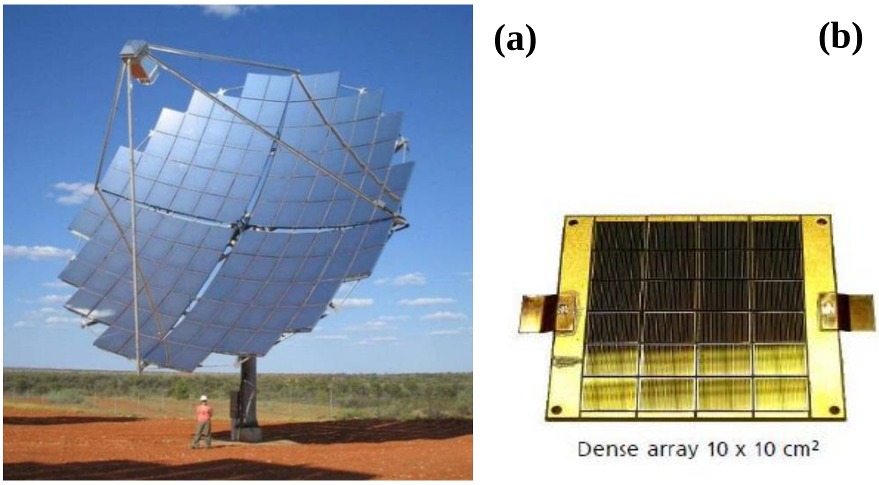

Figure 2.24: (a) Parabolic dish with densely packed modules at the receiver, (b) Area available for cooling is only the rear side of the dense array [60].

2.8.4. Literature review on High Concentrator PV (HCPV) cooling

In this section, the two main methods of cooling i.e. passive and active for a single CPV geometry will be described.

In 1980, Edenburn carried out a cost-efficiency analysis of a point-focus Fresnel lens array under passive cooling [38,162]. The cooling device as shown in Figure 2.25 was made up of linear fins on all available heat sink surfaces. Concentration ratios considered are 50, 92 and 170 suns. The analysis includes the cost of the aperture (lens and cell) area and the heat sink area to optimise the cooling geometry. In his search for cost-effectiveness, Edenburn also suggested housing the cell assembly in a painted aluminium box and to use its bottom as finless heat sink. He stated that during calm air conditions, radiation is the most important component of heat loss. On extreme days at a concentration level of about 90 suns the heat sink was able to maintain the cell temperature below 150 ^{o}C. Edenburn concluded that for point-focus arrays, the cost of passive cooling increases with lens area. The reason is that as the concentrator area increases, a thicker and more expensive heat exchanger is required. On the other hand, the thermal resistance between the substrate and the heat sink becomes critical when the concentration level increases.

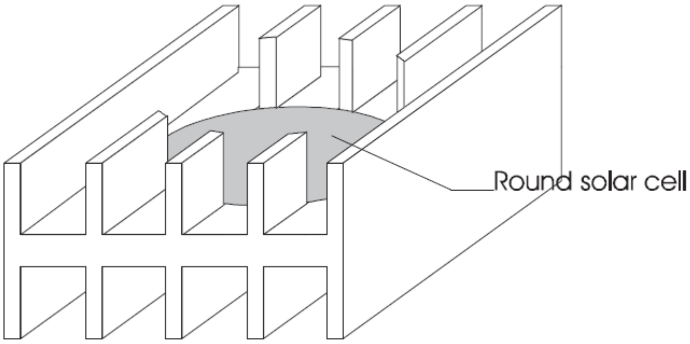

Figure 2.25: Passive heat sink for a single cell as suggested by Edenburn [38,162].

Edenburn also considered utilising active cooling on his point-focus arrays described above. Solar cells were placed in rows with one rectangular cooling channel running along the back of each row. For cost comparison purpose between the different cooling techniques, the possible advantage of using the thermal energy extracted by the coolant was not taken into consideration. However, he concluded that if this was considered, active cooling would almost certainly be the most cost-efficient solution [38,162]. Without utilising the output thermal energy, active cooling would be more expensive than passive cooling for single cells. The only exemption would be for very large lenses i.e. more than 30 cm in diameter as at this size the cost of active and passive cooling become almost the same.

Minano developed a thermal model for passive cooling of a single cell under high concentrations [38,163]. Similar to Edenburn, Minano concluded that passive cooling is more efficient for cells if their size is reduced. Minano recommended that cells should be maintained below 5 mm diameter and concluded that heat sinks mechanism for these cells would be similar to those used for power semiconductor devices.

Araki et al. presented results that show the effectiveness of passive cooling of single cells [38,164]. In this study, an array of Fresnel lenses focus the light onto single cells with concentration ratio of 500X mounted with a thin sheet of thermally conductive epoxy onto a heat spreading Aluminium plate. Outdoor experimental results show that the cells' temperature rise over the ambient temperature by only 18 ^{o}C without the need for a conventional heat sink. Moreover, the good thermal contact between the cell and the heat spreading plate is important to maintain the cell temperature low. Methods to enhance this could be to reduce the epoxy layer thickness, or to use an epoxy with high thermal conductivity.

The possibility of cheap and simple installation made finless type of heat sink in passive cooling more attractive for CPVs. In 2011, Mo et al. tested experimentally the passively cooled Fresnel lens CPV module using Aluminium plate as a heat spreader [165,166]. The experimental results show that under concentration ratio of 20 suns, the solar cell temperature was below 76 ^{o}C.

Anderson et al. investigated the heat pipe cooling for CPV using different working fluids and analysed the fin size and their spacing for absorbing the heat by natural convection from the CPV module with a total cell to ambient temperature rise of only 40 K under concentration ratio of 400X [167,168]. Heat pipe has the ability to transport large amount of heat from the evaporator to the condenser and perform effective cell cooling at high solar concentration. But, the possibility of dry-out at the evaporator section of the heat pipe will limit its heat transport capability under high solar concentration and damage the PV cell. Akbarzadeh and Wadowski also used heat pipe for CPV cooling of polycrystalline silicon solar cells and compared the PV power electrical output with and without heat pipe cooling and found that the output was doubled under the heat pipe cooling with cell-to-ambient rise of 46 K [169]. The comparison of the heat pipe cooling and water cooling on the performance of solar cell has been analysed by Farahat [170] who concluded that active cooling using water can become PV thermal (PV/T) collector which have advantages like lower produced energy cost and using the produced heat from the system.

Du et al. developed a CPV module with active water-cooling system in Southeast University, China [168]. They concluded that the electrical and thermal efficiency of the system increased with increasing the cooling water flow rate to a certain value then the heat extracted by the cooling water reached saturation level where the efficiency did not increase any further.

The microchannel heat sink is a concept suitable to many electronic applications due to its ability to remove large amount of heat from a small area [38]. Tuckerman and Pease first suggested the microchannel heat sink; it is based on the fact that the convection heat transfer coefficient is inversely proportional with the channel hydraulic diameter [171]. Later studies have revealed two major drawbacks to the microchannel heat sink. First, a large temperature gradient in the stream direction and a significant pressure drop that leads to high pumping power requirements [38].

Kessel et al. presented a geometrical concentration ratio of 2500 sun Fresnel lens concentrator for use with a triple-junction III-V solar cell from Spectrolab Inc [172]. The tested solar cell had a nominal cell efficiency of 35% and recommended operating cell temperature limit of 85 °C. A high performance metal thermal interface and an active liquid cooling method for dissipating the high solar heat flux were used in the cooling system as shown in Figure 2.26 [166,172]. Experimental results showed the effectiveness of the cooling system such that the cell temperature was maintained below 85 °C under concentration ratio of 2000X.

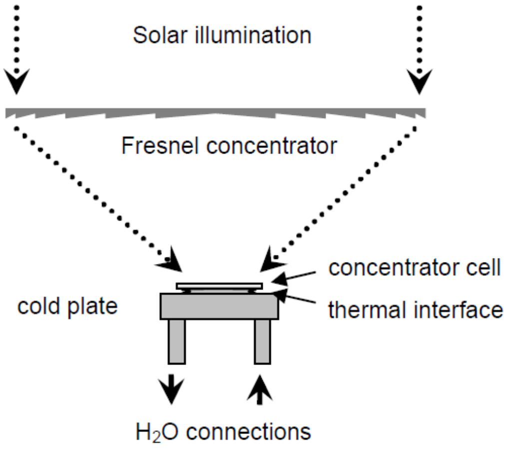

Figure 2.26: Active liquid cooling system for triple junction solar cell at 2000 suns solar concentration [172].

Theristis et al. developed a thermal model to predict the thermal behaviour of a 10x10 mm^2

PV cell in order to examine the most efficient and cost effective cooling system for a 500X concentrating PV cell [173]. It was shown that passive cooling of a HCPV system with concentration ratio of 500X is insufficient to maintain the solar cell below 80 ^{o}C (the operating temperature limit set by the manufacturer) especially at high ambient temperatures.

The analysis in the literature above shows that passive and active cooling have been utilised for removing heat from high-illumination photovoltaic cells. Passive cooling method is more reliable and cost effective due to the absence of moving parts. However, passive cooling has lower heat dissipation rates than active cooling system and its dissipation performance is mainly influenced by the ambient conditions such as air temperature and wind speed. Therefore, more investigations have to be undertaken to find the optimum solution for each case of CPV system. Hybrid concentrating PV systems which produce electrical and thermal energy is reviewed below.

2.8.5. Literature review on High Concentrator PV/Thermal (HCPV/T)

There are many advantages of concentrator Photovoltaic and thermal (CPV/T) over the CPV cooling system. If the CPV receiver is actively cooled, the additional thermal energy product is attained at almost no additional cost. Also, delivering the output heat to the consumer should add no more than 5% to the system cost [160]. In contrast to PV/thermal (PV/T) flat collectors, the by-product heat from PV/T is only limited to low-temperature applications for instance water and space heating [160] while in CPV/T the generated heat from the receiver can be utilised in more demanding processes such as industrial process heat, solar thermal water desalination, or solar cooling and air-conditioning [174].

Kribus et al. presented and analysed the electrical and thermal performance of a developed novel miniature CPV/T [160]. The total efficiency of the system was high, about 80%, with electrical efficiency of about 20% at low temperature and was gradually reduced at elevated temperature but the lost electrical energy was mostly recaptured as thermal energy. The

Australian National University has developed a concentrating solar PV-thermal system by using parabolic trough with geometric concentration ratio of 37X [175]. The thermal efficiency of the system was around 58% and electrical efficiency was about 11%, therefore total efficiency of 69% under typical operating conditions.

Mittelman et al. [159] studied the economic feasibility and performance of a CPV/T system with single effect absorption cooling. The results show that the combined solar cooling and power generation plant can be comparable to, and sometimes better than, the conventional alternative. Also, Mittelman et al. [116] performed a study on a combined CPV/T and a multi-effect evaporation desalination plant to produce electricity and simultaneously exploits the waste heat of the PV cells to desalinate water. A detailed FEA/CFD simulation was carried out to determine the annual production of electricity and desalinated water. The cost of desalinated water was estimated and compared to that of alternative conventional and solar desalination plants. The results show that the proposed coupled plant can have a significant advantage relative to other solar desalination methods. Moreover, CPV/T desalination in some cases is more cost-effective than conventional desalination.

Kerzmann and Schaefer presented a thermal simulation of a linear CPV system with an active cooling system under Phoenix Arizona solar and climatic conditions for a full year [176]. The simulation included the modelling of a GaInP/GaAs/Ge triple-junction solar cell, the fluid and heat transfer properties of the cooling system and the storage tank. The output data from the simulation was used to evaluate the linear CPV system from an economic and environmental view. Results showed that using the linear CPV over one year would save a residential user \$1623 in electricity and water heating at the same time displaces 10.35 tons of CO_2.

Renno and Petito developed a mathematical model in order to evaluate the thermal and electrical performance of different configurations of CPV/T system including triple-junction solar cell for domestic application in Italy [158]. Two different types of optical devices were considered: Fresnel lenses and parabolic mirrors. The model allowed the analysis of CPV/T system at different time levels (yearly, monthly, daily and hourly) in terms of: cell efficiency, cell and fluid temperatures, thermal and electrical energy provided by the single cells. It has been observed that the fluid outlet temperature equal to about 90 ^{o}C allows using an absorption heat pump with a CPV/T.

Xu et al. presented the outdoor performance of a point-focus Fresnel HCPV/T with triple-junction solar cells [40]. The system produced both electricity and heat with electrical efficiency of 28% and the highest thermal efficiency achieved was 54% which means the overall system efficiency can reach 80%. In order to overcome the difficulty of measuring the cell temperature in the system, a mathematical model was developed. The characteristics of the electrical performance under various irradiations and cell temperatures were also studied. The results showed that direct solar radiation dominantly affects the electrical performance. In 2016, Xu et al. also developed electrical and thermal models for a point-focus Fresnel lens HCPV/T module by numerical methods [161]. The electrical model was based on the Shockley diode equation, and the thermal model was based on a two-dimensional steady-state heat transfer. The inputs to the models consisted of irradiance, ambient temperature, wind speed, water temperature and mass flow rate. The outputs included mainly electrical and thermal efficiency. The simulation results of both models were compared with outdoor experimental results for validation purposes. The results showed that the overall efficiency of the HCPV/T can exceed 80% with electrical and thermal efficiency of 28% and 60% respectively. Also, it was found that electrical efficiency was mainly influenced by solar irradiation and the thermal efficiency increased with the increment of irradiance, ambient temperature and water mass flow rate. The HCPV/T module produced hot water at temperature as high as 70 ^{o}C without decreasing the electrical efficiency significantly. Finally, it was indicated that the integration of CPV module with point-focus Fresnel lens and thermal collector can enhance the overall solar conversion efficiency.

Utilising the thermal energy in HCPV/T system is a promising concept where the cost of active cooling can be compensated. Most of the research work was based on silicon low or medium CPV/T. Reports on outdoor performance of a single cell high concentrator Photovoltaic/Thermal (HCPV/T) system integrating point-focus Fresnel lens and multi-junction solar cell with geometric concentration ratio of more than 100X are limited, and even less in harsh environments like Saudi Arabia.

2.9. Summary

From the literature survey conducted, the following conclusions are put forward:

- Unlike crystalline silicon PV, multi-junction PV is an emerging technology where more research and investigation needs to be carried out to evaluate its performance in different areas of the world where climate conditions differ significantly.
- Multi-junction solar cell is a promising technology with electrical efficiency of more than 40% which has been recently integrated with high concentration systems for terrestrial applications.
- Point-focus Fresnel lens is effectively able to increase the energy density on the receiver to a high concentration.
- Although, several designs have been reported for HCPV systems, certain issues still arise during operations which are: solar cell high surface temperature, non-uniform illumination and the formation of hot spot on the PV surface, small acceptance angle and high cost. More research is needed in this area to quantify the performance of HCPV systems at different environments and to take the necessary steps for optimisation purpose.

- Optical modelling using ray tracing method is an effective tool to examine HCPV optical performance. In this study, this method will be used for developing the primary and secondary optical element with minimum irradiation non-uniformity on the receiver and increased acceptance angle to maximise the optical efficiency.
- Electrical modelling for a Single-Junction solar cell using Shockley equation has been used to evaluate the PV electrical performance. In this research, a mathematical model will be developed and assessed to predict the performance of the multi-junction solar cell.
- Thermal modelling using Finite Element Analysis (FEA) and Computational Fluid Dynamics (CFD) is a valuable tool to predict the PV surface temperature under different concentration ratios and ambient temperatures and consequently the level of cooling needed.
- The literature described various passive and active cooling methods which have been incorporated into CPV systems to keep the cell temperature below the operational limit recommended by the solar cell’s manufacturers. Some researchers state that passive cooling can be adequate for a single cell HCPV while other studies concluded that passive cooling is not dissipating enough heat from the cell even when a large heat sink is used especially at high ambient temperature areas. Therefore, more investigation needs to be undertaken to find the optimum solution for cooling the HCPV system in hot climates such as that of Saudi Arabia.
- Thermal collector principle is an effective method when integrated with the cooling system to increase the overall efficiency of the HCPV and compensate the cost of the tracking system and the active cooling.

- Thermal energy produced by a single HCPV/T system can be evaluated and analysed using CFD modelling to study the feasibility of coupling it with different solar thermal applications.
- Most of the previous studies on HCPV systems were implemented indoors where all relevant parameters are controlled. Only few studies were undertaken outdoors to evaluate the HCPV performance; in this project an outdoor HCPV experimental set-up will be developed to characterise its performance.
- Reports on a single cell high concentrator photovoltaic/thermal (HCPV/T) system with geometric concentration ratio more than 100X are limited. Moreover, most of the previous work focused only on one or two aspects of the HCPV/T performance while in the current study optical, electrical and thermal analysis will be covered.

CHAPTER 3

Development of HCPV/T system for outdoor optical, electrical and thermal characterisation

3.1. Introduction

This chapter presents the experimental facility development of a HCPV/T comprising a primary and secondary optical element, multi-junction solar cell and cooling device to examine its optical, electrical and thermal performance under different concentration ratios and PV surface temperature. The equipment and instrumentation that were used and the experimental procedure that was followed to perform the above investigations will be discussed. Moreover, calibration of the measuring devices and measurement accuracy analysis will be presented.

3.2. Description of the Outdoor HCPV/T system

As stated in the previous chapter, a typical CPV system consists of the following main components: optical elements, solar cell, cooling system and tracking mechanism. There are two optical elements in this HCPV/T set-up, Fresnel lens as a primary optical element (POE) and hollow inverted truncated pyramid reflector (HITPR) as a secondary optical element (SOE). The solar cell integrated in this set-up, is triple-junction type and the cooling system is based on a rectangular cooling channel where water flows inside it in one direction. A manual tracking mechanism is used instead of an automated one to reduce the complication and cost of the system. Moreover, the main purpose of this set-up is to validate the developed theoretical optical, electrical and thermal models rather than perform long term experimental work where automated tracking system is crucial. Figure 3.1 shows the main components and principle of the HCPV/T system.

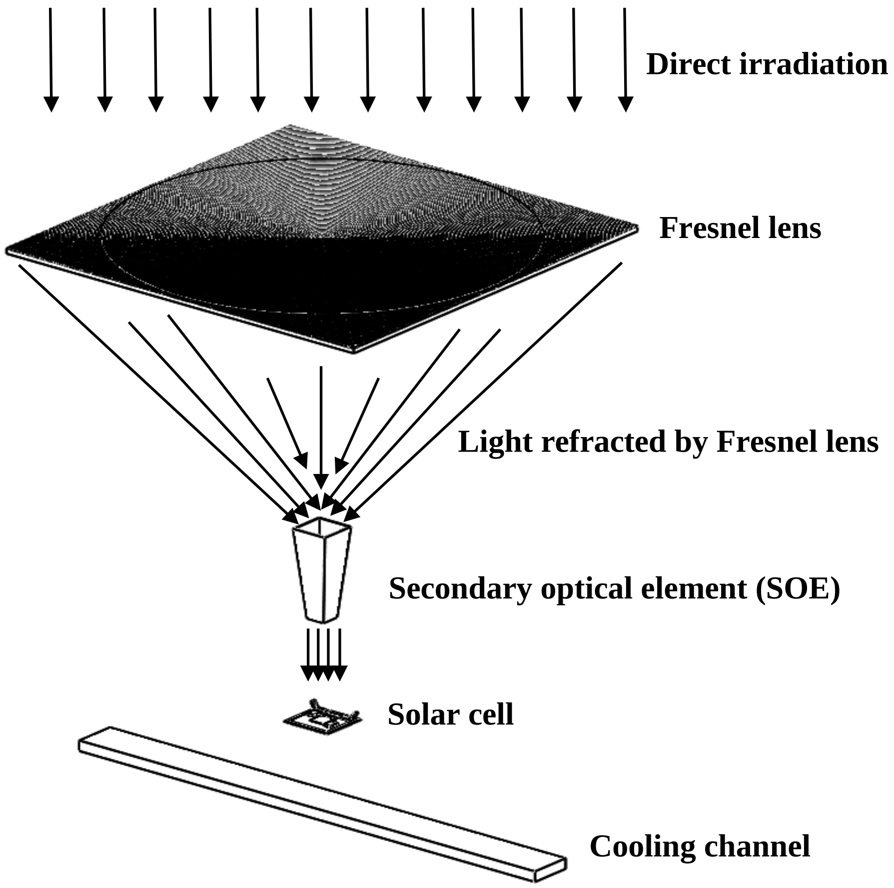

Figure 3.1: HCPV/T system principle and exploded view of its components.

Beside the above components, a HCPV housing was fabricated to protect the Fresnel lens and solar cell from dust and dirt deposits and to enhance the heat dissipation from the system. It was made from light weight and weather resistant 0.0007 m Aluminium sheet and assembled as shown in Figure 3.2. The dimensions of the HCPV housing were chosen based on the Fresnel lens size and its focal length which are 0.25x0.25x0.25 m^3. Also, a housing base with dimensions 0.26x0.26 m^2 was fabricated from 0.0007 m Aluminium sheet and 0.01m from each side of the housing base was bended up to attach the HCPV housing firmly on a 1x1x0.02 m^3 flat surface wooden plate using four screws as shown in Figure 3.3. A 0.07x0.07 m^2 square hole was made in the housing base and wooden plate to accommodate the cooling channel or the Peltier cooling module where the PV assembly is attached. The wooden plate was securely screwed to an adjustable angle plate where the whole assembly can be tilted at the required angle. The adjustable angle plate which carries the whole assembly is also securely screwed on a workshop wheel trolley for easy movement.

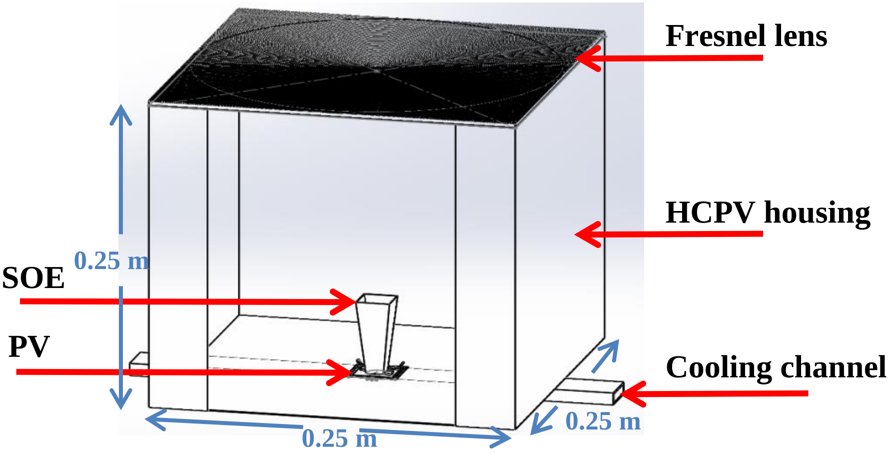

Figure 3.2: A single HCPV/T system and its components.

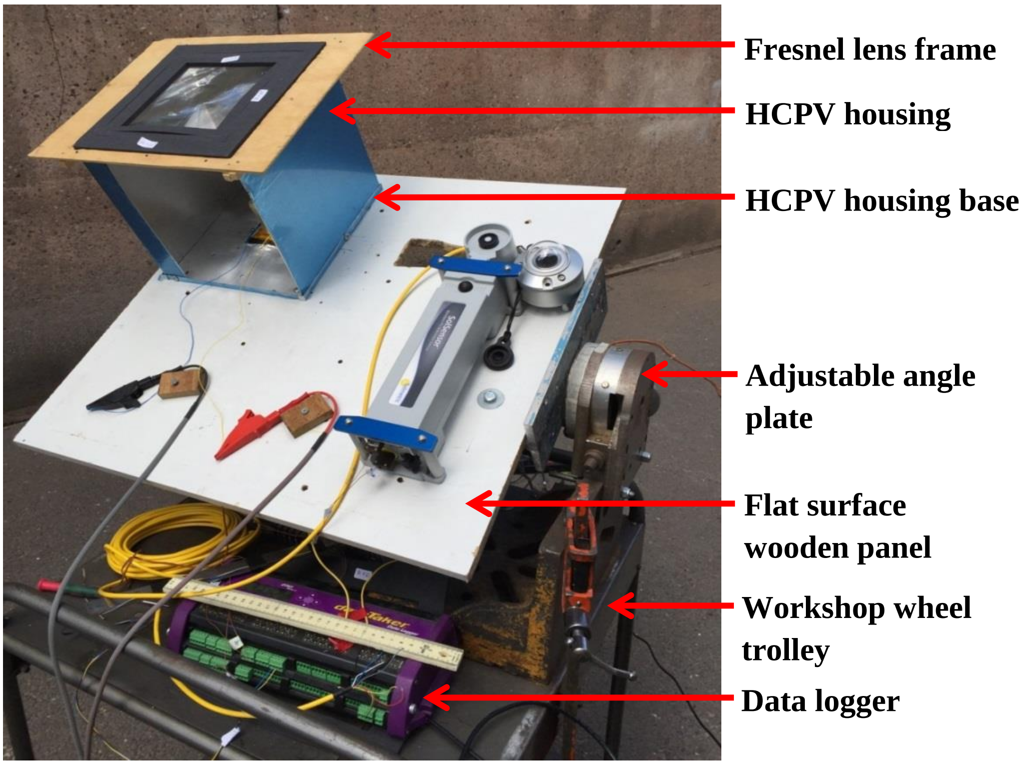

Figure 3.3: Workshop wheel trolley carries the whole HCPV assembly.

3.2.1. Primary optical element

The primary optical element in this HCPV/T experimental set-up is the Fresnel lens. Nowadays, the quality of Fresnel lenses has improved due to modern plastics, new molding techniques and computer-controlled diamond turning [134]. The advancement in the manufacturing process allows designing Fresnel lenses for numerous applications. Fresnel lenses can be compression-molded, injection-molded, cut, or extruded from a variety of plastics [134]. So far, the highest performance point-focus Fresnel lenses have been made by compression molding [47]. Due to the absence of the necessary advanced technology for manufacturing a Fresnel lens in house, it was obtained from a South Korean CPV company called DiYPRO [177] with the listed parameters in Table 3.1 for characterisation, simulation validation and optimisation purposes.

Table 3.1: Off-the-shelf Fresnel lens parameters.

Parameter	**Value**
Fresnel lens size (m^2)	0.25x0.25
Focal length (m)	0.25
Thickness (m)	0.003
Groove pitch (m)	0.001
Grooves direction	grooves in (upside down)
Transmissivity (%)	92
Material	PMMA

The active size of the Fresnel lens and the PV (receiver) are 0.0625 m^2 and 0.0001 m^2 respectively. Hence, the resulted geometrical concentration ratio (GCR) is 625X which is the maximum concentration ratio (CR) that can be achieved if no optical losses occurred. However, this GCR can be controlled by controlling the Fresnel lens aperture area exposed to the sun light. For example, if the needed GCR is 100X then the aperture area of 0.1x0.1 m^2 can only be exposed to the sun light and the rest can be covered as shown in Figure 3.4.

Figure 3.4: Controlling the GCR by controlling the Fresnel lens exposed area to the sun light.

To support and align the Fresnel lens, two wooden frames were designed. A square hole was made based on the Fresnel lens size on a 0.002 m thick 0.35x 0.35 m^2 size wooden piece to make the external frame. Also, to make the internal frame where the Fresnel lens can slide in and holds its position two 0.35x0.01x0.01 m^3 and two 0.25x0.01x0.01 m^3 wooden pieces were used as shown in Figure 3.5. A 0.003x0.25 m^2 slot was also made to slide the Fresnel lens and take its position at the centre of the internal frame with the help of the two opposite sides 0.01 m inactive margin in the Fresnel lens.

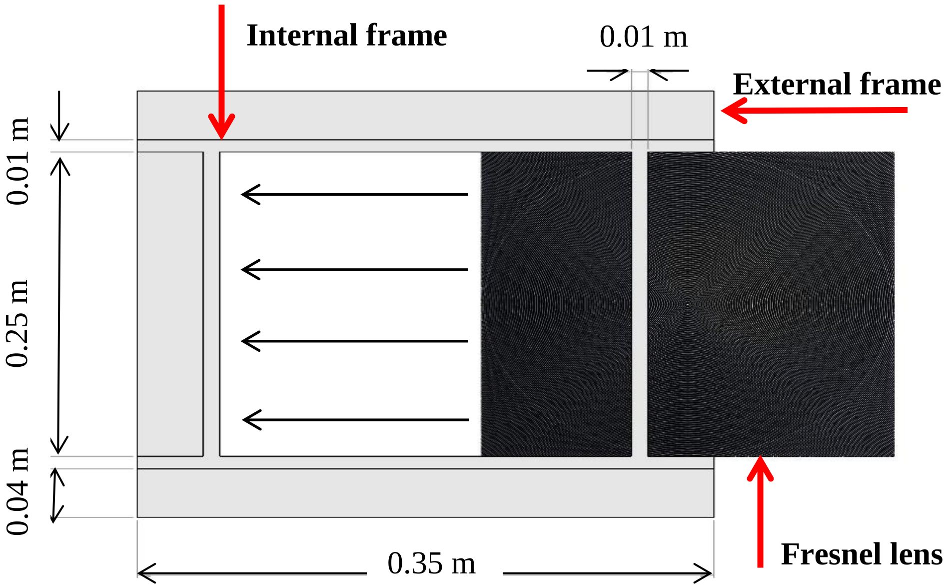

Figure 3.5: Fresnel lens wooden frame.

3.2.2. Multi-junction solar cell

AZURSPACE GaInP-GaInAs-Ge MJ PV assembly [90] with an area of 0.0316x0.0296 m^2 and active surface of 0.0001 m^2 was used for the HCPV/T outdoor experimental electrical testing. The typical electrical conversion efficiency of the solar cell obtained at standard controlled lab conditions using flash simulator was about 40% under the following measurement conditions: X = 1000 W/m^2, PV temperature of 25°C, air mass (AM) of 1.5, solar spectral irradiance of ASTM G173-03 and uniform direct irradiance [90]. The performance of the MJ cell at the indoor flash test with concentration ratios of 250X, 500X and 1000X is reported in Table 3.2 including the following parameters: I_{SC}, V_{OC}, I_m, V_m, P_m and FF.

Table 3.2: Performance of the MJ solar cell at the indoor flash test.

	I_{SC} (A)	V_{OC} (V)	I_m (A)	V_m (V)	P_m (W)	FF (%)
250X	3.79	3.07	3.71	2.80	10.40	89.40
500X	7.58	3.12	7.42	2.79	20.71	87.60
1000X	15.07	3.16	14.77	2.64	39.00	81.90

Figure 3.6 shows the multi-junction PV assembly including 0.01x0.01 m^2 cell, two electrical terminals and two by-pass diodes.

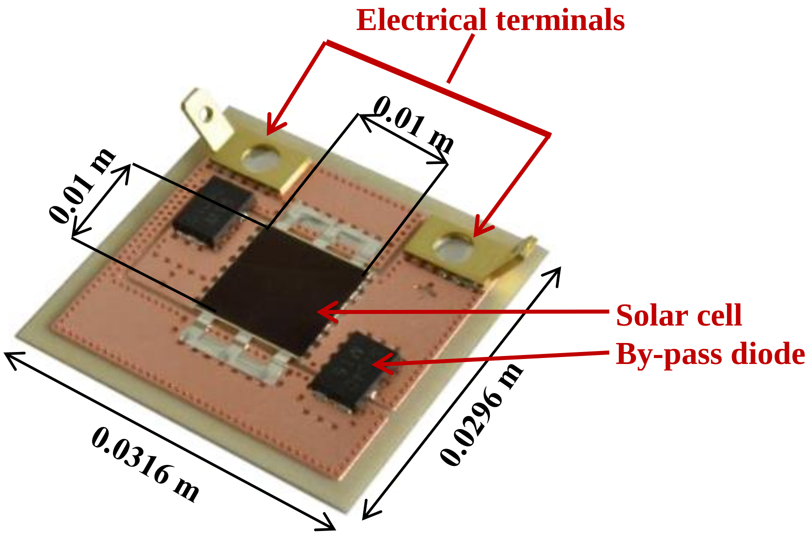

Figure 3.6: Multi-junction PV assembly dimensions.

3.2.3. Cooling system

A cooling channel was used to actively cool the HCPV cell using water. The bottom side of the solar cell assembly was attached to a 0.0015 m thick Aluminium rectangular cooling channel with the following dimensions: 0.328m length, 0.03 m width and 0.01 m height using high conductivity thermal paste (3 W/m·K) [178]. The calculated hydraulic diameter of this cooling channel is 1.11x10^{-2} m. The width of the cooling channel was chosen to accommodate the PV assembly back surface width (0.0296 m) while the internal height of the cooling channel (0.007 m) was chosen to cool the PV assembly with minimum mass flow rate of cooling water. Moreover, Aluminium was chosen for its good thermal conductivity (205 W/(m·K)), low cost and light mass density. A manifold was designed to be fitted at the inlet and outlet of the cooling channel. Figure 3.7 shows the design of the cooling channel manifold; all dimensions are in mm. The manifold includes two parts: the rectangular part which was fitted to the cooling channel and circular part which was fitted to the water supply hose as shown in the Figure. The inner dimension of the rectangular part was 0.03075 m i.e. 0.00075 m more than the cooling channel outer part to allow applying some glue. Also, the outer diameter of the circular part was 0.0145 m i.e. 0.0005 m less than water supply hose for tight fit.

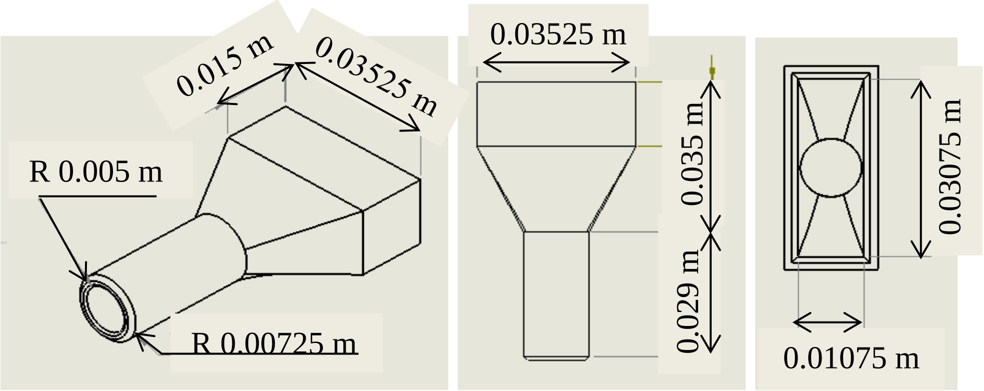

Figure 3.7: Cooling channel manifold design.

The manifold was fabricated by a 3-D printer using a transparent FullCure 720 rigid material [179]. Figure 3.8 shows the fabricated manifold attached to the cooling channel inlet.

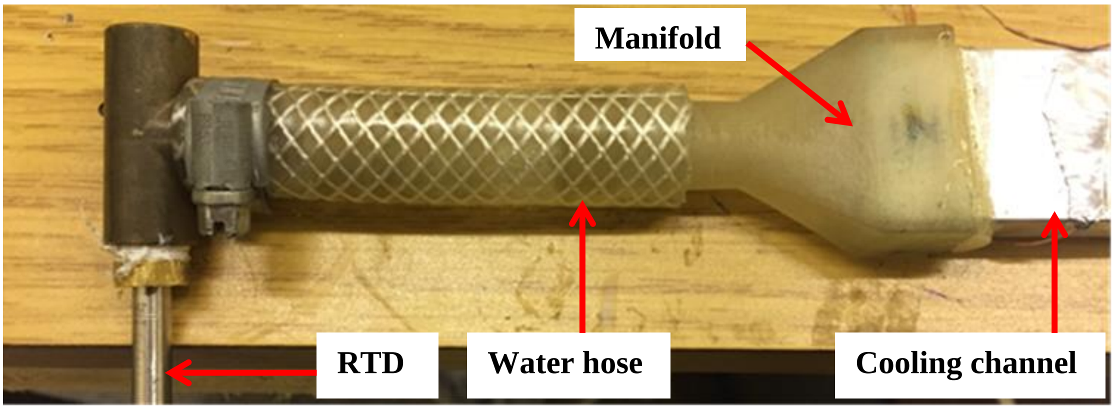

Figure 3.8: Manifold coupled to the cooling channel inlet.

Also, a 60 W Peltier cooling module with an area of 0.04x0.04 m^2 powered by a DC power supply was used [180]. The power selection criteria of this Peltier module were based on the following calculation:

- Maximum exposure area of the Fresnel lens = 0.25x0.25 = 0.0625m^2;
- Maximum input solar irradiation = 1000 W/m^2;
- Maximum optical efficiency of the Fresnel lens = 80%

Therefore, the maximum received power at the receiver (cell) = 0.0625x1000x0.8 = 50 W i.e. less than the rated power of the Peltier cooling module.

Unlike water cooling, this electrical device is capable of controlling the PV temperature more easily in less time. Moreover, it has the capacity to reduce the PV temperature under high concentration to a level that is difficult to be reached by water cooling like 25 ^{o}C when the HCPV system is required to be tested at standard test temperature.

3.2.4. Secondary optical element

Secondary optical elements (SOEs) are used to improve the illumination homogeneity of point-focus Fresnel lens high concentration systems and to increase the acceptance angle of the optical system. SOEs can be either made from reflective or refractive material. Unlike refractive SOEs, reflective ones are cheaper and easy to make. The SOE was designed using SolidWorks and its optical performance was evaluated using the advanced ray tracing software OptisWorks. A schematic diagram of the developed SOE with its geometrical dimensions is shown in Figure 3.9. The exit aperture area of the SOE (0.011x0.011 m^2) was chosen based on the PV area (0.01x0.01 m^2) with 0.0005 m margin from each side and the area of the entrance aperture (0.000484 m^2) is four times the exit aperture area (0.000121 m^2) to collect the highest amount of refracted rays. The design process and the geometry optimisation of the SOE will be discussed in detail in the next chapter. The SOE was made by a 3-D printer using a transparent FullCure 720 rigid material [179]. After making the SOE, the four inner walls were covered by four pieces of high reflective material with overall average reflectivity of 90% [181] using 3M double face tape as shown in Figure 3.10. More Information about the reflective material and 3M tape can be found in Appendix A.

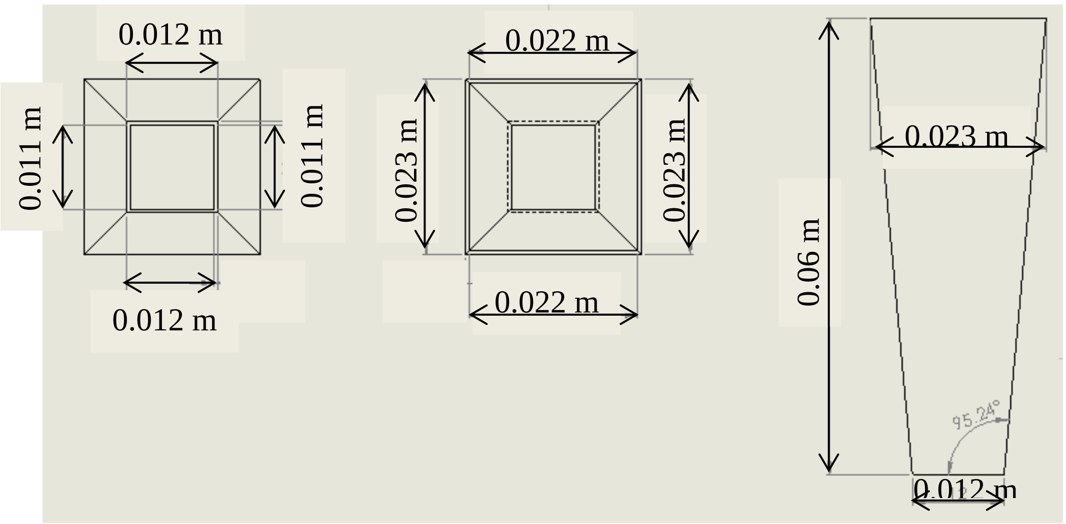

Figure 3.9: Schematic diagram of the developed SOE.

3.3. Equipment and instrumentation for outdoor HCPV/T characterisation

The developed HCPV/T system is characterised outdoors in terms of optical, electrical and thermal performance. In this section, the equipment and measuring devices that were used to characterise the HCPV/T system performance will be described. Figure 3.11 shows a schematic diagram of the test rig including the measuring devices and Table 3.3 describes each item in the diagram.

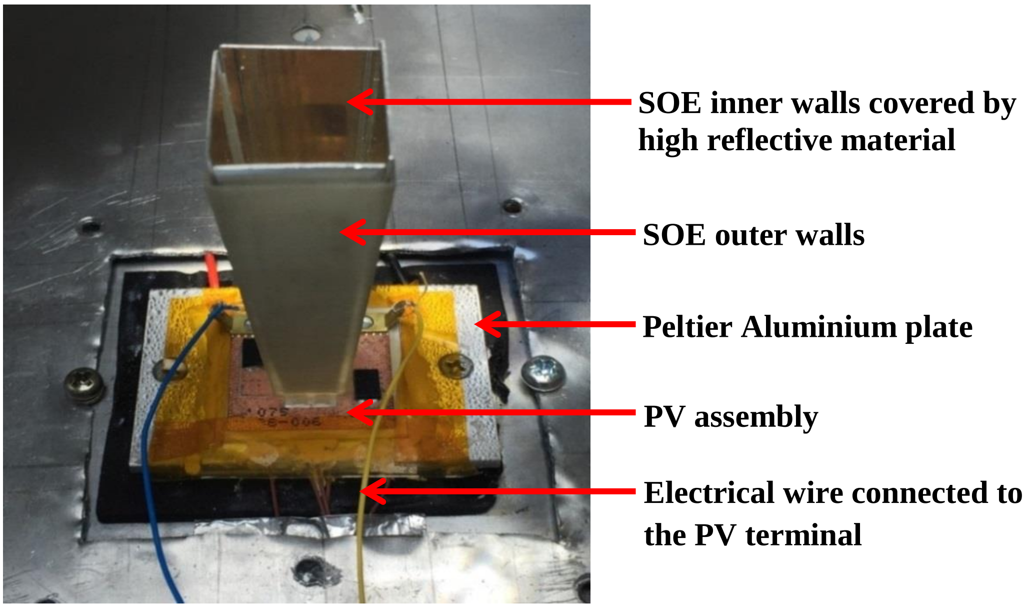

Figure 3.10: SOE inner walls covered by high reflective material.

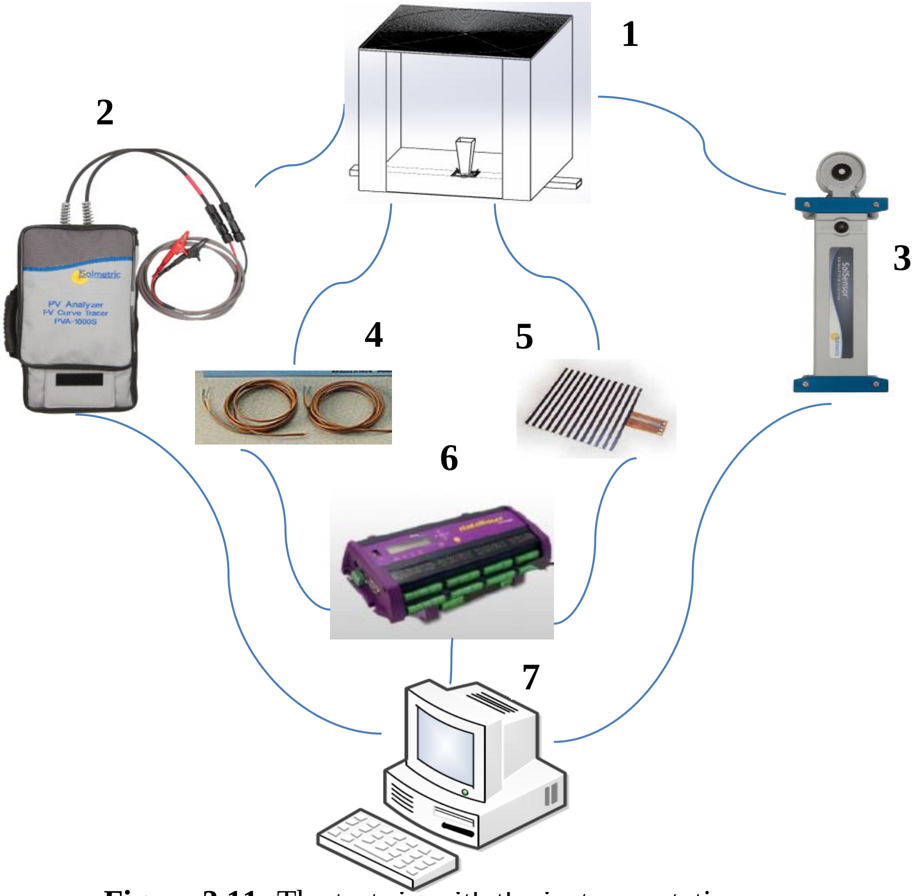

Figure 3.11: The test rig with the instrumentations.

Table 3.3: Description of each item in the schematic diagram.

Indicator	Description	Indicator	Description
1	HCPV/T system	5	Radiation sensor
2	I-V curve tracer	6	Data logger
3	PV reference sensor	7	Data processor
4	Thermocouples and RTDs		

3.3.1. PV analyser kit

Solmetric PV analyser kit (PVA-1000S) [182] was used to characterise the electrical performance of the HCPV/T outdoor. This kit includes two main units: I-V curve tracer and wireless PV reference sensor. The I-V curve tracer is able to produce an instant I-V and P-V curves for the solar cell and measure the following electrical parameters: V_{OC}, I_{SC}, I_m, V_m , P_m and FF. Simultaneously, the wireless PV reference sensor unit measures the following parameters: cell and ambient temperature, solar irradiance at the aperture and tilt angle of the system to evaluate the HCPV/T performance. According to the Solmetric PV analyser kit data sheet [183], the measurement duration including the I-V curve sweep is 4 seconds. Figure 3.12 shows the I-V curve tracer (on the right) and wireless PV reference sensor.

Figure 3.12: wireless PV reference sensor (on the left) and I-V curve tracer.

Table 3.4 summarises the specifications of the above two measuring units i.e. I-V curve tracer and wireless PV reference sensor including the measurement range, resolution and accuracy of the measured parameters.

Table 3.4: Specifications of the I-V curve tracer and wireless PV reference sensor [186].

Parameter	**Measurement range**	**Resolution**	**Accuracy**
Voltage (V)	0 – 1000	0.025	±0.5% ± 0.25
Current (A)	0 – 30	0.002	±0.5% ± 0.04
Irradiation (W/m^2)	0 – 1500	1	±2%
Temperature (^oC)	0 – 100	0.1	±0.2
Tilt angle (deg)	0 – 45	0.1	±1

To control the two measuring units above, PVA Software for Windows is provided to be installed on a Personal Computer (PC). A wireless USB is also provided to control these units within a range of 100 m. Also, this software allows presenting the generated curves and exporting the data to Microsoft Excel for further analysis. Figure 3.13 shows the interface of the PVA software in Windows.

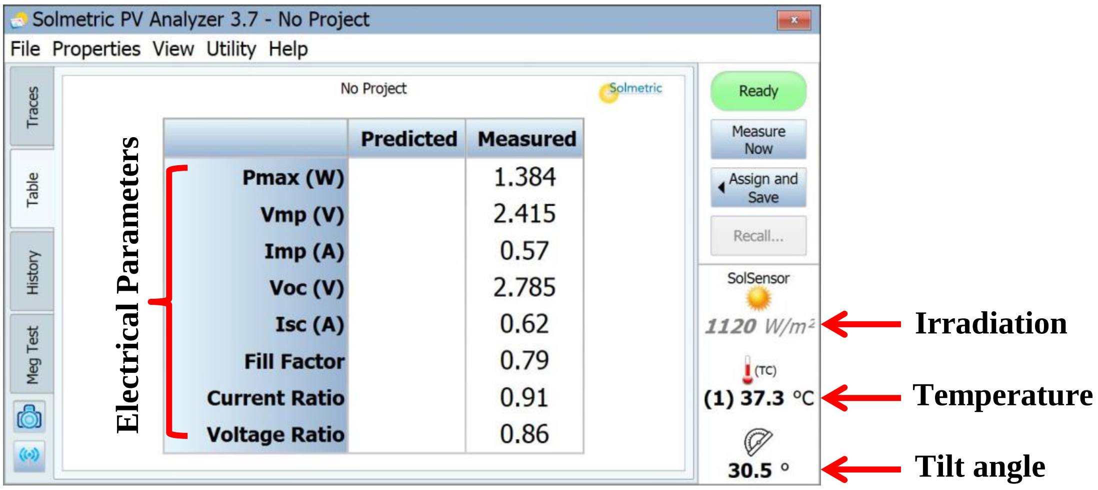

	Predicted	Measured
Pmax (W)		1.384
Vmp (V)		2.415
Imp (A)		0.57
Voc (V)		2.785
Isc (A)		0.62
Fill Factor		0.79
Current Ratio		0.91
Voltage Ratio		0.86

Figure 3.13: PVA software interface on Windows.

3.3.2. Radiation flux measurement at the receiver

The concentrated solar flux at the receiver (solar cell) is measured using high sensitivity 0.000025 m^2 radiant flux sensor from Captec Enterprise which can measure wide range of radiation wavelength including visible and infrared [184]. Table 3.5 summarises the specifications of the radiation flux sensor. DataTaker model DT85 [185] which has up to 32 channels isolated or 48 common was used for logging the radiation and various measurements taken in this work with 1 second sampling rate. The sensor’s voltage signal is sent to the

DT85 data taker where the sensitivity of the sensor defined in the scaling of the logger converts the signal to W/m^2. Figure 3.14 shows a photograph of the sensor used in the irradiance measurement.

Table 3.5: Specifications of the radiation sensor [187].

Specification	**Value**
Sensing area (m^2)	0.005x0.005
Thickness (m)	0.0004
Sensitivity (μV/ (W/m^2))	0.111
Electrical resistance (Ω)	< 500
Response time (sec)	0.05
Operating temperature (^{o}C)	-180 to 200

Figure 3.14: A photograph of 0.005x0.005 m^2 Radiant flux sensor [186].

In order to measure the concentrated radiation, mapping of the solar cell was carried out as shown in Figure 3.15 by dividing the active area into four equal smaller areas i.e. 0.005x0.005 m^2 which is the same size of the radiation sensor. Thus, 4 measurements on the solar cell are taken to calculate the average received flux.

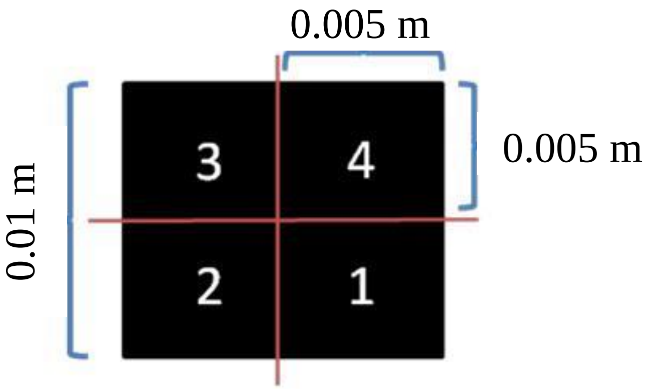

Figure 3.15: Mapping of the solar cell to measure the concentrated radiation flux.

At very high concentration i.e. >100X or if the PV is covered by a SOE it is difficult to directly measure the incident radiation using the sensor as the high radiation caused burning of the sensors. Therefore, in those cases concentration ratios were determined by assuming the short circuit current (I_{SC}) is directly proportional to irradiance which is widely used in the literature [92–94]. For example, if the I_{SC} of the solar cell at 1X and at reference temperature i.e. 25 ^{o}C is confirmed to be 0.01516 A, then at I_{SC} = 1.516 A the concentration ratio is 100X. To validate this assumption experimentally, 10 radiation sensor measurements using the mapping procedure described above at reference temperature of 25 ^{o}C and under geometrical concentration ratio of 49X were compared against the calculated received radiation based on I_{SC} as shown in Figure 3.16. The results of the two methods are in close agreement with maximum deviation of less than 4%.

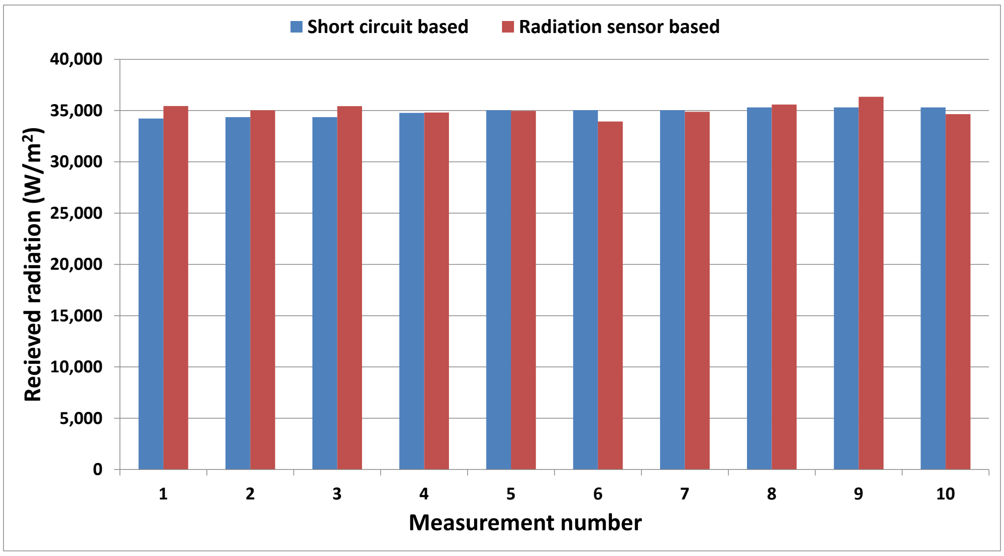

Figure 3.16: Measurement of the concentrated solar flux by short circuit method and radiation sensor.

3.3.3. Temperature measurement

Two types of temperature sensors were used in this experimental set-up which are: T- type surface thermocouple and Resistance Temperature Detector (RTD). Omega 5TC-TT-TI-36-1M surface thermocouples were used for measuring the PV surface temperature and their specifications are given in Table 3.6 as obtained from the database of the manufacturer.

Table 3.6: Specifications of the surface thermocouple.

Specification	**Value**
Diameter (m)	0.00013
Length (m)	1
Type	T-type
Insulation	PFA (Teflon)
Wire gauge	36
Measurement Range (^{o}C)	0 to 180

To measure the PV average temperature experimentally and assess the hot spot produced by the non-uniform ray distribution, three T- type surface thermocouples were attached at the back of the solar cell surface using Aluminium Foil tape and their tips were fully covered from the surrounding air as shown in Figure 3.17a. Figure 3.17b shows a schematic diagram of the PV assembly with three thermocouples located at the centre, side and corner under the PV active surface represented by a blue letter (X). The selection of the thermocouple locations is based on the assumption that the selected side temperature of the PV represents all other three sides and the selected corner temperature also represents the other three corners of the PV as the incident light profile is symmetric. U-shaped grooves on the cooling channel (Figure 3.18) with dimensions of 0.0015m × 0.00075m were made to accommodate the three 0.00013m diameter thermocouples underneath the PV and to ensure that the PV assembly is in full contact with the cooling channel.

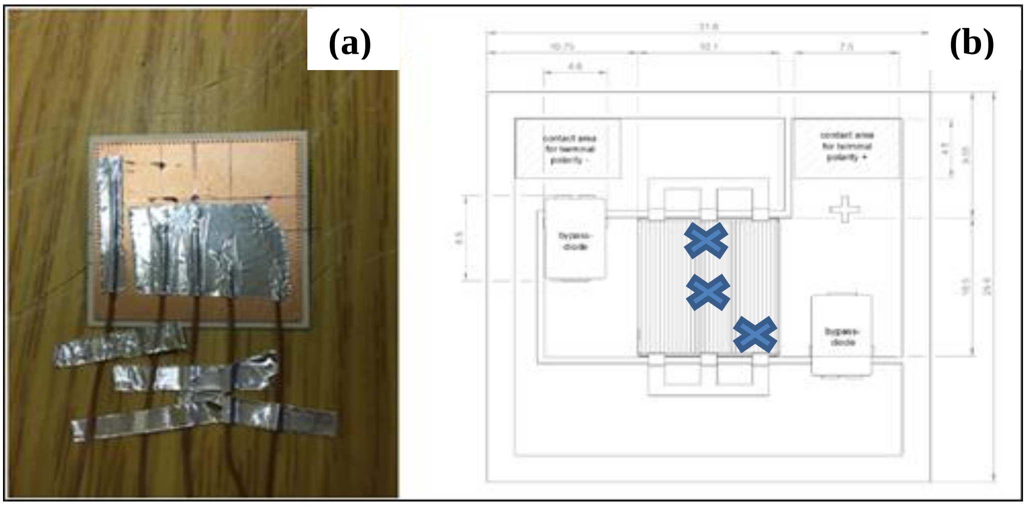

Figure 3.17: a) Thermocouples attached at the back of the solar cell assembly & b) their locations (letter X).

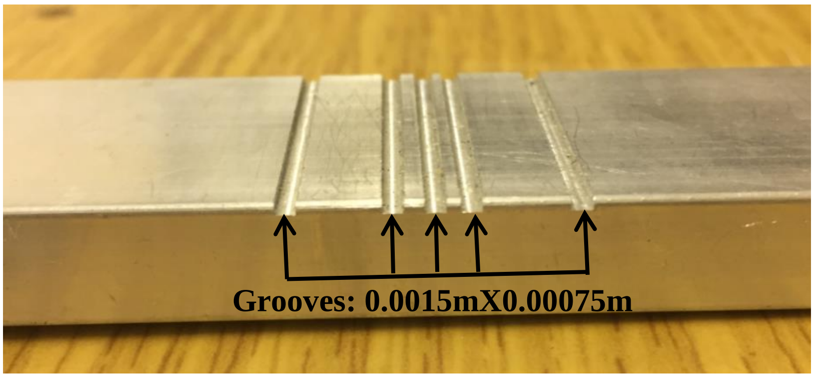

Figure 3.18: U-shape grooves on the cooling channel.

The inlet and outlet cooling water temperatures were measured using RTD Platinum100 (RTD Pt100) with high accuracy of ±0.025K. All the temperature signals were logged by the data logger DT85 and monitored by a personal computer.

3.3.4. Flow rate measurement

The cooling water flow rate was measured using an analogue CT Platon NG standard glass variable area flow meter with accuracy of ±1.25% and flow rate ranging from 0-1.33x10^{-5} m^3/s [187]. The required flow rate for this experimental work ranged from 8.33x10^{-7} – 4.17x10^{-6} m^3/s i.e. within the range of the selected flow meter capacity. The flow meter was calibrated using labelled standard bucket and stop watch as discussed in the next section.

3.4. Calibration of the instruments

In this section the calibration process of the used instruments will be described including: solar irradiance wireless PV reference sensor, concentrated radiation flux sensor, T- type surface thermocouples and the glass variable area water flow meter.

3.4.1. Solar irradiance wireless PV reference sensor calibration

The wireless PV reference sensor was calibrated against a new certified and calibrated Kipp & Zonen SMP10 Pyranometer which has a spectral range of 285-2800 nm and sensitivity of 11.5 μV/ (W/m^2) to measure the global radiation of the incident light [188]. Figure 3.19

shows the wireless PV reference sensor and the Pyranometer during the calibration process. The Pyranometer was powered by TSx1820P Programmable DC PSU 18V/20A power regulator with accuracy of ± (0.1% +1 digit) and ± (0.5% + 1 digit) for voltage and current respectively and DataTaker DT85 was used for logging and monitoring the irradiance measurements from the Pyranometer while the PVA Software installed on a laptop was used to monitor the solar irradiance sensor readings.

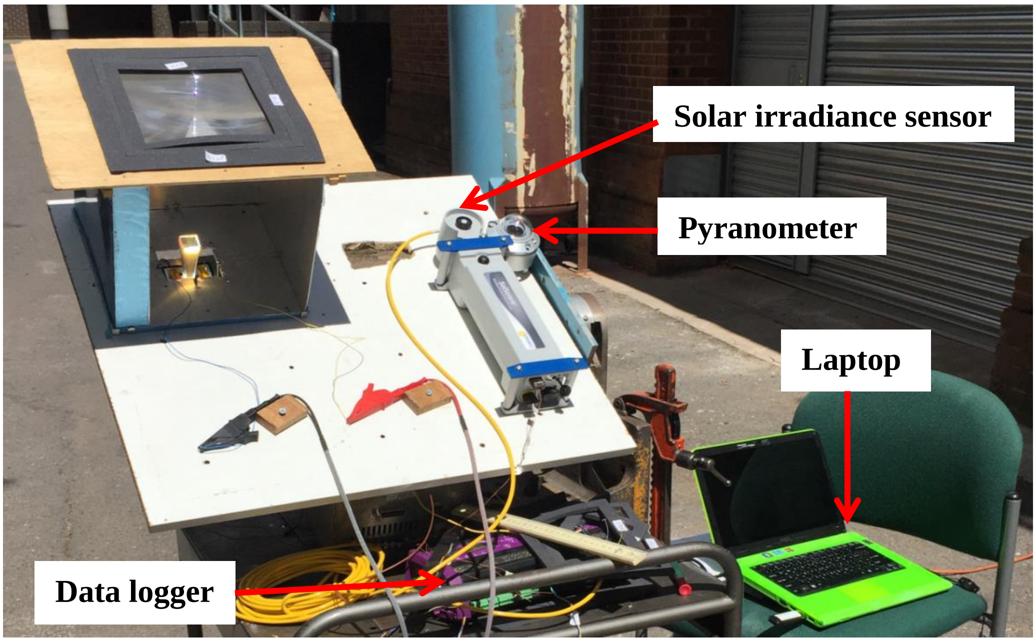

Figure 3.19: Solar irradiance sensor calibration set-up.

The two measuring devices were tested at various solar radiation values and different times of the day. Figure 3.20 shows the relation between wireless PV reference sensor and the Pyranometer readings. The R^2 value (0.9999) of the linear fitting is given by equation 3.1. This equation is used to calculate the curve fit value ($\bar{x}$) required to determine the uncertainty of the wireless PV reference sensor as shown in the measurements accuracy section.

$$y = 1.0017x - 0.5964 \tag{3.1}$$

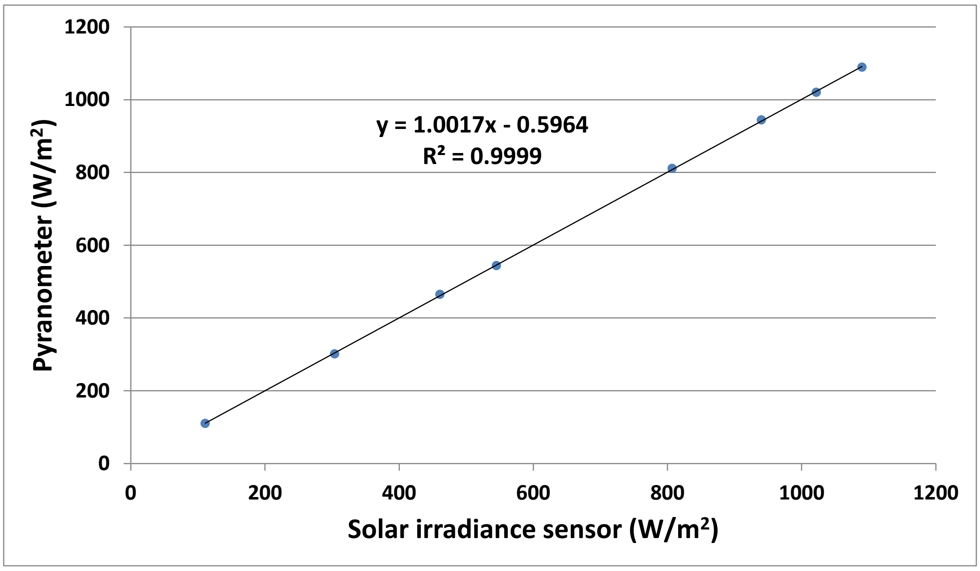

Figure 3.20: Solar irradiance relations between solar irradiance sensor and the Pyranometer.

3.4.2. Surface thermocouples calibration

The thermocouples used to measure the surface temperature in this work were calibrated against RTD Pt100. Thirteen thermocouples and the RTD were tied together and immersed in a water bath at the same level and the heat supplied to the water bath was controlled by a heating mantle as shown in Figure 3.21. The calibration process was conducted over the temperature range 0 to 100 °C. After reaching steady state, the readings of the thermocouples and the RTD were logged by the data taker and retrieved in a PC.

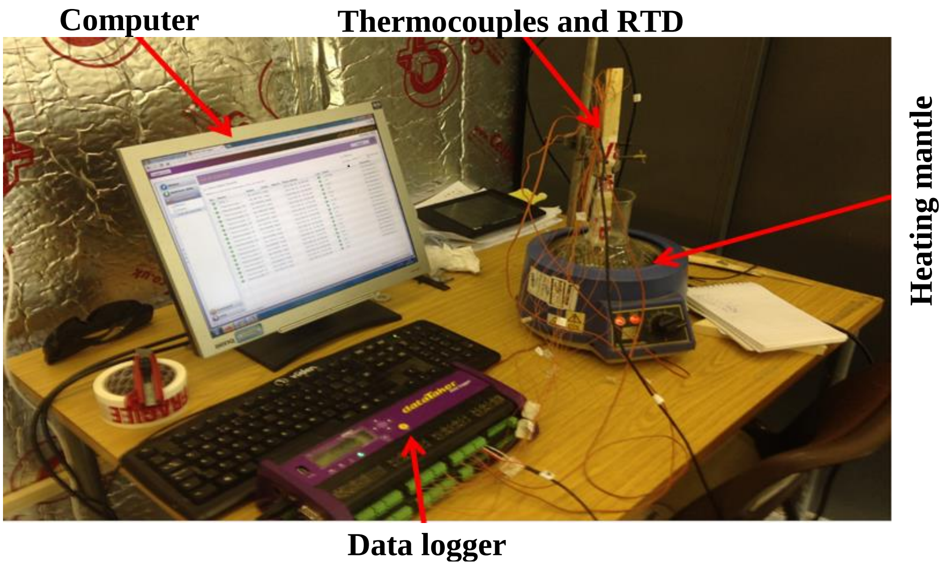

Figure 3.21: Thermocouples calibration set-up.

Figure 3.22 shows an example of the relation between RTD Pt100 and the thermocouple readings where R^2 value of the linear fitting using equation 3.2 is 0.9999. All the thermocouples have shown similar relationships to the RTD and the calibration curve Figures of the other 12 thermocouples used in this work are presented in appendix B.

$$y = 1.0008x + 0.2466 \tag{3.2}$$

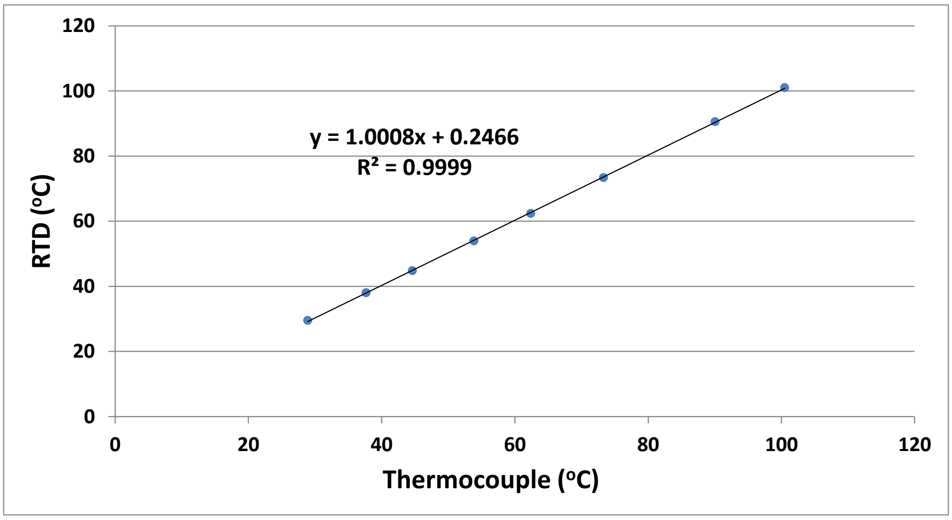

Figure 3.22: Calibration curve of the surface thermocouples.

3.4.3. Water flow meter calibration

The CT Platon NG standard glass variable area flow meter was calibrated using 1000 ml graduated cylinder and stop watch. The flow to the flow meter is controlled by a valve and the time taken to fill the cylinder is recorded for a particular opening. Eight different runs at increasing of valve openings were carried out and the flow rates were obtained by dividing the volume in ml by the time taken in minutes for each run. The flow rate relation between the CT Platon flow meter and the standard bucket filling is shown in Figure 3.23. The R^2 value of the linear fitting using equation 3.3 is 0.9978.

$$y = 1.0004x - 0.9911 \tag{3.3}$$

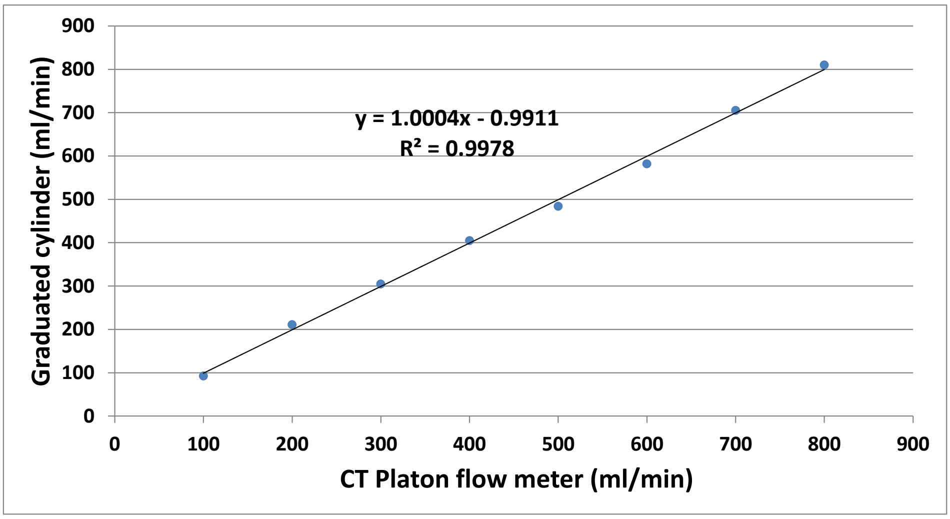

Figure 3.23: Calibration curve of the CT Platon flow meter.

3.5. Outdoor experimental procedure

The HCPV/T system was tested outdoor at the University of Birmingham (52.45° N, 1.93° W) in the city of Birmingham, United Kingdom. The outdoor experiment was carried out between April and October 2016 for optical, electrical and thermal characterisation. The test facility was completed when all the parts were assembled and all measuring devices were connected. All the measuring data was collected at reference temperature of the PV of 25 ^{o}C unless stated otherwise. Before any data collection, the adjustable angle plate was set to zero i.e. in horizontal position and a spirit level was placed at different locations on the Fresnel lens top surface to confirm that the whole assembly is properly aligned. Due to the movement of the sun, the adjustable angle plate and workshop wheel trolley were used to point the HCPV/T system toward the sun position during the data collection. A shadow stick was placed on the reference surface where the HCPV/T was seated to confirm that the assembly is normal to sun light by observing the shadow direction and length where no shadow may indicate that the assembly is normal to the sunlight [189]. The testing procedure of the HCPV/T characterisation will be described below.

3.5.1. Optical characterisation

The developed HCPV/T was examined outdoor in terms of optical efficiency and incident illumination uniformity with and without SOE. For optical efficiency calculation, the ratio of the average irradiation power on the receiver to the average irradiation power on the aperture has to be determined. To measure the average solar flux on the aperture, the wireless PV reference sensor was used. While, the I_{SC} was measured using the I-V curve tracer to determine the incident solar irradiance on the receiver. Then, each value was multiplied by the incident area to determine the average power in Watt (W). The I-V curve tracer terminals were connected to the PV electrical terminals by two low resistance wires. Also, to examine the hot spot caused by the non-uniform illumination, 3 thermocouples were attached at the back surface of the active area of the PV assembly and data was recorded using the data logger.

3.5.2. Electrical characterisation

The developed HCPV/T system was electrically examined outdoors under different concentration ratios and PV surface temperatures. To test the HCPV/T under different concentration ratios, the Fresnel lens aperture was varied by varying the exposure area to the sun light. The PV temperature was controlled by the Peltier cooling module powered by a variable DC power supply. Also, the electrical performance of the MJ solar cell was examined under different incident illumination profile such as point-focus and more uniform illumination to evaluate its influence. For electrical efficiency calculation, the ratio of the maximum electrical power (P_m) generated by the solar cell to the average irradiation power on the receiver has to be determined. The P_m can be measured directly by the I-V tracer and the average power on the receiver can be calculated from the measured $I_{SC.}$

3.5.3. Thermal characterisation

The developed HCPV/T system was thermally examined outdoors under different cooling water volume flow rate to examine its influence on the PV temperature and the thermal energy absorbed by the coolant. As previously stated, to measure the PV temperature, 3 thermocouples were attached at the back surface of the active area of the PV cell and temperature was recorded using the data logger. The ambient temperature was measured using a thermocouple connected to the wireless PV reference sensor or to the data logger. To calculate the thermal efficiency of the system, the ratio of the thermal energy extracted by the coolant water to the average power on the receiver was determined. The ΔT was calculated by measuring the inlet and outlet water cooling temperatures using RTD Pt100.

3.6. Measurements accuracy

Human and measuring device errors are encountered in engineering measurements which are considered to be either systematic or random. Systematic error is fixed for each reading but random error is not the same. The measuring instruments have been calibrated which can correct systematic error while random error can be removed by uncertainty analysis. The random errors (repeatability errors) are statistical in nature and can be estimated using the mean standard deviation with 95 % confidence level [190,191].

3.6.1. Uncertainty of surface thermocouples

All surface thermocouples used in the experiment were calibrated using RTD Pt100 with high accuracy of ±0.025K and the uncertainties in their measurement can be calculated using Root Square Sum (RSS) of the systematic and random errors [190,191]:

$$U_{thermo} = \pm\sqrt{(U_{st})^2 + (U_{curve-fit})^2} \tag{3.4}$$

Where U_{st} is uncertainty of the standard (RTD), $U_{curve\text{-}fit}$ is the uncertainty of the curve fit and U_{thermo} is the overall uncertainty of the thermocouple sensors.

The curve fit error is statistical and can be calculated as [191]:

$$U_{curve-fit} = t_{n-1,95\%} S_{\bar{x}} \tag{3.5}$$

Where $t_{n-1,95\%}$ is the student distribution factor for degree of freedom *n -1* and *n* is the number of sample data.

$S_{\bar{x}}$ is the standard deviation of the mean given by [191]:

$$S_{\bar{x}} = \frac{\sigma}{\sqrt{n}} \tag{3.6}$$

σ is the standard deviation which can be calculated using:

$$\sigma = \sqrt{\frac{1}{n-1}\sum_{i=1}^{n}(x_i - \bar{x})^2} \tag{3.7}$$

Where x_i is the RTD reading, $\bar{x}$ is the curve fit value and $x_i - \bar{x}^2$ is the deviation squared. Table 3.7 shows the calculation of the uncertainty for one of the surface thermocouples.

Table 3.7: Surface thermocouple measurement uncertainty calculations.

Data point	RTD Pt100 reading (x_i)	Measurement of thermocouple	Curve fit equation ($\bar{x}$) T = 1.0008x + 0.2466	Deviation $(x_i - \bar{x})^2$
1	29.53	28.91	29.18	0.1229
2	38.01	37.68	37.95	0.0035
3	44.83	44.62	44.90	0.0052
4	53.95	53.86	54.15	0.0408
5	62.39	62.40	62.70	0.0922
6	73.39	73.32	73.63	0.0553
7	90.60	90.06	90.38	0.0474
8	100.99	100.49	100.82	0.0306
Summation of deviation points ($\sum_{i=1}^{n}(x_i - \bar{x})^2$) = 0.397935				
Degree of freedom (n-1) = 7				
Standard deviation (σ) = 0.238428				
Standard deviation of mean ($S_{\bar{x}}$)= 0.084297				
Student distribution factor $t_{n-1,95\%}$ = 2.365				
Uncertainty curve fit ($U_{curve-fit}$) = 0.20K				
Uncertainty of surface thermocouple $U_{thermo} = \pm\sqrt{(U_{st})^2 + (U_{curve-fit})^2}$ = ±0.20K				

The standard device used in the calibration is high precision RTD which was calibrated against ice temperature i.e. at 0 °C as it was placed in the ice water mixture and the temperature was recorded at different points as shown in Figure 3.24. The uncertainty of the RTD Pt100 sensor (U_{st}) is small i.e. ±0.025K compared to the uncertainty of the measuring device ($U_{curve\text{-}fit}$). Therefore, the overall uncertainty of the surface thermocouple sensors calculated using equation 3.4 is ±0.20K.

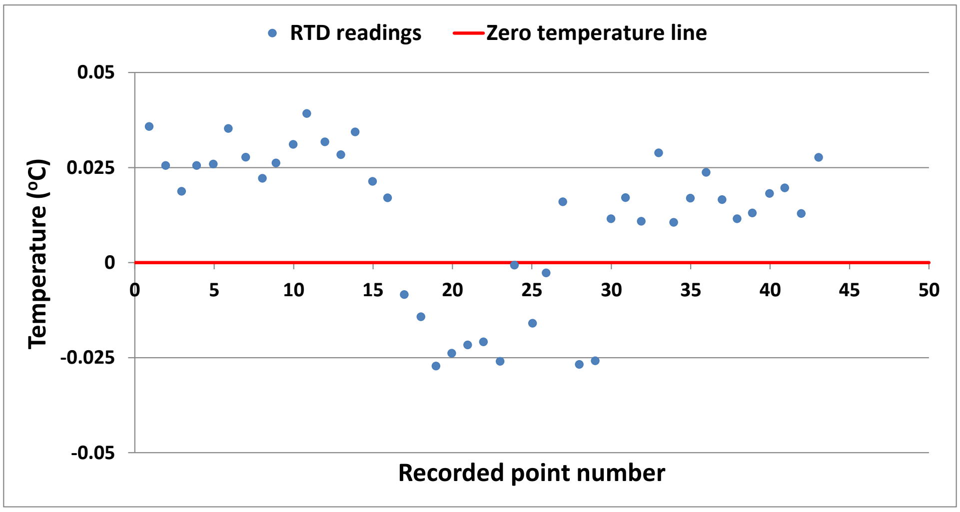

Figure 3.24: Calibration of the RTD thermocouple reading.

3.6.2. Uncertainty of solar irradiance PV reference sensor

The wireless PV reference sensor is used to measure the solar radiation at the aperture of the Fresnel lens. It was calibrated against a certified new Kipp & Zonen SMP10 Pyranometer. The uncertainty of the irradiance PV reference sensor (U_{irr}) is then calculated based on the uncertainty of the curve fitting ($U_{curve\text{-}fit}$) and uncertainty of the Pyranometer (U_{pyr}) as shown in equation 3.8 [191].

$$U_{irr} = \sqrt{(U_{pyr})^2 + (U_{curve-fit})^2} \tag{3.8}$$

The uncertainty of the Pyranometer is given by the manufacturer in the calibration certificate (U_{pyr}) to be ±0.76 W/m^2 and the uncertainty of the measuring device ($U_{curve\text{-}fit}$) is 2.44 W/m^2 as shown in Table 3.8. Therefore, the overall uncertainty of the radiation sensor calculated using equation 3.8 is ±2.56W/m^2.

Table 3.8: Radiation measurement at the aperture uncertainty calculations.

Data point	Pyranometer (x_i)	Radiation sensor	Curve fit equation ($\bar{x}$) $V_w = 1.0017x - 0.5964$	Deviation $(x_i - \bar{x})^2$
1	544	545	545.33	1.7692
2	110	111	110.59	0.3508
3	1089	1090	1091.26	5.0922
4	1020	1022	1023.14	9.8659
5	301	304	303.92	8.5287
6	465	461	461.19	14.5367
7	811	807	807.78	10.3974
8	944	940	941.00	8.9904
Summation of deviation points ($\sum_{i=1}^{n}(x_i - \bar{x})^2$) = 59.5313				
Degree of freedom (n-1) = 7				
Standard deviation (σ) = 2.916243428				
Standard deviation of mean ($S_{\bar{x}}$)= 1.031047752				
Student distribution factor $t_{n-1,95\%}$ = 2.365				
Uncertainty curve fit ($U_{curve\text{-}fit}$) = 2.44 W/m^2				
Uncertainty of PV reference sensor $U_{irr} = \sqrt{(U_{pyr})^2 + (U_{curve\text{-}fit})^2}$ = ±2.56W/m^2				

3.6.3. Uncertainty of the flow meter

The CT Platon flow meter used in the test facility was calibrated using graduated cylinder and stop watch. The flow meter readings were then plotted versus the calculated flow rate (V_w) using equation (3.9). The uncertainty of the CT Platon flow meter (U_{fm}) is then calculated based on the uncertainty of the curve fitting ($U_{curve\text{-}fit}$) and uncertainty of the calibration method (U_{vc}) as shown in equation (3.10) [191].

$$\mathrm{V_w} = \frac{\Delta \mathrm{V_f}}{\Delta \mathrm{t}} \tag{3.9}$$

$$U_{fm} = \sqrt{(U_{vc})^2 + (U_{curve-fit})^2} \tag{3.10}$$

U_{vc} the uncertainty of the cylinder graduated volume i.e. the calibrating method is given by equation 3.11 [186,191].

$$U_{VC} = \sqrt{\left(\frac{\partial V_w}{\partial V_f}\Delta V\right)^2 + \left(\frac{\partial V_w}{\partial t}\Delta t\right)^2} \tag{3.11}$$

Where V_w is the water flow rate calculated using equation 3.9 in (ml/min), V_f is the total volume of the collecting cylinder in (ml), ΔV is the error in measuring the volume which equals to the step in the graduating scale of the measuring cylinder, Δt is the minimum time that can be counted when cylinder is filling with water and t is time in minutes. The uncertainty of the calibration method is estimated using equation 3.12 [191].

$$U_{VC} = \sqrt{\left(\frac{1}{t}\Delta V\right)^2 + \left(\frac{V_f}{t^2}\Delta t\right)^2} \tag{3.12}$$

Using ΔV of 10 ml, Δt of 1/60, the calculated uncertainty U_{vc} is ±0.32 ml/s. Table 3.9 shows the calculation of the uncertainty for the flow rate measurement.

Table 3.9: Flow meter measurement uncertainty calculations.

Data point	Cylinder volume (x_i)	CT Platon flow meter	Curve fit equation ($\bar{x}$) $V_w = 1.0004x - 0.9911$	Deviation $(x_i - \bar{x})^2$
1	92.37	100.00	99.05	44.6077
2	210.97	200.00	199.09	141.1605
3	304.57	300.00	299.13	29.6056
4	404.86	400.00	399.17	32.3886
5	483.87	500.00	499.21	235.2819
6	581.96	600.00	599.25	298.9061
7	705.05	700.00	699.29	33.1903
8	809.72	800.00	799.33	107.9750
Summation of deviation points ($\sum_{i=1}^{n}(x_i - \bar{x})^2$) = 923.1156				
Degree of freedom (n-1) = 7				
Standard deviation (σ) = 11.4836255				
Standard deviation of mean ($S_{\bar{x}}$)= 4.06007473				
Student distribution factor $t_{n-1,95\%}$ = 2.365				
Uncertainty curve fit ($U_{curve\text{-}fit}$) = 0.16 ml/s				
Uncertainty of the flow meter $U_{fm} = \sqrt{(U_{vc})^2 + (U_{curve-fit})^2}$ = ±0.36ml/s				

The uncertainty of the calibration method (U_{vc}) is ±0.32ml/s and the uncertainty of the measuring device ($U_{curve\text{-}fit}$) is 0.16 ml/s. Therefore, the overall uncertainty of the flow meter calculated using equation 3.10 is ±0.36ml/s or ±2.2% of full scale.

3.7. Summary

In this chapter the experimental facility developed to investigate the optical, electrical and thermal performance of the HCPV/T is fully described. The outdoor experimental set-up mainly consists of HCPV/T assembly and measuring instruments. The HCPV/T assembly includes optical elements, multi-junction solar cell, cooling mechanism and manual tracking system. The main measuring instruments are wireless PV reference sensor, radiation sensor, I-V curve tracer, surface thermocouples, RTD and flow meter which were used to measure the following: solar irradiation at the concentrator, solar irradiation at the receiver, the generated electricity from the solar cell, the PV temperature, the inlet and outlet coolant temperature and the cooling water flow rate respectively.

In reference to the optical characterisation, the optical efficiency was calculated by determining the average irradiation power on the receiver and the average irradiation power on the aperture. Also, the hot spot caused by the non-uniform illumination was examined by attaching thermocouples at the back surface of the PV before it was seated on the cooling device. On the other hand, the electrical efficiency of the solar cell at different concentration ratios and PV temperatures was determined by measuring the maximum electrical power generated by the solar cell and the average irradiation power on the receiver. Moreover, to determine the thermal efficiency of the system the ratio of the thermal energy extracted by the cooling water and the average power on the receiver has to be calculated. Calibration of the measuring devices including PV reference sensor, surface thermocouples and flow meter were carried out and measurement accuracy was evaluated by performing uncertainty analysis.

The optical, electrical and thermal data measured from this experimental facility are used to validate the developed optical, electrical and thermal theoretical models as demonstrated in chapters 4, 6 and 7.

CHAPTER 4

Optical simulation and outdoor characterisation of the HCPV system

4.1. Introduction

This chapter describes the optical simulation and characterisation of a primary optical element (Fresnel lens) and the development of a secondary optical element for HCPV system using ray tracing technique. The optical efficiency of the optical system will be analysed with and without a secondary optical element. Moreover, the irradiation uniformity on the receiver will be investigated before and after the placement of the secondary optical element (SOE). Finally, outdoor experimental results to validate the developed optical simulation and to examine the influence of the non-uniform illumination on the electrical performance of the multi-junction solar cell will be presented.

4.2. Performance characterisation of a point-focus Fresnel lens

In this section, the optical efficiency and irradiation distribution on the receiver was examined with and without secondary optical element using ray tracing technique.

4.2.1. Fresnel lens development governing equations

Polymethyl methacrylate (PMMA) Fresnel lens is a well-known optical element as a concentrator because it has various advantages such as compact size, lower weight and material cost saving [100,108]. Imaging point-focus Fresnel lens consists of serial pitches of Fresnel lens facets as shown schematically in Figure 4.1. The following governing equations (4.1-4.4) can describe each pitch of the Fresnel lens [134]:

$$n\sin\alpha = \sin\beta \tag{4.1}$$

$$\tan\omega = \frac{R}{f} \tag{4.2}$$

$$\beta = \alpha + \omega \tag{4.3}$$

$$\tan\alpha = \frac{R}{n\sqrt{R^2 + f^2} - f} \tag{4.4}$$

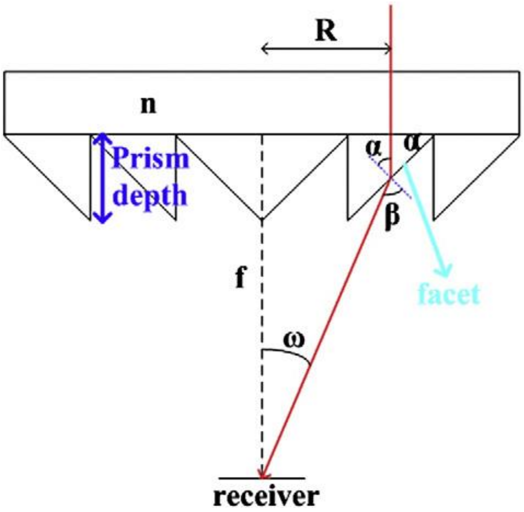

Figure 4.1: Schematic of planar Fresnel lens [108].

Snell's law is applied on the incident ray as shown in Figure 4.1 and equation 4.1-4.4 defines each facet's angle where *R* is the distance between incident ray and the centre axis of the Fresnel lens, *n* is the refractive index of the Fresnel lens material, α (slope angle) is the angle between the normal to the Fresnel lens's facet and the incident ray, ω is the angle between the normal to the receiver and the refracted ray, β is the angle between the normal to the Fresnel lens's facet and the refracted ray and *f* is the focal length. A computer program was developed in Excel spreadsheet using equation 4.4 for calculating the slope angle (α). Fresnel lens grooves are chosen to be upside down (grooves in) which is suitable for dusty environment as dust can deposit within these grooves and cause shadows on the PV surface [134].

SolidWorks was used to develop the Fresnel lens geometry taking into consideration the angle definition of each Fresnel lens prism as can be seen in Figure 4.2. Fresnel lens focal length, size, thickness and groove pitch are the main geometrical parameters that were needed to be identified. The initial developed Fresnel lens was circular in shape, but as the receiver is square it would be easier for geometrical concentration ratio calculation to have a square Fresnel lens as well. Extrude cut feature in SolidWorks was used to cut the Fresnel lens as shown in Figure 4.3.

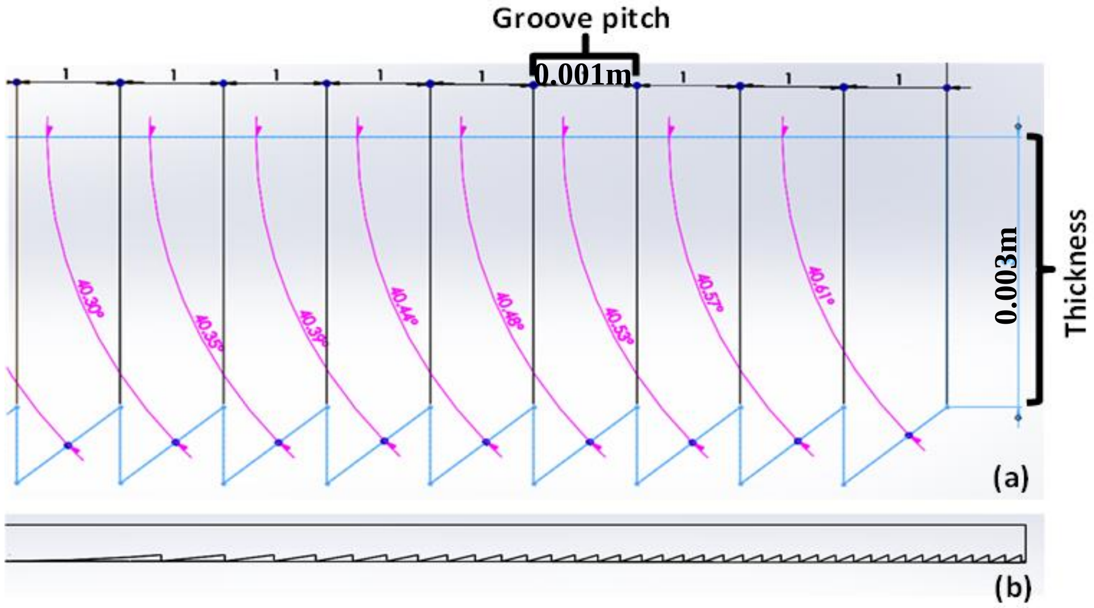

Figure 4.2: a) Angle definition of each prism; b) Fresnel lens prism profile.

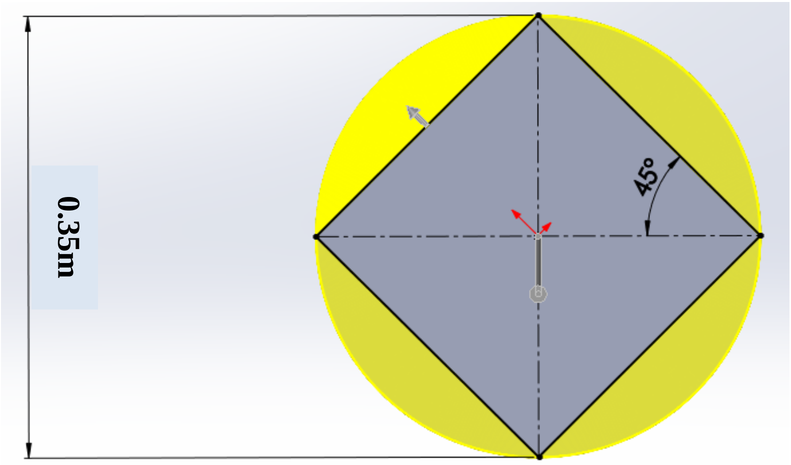

Figure 4.3: Extrude cut to the developed 0.25x 0.25 m^2 Fresnel lens.

A flow chart summarizing the procedure of developing the Fresnel lens is shown in Figure 4.4. The light source, developed Fresnel lens and the receiver were assembled and coupled in one assembly to be used for ray tracing simulation.

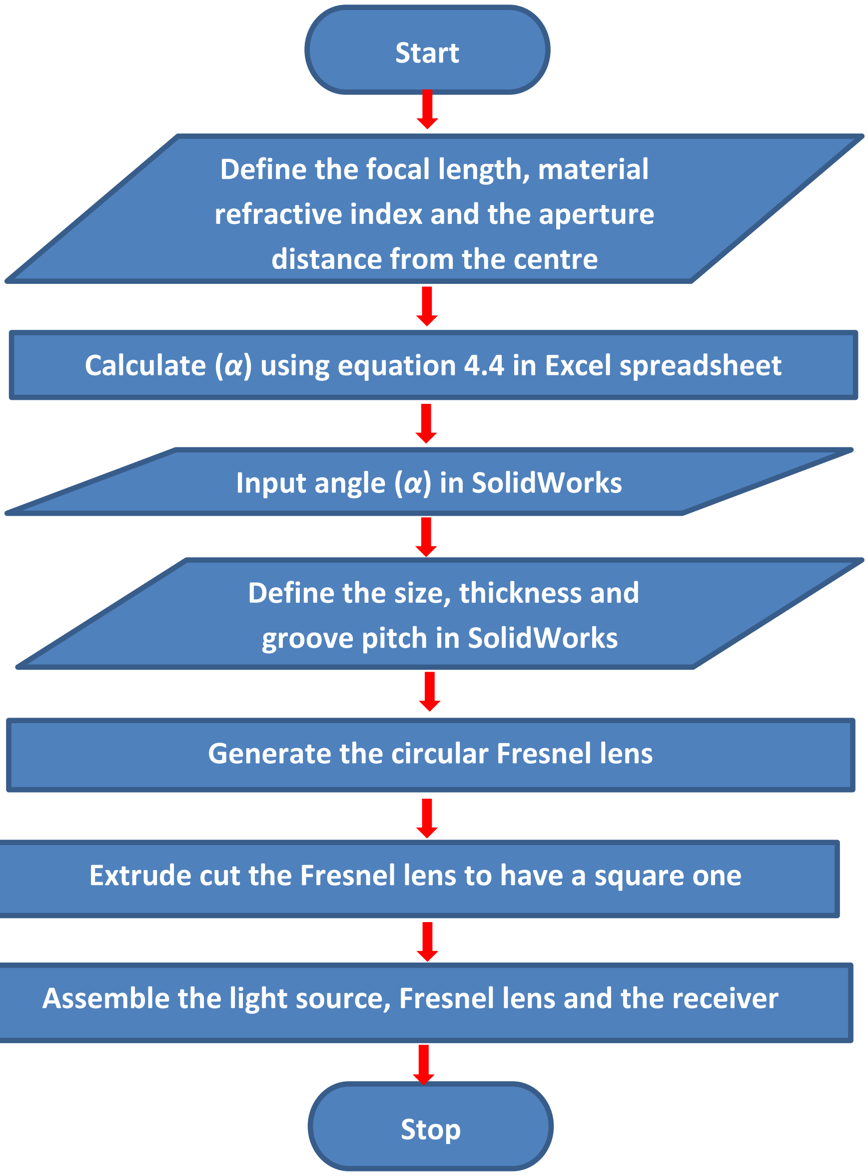

Figure 4.4: Flow chart of the developing process of point-focus Fresnel lens using SolidWorks.

4.2.2. Ray tracing technique theory and assumptions

OptisWorks is a powerful commercial software widely used by architecture, lighting and car industries to evaluate and optimise the optical performance in many applications. It offers the solution for the optical study using the ray tracing technique taking into consideration the different physical characteristics varying from the nature of the source of light to properties of the reflector and refractors materials. The technique is capable of simulating the sun intensity to show irradiance, power and flux distributions on the concentrator aperture and on the receiver surface. Therefore, OptisWorks was used in this research to develop the optical system required for high concentration of radiation on PV cell. A brief literature review on ray tracing method for optical modelling of solar concentrators can be found in Appendix C. Snell’s laws describe the behaviour of the refracting and reflecting rays by defining the relationship between the angles of incidence and refraction for rays striking a surface between two media of different refractive indices. It is more convenient to implement ray tracing algorithms in vector-based design software, where each ray is represented by a vector, than in a scalar-based one. To use Snell’s law of reflection in vector form, it is required first to find the point of incidence of the incoming ray on the reflecting surface. Then, a unit vector normal to the surface (normal vector) at the point of interest and a unit vector incident into that point (incident ray vector) can be defined as demonstrated in Figure 4.5a. Here, *i* is the unit vector along the incident ray, and *n* is the unit vector normal to the surface. The vector *r*, which is the unit vector along the reflected rays, can be calculated using equation 4.5 [186,192,193]:

$$r = i - 2\left(\mathrm{n} \bullet i\right) n \tag{4.5}$$

The calculation of the refracted rays is performed in a similar technique. Firstly, for a given ray, the point of incidence at the boundary of the refracting media must be found, and a unit vector corresponding to the incident ray must be traced as shown in Figure 4.5b. Here, n_1 represents the index of refraction of the input media, n_2 represents the index of refraction of the concentrator, *i* is the unit vector along the incident ray and *t* is the unit vector along the refracted ray. The vectors of the rays are analysed in a numerical computation through their vector components. The vector *t* is calculated by [193]:

$$n_2 t \times n = n_1 i \times n \tag{4.6}$$

This relation assumes that the incident and the refracted rays in the figure are in the same plane. It can be observed that this expression is equivalent to the scalar form of Snell’s law of refraction, where t x $n = sin\theta_i$ and i x $n = sin\theta_t$. A more useful expression of ray tracing can be obtained from equation 4.6 by multiplying it vectorially by *n* which gives [193]:

$$n_2 t = n_1 i + (n_2 t \bullet n - n_1 i \bullet n) n_1 \tag{4.7}$$

This is equivalent to:

$$n_2 t \bullet n - n_1 i \bullet n = n_2 \cos\theta_t - n_1 \cos\theta_i \tag{4.8}$$

The angle of refraction θ_t can be calculated using equation 4.9:

$$\theta_t = \sin^{-1}\left(\frac{n_1 \sin\theta_i}{n_2}\right) \tag{4.9}$$

Depending on the surface quality and material used, a ray which is incident at the Fresnel lens surface may be reflected back, absorbed or transmitted through the lens as shown in Figure 4.5 [33,47,60] where the direction of the transmitted rays is described by Snell's law. PV solar cells used in HCPV systems are assumed perfect black bodies; therefore all incident energy will be absorbed by the photovoltaic solar cell and either converted into electrical or thermal energy [192].

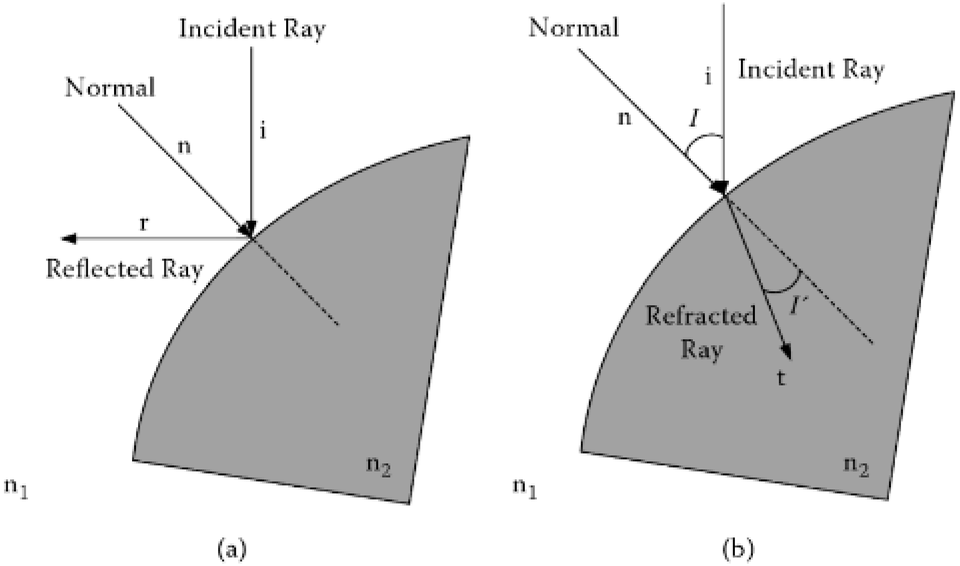

Figure 4.5: Vector formulation of Snell's laws: a) law of reflection; b) law of refraction [193].

If a reflector is introduced as a secondary optical element (SOE), some of the rays striking the reflector are reflected back whereas some are absorbed causing loss of energy depending on the reflectivity of the material. Rays entering the SOE intersect with the Fresnel lens first and then as shown in Figure 4.6 either strike the absorber (PV) with no previous reflections, reflect a finite number of times before intersecting with the absorber, or reflect a finite number of times before exiting.

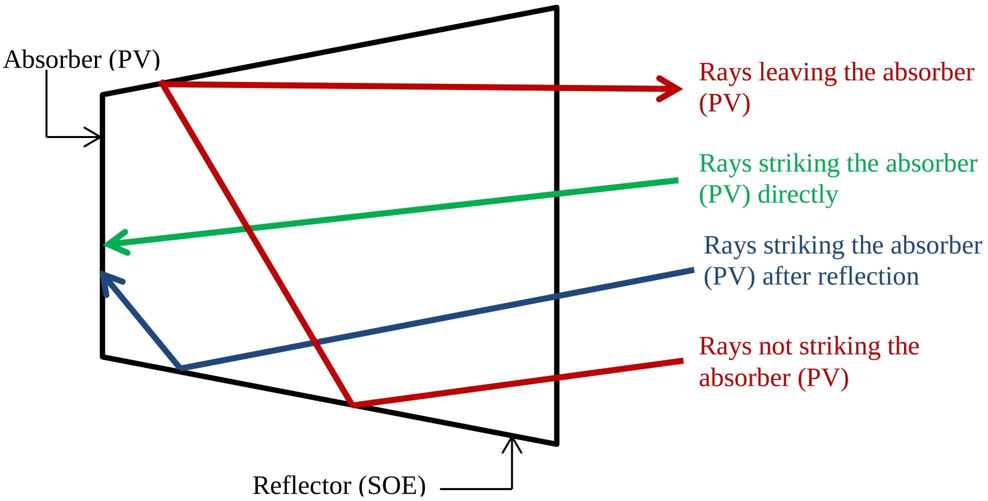

Figure 4.6: Rays entering the SOE after intersecting the Fresnel lens.

The following assumptions were made for the ray tracing analysis [192]:

I. All rays follow Fermat's principle which states that rays follow shortest distance and take minimum time when travelling from one point to another.
II. All reflections are specular (angle of incidence equals the angle of reflection).
III. The incident solar radiation is made up of parallel rays carrying equal amount of energy.

The optical efficiency of the developed point-focus Fresnel lens with and without SOE and the flux distribution on the receiver with and without the secondary optical element were investigated using the ray tracing technique. The acceptance angle of the Fresnel lens with and without SOE will be discussed in the next chapter. In order to characterise the optical system of the HCPV, the material and the optical properties for each part of the assembly (source, optical elements and the receiver) has to be defined.

4.2.3. Optical simulation set-up

The use of OptisWorks for ray tracing simulation of the optical system involves five major stages (shown in Figure 4.7) including drawing the Fresnel lens geometry, modelling the source (sun), defining material properties, defining the incoming and receiver detectors and running the ray tracing simulation.

4.2.3.1. Light source and receiver modelling

The source can be modelled to represent the real sun or a light source like lamp in a solar simulator. Its definition involves defining the power (W), emittance type (uniform or variable), intensity type (Lambertian, Cos or Gaussian), spectrum (Monochromatic or blackbody), temperature, ray tracing (true or false colour) and the number of rays. The boundary conditions applied include the irradiance in the source, refractivity/reflectivity of the concentrator, absorptivity of the receiver and half acceptance angle.

The simulation was carried out according to the process outlined in Figure 4.7 with circular light source set to be uniform and radiation value of 1000 W/m^2. Moreover, in this simulation the source was set to generate 10 Mega rays and the shape of the source was defined as planar and its size was made larger than the Fresnel lens length, so that the rays emitted cover the entire Fresnel lens aperture. The intensity type used is Lambertian and half angle of 0^o was set for the source. The spectrum of the light source is set to a spectrum emitted by a blackbody at 5400 K to simulate the spectrum of the sun.

Figure 4.8 shows the light source spectrum taken from the ray tracing software. Finally, the absorptivity of the receiver was set to have 100% absorption.

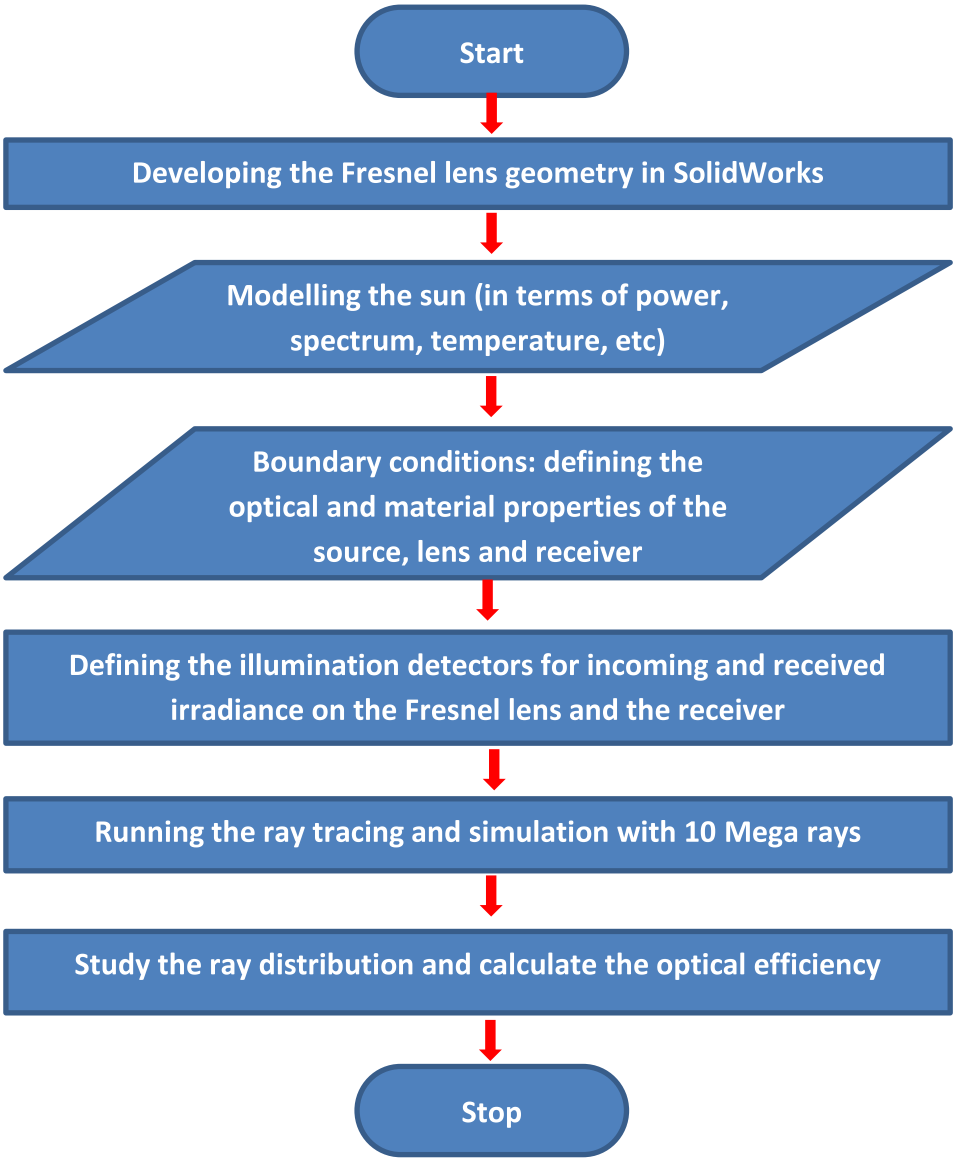

Figure 4.7: Flow chart of the modelling process of point-focus Fresnel lens using ray tracing method.

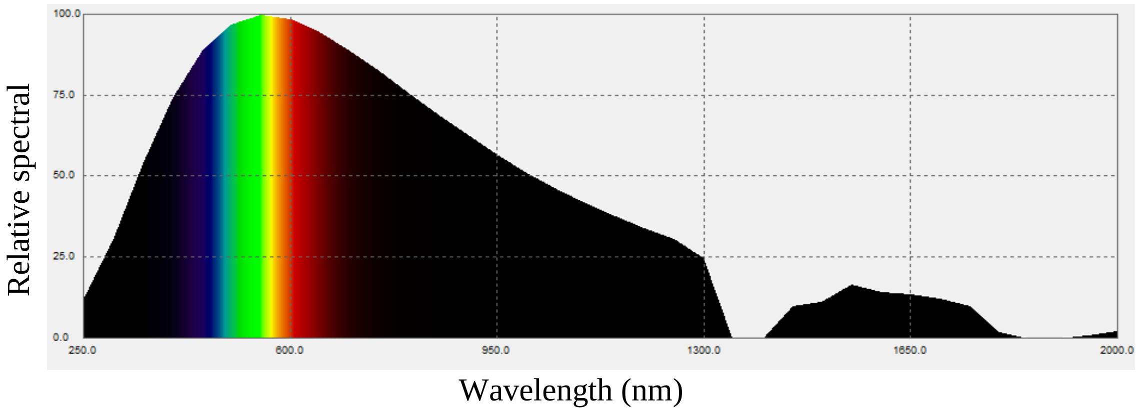

Figure 4.8: Solar radiation spectrum of the simulation light source.

4.2.3.2. Fresnel lens modelling

After generating the Fresnel lens geometry, the Fresnel lens material and optical properties were set. In this Fresnel lens, the material is PMMA which is a typical optical plastic with a refractive index varying from 1.48 to 1.5 for a wavelength from 1600 to 400 nm [108]. Since the refraction index of the PMMA material is a function of the solar radiation wavelength, Figure 4.9 shows the refractive index spectrum that was set in the optical simulation.

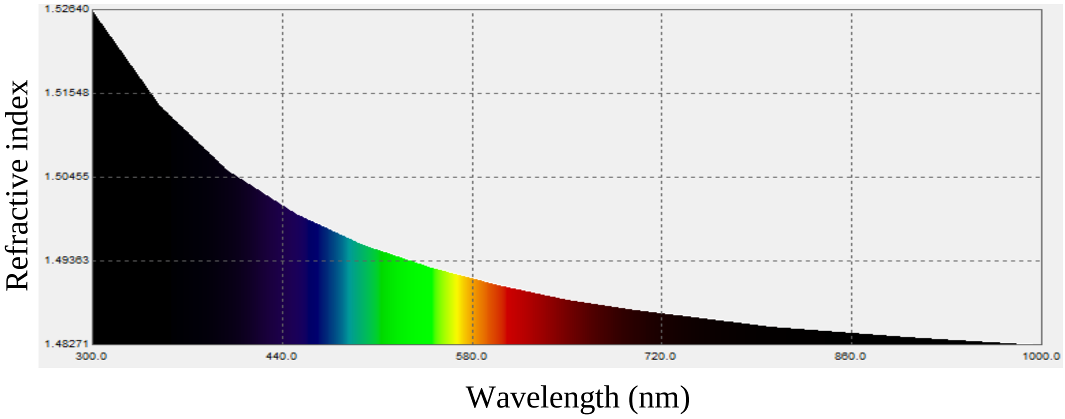

Figure 4.9: The Refractive index spectrum of the PMMA along the wavelength.

Moreover, the light absorption of the PMMA material is a function of the radiation wavelength. Figure 4.10 shows the absorption spectrum of the PMMA material with the wavelength that was set for the optical simulation.

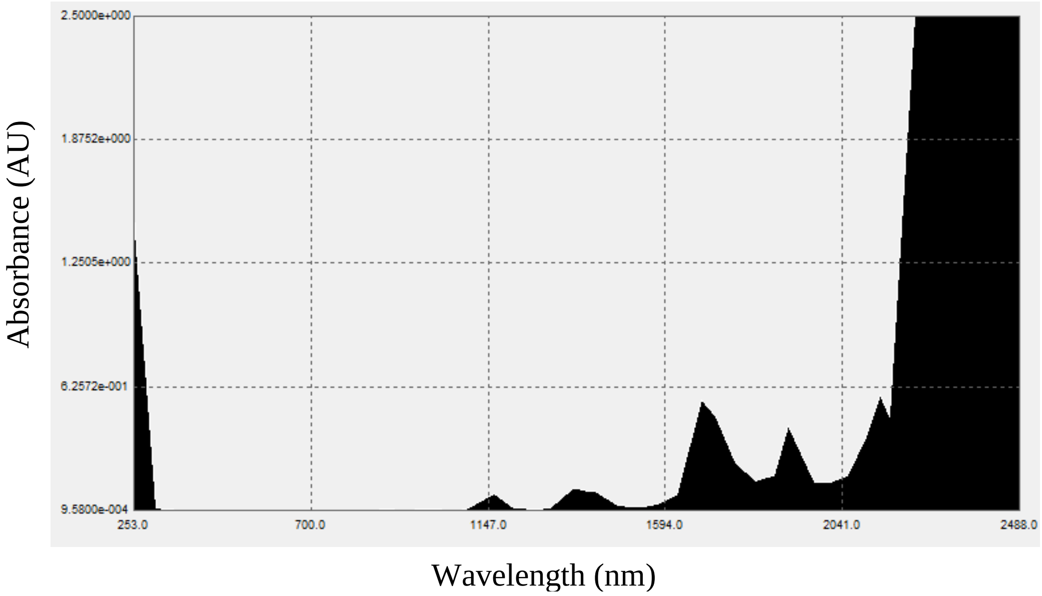

Figure 4.10: The absorption spectrum of the PMMA along the wavelength.

4.2.4. Optical simulation characterisation of off-the-shelf Fresnel lens

The available Fresnel lens with the listed parameters in Table 3.1 (chapter 3) will be characterised with and without secondary optical element in terms of optical efficiency and ray distribution uniformity and the output results will be compared against the experimental work.

4.2.4.1. Optical efficiency investigation

Although Fresnel lenses can be fabricated in large geometries, their size is chosen based on the target concentration, the cell size and its thermal management requirements and the maximum reasonable depth of the enclosure [33]. High geometrical concentration ratio is targeted i.e. above 100X, so the aperture area of the Fresnel lens was varied as per the following: $0.13x0.13m^2$, $0.15x0.15m^2$, $0.18x0.18m^2$, $0.2x0.2m^2$ and $0.25x0.25m^2$ to produce geometrical concentration ratios of: 169X, 225X, 324X, 400X and 625X respectively as the area of the receiver is $0.01x0.01m^2$. The applied radiation flux was set to $1X=1000\ W/m^2$ through all the simulations. The optical efficiency (η_{opt}) of a point-focus Fresnel lens can be calculated using the following equation [194]:

$$\eta_{opt} = \frac{\text{Average power on the receiver}}{\text{Average power on the aperture}} \tag{4.10}$$

Figure 4.11 shows the HCPV optical assembly, including the ray source, Fresnel lens and the receiver; the incident rays refracted by the Fresnel lens to the receiver.

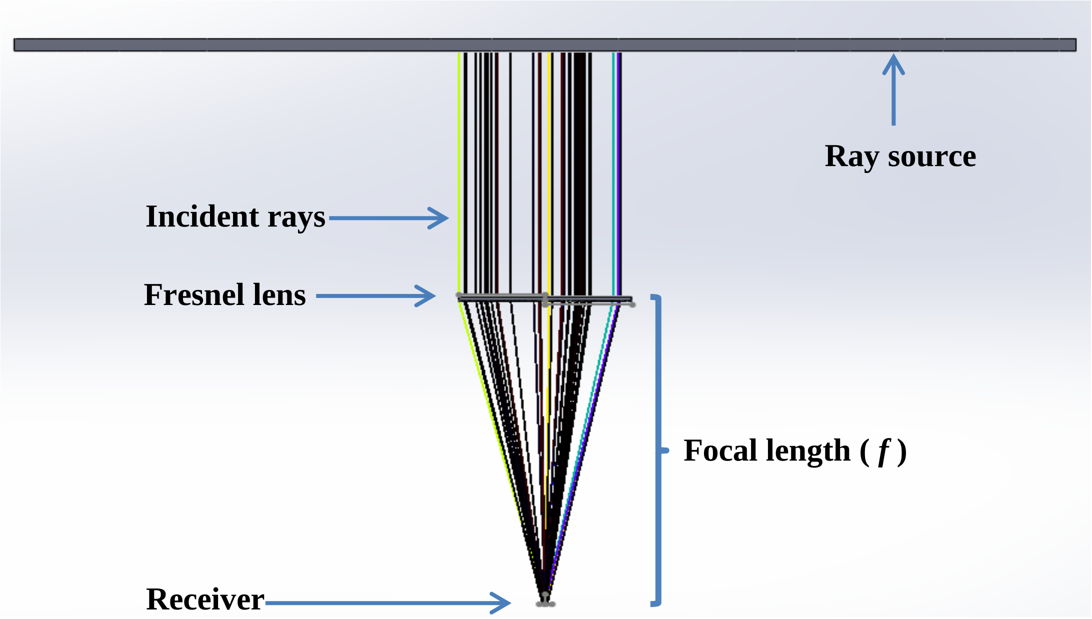

Figure 4.11: CPV assembly shows incident rays after refracted by the Fresnel lens.

Figure 4.12 shows the 2-D image of the incident rays on the receiver for the case of 0.18x0.18m^2 aperture area Fresnel lens. The Fresnel lens produces a high concentration of energy at the centre of the receiver limited between -0.5mm to +0.5mm region.

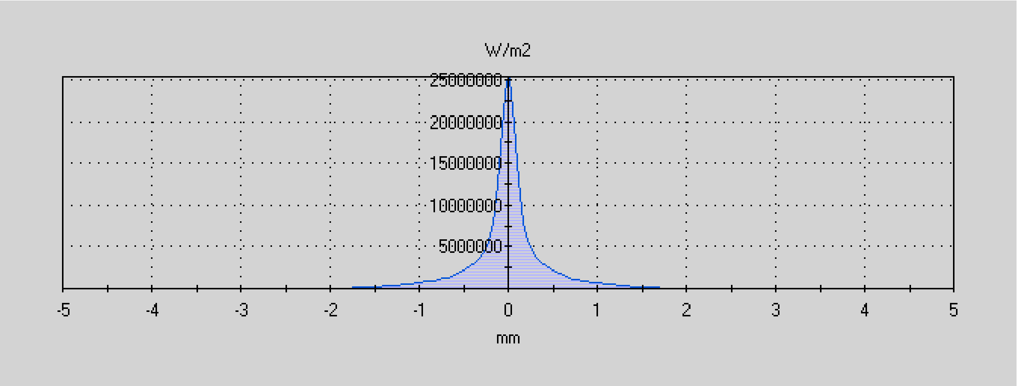

Figure 4.12: 2-D Incident rays distribution and magnitude on the receiver for 0.18x0.18m^2 aperture area lens.

Figure 4.13 shows a 3-D image of the incident radiation flux in W/m^2 and its distribution on the receiver for the 0.18x0.18m^2 aperture area Fresnel lens.

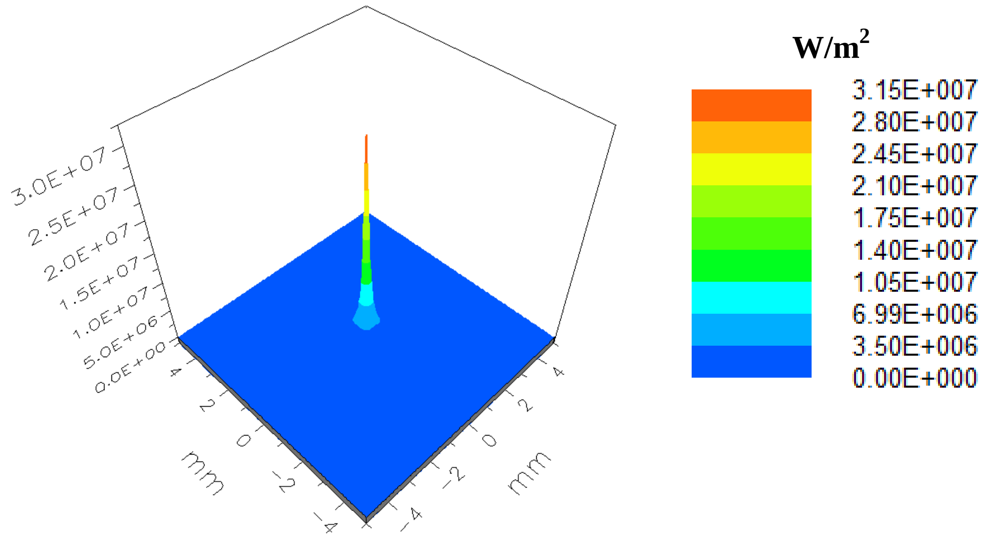

Figure 4.13: 3-D Incident rays distribution and magnitude on the absorber for 0.18x0.18m^2 aperture area lens.

The 2-D and 3-D images above are the typical incident flux profile on the receiver when a point-focus Fresnel lens is used without SOE.

Table 4.1 shows the simulation results including the F-number, received flux distribution, received power and the optical efficiency of the five different Fresnel lens aperture areas. It can be observed that for the same focal length, reducing the aperture area results in better optical efficiency. For instance, the optical efficiency for 0.13x0.13m^2 and 0.25x0.25m^2 apertures is about 66% and 59% respectively. The depth of the Fresnel lens prisms increases with the distance from the centre axis of the Fresnel lens since the slope angle (α) is increased. Therefore, increasing the aperture area results in higher number of deeper prisms which experience more reflection losses and material absorption than shallow ones [33,46,79,126,134].

The F-number of a Fresnel lens can be defined as the ratio of the focal length (f) to the aperture diameter (D) as shown in the following equation:

$$\text{F-number} = \frac{\text{focal length}(\,f\,)}{\text{diameter }(D)} \tag{4.11}$$

The highest and lowest optical efficiency are achieved at F-number of 1.36 and 0.71

respectively where the Fresnel lens aperture areas are 0.13x0.13m^2 and 0.25x0.25m^2. For the same Fresnel lens aperture area, the optical efficiency can be enhanced by increasing its focal length; this will be discussed further in the optimisation chapter. It can be concluded that optical efficiency is directly proportional to the F-number.

Table 4.1: Summary of increasing the Fresnel lens aperture area on the simulated optical efficiency.

Aperture area (m^2)	Fresnel lens F-number	Received flux distribution	Input power (W)	Received power (W)	Optical efficiency (%)
0.25x0.25	0.71	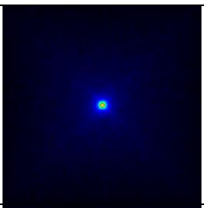	62.5	37.12	59.4
0.2x0.2	0.88	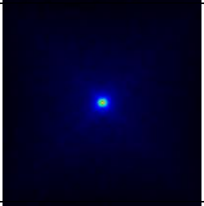	40	25.12	62.8
0.18x0.18	0.98	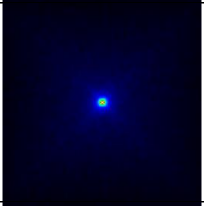	32.4	20.73	64.0
0.15x0.15	1.18	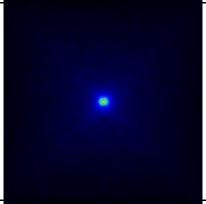	22.5	14.72	65.4
0.13x0.13	1.36	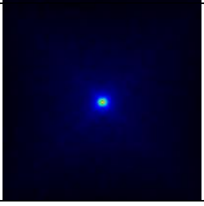	16.90	11.20	66.3

From the simulation results, it can be concluded that the tested Fresnel lens produced high peak power but with non-uniform ray distribution profile where energy is concentrated in a very small area of the receiver. This illumination profile is typical for point-focus Fresnel lens which tends to cause a hot spot and current mismatch leading to a reduction in the electrical efficiency of the system and degrade the life of the solar cell [25,38,155,157]. Methods to improve the distribution of the incident rays will be covered in the following sections.

4.2.4.2. Incident rays uniformity characterisation

Non-uniform illumination is one of the main operational challenges that degrades the HCPV system performance [101,142,143]. A cell under non-uniform illumination may experience a drop in both open-circuit voltage and efficiency compared to a cell under uniform illumination, although both cells could receive identical total illumination [95]. In order to increase the uniformity on the receiver (PV), two techniques were investigated: varying the distance between the Fresnel lens and the PV and introducing a secondary optical element (SOE) on the receiver. The main objective is to have a uniform irradiation on the receiver with minimum loss in the received energy i.e. minimum loss in the optical efficiency.

The spatial radiation power of the incident rays can be exported from OptisWorks to Excel spreadsheet to assess the degree of non-uniformity by calculating the standard deviation which can illustrate how much the spatial incident rays differ from the mean value of the whole incident rays. A low standard deviation indicates that all the spatial rays received by the solar cell are close to the mean value i.e. more uniform and vice versa [154]. The equation below is used to calculate the standard deviation of a sample of data:

$$\sigma = \sqrt{\frac{\sum\left(x-\bar{x}\right)^2}{n-1}} \tag{4.12}$$

Where x represents the value of each member, $\bar{x}$ is the average of all values and (n) is the number of values.

The incident rays profile, as shown in Figure 4.14, is symmetrical in shape; therefore, the radiation flux on the receiver was taken along the horizontal, vertical and diagonal axis to calculate the uniformity. The user can select the line where to take the incident radiation power values using a cursor as shown in Figure 4.14b and the number of samples which was set to 200 for each line.

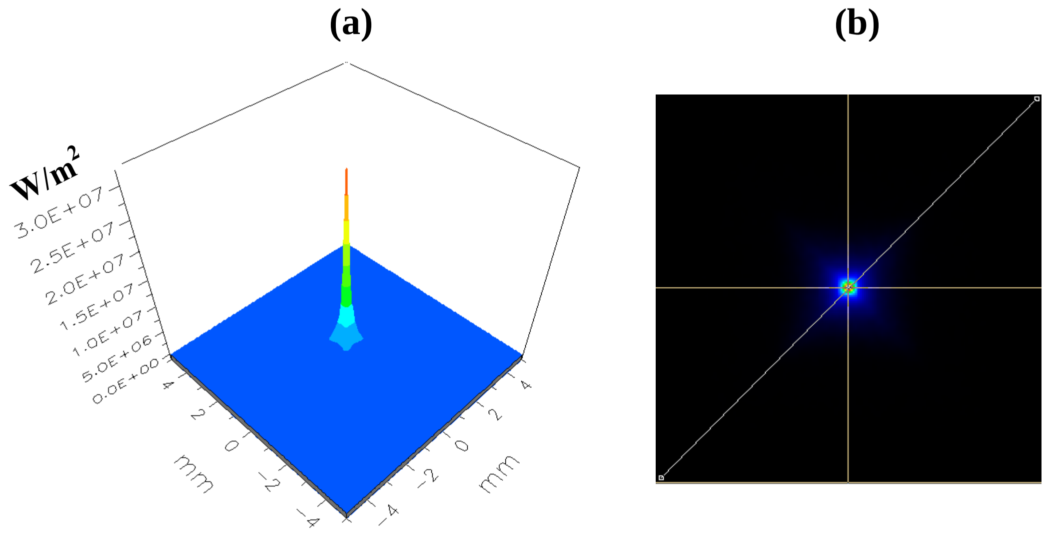

Figure 4.14: a) 3-D image of ray distribution for 0.18x0.18m^2 lens in W/m^2; b) 2-D image of ray distribution.

Three Fresnel lens aperture areas of 0.13x0.13m^2, 0.18x0.18m^2 and 0.25mx0.25m^2 equivalent to geometrical concentration ratios of 169X, 324X and 625X respectively will be used in the uniformity tests.

Effect of varying the distance between the Fresnel lens and the receiver (*l*)

The concept of varying the distance between the Fresnel lens and the receiver, (*l*), can be illustrated in Figure 4.15 [113]. At a distance higher than the focal length (f = 0.25m) rays start to diverge forming different profile on the receiver as the distance (*l*) increases. The uniformity and the received power on the receiver were investigated at various distance (*l*): 0.235m, 0.24m, 0.245m, $l = f$ = 0.25m, 0.255m, 0.26m, 0.265m, 0.27m, 0.275m, 0.28m, 0.285m and 0.29m.

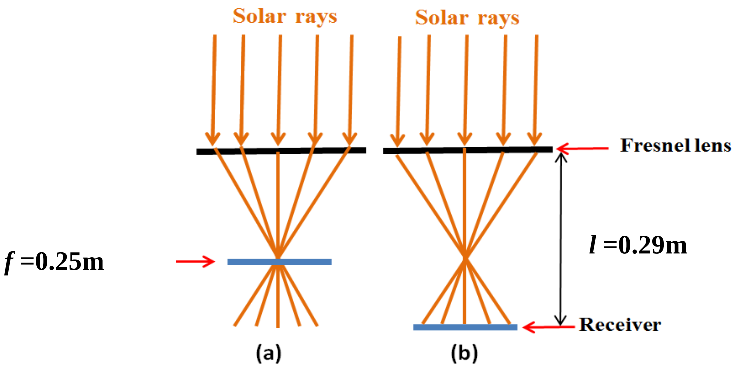

Figure 4.15: a) Rays converging at focal length; b) rays diverging after focal length.

Figure 4.16 shows the influence of varying the distance (*l*) on the received power and uniformity for 0.18x0.18m^2 aperture Fresnel lens. It is clear from the Figure that the received power is negatively influenced by increasing the distance (*l*) from the focal length height (*l* = *f* =0.25m) while the non-uniformity is improved. For example, the received power at focal length, i.e. *l* = *f* =0.25m, is 20.73 W with optical efficiency of 64% while the power at *l* = 0.28m is 7.48 W with optical efficiency of about 23%. On the other hand, the incident rays non-uniformity is maximum at the focal length (σ = 692.45) while it is minimum at *l* = 0.29m (σ < 1). The same behaviour with less uniformity is observed when the distance (*l*) becomes shorter than the focal length height. It can be concluded that increasing the distance (*l*) leads to a better uniformity but with higher optical losses.

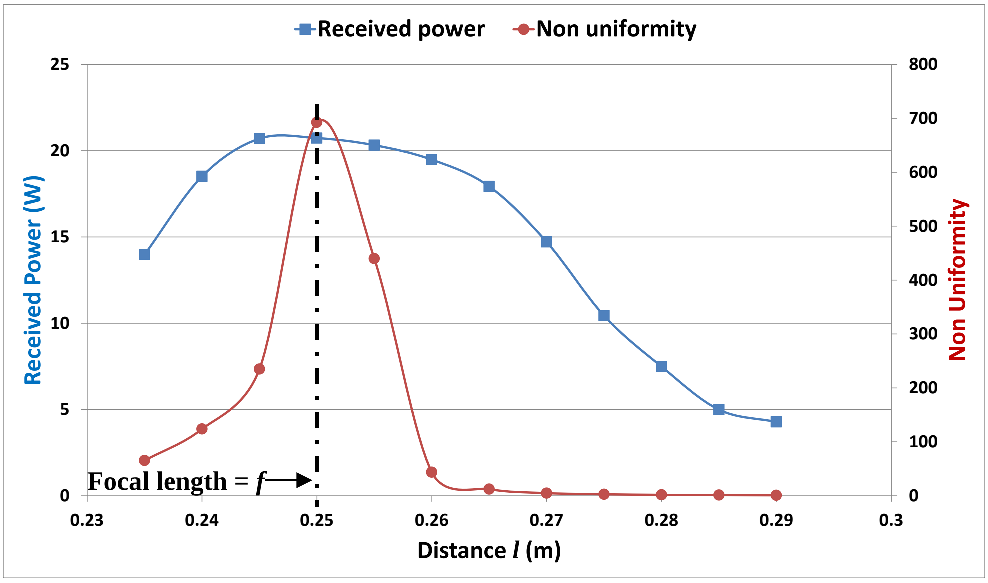

Figure 4.16: Effect of varying the distance (*l*) on the received power and uniformity.

Figure 4.17 shows the optical efficiency of the three different apertures of Fresnel lens at different distance (*l*). It can be observed that the maximum optical efficiency is when the receiver at the focus point i.e. at 0.250m. Moreover, due to the reduction of the received power on the receiver as the distance (*l*) varied from the focus point, the optical efficiency decreases as well.

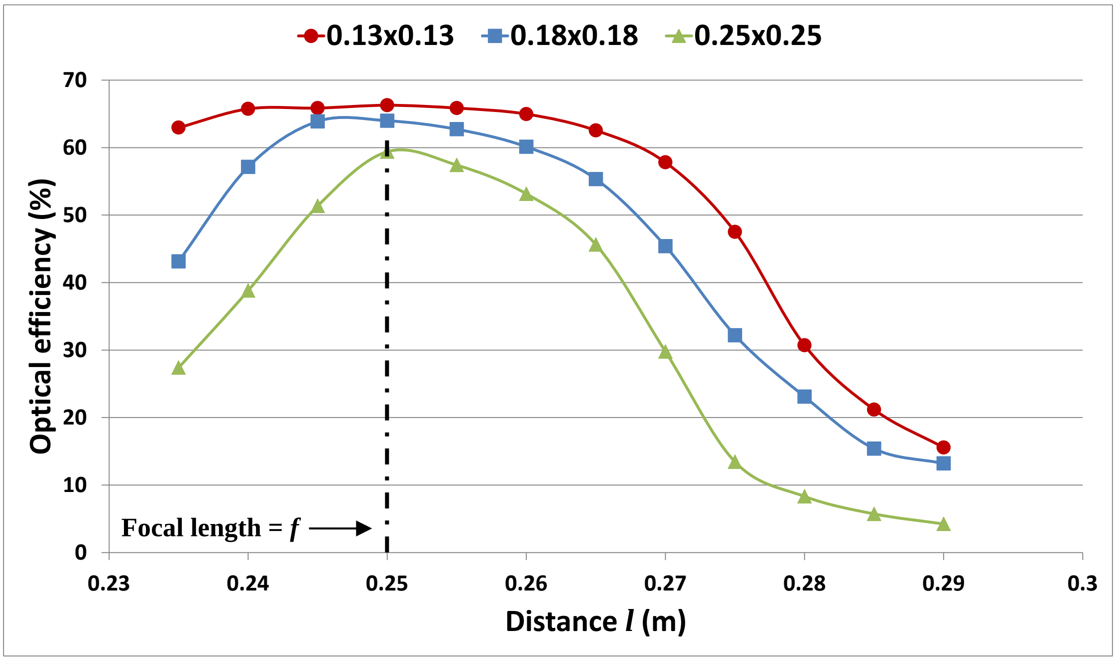

Figure 4.17: Effect of varying the distance (*l*) on the optical efficiency.

Figure 4.18 illustrates the influence of varying the distance (*l*) on the received rays uniformity for the three different Fresnel lens apertures. The non-uniformity is maximal at the focus point for all the tested apertures of the Fresnel lens. It is clear that the degree of non-uniformity is directly proportional to the Fresnel lens geometrical concentration ratio. For example, the non-uniformity for 0.25x0.25m^2 Fresnel lens aperture exceeds 850 while it is about 450 in case of 0.13x0.13m^2 Fresnel lens aperture. Increasing the distance (*l*) would increase the divergence of the rays on the receiver which ultimately improves the incident rays uniformity noticeably. For the three Fresnel lens apertures, the degree of non-uniformity drops dramatically after the focus point i.e *l*= *f* =0.25m.

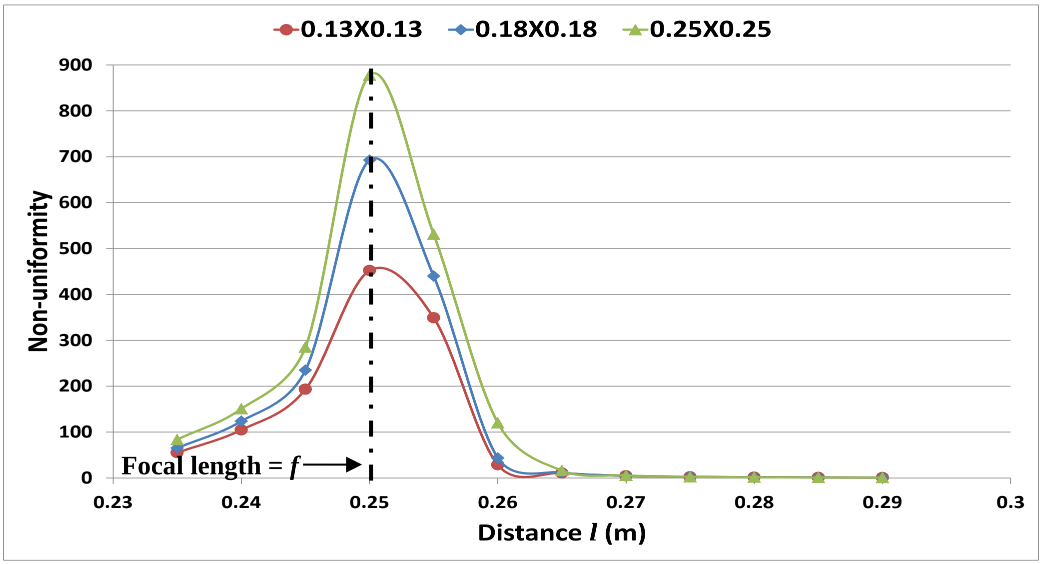

Figure 4.18: Effect of varying the distance (*l*) on the uniformity.

Table 4.2 shows a summary of the testing results including the received power, optical efficiency, non-uniformity and received radiation flux profile for the Fresnel lens with aperture area of 0.18x0.18m^2 at different distances of (*l*). Although the uniformity was significantly improved using this technique from about 692 at $l = f = 0.25$m to less than 1 at *l*=0.290m, the received power is very low. It is crucial to have an optical system able to keep the illumination distribution uniform with minimum optical losses compared to the point-focus case. Similar trends were also observed with Fresnel lens apertures of 0.13x0.13m^2 and 0.25x0.25m^2.

Table 4.2: Summary of increasing the distance (*l*) on the simulated received power and uniformity without SOE for 0.18x0.18 m^2 lens.

Distance (*l*) (m)	Non-uniformity	Received flux distribution	Input power(W)	Received power (W)	Optical efficiency (%)
l=*f* =0.25	692.45	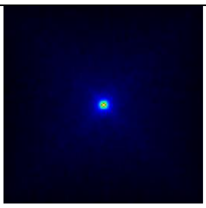	32.40	20.73	64.0
0.255	439.81	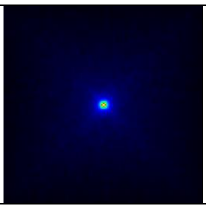	32.40	20.32	62.7

0.26	43.69	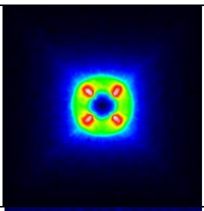	32.40	19.48	60.1
0.265	12.32	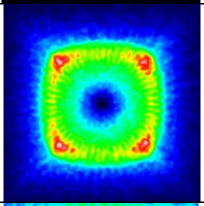	32.40	17.93	55.3
0.270	4.84	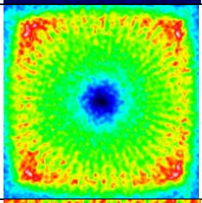	32.40	14.71	45.4
0.275	2.75	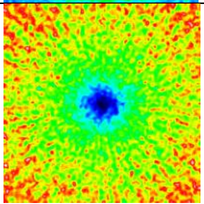	32.40	10.43	32.2
0.280	1.64	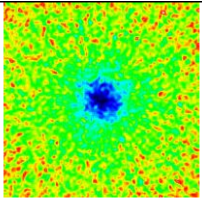	32.40	7.48	23.1
0.285	1.16	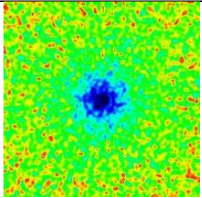	32.40	4.99	15.4
0.290	0.84	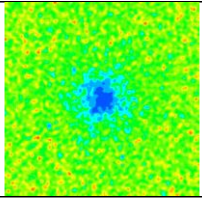	32.40	4.28	13.2

Effect of introducing Secondary Optical Element (SOE)

Secondary optical element is used to improve the spectral homogeneity of point-focus Fresnel lens high concentration systems. A hollow inverted truncated pyramid reflector (HITPR) is one of the easiest SOE to manufacture and the lowest cost among other types of SOE which has been widely integrated with HCPV systems [109,126,128,132,195]. This SOE type was utilised by the CPV specialist Company (Amonix) which claimed to have the highest concentrator module efficiency after the NREL measured its 35.9% module [132,196]. The only disadvantage of using more than one optical element in the optical system is that the total optical efficiency will decrease by increasing its number due to the increase in the optical losses [151]. In the current study, HITPR was designed using SolidWorks and then inserted to the developed HCPV assembly for optical analysis using OptisWorks as shown in Figure 4.19.

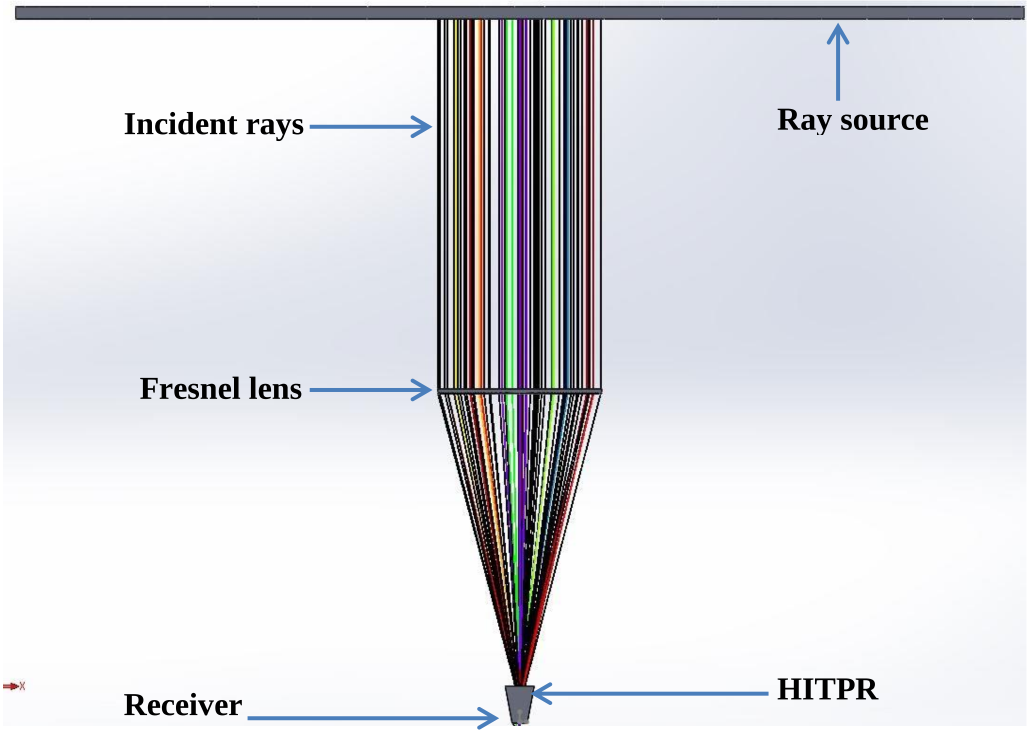

Figure 4.19: HCPV assembly including the HITPR SOE.

After increasing the distance (*l*), the SOE is placed so that the diverging rays after the focus point are reflected to the receiver as illustrated in Figure 4.20a. The material reflectivity of the HITPR inner walls has overall average of 90%. The objective is to have a uniform irradiation on the receiver with minimum loss in received energy compared to the received power at focal length. The Fresnel lens with aperture area of $0.18x0.18m^2$ and geometrical concentration ratio of 324X was used in the simulation with value of (*l*) ranging from 0.255-0.300m with a step of 0.005m.

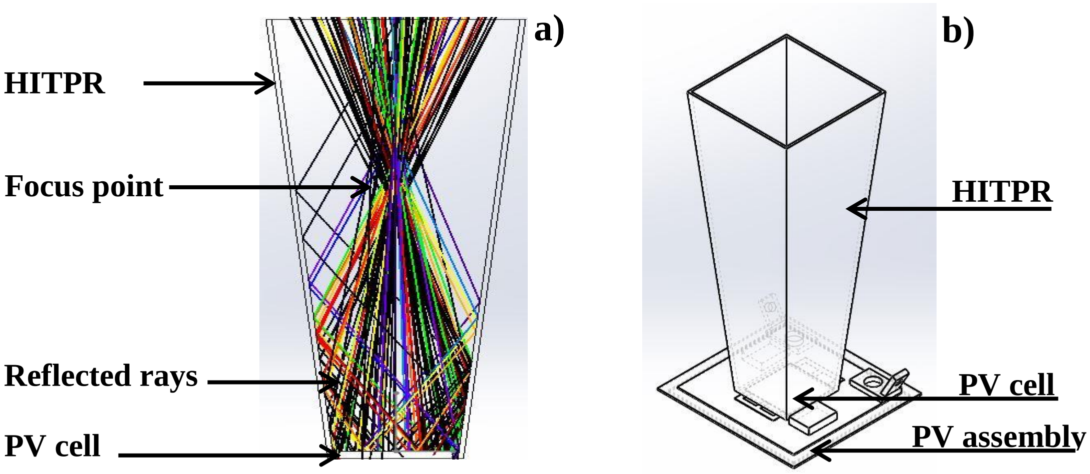

Figure 4.20: a) Diverging rays after the focus point are reflected to the receiver using HITPR; b) 3D schematic diagram of HITRP above the PV cell.

Six HITPRs (Figure 4.21) with the following heights were placed above the PV assembly to examine their influence on the illumination uniformity: 0.01m, 0.02m, 0.03m, 0.04m, 0.05m and 0.06m. The SOE height was limited to 0.06m to facilitate cleaning the PV surface and for economic reasons. For each HITPR the distance (*l*) was varied 10 times which means there were 60 cases investigated to find out the optimum combination of reflector height and distance (*l*).

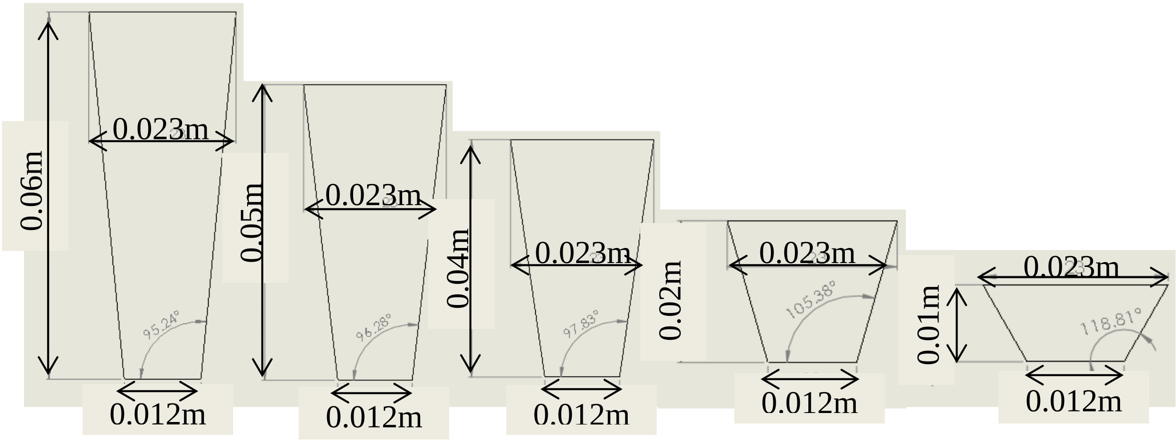

Figure 4.21: Different height of HITPRs investigated.

Figure 4.22 compares the non-uniformity achieved using all the SOEs showing that the non-uniformity is maximal close to the focus point (*f* = 0.25m) and reduces as the distance (*l*) increases. Moreover, Figure 4.22 shows that 0.01m, 0.02m and 0.03m SOEs produce almost the same level of non-uniformity at different values of distance (*l*) while 0.06m SOE produces better ray distribution along the distance (*l*).

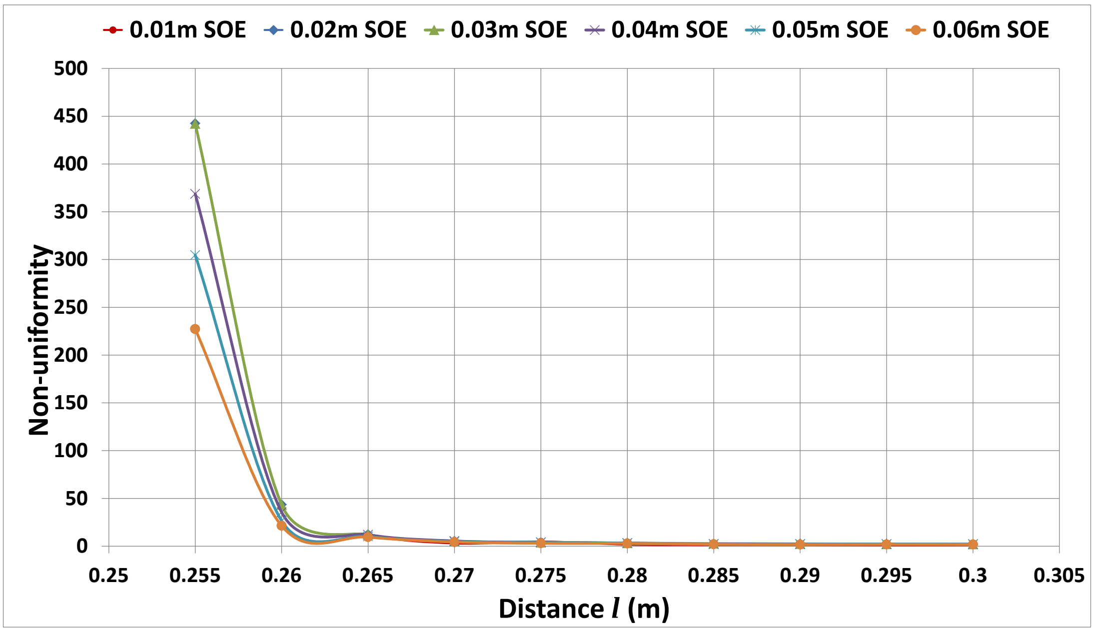

Figure 4.22: Effect of varying the distance (*l*) on the uniformity.

The best three SOEs in terms of uniformity were examined further to determine the optical efficiency. Focusing on the range of (*l*) = 0.285-0.3m where the uniformity is high, 0.06m height SOE has shown the best optical efficiency as shown in Figure 4.23.

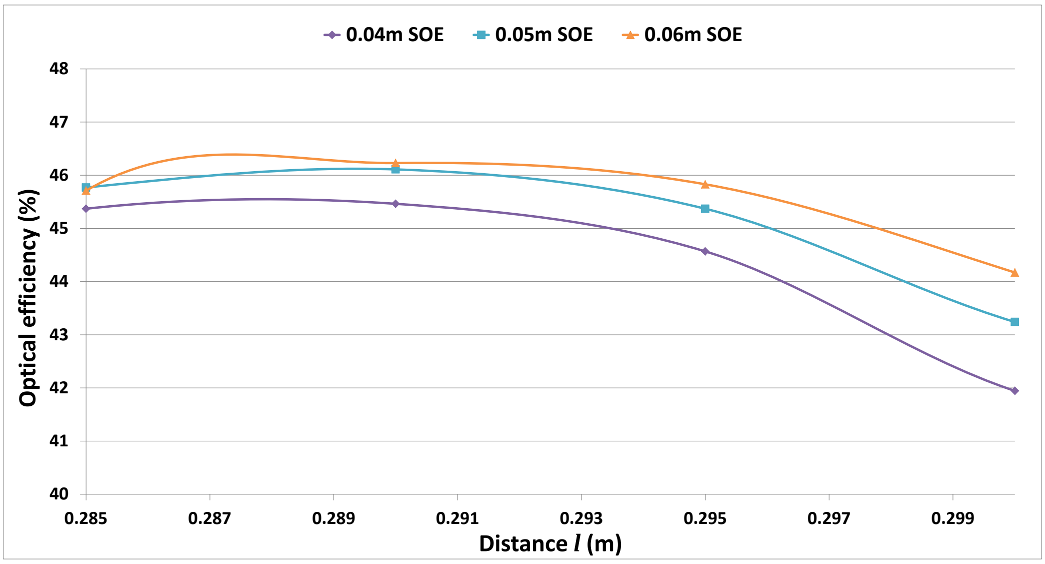

Figure 4.23: Effect of varying the distance (*l*) on the optical efficiency.

Figure 4.24 shows the optical efficiency and non-uniformity curves of the optical system with 0.06m SOE along the distance (*l*). The optimum distance (*l*) is a distance that ensures low degree of non-uniformity and at the same time minimum optical losses compared to the focus point case. From Figure 4.24 it can be concluded that *l*=0.29m is the optimum distance where the total optical efficiency is the highest. The non-uniformity dropped from 692 at focus point without SOE (Table 4.2) to 1.67 at *l*=0.29m. Moreover, the total optical efficiency increased more than 250% after introducing the SOE i.e. from 13% at *l*=0.29m (Table 4.2) to more than 46%.

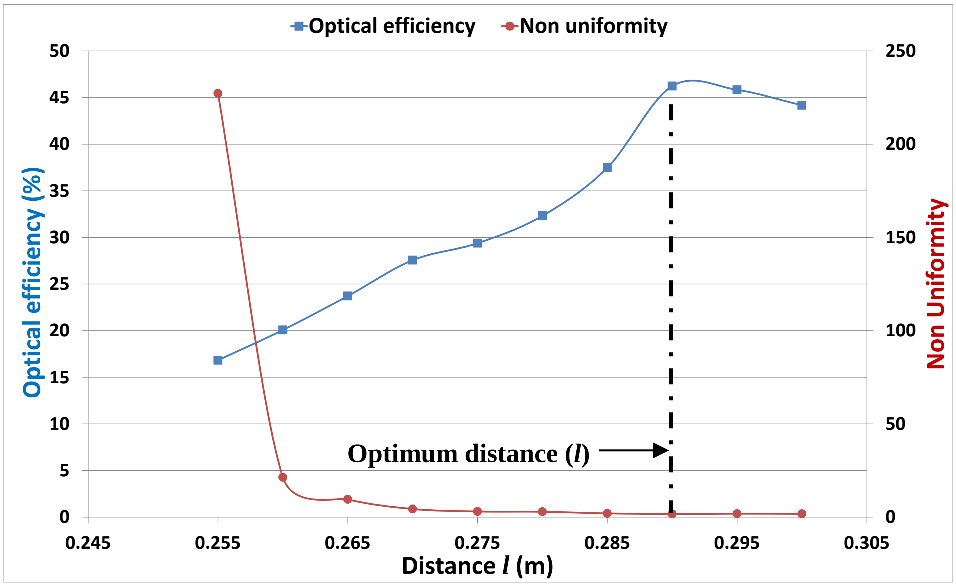

Figure 4.24: Optical efficiency and non-uniformity curves along distance (*l*) for 0.06m SOE.

Figure 4.25 shows 3-D images of the incident ray profile on the receiver for the 0.18x0.18 m^2 Fresnel lens at focus point without SOE (a) and at *l*=0.29m with 0.06m SOE (b). It is clear that the incident ray distribution has improved noticeably where rays cover most of the receiver area.

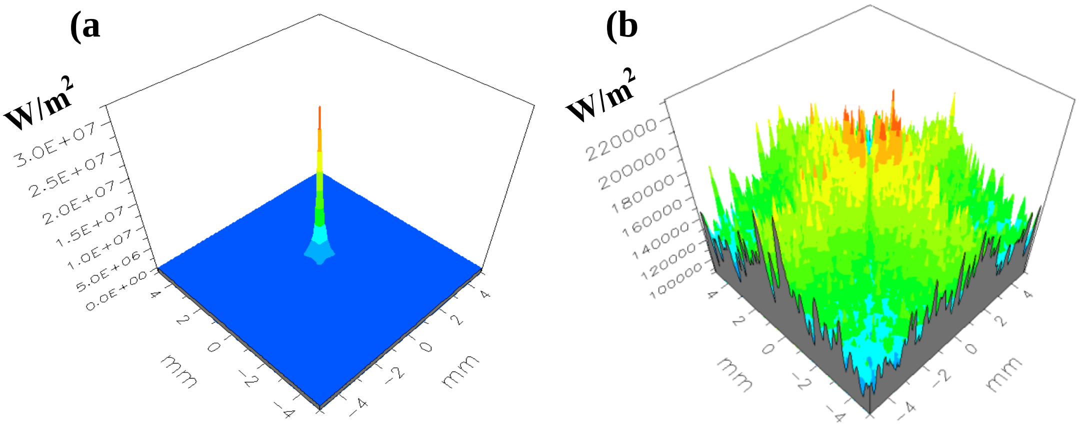

Figure 4.25: a) Incident radiation flux in W/m^2 for point-focus case & b) combination of *l*=0.29m and 0.06m reflector case.

Table 4.3 shows a summary of the modelling results including the received power, optical efficiency, non- uniformity and received radiation flux profile for the 0.18x0.18m^2 Fresnel lens at focus point i.e. *l*= 0.250m, at *l*= 0.29m and at *l*= 0.29m with integrating 0.06m SOE. The received power has increased 3 times after introducing the SOE at *l*= 0.29m from about 4 W to about 15 W with relatively slight increase in the irradiation non-uniformity. Therefore, the optical efficiency was increased after placing the SOE compared to the case at the same distance (*l*) but without SOE from about 13% to more than 46%. Moreover, the degree of non-uniformity of incident rays was improved from about 692 at focus point to about 2 by increasing the distance (*l*) and introducing the 0.06m SOE.

Table 4.3: Summary of simulated received power and uniformity for 0.18x0.18m^2 lens.

Distance (*l*) (m)	Non-uniformity	Received flux distribution	Input power (W)	Received power (W)	Optical efficiency (%)
l= *f* =0.25, no SOE	692.45	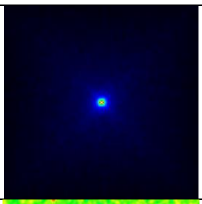	32.40	20.73	64.0
l=0.29, no SOE	0.84	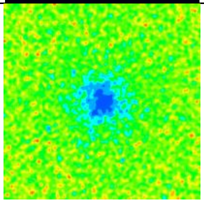	32.40	4.28	13.2
*l=0.*29 & 0.06m SOE	1.67	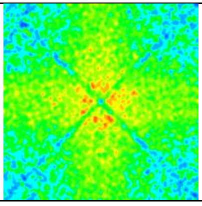	32.40	14.98	46.2

4.3. Outdoor experimental validation of the developed optical simulation

A HCPV system consisting of primary and secondary optical elements, multi-junction solar cell and cooling system was assembled and tested outdoor to examine its optical and electrical performance. The optical performance examination includes the optical efficiency of the optical system and the illumination uniformity on the receiver with and without SOE.

Moreover, the electrical performance of the HCPV system was investigated with and without SOE to examine the effect of non-uniform illumination on the electrical output.

4.3.1. Outdoor optical efficiency investigation

Five different Fresnel lens aperture areas 0.13x0.13, 0.15x0.15, 0.18x0.18, 0.2x0.2 and 0.25x0.25 m^2 with the following geometrical concentration ratios were examined experimentally to determine their optical efficiency at the focus point (*l*=0.25m) without SOE: 169X, 225X, 324X, 400X and 625X. Figure 4.26 shows the experimental optical efficiency results compared to the simulation work.

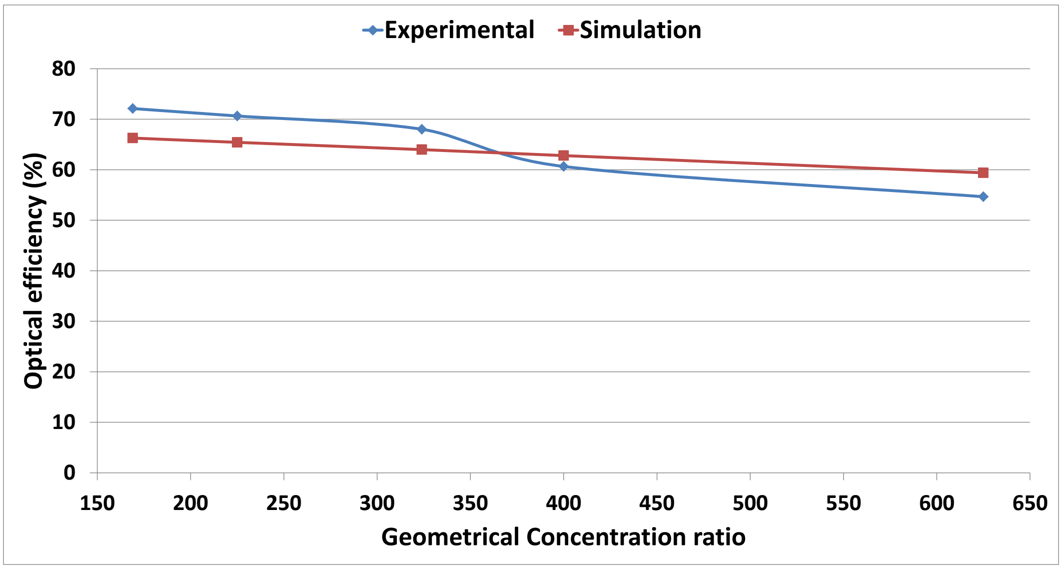

Figure 4.26: Experimental and simulation optical efficiency comparison.

It can be observed the close agreement between the experimental and simulation optical efficiency values. The simulation maximum variation from the experimental output is less than 9% at concentration ratio of 169X i.e. Fresnel lens with aperture area of 0.13x0.13m^2.

4.3.2. Outdoor incident irradiation uniformity investigation

In this section, the incident rays uniformity was experimentally investigated outdoor at focus point, at different distance of (*l*) and after placing the SOE. The degree of non-uniformity was assessed experimentally by visual inspection, temperature distribution underneath the solar cell and its influence on the electrical performance of the HCPV system.

4.3.2.1. Illumination uniformity at focus point

A multi-junction solar cell was placed underneath the Fresnel lens with aperture area of 0.18x0.18 m^2 at its focus point i.e. at distance f = 0.25m. Figure 4.27 shows the simulation and experimental illumination profile on the solar cell; the point-focus profile is clear on the PV surface for both cases.

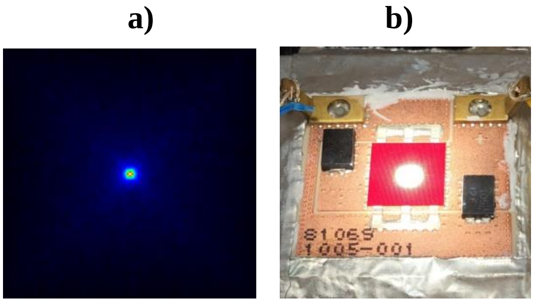

Figure 4.27: a) Simulation incident rays profile; b) Experimental incident rays profile.

Figure 4.28 shows the temperature distribution including the centre and sides temperature of the solar cell for the Fresnel lens with aperture areas of 0.13x0.13 m^2, 0.18x0.18 m^2 and 0.25x0.25 m^2. As shown in the Figure, the temperature at the centre of the PV in all tested Fresnel lens apertures was higher than the sides and the temperature difference was dependent on the concentration ratio. For example, the centre temperature of the 0.25x0.25 m^2 aperture area Fresnel lens was 17°C higher than the two sides while in case of 0.13x0.13 m^2 the difference was less than 5°C.

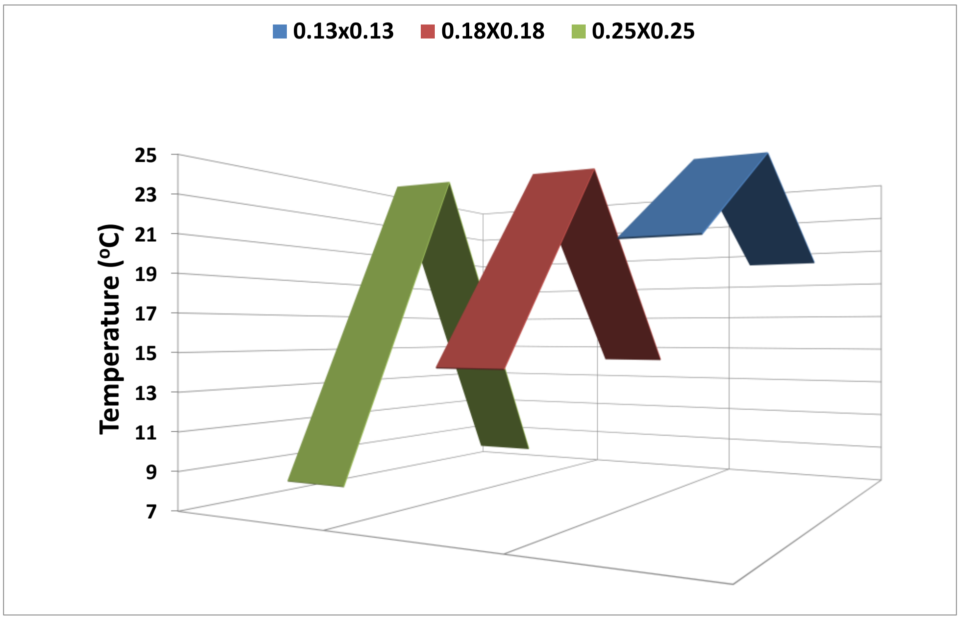

Figure 4.28: 2-D Measured temperature distribution of the solar cell for different Fresnel lens aperture areas.

Figure 4.29 shows the experimental 3D temperature distribution measured underneath the PV for the Fresnel lens with aperture areas of 0.13x0.13 m^2, 0.18x0.18 m^2 and 0.25x0.25 m^2.

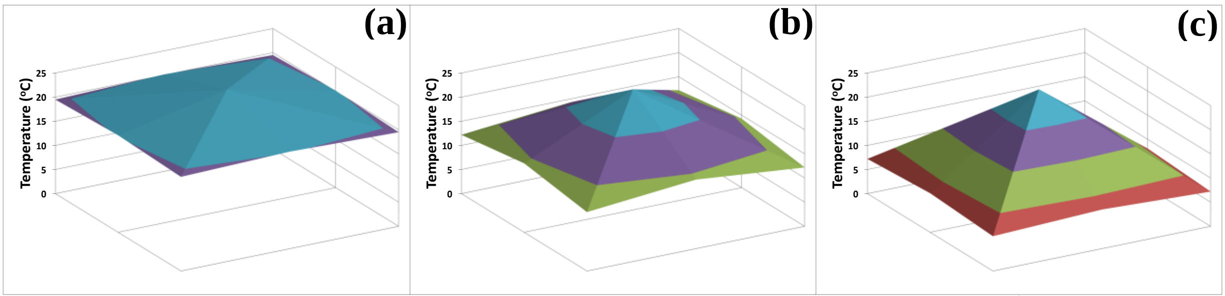

Figure 4.29: a) 3-D PV measured temperature distribution for 0.13x0.13 m^2 aperture area Fresnel lens; b) for 0.18x0.18 m^2; c) for 0.25x0.25 m^2.

The electrical conversion efficiency of the HCPV system is calculated using the following equation:

$$\eta_{elec} = \frac{P_{\max}}{P_{in}} = \frac{P_{\max}}{G \times A_r} \qquad (4.13)$$

Where P_{max} in (W) is the maximum electrical power produced by the multi-junction solar cell, P_{in} in (W) is the input solar power, G is the incident ray on the PV (W/m^2) and A_r (m^2) is the area of the receiver. To eliminate any output power reduction due to the temperature effect, the maximum power was measured using the I-V curve tracer as described in chapter 3 at reference temperature i.e. 25°C in all the cases. Based on the equation above, the experimental electrical efficiency of the MJ solar cell underneath the Fresnel lens with aperture area of 0.18x0.18 m^2 at focus point was found to be about 22% compared to the efficiency of the solar cell obtained at standard controlled lab conditions which was about 40%, with a reduction of 45%.

4.3.2.2. Illumination uniformity at different values of (*l*) without SOE

The influence of varying the distance (*l*) on the optical and electrical performances of the HCPV and received irradiance uniformity for 0.18x0.18m^2 Fresnel lens aperture area was examined experimentally and compared with the simulation results. The distance (*l*) was increased from 0.25-0.295m with a step of 0.005m. Figure 4.30 shows that the optical efficiency is negatively influenced by increasing the distance (*l*). It can be seen that the experimental optical efficiency drops from about 63% at focus point i.e. $f = l = 0.25$m to about 15% at l=0.29m. Figure 4.30 shows the close agreement between the simulation and experimental results with maximum difference of about 10%.

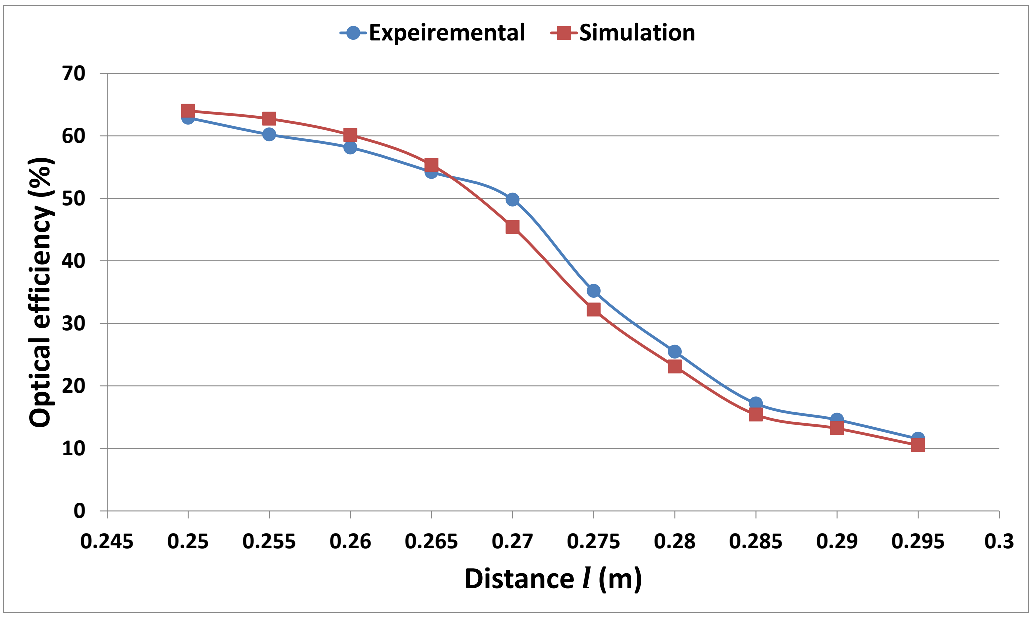

Figure 4.30: Experimental and simulation optical efficiency at different distance of (*l*).

Figure 4.31 shows the effect of increasing the distance (*l*) on both experimental optical and electrical efficiency. As the distance (*l*) increases the electrical efficiency increases; this may be explained by the improvement in the incident illumination uniformity. The electrical efficiency increased from about 22% at focus point to about 37% at *l*=0.295m with increase of about 68%.

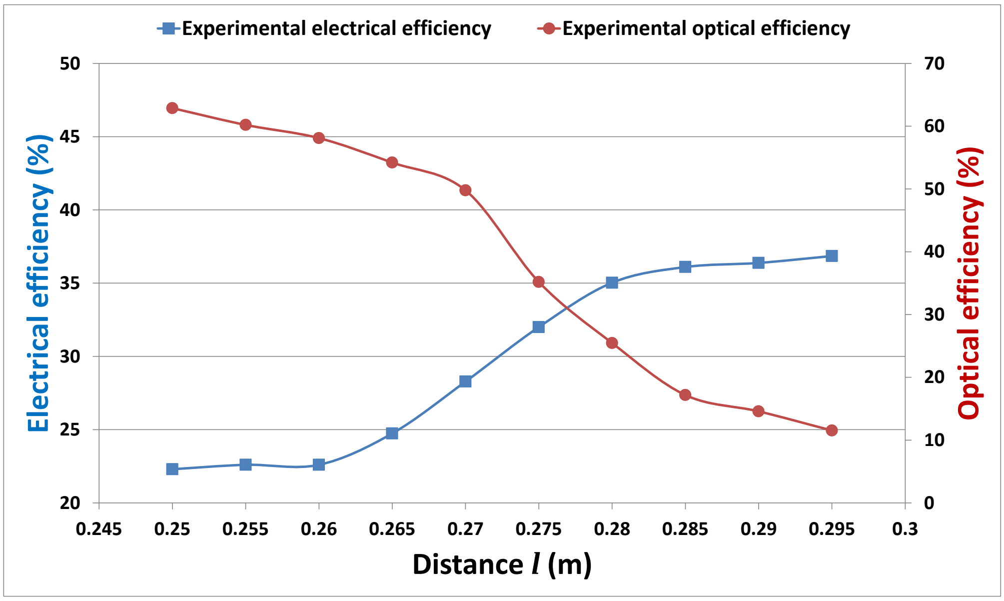

Figure 4.31: Experimental optical and electrical efficiency of HCPV with distance (*l*).

Figure 4.32 shows the relationship between the calculated illumination non-uniformity using the standard deviation and the experimental electrical efficiency. It shows that the maximum HCPV electrical performance is at distance (*l*) where the non-uniformity is minimum. The electrical efficiency is adversely affected by the increase in the incident rays non-uniformity.

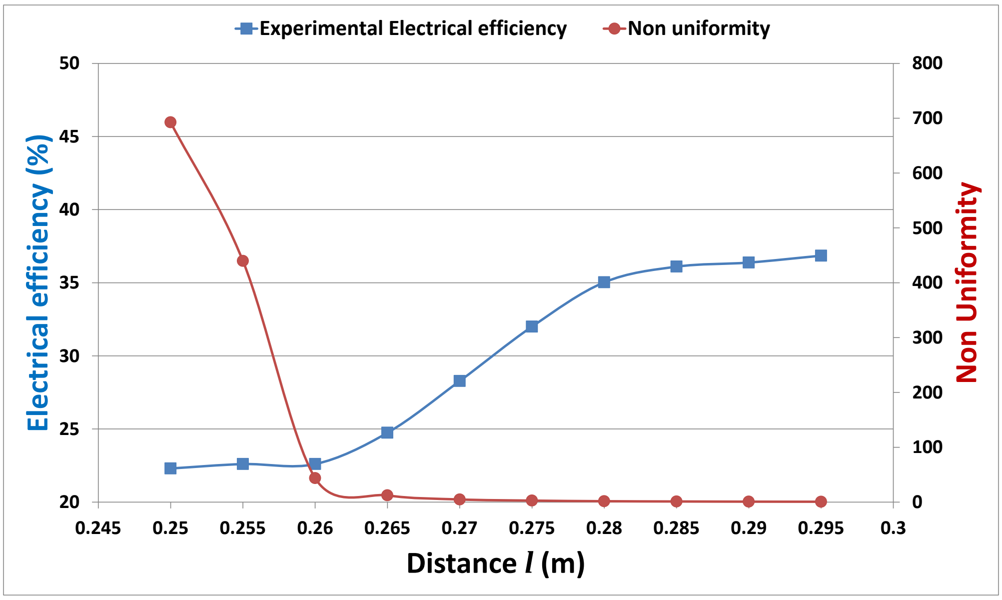

Figure 4.32: Relationship between experimental electrical efficiency and calculated non-uniform illumination.

Figure 4.33 shows the 2& 3-D measured temperature distribution underneath the PV for the 0.18x0.18m^2 aperture area Fresnel lens. Figure 4.33a shows the 2-D measured temperature distribution at focus point and at *l*=0.295m. Whereas, Figure 4.33c shows the 3-D measured temperature distribution at *l*=0.295m where the centre, sides and corners temperature are almost the same with maximum difference of about 1 ^{o}C while at point-focus illumination the maximum difference is about 13 ^{o}C (4.33b). The hot spot is almost eliminated by increasing the incident rays uniformity.

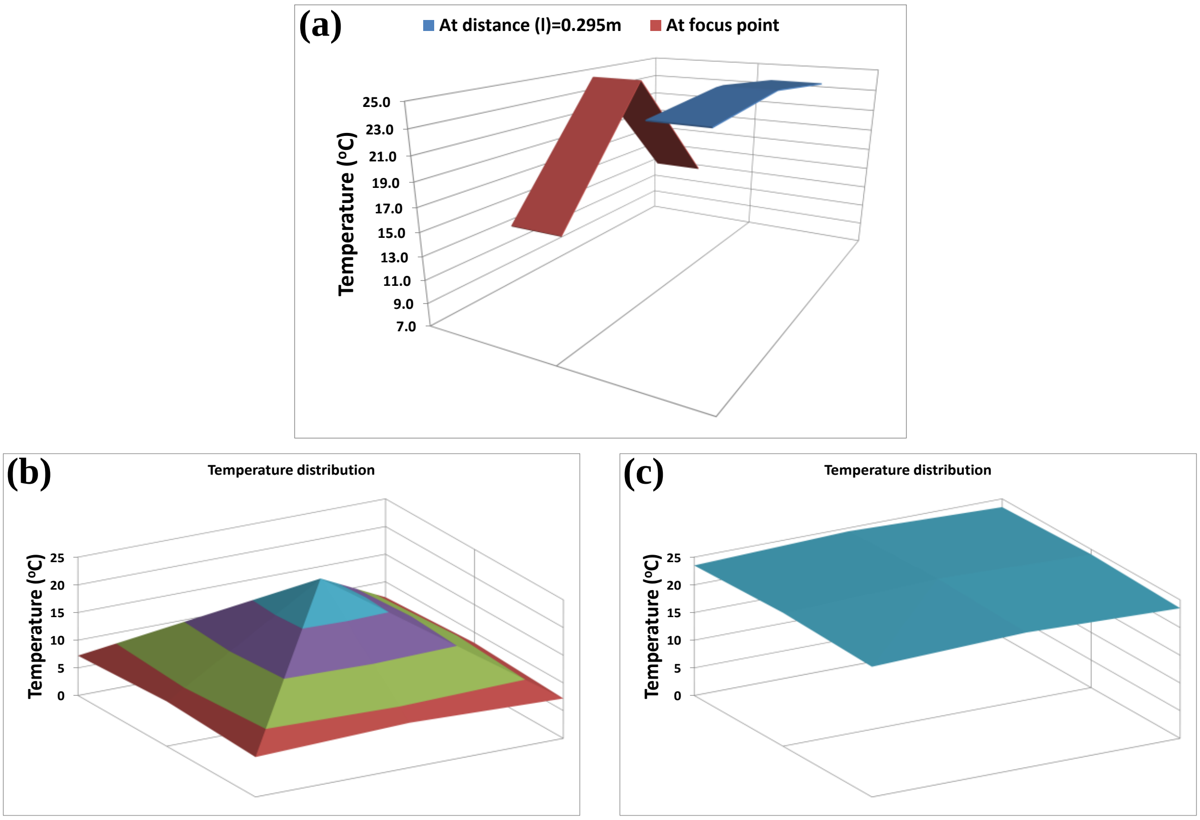

Figure 4.33: a) 2-D PV measured temperature distribution at focus point and at *l*=0.295m; b) 3-D PV measured temperature distribution at focus point; c) 3-D measured temperature distribution at *l*=0.295m.

Table 4.4 shows a summary of the testing results including the experimental electrical efficiency, experimental optical efficiency, non- uniformity and received radiation flux profile as the distance (*l*) increases for the Fresnel lens with aperture area of 0.18x0.18m^2. It shows clearly the effect of increasing the distance (*l*) in improving the irradiance uniformity as the incident illumination is spread over the PV assembly which enhances the electrical performance of the HCPV. Although the electrical efficiency was improved due to the better incident rays distribution on the solar cell, the optical efficiency was dropped from about 63% at focus point to about 15% at (*l*) =0.29m. It is crucial to maintain the received power i.e. optical efficiency while improving the incident rays uniformity. In the following section the influence of introducing the SOE on the optical and electrical performance of the CPV system was examined.

Table 4.4: Summary of optical and electrical examinations at different values of (*l*).

Distance (*l*) (m)	Non-uniformity	Simulation flux distribution	Experimental flux distribution	Experimental electrical efficiency (%)	Experimental optical efficiency (%)
l=f =0.25	692.45	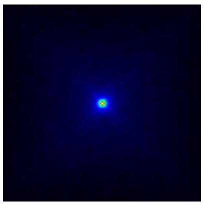	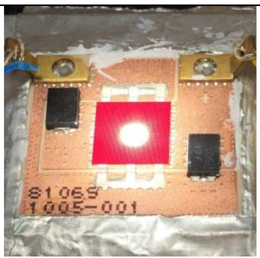	22.3	62.9
0.26	43.69	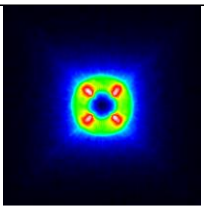	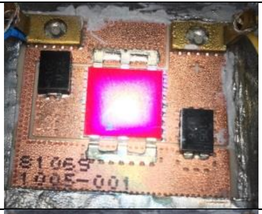	22.6	58.1
0.27	4.84	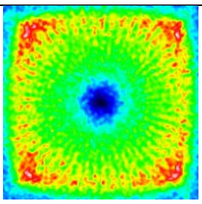	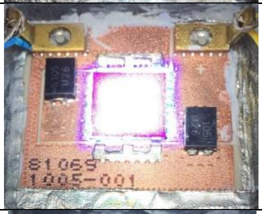	28.3	49.8
0.28	1.64	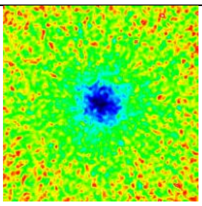	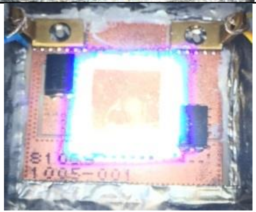	35.0	25.5
0.29	0.84	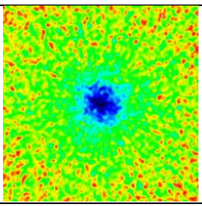	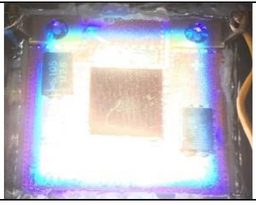	36.4	14.6

4.3.2.3. Illumination uniformity after introducing the SOE

In-house developed 0.06m HITPR with reflectivity of 90% was introduced to the HCPV system as shown in Figure 4.34 to examine its ability to improve the illumination uniformity without losing the received power i.e. maintaining the optical efficiency. The same procedure of increasing the distance (*l*) was repeated here but with SOE to examine its influence on the optical and electrical performance of the HCPV. The distance (*l*) was increased from 0.25-0.3 m with a distance step of 0.005m.

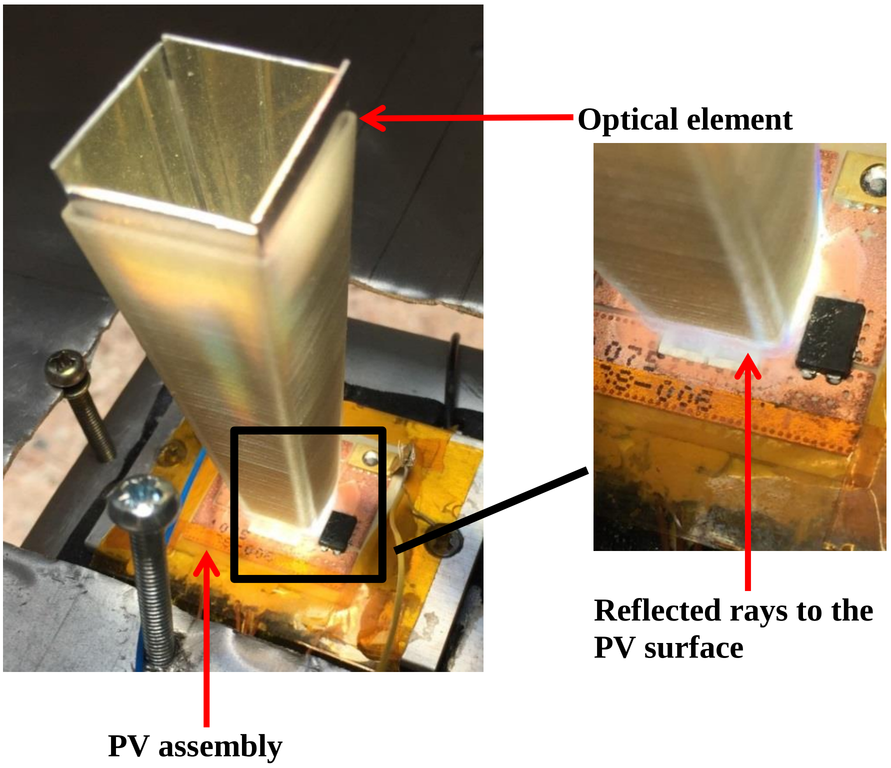

Figure 4.34: Secondary optical element above the multi-junction PV assembly.

Figure 4.35 shows the experimental and simulation optical efficiency of the HCPV after introducing the 0.06m SOE. There is a close agreement between the experimental and simulation optical efficiency with maximum difference of about 9%. Unlike the optical efficiency descending trend when increasing the distance (*l*) without SOE, with SOE the optical efficiency increases as the distance (*l*) increased. This can be referred to the increase in the total acceptance angle of the optical system as the distance (*l*) increases which allow more rays to enter the SOE aperture and reflected to the solar cell.

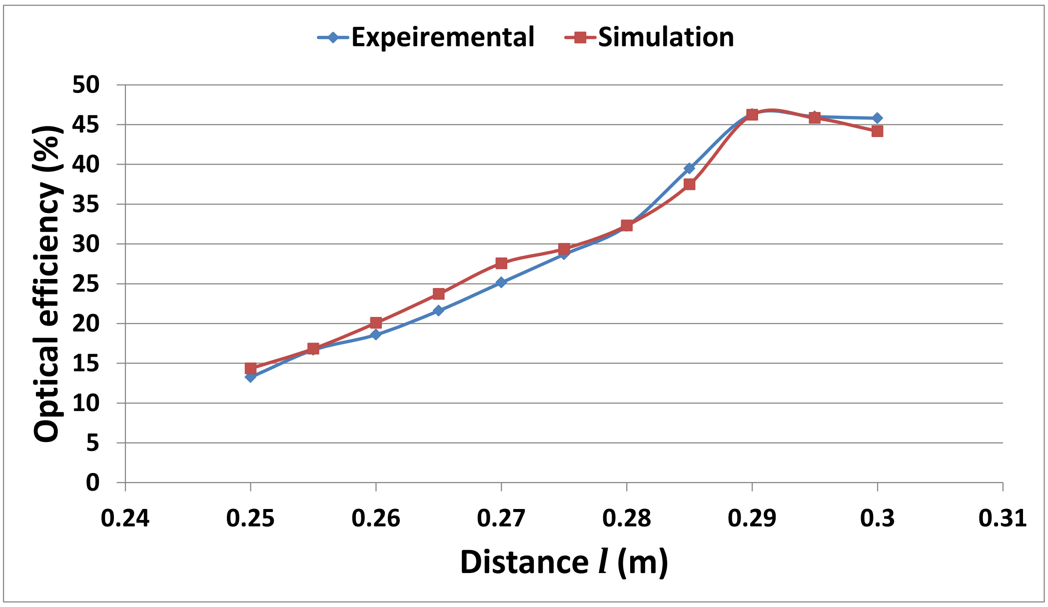

Figure 4.35: Experimental and simulation optical efficiency of the lens at different distance of (*l*) with SOE.

Figure 4.36 shows the experimental electrical and optical efficiencies of the HCPV after incorporating the SOE. For both optical and electrical parameters, efficiencies increase till reaching the optimum distance at *l*=0.29m where after this point the curve starts descending. It can be concluded that (*l*) =0.29m is the optimum point where the electrical and optical efficiencies are the highest. The optical experimental efficiency increased from about 13% at the focus point to more than 46% at *l* = 0.29m while the electrical efficiency increased from about 28% to about 36%. The electrical efficiency at focus point with SOE is higher than the electrical efficiency at focus point without SOE i.e. 28% compared to 22% respectively. This may be due to the reduction in degree of non-uniform illumination after placing the SOE as some of the refracted rays are blocked by the outer walls of the SOE which reduced the intensity of the non-uniform illumination.

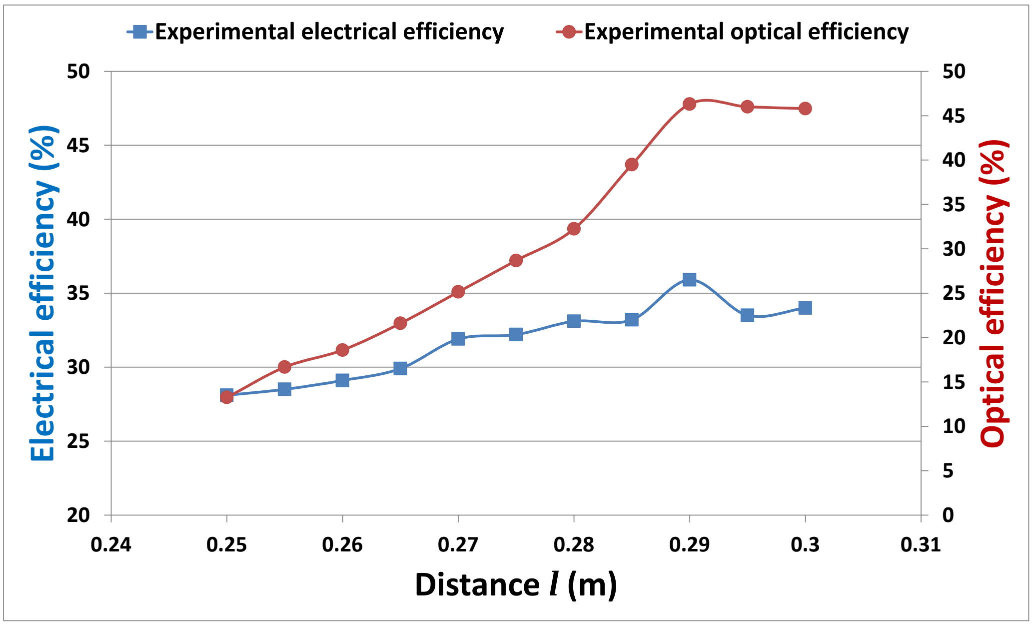

Figure 4.36: Experimental optical and electrical efficiencies of the HCPV at different distance of (*l*) with SOE.

Figure 4.37 shows the relationship between the experimental electrical efficiency and the calculated non uniformity. The lowest electrical efficiency (28.1%) is at the highest non-uniformity (261.6) i.e. at *l* = *f* = 0.25m and the maximum electrical efficiency (35.9%) is at the minimum non-uniformity (1.7) i.e. *l*=0.29m. This shows that the non-uniformity calculation based on the standard deviation method is a reliable tool to examine the degree of uniformity and relate it to the electrical performance.

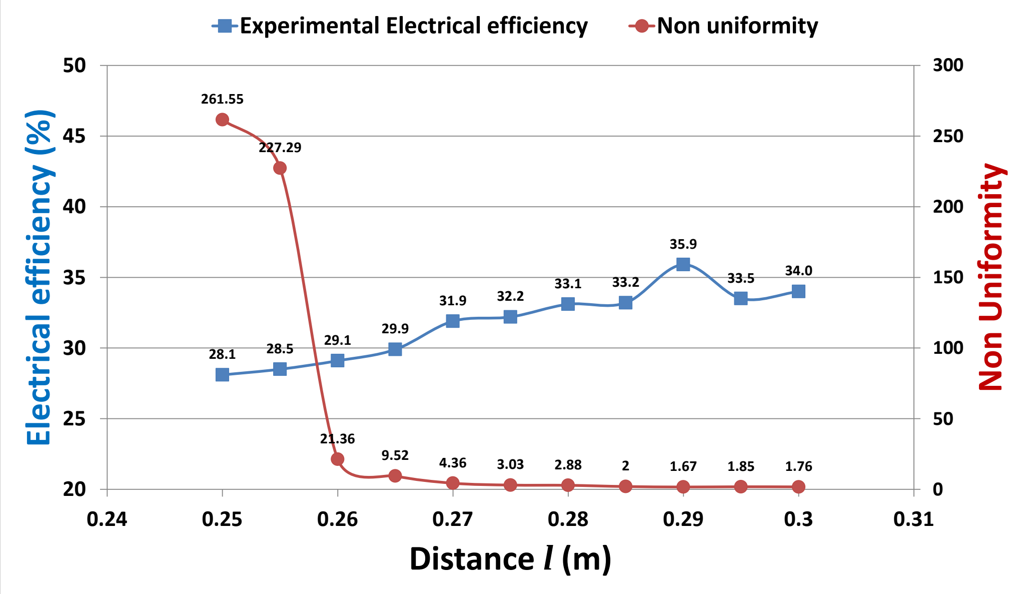

Figure 4.37: The relationship between the experimental electrical efficiency and the calculated non-uniformity.

Table 4.5 shows a summary of the testing results including the experimental electrical and optical efficiency, non- uniformity and received radiation flux profile for the Fresnel lens with aperture area of 0.18x0.18m^2 at focus point (*l*=0.25m), at *l*=0.29m and at *l*= 0.29m with integrating 0.06m SOE. The experimental optical efficiency increased more than 200% after placing the SOE compared to the case at the same distance (*l*) but without SOE. It increased from about 15% to 45% with relatively slight increase in the irradiation non-uniformity leading to a slight decrease in the electrical efficiency i.e. 0.84 compared to 1.67 and 36.4% compared to 35.9% respectively. Therefore, it can be concluded that a combination of placing a SOE and increasing distance (*l*) is better than only increasing the distance (*l*) to improve the irradiation uniformity and enhance the HCPV performance.

Table 4.5: Summary of optical and electrical examinations with and without SOE.

Distance (*l*) (m)	Non-uniformity	Simulation flux distribution	Experimental electrical efficiency (%)	Experimental optical efficiency (%)
l=*f* =0.25, no SOE	692.45	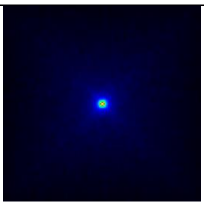	22.3	62.9
l=0.29, no SOE	0.84	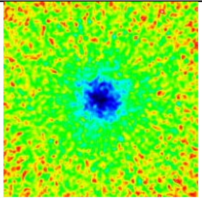	36.4	14.6
l=0.29 & 0.06m SOE	1.67	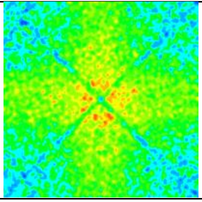	35.9	45.0

The optical losses increase by increasing the number of the optical elements in a CPV system which can be observed from the Table above where the total optical efficiency reduced from about 63% to 45% after introducing the SOE with reduction of about 29%. But, the gain in the electrical efficiency after improving the incident flux uniformity using the SOE is more than 60% which can compensate this loss.

4.4. Summary

A Fresnel lens was outsourced and its performance characterised using ray tracing method and outdoor experimental testing. The optical efficiency and the incident illumination uniformity on the receiver were examined. It was found that the Fresnel lens optical efficiency is inversely proportional to the aperture area. Also, all different Fresnel lens aperture areas produced non-uniform illumination on the receiver and the degree of non-uniformity is directly proportional to the geometrical concentration ratio. The distance between the concentrator and the receiver (*l*) was increased to improve the non-uniform illumination. Although, non-uniform illumination was improved by increasing the distance (*l*), the optical efficiency was reduced significantly. In order to increase the optical efficiency and maintain the same level of irradiation uniformity, the distance (*l*) was increased and a SOE was placed above the PV assembly. It was found that the simulated optical efficiency increased more than 250% from 13% to about 46% with almost the same degree of uniformity and electrical efficiency.

Outdoor experimental HCPV set-up was assembled to validate the optical simulation and to test the electrical performance of the system. The optical efficiency of five different Fresnel lens aperture areas was investigated outdoor and compared against the developed simulation. There was close agreement between the simulation optical efficiency and the experimental work with maximum difference of about 9%. Moreover, the optical efficiency results with and without SOE as the distance (*l*) increases were also confirmed by the experimental work. The electrical efficiency of the multi-junction solar cell was examined outdoor before and after improving the incident illumination uniformity. Outdoor investigation revealed that non-uniform illumination on the solar cell may reduce the MJ electrical output by more than 40%

when compared to the case with improved uniformity after placing the SOE at the optimum distance *l* and by 45% when compared to the efficiency of the solar cell obtained at standard controlled lab conditions. The electrical efficiency that was measured under point-focus profile is about 22% and after increasing the distance (*l*) where the illumination spread over the PV assembly, the electrical efficiency increased to about 37% with increase of about 68%. The hot spot initiated by the non-uniform illumination was assessed experimentally by measuring the centre, side and corner surface temperatures of the PV under Fresnel lens with aperture area of 0.18x0.18m^2. At focus point i.e. l= 0.25 m, a difference of about 13 ^{o}C was found between the centre and the side (0.005m distance) of the PV surface; but after improving the illumination uniformity by increasing the distance (*l*) a difference of about 1^{o}C was measured. Although the experimental electrical performance of the HCPV was enhanced by more than 60% after improving the irradiation uniformity on the receiver, the total optical efficiency reduced about 29% after inserting the SOE. Therefore, in the next chapter a parametric study of the primary optical element (Fresnel lens) to enhance the HCPV optical performance will be discussed.

CHAPTER 5

Optical and electrical optimisation of the HCPV system

5.1. Introduction

The developed optical simulation to characterise the HCPV Fresnel lens optical performance was validated using the outdoor experimental work as described in chapter 4. In this chapter, this validated optical simulation was used to carry out a parametric study on the primary optical element (Fresnel lens) to enhance the performance of the HCPV optical system using ray tracing technique. The optimised optical system was examined in terms of optical efficiency, incident rays uniformity and acceptance angle with and without a secondary optical element. Moreover, linear and non-linear assembly of more than HCPV systems before and after optical optimisation were investigated to examine the possibility of reducing space and cost.

5.2. Optimisation of the HCPV optical system

5.2.1. Parametric study of the primary optical element

The validated optical simulation presented in the previous chapter will be used here to perform a parametric study on the Fresnel lens in order to enhance the HCPV optical system performance. The following Fresnel lens parameters will be investigated: focal length, groove pitch, surface thickness and surface transmissivity. High geometrical concentration ratio is targeted i.e. above 100X so five geometrical concentration ratios were chosen to be examined: 169X, 225X, 324X, 400X and 625X. The applied radiation flux was set to 1X=1000 W/m^2 through all the simulation tests. Table 5.1 shows the initial parameters of the Fresnel lens characterised in the previous chapter.

Table 5.1: Initial Fresnel lens parameters.

Parameter	Value
Fresnel lens size (m^2)	0.25x0.25
Focal length (m)	0.25
F-number	0.71
Thickness (m)	0.003
Groove pitch (m)	0.001
Grooves direction	grooves in (upside down)
Transmissivity (%)	92
Material	PMMA

5.2.1.1. Effect of varying the Fresnel lens focal length (*f*)

Focal length (*f*) can be defined as the distance between the Fresnel lens and the focus point [197]. Five focal lengths were investigated in terms of the optical efficiency namely 0.25m, 0.35m, 0.45m, 0.55m and 0.65m. For each focal length, the slope angle (α) of each prism has to be recalculated and the Fresnel lens redesigned. Figure 5.1 shows the simulation results of varying the focal length (*f*) where increasing the focal length results in increasing the optical efficiency of the Fresnel lens. For example, the optical efficiency in case of focal length (*f*) = 0.25m and 0.25x0.25m^2 Fresnel lens aperture area is about 59% and increases to about 66% in case of (*f*) = 0.65m with increment of about 12%. In a short focal length lens, the angles of the exit rays and the facet surfaces are steeper which increase the reflection losses [33,46,79,126,134]. Increasing the focal length would reduce this steepness which ultimately minimises the optical loss. Figure 5.1 also shows that the positive influence of increasing the focal length on the optical efficiency is higher in large lenses than small ones. Although increasing the focal length would enhance the optical efficiency, this will be on the expense of the compactness of the HCPV system which may lead to more material consumption i.e. more costly system. Therefore, it is crucial to consider both the optical efficiency and compactness of the system during the focal length selection process. Figure 5.2 shows the relationship between the optical efficiency and F-number. The F-number as described in chapter 4 is the ratio of the focal length to the diameter of the Fresnel lens. The F-number of the Fresnel lens increases by increasing the focal length and as a result the optical efficiency improves.

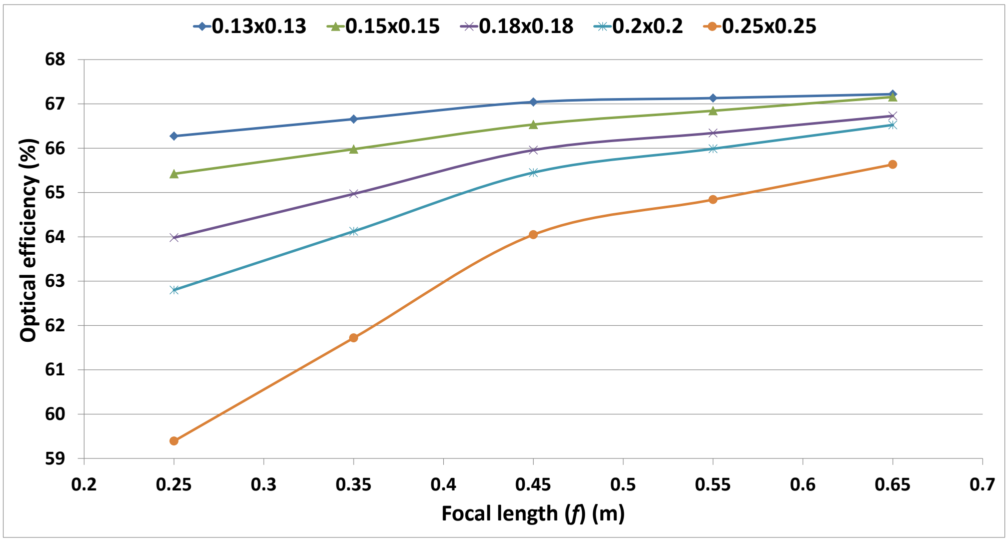

Figure 5.1: Influence of increasing the focal length on the Fresnel lens optical efficiency.

As shown in Figure 5.2, the optical efficiency has increased dramatically between F-number of 0.7 to 1.3 and after that the curve is almost horizontal. Therefore, it can be concluded that for the best optical efficiency F-number of ≥1.3 is recommended.

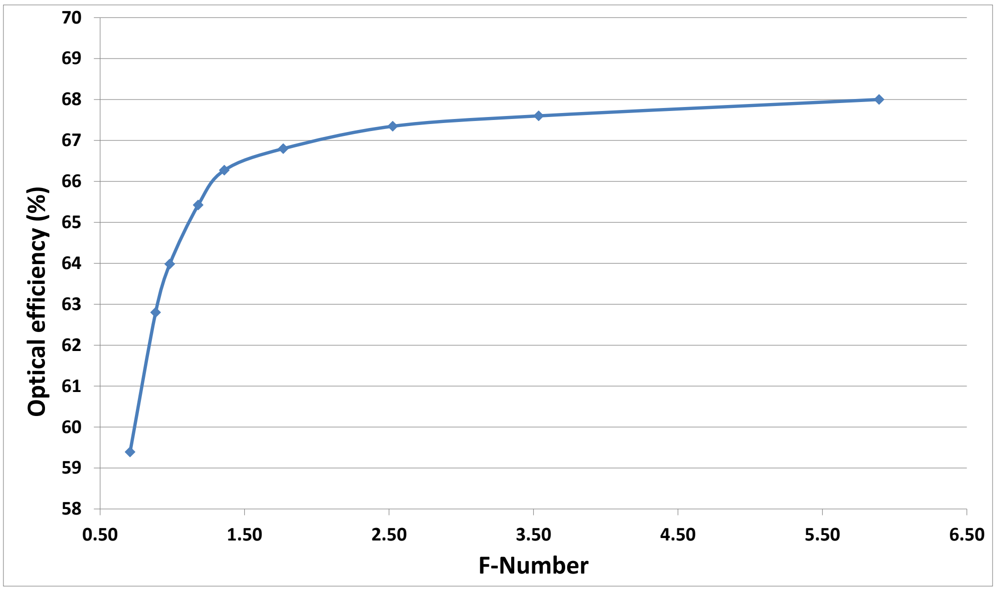

Figure 5.2: Optical efficiency versus F-number.

5.2.1.2. Effect of varying the Fresnel lens groove pitch

Groove pitch is the width of each groove in the Fresnel lens. The groove pitch of the Fresnel lens was varied to examine its influence on the optical efficiency. Five groove pitches were investigated 0.001m, 0.002m, 0.003m, 0.004m and 0.005m. By increasing the groove pitch for a fixed Fresnel lens size, the number of prisms decreased and vice versa. Figure 5.3 shows the influence of increasing the groove pitch on the optical performance. The optical efficiency increased by increasing the groove pitch to reach maximum at groove pitch of 0.003m then starts decreasing at higher values. It can be concluded from this Figure that 0.003m groove pitch is the optimum value where the optical efficiency is maximum. As the pitch becomes smaller, like the case of 0.001m groove pitch, the prisms will deliver more light into higher diffractive orders away from the desired focal position causing optical losses [33,126,134,197]. On the other hand, the size of the Fresnel lens prisms is increased when large groove pitch is used like the case of 0.005m which may lead to more internal reflection losses and material absorption i.e. more optical losses [33,46,79,126,134].

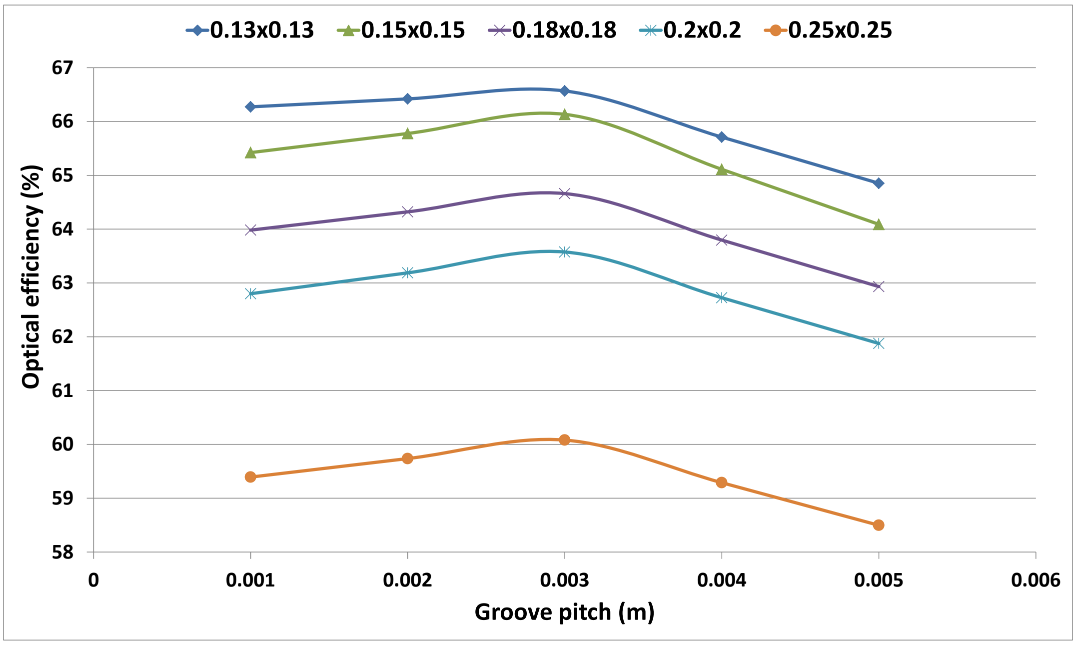

Figure 5.3: Optical efficiency versus groove pitch.

5.2.1.3. Effect of varying the Fresnel lens surface thickness

The thickness of the Fresnel lens was varied to examine its influence on the optical efficiency. Five surface thicknesses were investigated 0.001m, 0.002m, 0.003m, 0.004m and 0.005m. Figure 5.4 shows that the optical efficiency decreased by increasing the Fresnel lens thickness for all the tested cases. For instance, the optical efficiency of 0.001m and 0.005m thick

Fresnel lens with aperture area of 0.13x0.13m^2 are about 70% and 65% respectively with optical efficiency drop of about 7%. The loss in the optical efficiency can be referred to the reduction in the light transmissivity, which decreases when the Fresnel lens thickness increases [134].

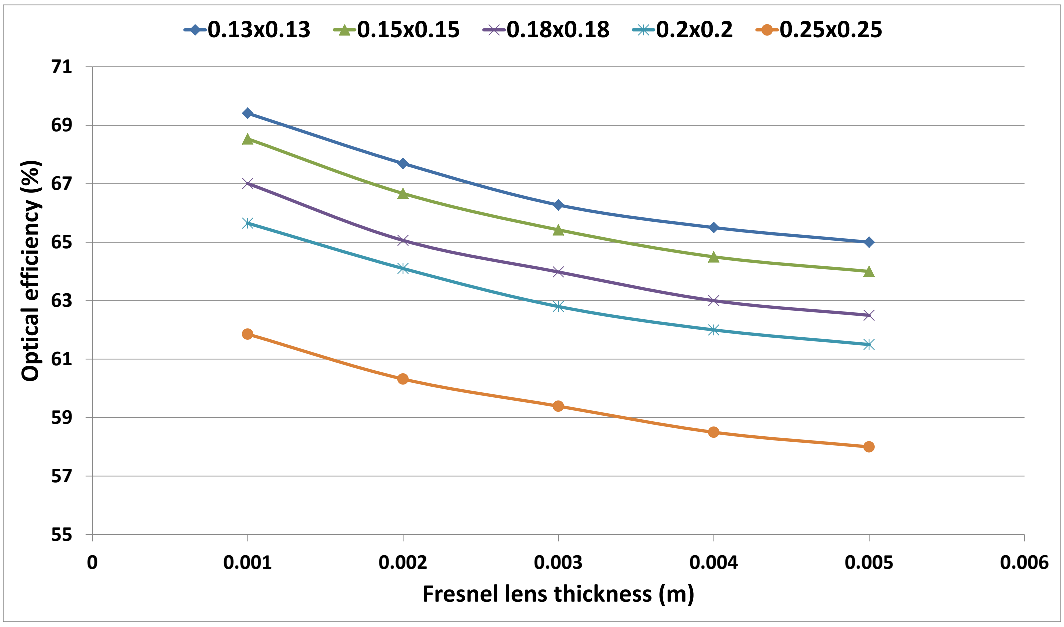

Figure 5.4: Influence of Fresnel lens thickness on the optical efficiency.

5.2.1.4. Effect of varying the Fresnel lens surface transmissivity

Reflection at the surface, not absorption within the material, is the leading cause for transmission losses [134]. Anti-reflection coatings can be placed on the flat part of the Fresnel lens to reduce the reflection losses [33,47]. Nowadays, many processes are applied to reduce the surface reflectance of polymer substrates to less than 2% [198,199]. In this section the transmissivity of the Fresnel lens was varied to examine its effect on the optical efficiency. Six Fresnel lens surface transmissivity values were chosen for the optical efficiency examination 80%, 85%, 90%, 92%, 95% and 100% which are equivalent to the following surface reflectivity 20%, 15%, 10%, 8%, 5% and 0% respectively. Figure 5.5 shows that the optical efficiency increased noticeably by increasing the surface transmissivity as more rays are passing through the top surface of the Fresnel lens. For example, the optical efficiency of the Fresnel with aperture area of 0.25x0.25m^2 increased from about 45% to about 63% for transmissivity of 80% and 95% respectively with increment of about 40%. It can be concluded that enhancing the surface quality of the Fresnel lens would enhance the optical efficiency.

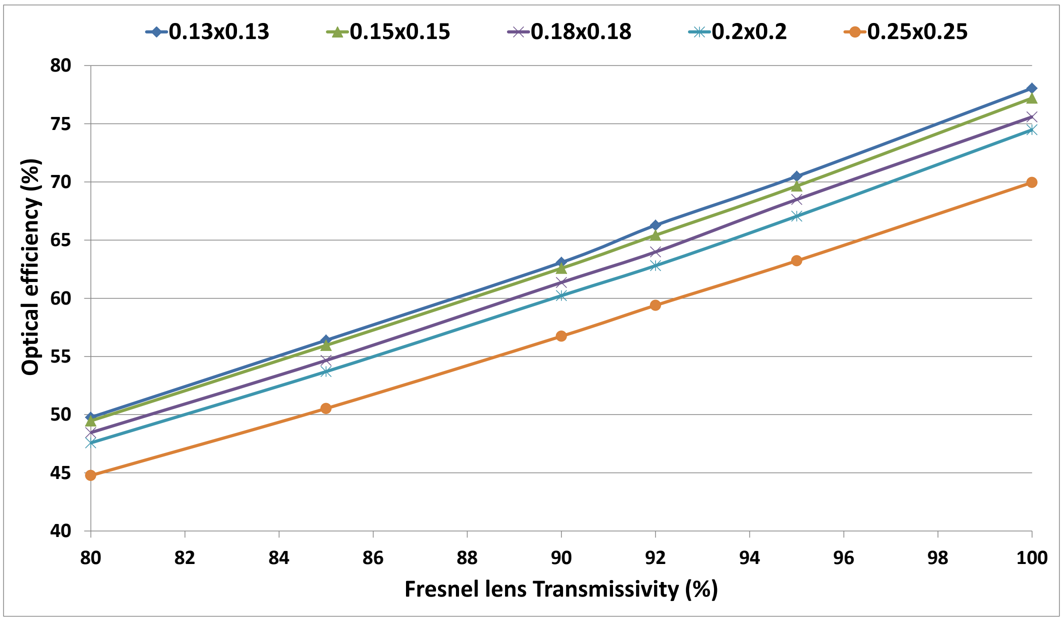

Figure 5.5: Influence of Fresnel lens top surface transmissivity on the optical efficiency.

It can be concluded that Fresnel lenses with focal length that produces F-number of ≥1.3 will have a better optical efficiency. Moreover, Fresnel lens with too many prisms causes loss in optical efficiency which is true also for the case of too few of them. Therefore, the optimum groove pitch is a value in between. Also, thinner Fresnel lens is better in transmitting light than bulky one. Finally, low reflective surface will allow more light rays to get through the Fresnel lens which ultimately improves the optical efficiency.

5.2.2. Optical analysis of the optimised HCPV optical system

5.2.2.1. Optical efficiency investigation

The investigation process here is based on choosing the optimum Fresnel lens parameters that were examined in the previous section to evaluate the optical performance improvement. Table 5.2 shows the parameters of the Fresnel lens to be tested. The Fresnel lens aperture areas to be examined are: 0.13x0.13m^2, 0.15x0.15m^2, 0.18x0.18m^2, 0.2x0.2m^2 and 0.25x0.25m^2 which are equivalent to the following geometrical concentration ratios: 169X, 225X, 324X, 400X and 625X. Moreover, for the selected geometrical concentration ratios the focal length (0.46m) was chosen to have F-number ≥ 1.3. From the previous section it was found that thinner Fresnel lens performs better; therefore 0.001m thickness was chosen. Also, it was found that 0.003m groove pitch is the optimum choice in terms of optical efficiency. The reflection losses at the Fresnel lens surfaces are dependent on the angle of incidence but if the light incidence angle is zero i.e. the Fresnel lens is normal to the sun then the transmissivity of the PMMA Fresnel lens can be in the range of 92% - 96% [104,200]; therefore, the transmissivity of the tested Fresnel lens surface was set to 95% based on this range.

Table 5.2: Optimised Fresnel lens parameters.

Parameter	**Value**
Focal length (m)	0.46
Thickness (m)	0.001
Groove pitch (m)	0.003
Grooves direction	grooves in (upside down)
Transmissivity (%)	95
Material	PMMA

Table 5.3 shows the optical simulation results of the optimised Fresnel lens including the received flux distribution, received power and the optical efficiency. For comparison purpose, Figure 5.6 shows the performance of the Fresnel lens before and after the optimisation. The optimised Fresnel lens optical efficiency ranged from about 74% to 79% while the Fresnel lens before the optimisation process ranged from 59 to 67% with average increase of about 21%. The improvement in the optical efficiency is more on large aperture areas Fresnel lens than smaller ones. For example, 0.25x0.25m^2 Fresnel lens aperture area optical efficiency improvement is about 24% while it is about 18% for 0.13x0.13m^2 one.

Table 5.3: Summary of optimised Fresnel lens simulation results.

Aperture area (m^2)	Fresnel lens F-number	Received flux distribution	Input Power (W)	Received power (W)	Optical efficiency (%)
0.25x0.25	1.30	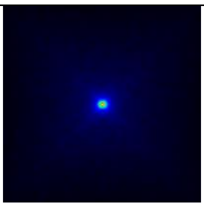	62.5	46.09	73.7
0.2x0.2	1.63	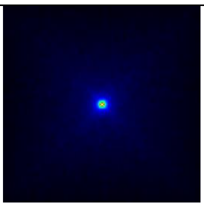	40	30.35	75.9
0.18x0.18	1.81	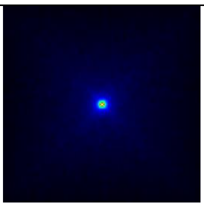	32.4	24.80	76.5
0.15x0.15	2.17	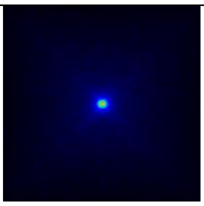	22.5	17.48	77.7
0.13x0.13	2.50	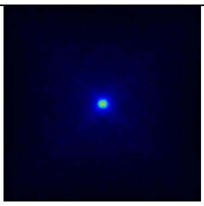	16.90	13.27	78.5

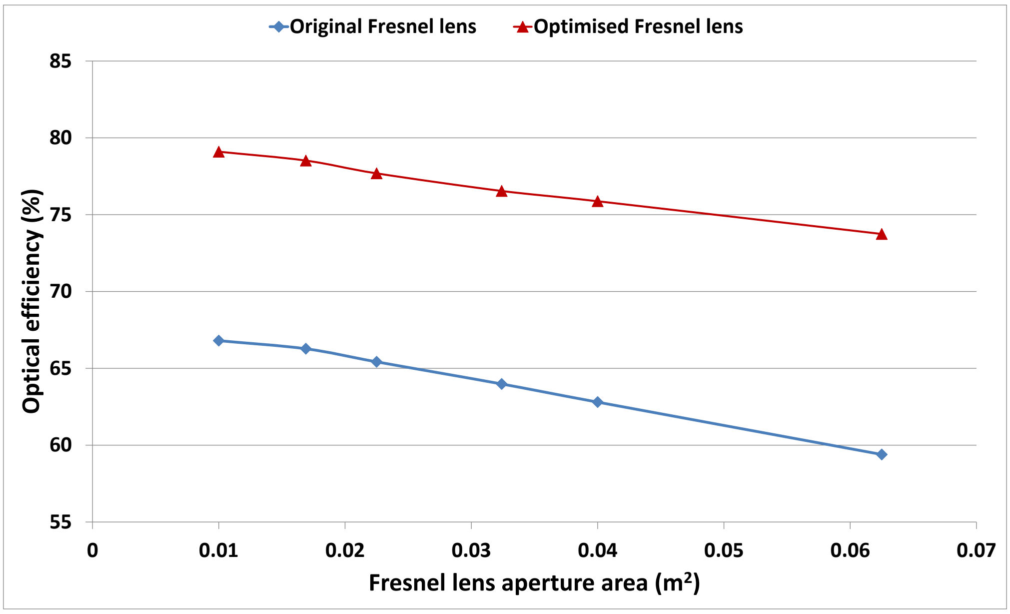

Figure 5.6: Fresnel lens performance before and after optimisation.

5.2.2.2. Incident rays uniformity investigation

The optimised HCPV optical system above will be investigated in order to increase the incident irradiation uniformity on the receiver (PV cell). As implemented in the previous chapter, two techniques will be followed: increasing the distance between the Fresnel lens and the PV cell (*l*) and increase the distance between the Fresnel lens and the PV cell (*l*) with introducing a SOE on the receiver. The objective is to achieve a uniform irradiation on the receiver with minimum loss in the received energy i.e. minimum loss in optical efficiency compared to the focus point case i.e. at *l*= 0.46m. Three aperture areas of the optimised Fresnel lens 0.13x0.13m^2, 0.18x0.18m^2 and 0.25mx0.25m^2 with geometrical concentration ratio of 169X, 324X and 625X respectively will be investigated.

Effect of varying the distance between the Fresnel lens and the receiver (*l*)

The uniformity and the received power on the receiver were examined as the distance (*l*) varied. The range value of (*l*) to be investigated is 0.445-0.55m with a distance step of 0.005m without a SOE. Figure 5.7 shows the influence of varying the distance (*l*) on the received power and uniformity for optimised Fresnel lens with aperture area of 0.18x0.18m^2. As illustrated, the maximum received power and non-uniformity is at the focus point i.e. $l = f$ =0.46m. It is clear from the Figure that the received power is negatively influenced by increasing the distance (*l*) from the focal length height ($l = f$ =0.46m) while the non-uniformity is reduced. For example, the received power at focal length is 24.80 W with optical efficiency of 76.5% (Figure 5.8) while the power at l = 0.55m is 1.11 W with optical efficiency of 3.4%. On the other hand, the non-uniformity is maximum (494.6) at the focal length while it is minimum (0.5) at l = 0.55m. The same behaviour is observed when the distance (*l*) becomes shorter than the focal length height. It can be concluded that increasing the distance (*l*) leads to a better uniformity but with clear optical efficiency drop.

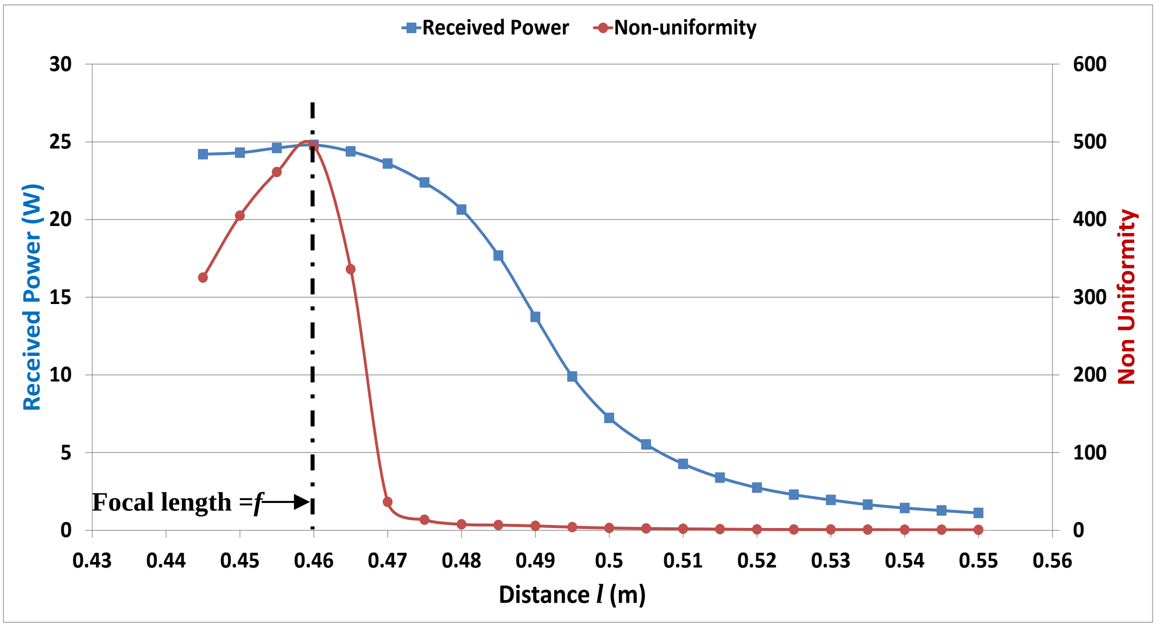

Figure 5.7: Effect of varying the distance (*l*) on the power and uniformity.

Figure 5.8 shows the optical efficiency of the three Fresnel lens aperture areas at different distances of (*l*). It can be observed that the maximum optical efficiency is at the focus point i.e. 0.46m. Moreover, due to the reduction in the received power, as the distance (*l*) varied from the focus point, the optical efficiency decreases as well.

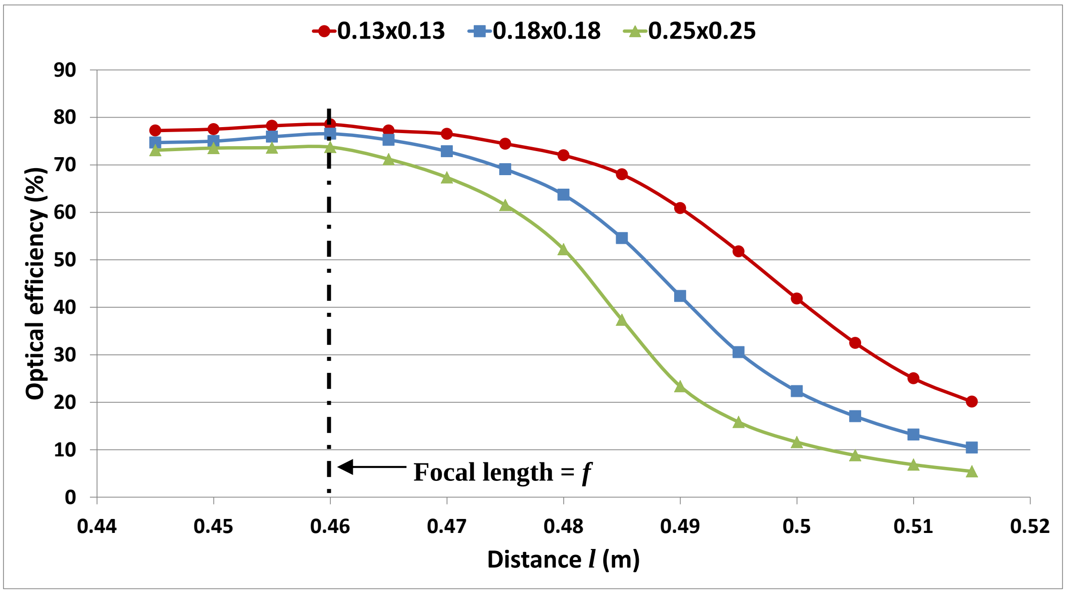

Figure 5.8: Effect of varying the distance (*l*) on the optical efficiency.

Figure 5.9 illustrates the influence of varying the distance (*l*) on the received rays uniformity for the three different Fresnel lens aperture areas. The non-uniformity is maximal at the focus point for all modelled cases. Moreover, it is clear that the degree of non-uniformity is directly proportional to the Fresnel lens geometrical concentration ratio. For example, the non-uniformity for Fresnel lens with aperture area of 0.25x0.25m^2 exceeds 800 while it is less than 300 in case of Fresnel lens with aperture area of 0.13x0.13m^2. In all cases, the degree of non-uniformity dropped dramatically after *l*=0.46m.

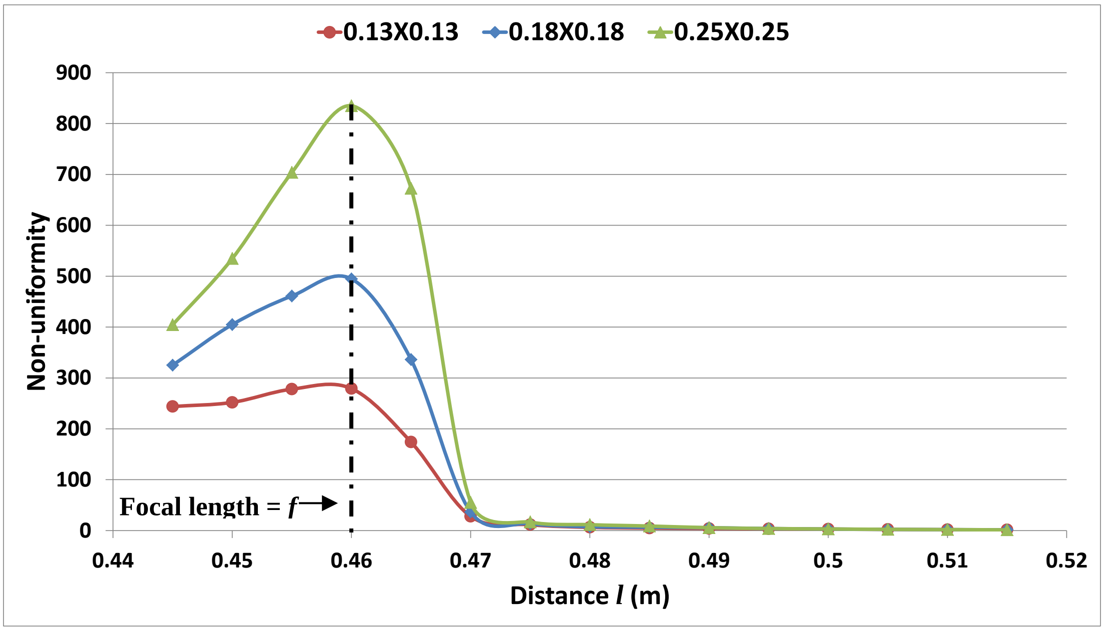

Figure 5.9: Effect of varying the distance (*l*) on the uniformity.

Table 5.4 shows a summary of the modelling results including the received power, optical efficiency, non-uniformity and received radiation flux profile for the Fresnel lens with aperture area of 0.18x0.18m^2. It can be seen that the received flux profile changes with the distance (*l*). Although the uniformity was significantly improved using this technique, the resulted received power is very low i.e. low optical efficiency. Therefore, a SOE will be used to enhance the received power while maintaining the uniformity of received radiation.

Table 5.4: Summary of increasing the distance (*l*) on the received power and uniformity.

Distance (*l*) (m)	Non-uniformity	Received flux distribution	Input power (W)	Received power (W)	Optical efficiency (%)
$l=f=0.46$	494.61	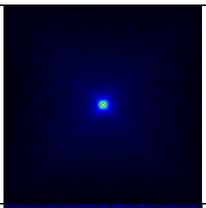	32.40	24.80	76.5
0.475	13.49	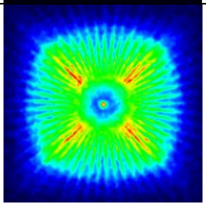	32.40	22.38	69.1
0.49	5.61	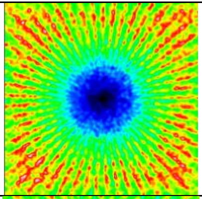	32.40	13.73	42.4
0.505	2.25	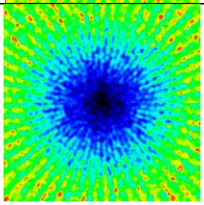	32.40	5.52	17.0
0.52	1.08	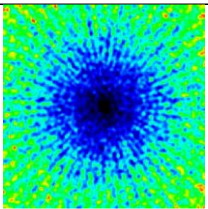	32.40	2.74	8.5
0.535	0.75	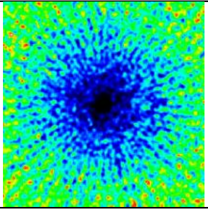	32.40	1.65	5.1

Effect of introducing Secondary optical element (SOE)

A hollow inverted truncated pyramid reflector (HITPR) used in the previous chapter was introduced here to the HCPV system. The material reflectivity of the HITPR four sides was set to 95% instead of the 90% used in chapter 4; this high reflectivity material is already available in the market [181]. The optimised Fresnel lens with aperture area of $0.18\text{x}0.18\text{m}^2$ with geometrical concentration ratio of 324X was used in the uniformity tests. The same procedure of varying the distance (*l*) carried out in the previous section was repeated here but with integrating HITPR. The range value of (*l*) examined was 0.460-0.535m with a distance step of 0.005m. Moreover, the following HITPR SOE heights were investigated: 0.01m, 0.02m, 0.03m, 0.04m, 0.05m and 0.06m. For each HITPR SOE height the distance (*l*) was varied 15 times which means there are 90 cases to be investigated to find out the optimum combination of SOE height and distance (*l*). Figure 5.10 compares all the SOEs in terms of uniformity which shows that the non-uniformity is maximum at focus point (*f* = 0.46m) and reduced as the distance (*l*) increases. Moreover, 0.01m, 0.02m, 0.03m, 0.04m and 0.05m SOEs produce almost the same level of non-uniformity at different value of distance (*l*) while the 0.06m SOE produces slightly better ray distribution.

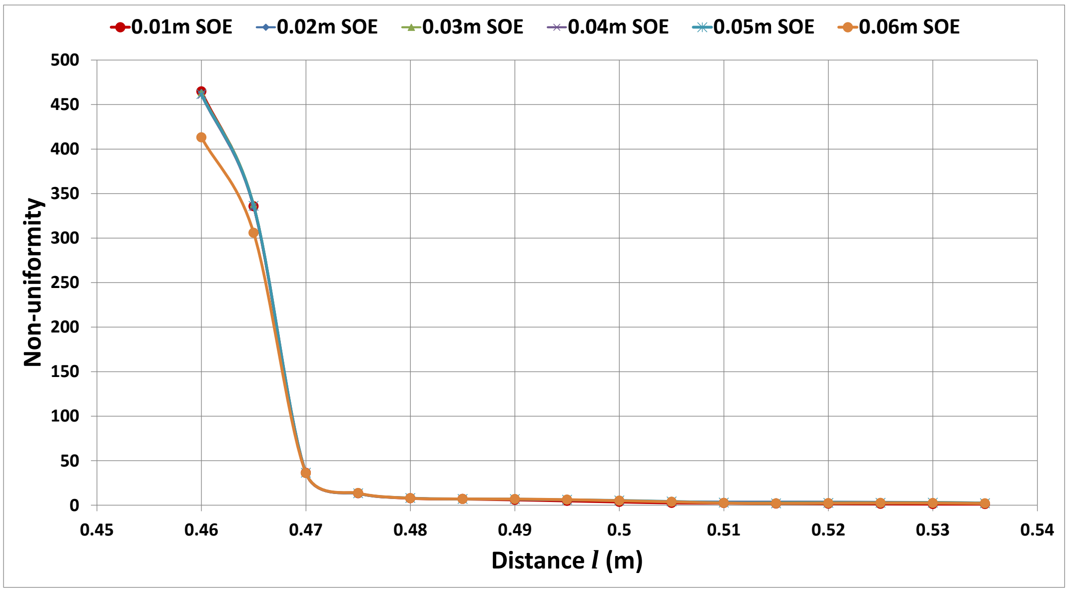

Figure 5.10: Effect of varying the combination of distance (*l*) and reflector height on the uniformity.

Figure 5.11 compares all the SOEs in terms of optical efficiency which shows that 0.06m SOE has the best optical efficiency almost at all values of distance (*l*). On the other hand, the 0.01m SOE shows the worst optical performance almost at all values of (*l*). Also, it can be observed that the optical efficiency decreased when the distance (*l*) increased for 0.02, 0.03, 0.04, 0.05 and 0.06m SOE till reach the lowest value at *l*=0.495m where after this point the optical efficiency showed increasing trend. This can be referred to the number of the rays that strike the SOE and reflected back without intersecting with the solar cell causing loss of optical energy. These reflected rays increased with distance *l* till reach maximum at *l*=0.495m where afterwards the number of these rays decreased. On the other hand, when 0.01m SOE used the optical efficiency showed only decreasing trend when distance (*l*) increased. This can be due to the large inclination angle of the SOE walls compared to other SOEs (Figure 4.21).

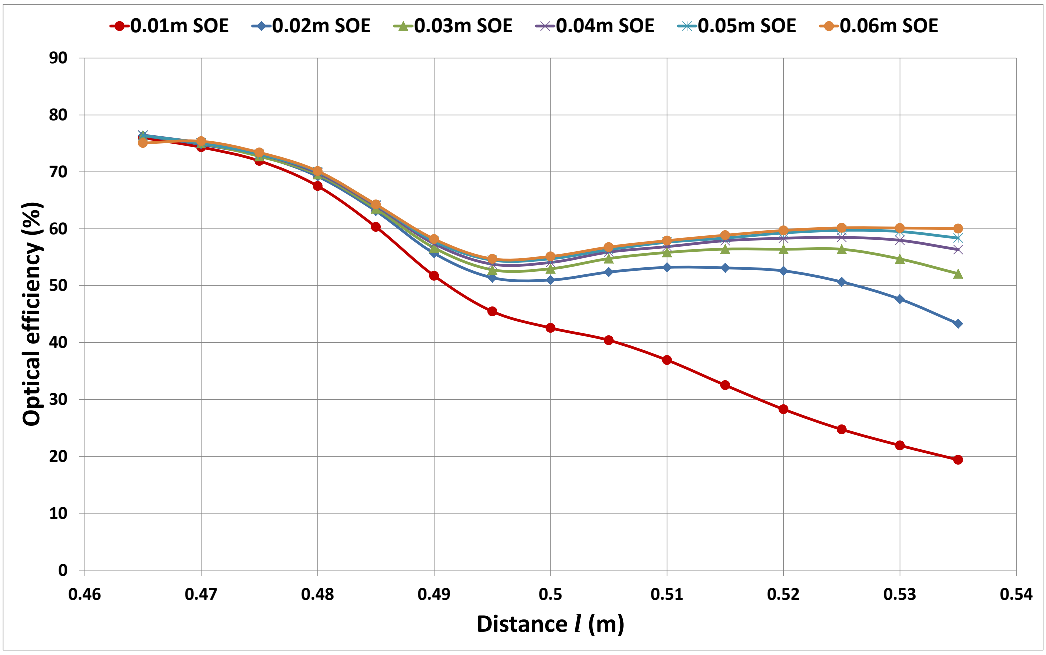

Figure 5.11: Effect of varying the combination of distance (*l*) and reflector height on the optical performance.

Figure 5.12 shows the optical efficiency and non-uniformity curves of the optical system with 0.06m SOE along the distance (*l*). As the distance (*l*) increases away from the focus point, the optical efficiency decreased till reaching the lowest value at *l*=0.495m then the curve goes slightly up. Moreover, the non-uniformity dropped from about 305.89 at *l* = 0.465m to 1.96 at *l* = 0.54m. The optimum distance (*l*) is a distance that ensures low degree of non-uniformity and at the same time minimum optical losses compared to the focus point case. From the experimental work presented in the previous chapter, the electrical efficiency is high when non-uniformity is less than 2. Therefore, *l*= 0.535m can be the optimum distance (*l*) where the non-uniformity is less than 2 and the optical efficiency is about 60%.

Figure 5.13 shows a 3-D image of the incident ray profile on the receiver for the point-focus case and the optimum case i.e. at *l*= 0.535m with the 0.06m SOE. It is clear that the incident ray distribution becomes more uniform where rays cover most of the receiver area.

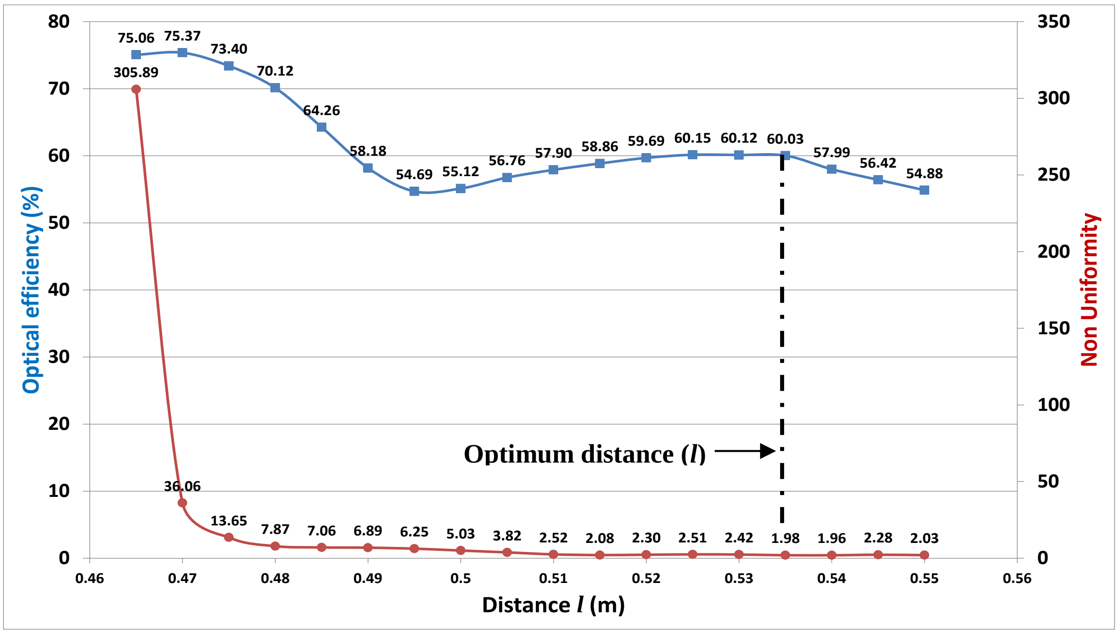

Figure 5.12: Optical efficiency and non-uniformity curves of the optical system.

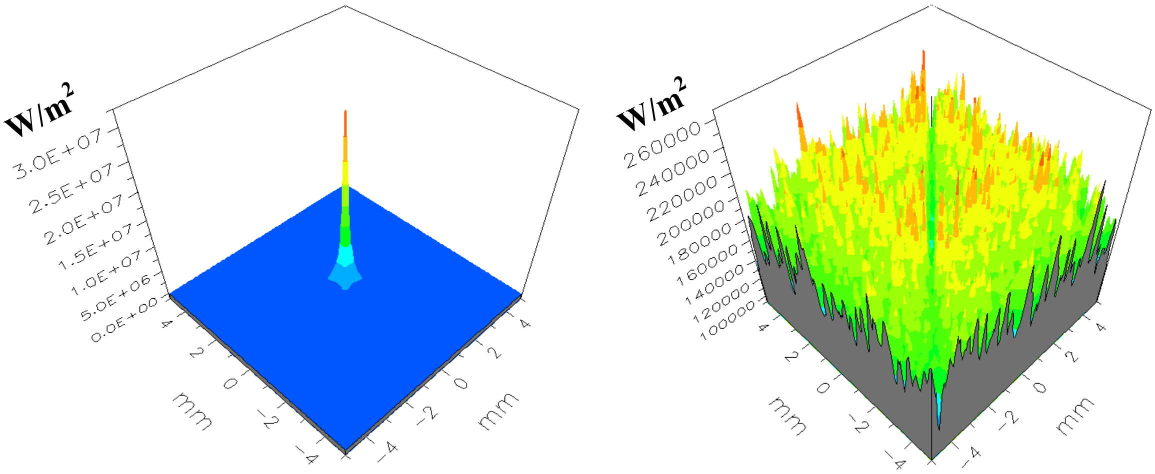

Figure 5.13: Incident rays for the point-focus case and combination of *l*=0.535m and 0.06m reflector.

Table 5.5 shows a summary of the testing results including the received power, optical efficiency, non- uniformity and received radiation flux profile for the optimised Fresnel lens with aperture area of 0.18x0.18m^2 at focus point, at *l*=0.535m and at *l*=0.535m with integrating the 0.06m SOE. The received power was increased about 12 times after introducing the SOE from about 1.7 W to about 19.5 W with relatively slight increment in the irradiation non-uniformity. As a result, the optical efficiency was increased after placing the SOE compared to the case at the same distance (*l*) but without SOE from about 5% to 60%. Moreover, the degree of non-uniformity of incident rays was improved from about 495 at focus point to less than 2 by increasing the distance (*l*) and introducing the SOE.

Table 5.5: Summary of received power and uniformity for optimised Fresnel lens.

Distance (*l*) (m)	Non-uniformity	Received flux distribution	Input power (W)	Received power (W)	Optical efficiency (%)
l=*f* =0.46, no SOE	494.61	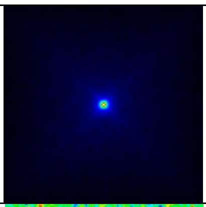	32.40	24.80	76.5
l=0.535, no SOE	0.75	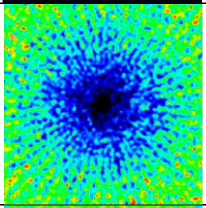	32.40	1.65	5.1
l=0.535 & 0.06m SOE	1.98	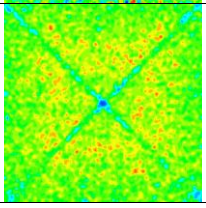	32.40	19.45	60.0

Table 5.6 shows a summary of the optical efficiency results for the initial and optimised optical system with and without introducing the 0.06m SOE. It can be seen that the Fresnel lens efficiency has increased after optimisation with average increment of about 21%. On the other hand, the optical efficiency of the HCPV optical system including the Fresnel lens and the SOE has increased after optimising the Fresnel lens design and increasing the reflectivity of the SOE surface with average increment of about 30% which will enhance the electrical output of the HCPV.

Table 5.6: Optical modelling results for the initial and optimised optical system with different Fresnel lens aperture areas.

	Optical efficiency without SOE (%)		**Optical efficiency with SOE (%)**	
Aperture area (m^2)	**Initial Fresnel lens**	**Optimised Fresnel lens**	**Initial Optical system**	**Optimised Optical system**
0.25x0.25	59.4	73.7	42.9	55.7
0.2x0.2	62.8	75.9	45.4	58.9
0.18x0.18	64.0	76.5	46.2	60.0
0.15x0.15	65.4	77.7	47.3	61.4
0.13x0.13	66.3	78.5	47.9	62.2

5.2.3. Acceptance angle investigation of the HCPV optical system

The acceptance angle of the HCPV optical system with and without SOE after optimisation was examined using the ray tracing technique. The acceptance angle (2θ) is commonly defined as the incidence angle corresponding to 90% of the maximum optical efficiency at normal incidence [33,108,128]. Figure 5.14 shows a schematic diagram of half acceptance angle (θ) of an incident ray. The acceptance angle will be found by increasing the incident ray angle from 0^o (normal incidence) to 2^o with a degree step of 0.05^o. Additionally, the influence of increasing the incidence ray angle on the optical system performance will be investigated in this range. The incidence angle will be increased by increasing the light source angle.

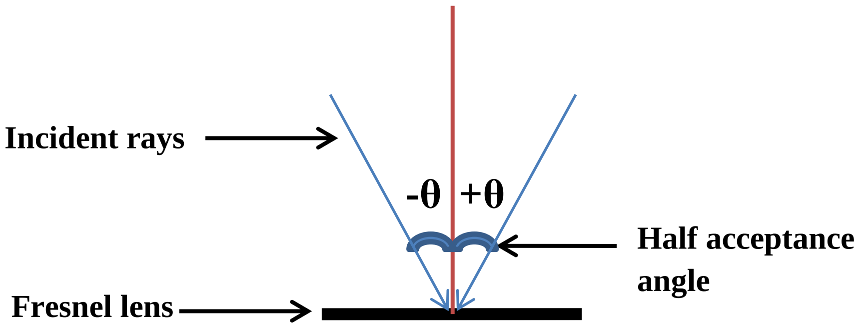

Figure 5.14: Schematic diagram of half acceptance angle of incident rays.

5.2.3.1. The acceptance angle of the optimised HCPV optical system without SOE

The optimised Fresnel lens with aperture areas of $0.25x0.25m^2$, $0.18x0.18m^2$ and $0.13x0.13m^2$ equivalent to the following geometrical concentration ratios 625X, 324X and 169X respectively were investigated. The influence of increasing the half acceptance angle on the optical efficiency is illustrated in Figure 5.15. The Figure shows that the optical efficiency is decreased by increasing the incidence angle till reaching almost 0% at incidence angle of >1^o for the three Fresnel lens aperture areas.

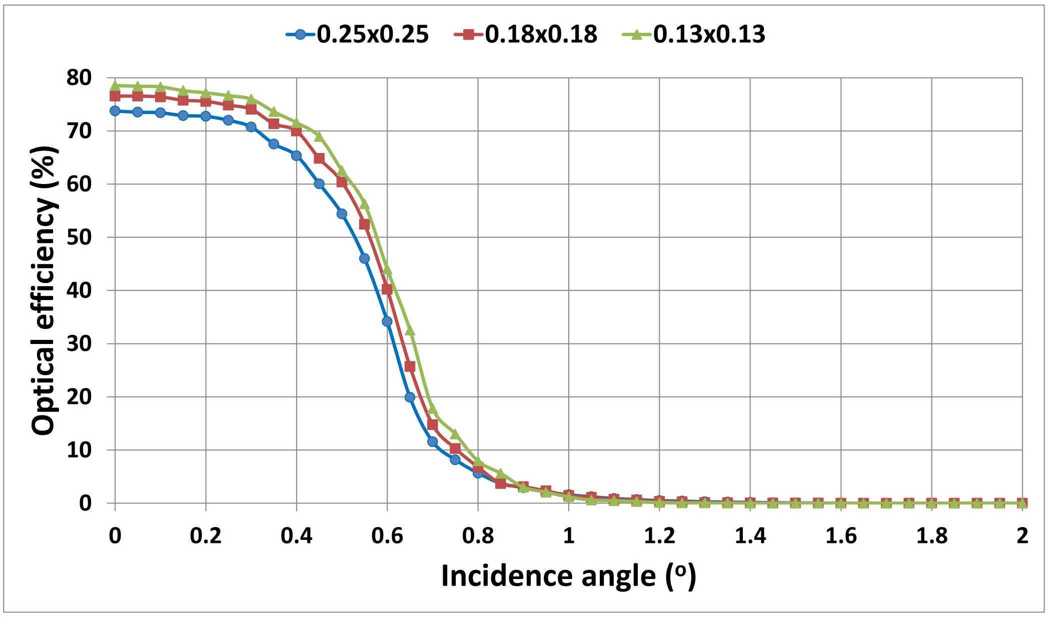

Figure 5.15: Influence of increasing incidence angle on the optical efficiency without SOE.

Table 5.7 shows a summary of the acceptance angle results including half acceptance angle, acceptance angle, optical efficiency under normal incidence and optical efficiency at the acceptance angle.

Table 5.7: Summary of acceptance angle examination for the optimised Fresnel lenses.

	Half acceptance angle (θ^o)	Acceptance angle ($2\theta^o$)	Optical efficiency under normal incidence (%)	Optical efficiency at the acceptance angle (%)
0.25x0.25 m^2	0.4	0.8	73.74	66.37
0.18x0.18 m^2	0.4	0.8	76.54	68.89
0.13x0.13 m^2	0.4	0.8	78.52	70.67

The half acceptance angle (θ) of the optical system plays a major role in selecting the tracking system for the HCPV. Optical system with smaller half acceptance angle requires higher precision tracking which may increase the total cost of the HCPV [122].

5.2.3.2. The acceptance angle of the optimised HCPV optical system with SOE

The same investigation carried out in the previous section on the optical system was repeated here but with increasing the distance (*l*) to 0.535 m and integrating the 0.06m SOE to the HCPV system. The negative effect of increasing the half acceptance angle on the optical efficiency is shown in Figure 5.16. After introducing the SOE this negative effect became lower compared to that of a HCPV system without SOE. Moreover, the larger Fresnel lens aperture areas were more negatively influenced by increasing the incidence angle than the smaller ones. For example, Fresnel lens with aperture area of 0.25x0.25m^2 optical efficiency has decreased after incidence angle of about 0.6^o while 0.13x0.13m^2 Fresnel lens aperture area shows almost stable performance till incidence angle of 0.85^o where the optical efficiency has decreased afterwards. It can be concluded that higher concentration ratio Fresnel lens is more sensitive to the increment of the light incidence angle than lower concentration ratio one.

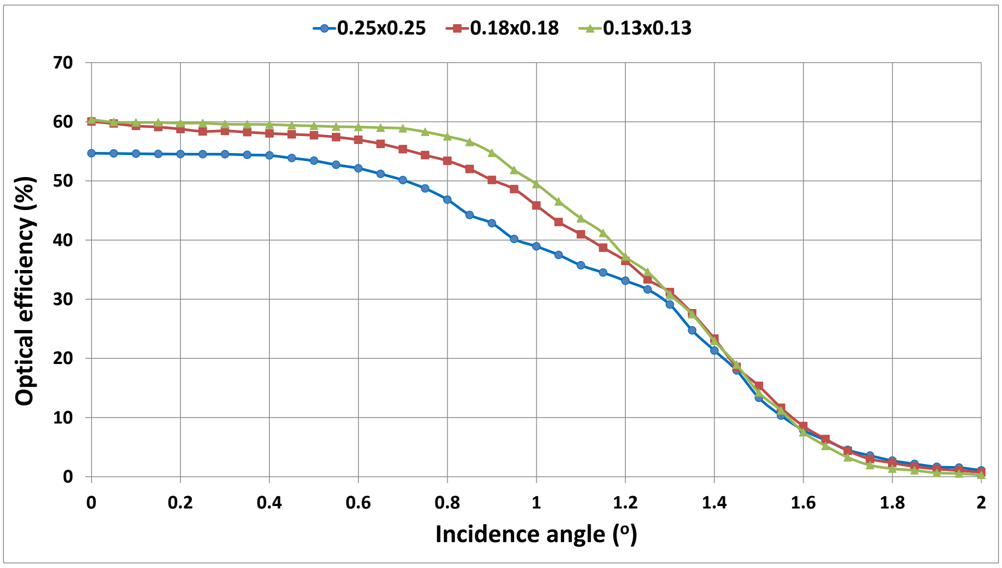

Figure 5.16: Influence of increasing incidence angle on the optical efficiency with SOE.

Figure 5.17 shows the influence of increasing the incidence angle on the HCPV optical efficiency with and without SOE for 0.18x0.18m^2 Fresnel lens aperture area. The two optical efficiency curves show that the negative influence of increasing the incidence angle of the rays on the optical efficiency is lower if the optical system is integrated with SOE. For example, the optical efficiency without SOE reaches to about zero at incidence angle of >1^o while with SOE case the optical efficiency at this incidence angle is higher than 45%.

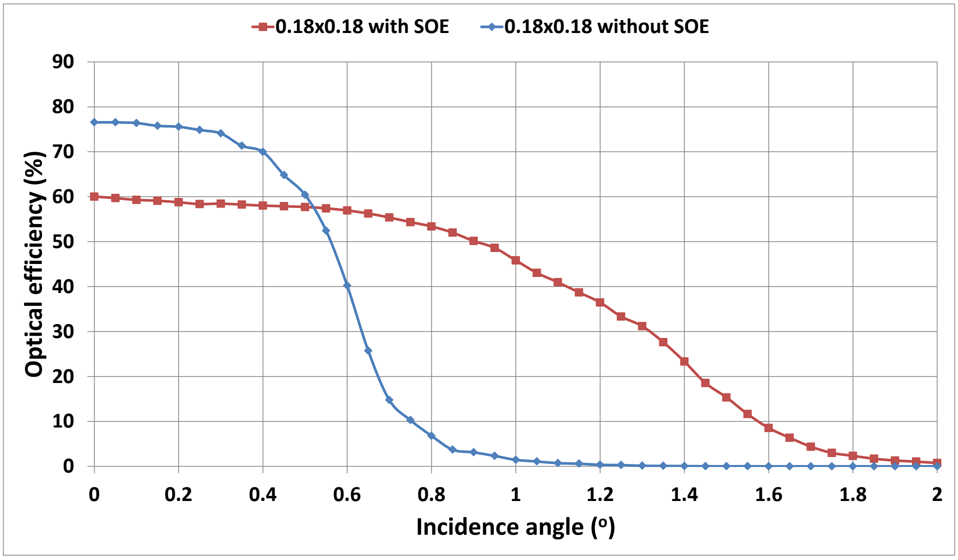

Figure 5.17: Influence of increasing incidence angle of the rays on the optical efficiency with and without SOE.

Figure 5.18 compares the acceptance angle of the three Fresnel lens aperture areas 0.25x0.25m^2, 0.18x0.18m^2 and 0.13x0.13m^2 with and without SOE. It is clear that the acceptance angle increases almost twice after placing the SOE from 0.8^o to 1.5^o, 0.8^o to 1.6^o and 0.8^o to 1.9^o for 0.25x0.25m^2, 0.18x0.18m^2 and 0.13x0.13m^2 Fresnel lenses respectively.

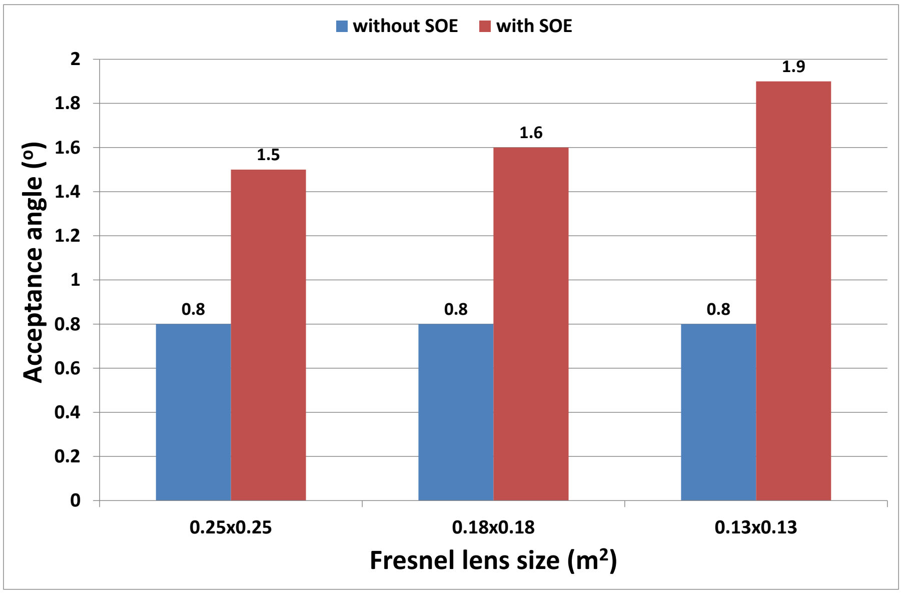

Figure 5.18: Acceptance angle with and without SOE.

Placing the developed SOE on the PV assembly not only improves the irradiation uniformity on the solar cell but also helps to increase the acceptance angel which would relax the demand for high precision tracking system.

5.3. Multi HCPV/T assembly configuration

More than one HCPV/T systems can be assembled in different forms such as linear and densely packed configuration. In this study, assembled HCPV units were examined in terms of tracking requirements, space occupation and electrical output before and after optical optimisation.

Four HCPV units including 0.18x0.18m^2 Fresnel lens, 0.06m SOE and 0.01x0.01m^2 multi-junction solar cell were assembled linearly using SolidWorks as shown in Figure 5.19. The distance between two solar cells' centres is the length of the Fresnel lens i.e. 0.18m while the total length of the assembly is 0.72m. Also, the width of the assembly is the width of the Fresnel lens i.e. 0.18m. The total area of the HCPV assembly is 0.1296m^2 i.e. about 0.13 m^2. Therefore, the area needed for connecting 16 HCPV units is about 0.5m^2.

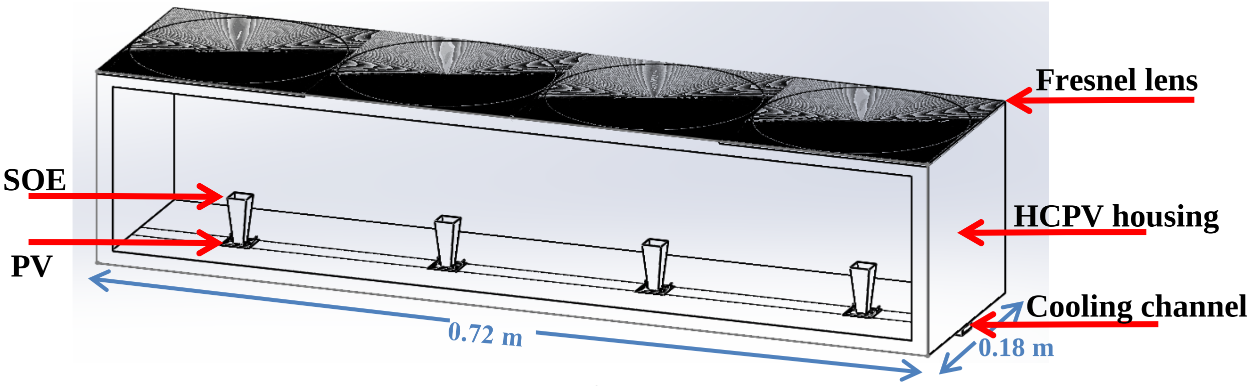

Figure 5.19: Four 0.18x0.18 m^2 HCPV systems assembled in series.

Roll-tilt tracking [126] arrangement using central torque tube or box frame tracking system can be used with this configuration. This configuration is easy to assemble including the electrical wiring connections and set-up of the cooling system.

Four HCPV units with the same size were densely packed as shown in Figure 5.20. The distance between two solar cells centres is 0.18m and the total size of the assembly is 0.1296m^2 i.e. about 0.13m^2. Pedestal form tracking system [126] can be used with this configuration which is known for its simplicity of installation. This configuration is easy to assemble and more convenient during cleaning and maintenance due to its compactness. But, the cooling fittings are more demanding in this configuration as the HCPV units are distributed in two rows instead of one which may also need more pumping power due to the channel joints friction.

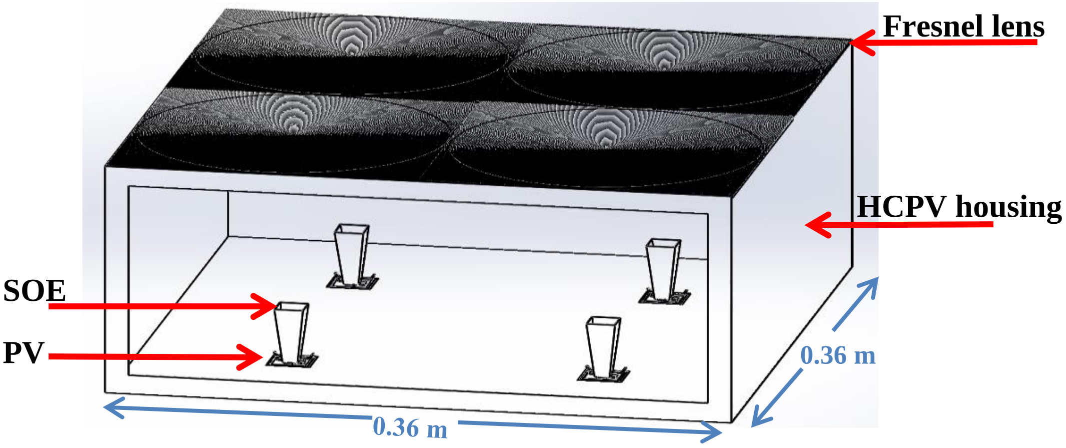

Figure 5.20: Four 0.18x0.18 m^2 HCPV systems densely packed.

Table 5.8 shows the optical power received by the multi-junction solar cell in W if the input flux at the aperture level is 1000 W/m^2 for 1, 4 and 16 units optimised and non-optimised optical system 0.18x0.18m^2 HCPV. It shows that 16 non-optimised HCPV units, which occupy about 0.5m^2 area, can provide optical power of about 240 W. While, 16 optimised HCPV units can provide about 311 W optical power with increment of about 30%. In terms of area, 13 optimised HCPV units can provide more optical power than 16 non-optimised units which leads to area saving of about 20%.

Table 5.8: Optical power for 1, 4 and 16 HCPV before and after optical optimisation.

HCPV size (m^2)	1 HCPV optical power (W)	4 HCPV optical power (W)	16 HCPV optical power (W)
0.18x0.18 before optimisation	14.97	59.88	239.52
0.18x0.18 after optimisation	19.45	77.76	311.04

The electrical output of the HCPV depends on the solar cell electrical efficiency. From chapter 4, it was found experimentally that the electrical efficiency is about 36% when the calculated non-uniformity value is <2. Therefore, 16 non-optimised HCPV assembly can produce up to 86.2 W electrical power while optimised assembly can produce up to 112.0 W with increment of about 30%.

5.4. Densely packed of PV assembly configuration

In this configuration, one HCPV optical system including 0.18x0.18 m^2 Fresnel lens and 0.06m height SOE was integrated with 4 densely packed PVs instead of one to save 75% of the area required if each PV was integrated with a separate optical system. Optical and electrical output of this receiver configuration was examined. The area of the receiver is 0.02x0.02 m^2 (Figure 5.21) and the geometrical concentration ratio is 81X. To keep the same geometrical concentration ratio of the above described SOE i.e. 4X, the exit and entrance aperture areas are chosen to be 0.021x0.021m^2 and 0.042x0.042 m^2 respectively.

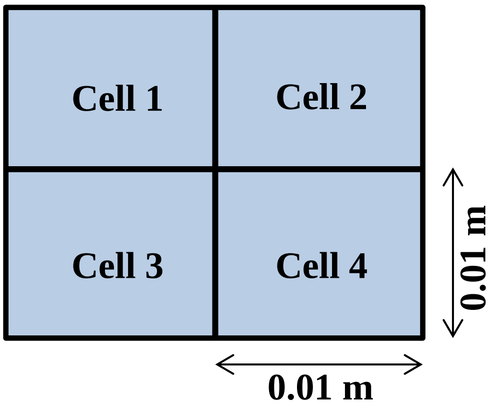

Figure 5.21: Four 0.01x0.01 m^2 densely packed receiver.

The distance (*l*) was varied for examination from 0.46 to 0.6m with a distance step of 0.005m. Figure 5.22 shows the optical efficiency and non-uniformity curves of the optical system with SOE along the distance (*l*). As the distance (*l*) increases away from the focus point, the optical efficiency decreased till reaching the lowest value at *l*=0.53m then the curve goes slightly up. Moreover, the non-uniformity dropped from more than 700 at *l* = 0.465m to about 2 at *l* = 0.565m. The optimum distance (*l*) is a distance that ensures low degree of non-uniformity and at the same time minimum optical losses compared to the focus point case. Therefore, *l*=0.565m can be the optimum distance (*l*) where the non-uniformity is minimum (about 2) and the optical efficiency is about 71%.

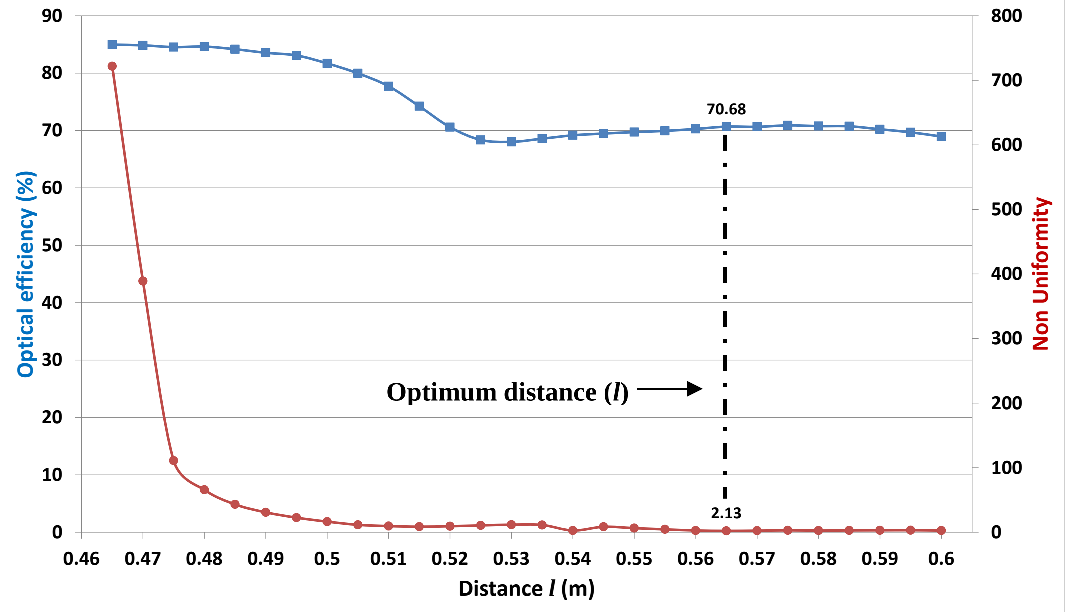

Figure 5.22: Optical efficiency and non-uniformity curves of the optical system with 4 densely packed receiver configuration.

Table 5.9 shows a summary of the densely packed PV module testing results including the received power, optical efficiency, non- uniformity and received radiation flux profile for the optimised Fresnel lens with aperture area of 0.18x0.18m^2 at focus point, at *l*=0.565m and at *l*= 0.565m with integrating the 0.06m SOE.

Table 5.9: Summary of the received power and uniformity for 4 densely packed reciever.

Distance (*l*) (m)	Non-uniformity	Received flux distribution	Input power (W)	Received power (W)	Optical efficiency (%)
l=*f* =0.46, no SOE	494.61	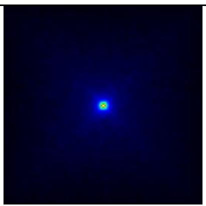	32.40	24.80	76.5
l=0.565, no SOE	2.08	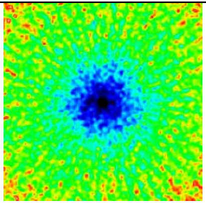	32.40	5.15	15.9
l=0.565 & 0.06m SOE	2.13	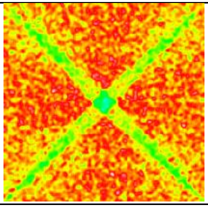	32.40	22.90	70.7

The received power increased more than 4 times after introducing the SOE at distance *l*= 0.565m from 5.15 W to 22.9 W with a slight increment in irradiation non-uniformity. As a result, the optical efficiency was increased after placing the SOE compared to the case at the same distance (*l*) but without SOE from about 16% to 71% with only 7.6% loss in the optical efficiency compared to the focus point case i.e. at *l*= 0.46m. Moreover, the degree of non-uniformity of incident rays was reduced from about 495 at focus point to about 2 after increasing the distance (*l*) and introducing the SOE.

Table 5.10 shows a summary of the optical and electrical power results for the two cases: single cell and 4 densely packed cells with 0.18x0.18 m^2 Fresnel lens and 0.06m SOE. The Table shows that 4 densely packed PVs configuration has received about 18% higher optical power than the single cell receiver due to the larger receiver area and acceptance angle allowing more rays to be accepted. It can be assumed that the electrical efficiency is 36% at non-uniformity degree of about 2 from chapter 4; thus the single cell HCPV configuration can produce 7.0 W electrical power while densely packed HCPV can produce about 8.3 W with increment of 18%. This configuration is more costly as it includes 3 more MJ solar cells but it saves 75% of the area needed. It can be considered if the area available is limited and in the future when the PV prices decrease further.

Table 5.10: Optical and electrical power for single and densely packed PVs.

	Optical power (W)	**Electrical power (W)**
Single cell	19.45	7.00
Four densely packed PVs	22.95	8.26

5.5. Summary

A parametric study including focal length, thickness, groove pitch and transmissivity on different Fresnel lens aperture areas was implemented to enhance the performance of the HCPV optical system using ray tracing technique. The optical efficiency of the system was enhanced with average increase of about 21%.

The HCPV optical system was also examined after introducing a 0.06m SOE to improve the incident rays uniformity on the receiver and compared with the HCPV before optimisation. It was found that the total optical efficiency was increased from 46.2% to 60.0% with increment of about 30%. The acceptance angle of the HCPV optical system with and without SOE was examined using ray tracing method. It was found that the acceptance angle increases after placing the developed SOE almost twice from 0.8^o to 1.5^o, 0.8^o to 1.6^o and 0.8^o to 1.9^o for $0.25x0.25m^2$, $0.18x0.18m^2$ and $0.13x0.13m^2$ Fresnel lens aperture areas respectively. Increasing the acceptance angle could reduce the overall cost of the developed HCPV as the demand for high precision tracking system will be alleviated.

Assembled HCPV units were examined in terms of tracking requirements, space occupation and electrical output before and after optical optimisation. It was found that an assembly of 16 non-optimised $0.18x0.18m^2$ HCPV units which occupy about $0.5m^2$ can produce optical power of about 240 W compared to 311 W for 16 optimised HCPV units with increment of about 30%. In terms of used area, 13 optimised HCPV units can provide more optical power than 16 non-optimised units which leads to area saving of about 20%. Finally, assuming that the multi-junction solar cell electrical efficiency is 36%, 16 non-optimised HCPV assembly can produce up to 86 W electrical power while optimised assembly can produce up to 112 W with increment of about 30%.

Densely packed receiver configuration including 4 PV cells was compared to the single PV configuration. It was found that densely packed configuration can increase the optical and electrical power by about 18% due to the larger receiver area and acceptance angle with area saving of 75%.

More theoretical and experimental detailed electrical analysis of the developed HCPV under different solar radiations and PV surface temperatures and under uniform and non-uniform illumination will be presented in the next chapter.

CHAPTER 6

Electrical modelling of a multi-junction solar cell and outdoor electrical characterisation of a HCPV system

6.1. Introduction

This chapter describes the development of a mathematical model able to generate an I-V curve for the multi-junction solar cell and predict its electrical performance under different solar concentration ratios (CR) and PV surface temperature (T_S). The model was developed and calibrated against the manufacturer indoor experimental output data before utilising it to evaluate the developed HCPV electrical performance. A single HCPV unit was installed outdoor to examine its electrical performance and compare it with the electrical output of the developed model. Moreover, the influence of non-uniform incident rays on the I-V curve parameters of the multi-junction solar cell was investigated by analysing the outdoor measured I-V curve and the received solar radiation.

6.2. Lumped diode solar cell circuit model

There are a number of methods used in the literature to predict the I-V characteristics of the multi-junction solar cell such as two diodes equivalent circuit model for each subcell, single diode equivalent circuit model for each subcell, lumped diode model and network cell model [156]. A brief literature review on electrical modelling of a multi-junction solar cell can be found in Appendix D. In this work, a lumped diode circuit will be used to develop a mathematical model using Engineering Equation Solver (EES) to characterise the IV curve of the AZURSPACE III-V triple-unction PV cell type 3C42A under different surface temperature and light intensity. A lumped diode model is less demanding in terms of empirical parameters to be evaluated i.e. more practical and time saving than single or two diodes models where the empirical parameters of each subcell of the multi-junction solar cell have to be estimated. The general electrical model of a solar cell consists of a current source that depends on illumination in parallel with a diode. For concentrator cells, this model is often extended to include voltage drop due to high current flow by means of a series resistance (R_s) [96]. Figure 6.1 shows the equivalent circuit diagram of the lumped diode model of the multi-junction solar cell.

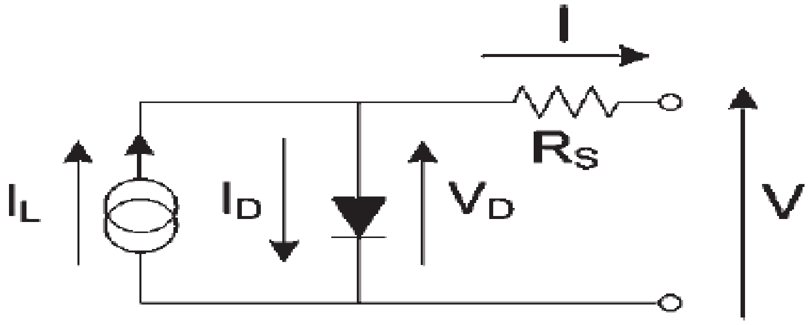

Figure 6.1: Equivalent single lumped diode solar cell circuit model [96].

The output current and voltage across the cell for a lumped diode model with R_s can be expressed by equations 6.1 and 6.2 [96]:

$$I = I_L - I_D \tag{6.1}$$

$$V = V_D - IR_S \tag{6.2}$$

where I is the current of the solar cell, V is the voltage, I_L is the light generated current, V_D and I_D are the voltage and current of the diode respectively and R_S is the series resistance. The current through the diode follows the Shockley equation [96]:

$$I_D = I_0\left[\exp\left(\frac{qV_D}{nkT}\right) - 1\right] \tag{6.3}$$

Where I_0 is the reverse saturation current, q is the electron charge (1.60217646 x 10^{-19}C), k is the Boltzmann constant (1.3806503 x 10^{-23} J/K), T is the temperature of the p-n junction in Kelvin and n is the diode ideality factor.

Therefore, the I–V characteristic of the solar cell, including the series resistance effect, is defined by equation (6.4):

$$I = I_L - I_0 \left[\exp\left(\frac{q(V + IR_S)}{nkT} \right) - 1 \right] \tag{6.4}$$

I_L, light-generated current, is a function of incident irradiation and PV surface temperature which can be calculated using the following equation [201]:

$$I_L = [I_{SC} + K_i(T - T_C)][\frac{S}{100}] \tag{6.5}$$

where I_{SC} is the short circuit current at reference temperature and radiation, K_i is the short circuit current temperature coefficient, T_C is the cell reference temperature and S is the solar irradiation in mW/cm^2.

Temperature dependence is due to the temperature term in the above equations and the temperature dependence of the saturation current equation [96,97]:

$$I_0 = T^{3+\gamma/2} \exp\left(-\frac{E_g}{kT} \right) \tag{6.6}$$

where E_g is the width of the semiconductor bandgap at temperature T and γ is the third order dependence of the square of the intrinsic carrier concentration on temperature [96].

Some of the above mentioned empirical parameters like n, R_S, E_g and γ are not available in the literature as they need to be found empirically for each CPV. Spectrolab multi-junction solar cell (C1MJ) empirical parameters available in the literature [156,97,202] were used as initial values to develop the electrical model. Then, the CPV manufacturer electrical output data [90] based on indoor experimental results were used to calibrate the developed model and produce more accurate value of these empirical constants. Finally, the calibrated model was used to predict the solar cell electrical output performance. The program code of the developed model using the lumped diode solar cell circuit including all the evaluated empirical parameters is shown in Appendix E.

6.3. Calibration of the developed I-V curve model against the manufacturer indoor experimental data

Figure 6.2 shows the I-V curve predicted by the developed electrical model compared to the manufacturer experimental data at the following concentration ratios: 250X, 500X and 1000X with PV surface temperature of 25°C.

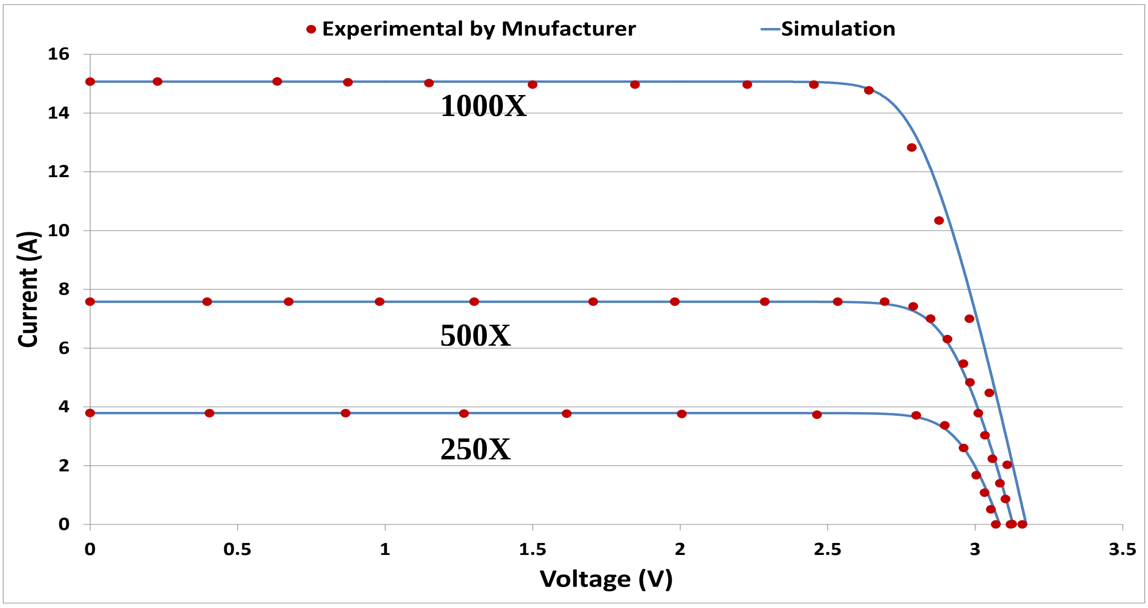

Figure 6.2: I-V curve at CR= 250X, 500X and 1000X and PV temperature of 25°C.

Although the variation of the V_{OC} with radiation is very low compared to the variation of the I_{SC}, the Figure shows clearly that both are increased with the input radiation. Furthermore, it can be noticed that close agreement between the manufacturer experimental data and the developed model at different concentration ratios.

Figure 6.3 shows the power curve predicted by the developed electrical model compared to the manufacturer experimental data at the following concentration ratios: 250X, 500X and 1000X with PV surface temperature of 25°C. The positive influence of raising the concentration ratio on the solar cell output power is clear where the output power increased from about 10 W at CR=250X to about 40 W at CR=1000X with the same PV area. The Figure also shows that the developed model is able to predict the experimental output power at different concentration ratios.

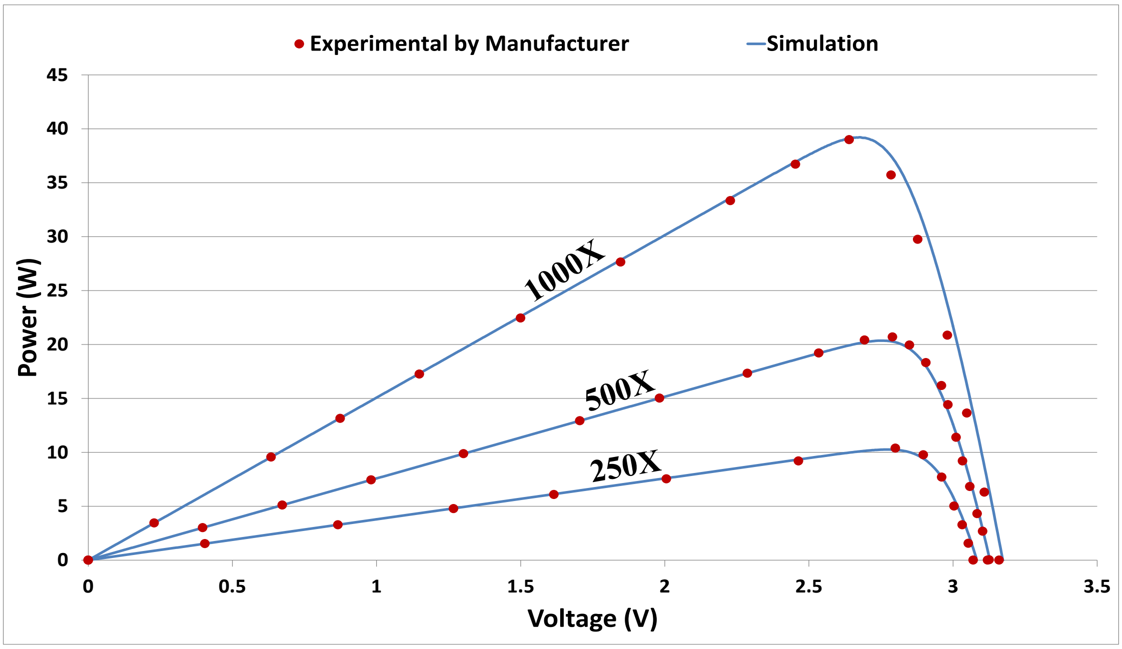

Figure 6.3: Power curve at CR= 250X, 500X and 1000X and PV temperature of 25°C.

In reference to the above I-V and power curves, Figure 6.4 below shows the electrical power comparison between the manufacturer data and the developed mathematical model. It can be noticed that the electrical power increases as the applied concentration ratio increases. The experimental output powers at concentration ratio of 250X, 500X and 1000X are 10.40 W, 20.71 W and 39.0 W respectively while the output power from the developed model at the same concentration ratios are 10.26 W, 20.36 W and 39.22 W with maximum difference of about 1.7% at CR=500X.

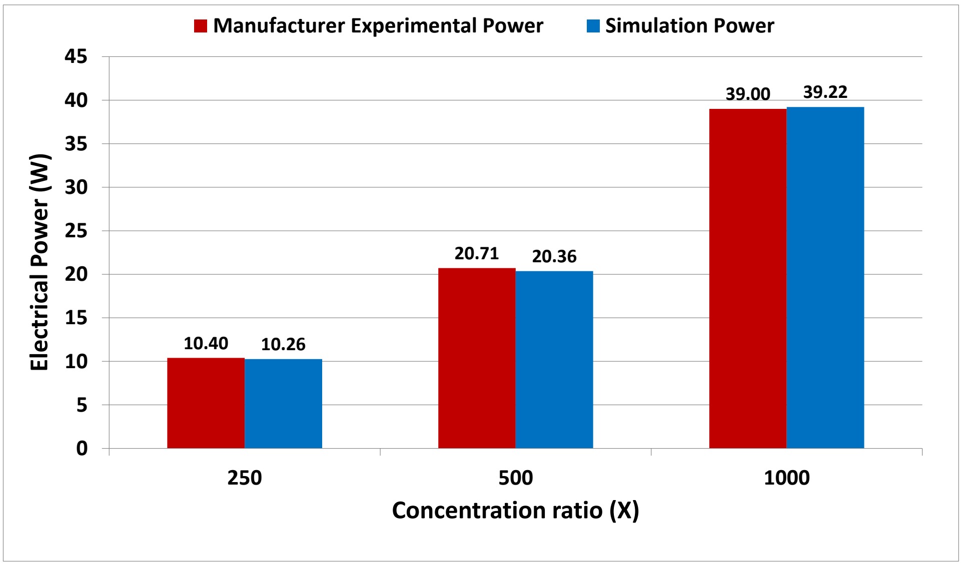

Figure 6.4: Electrical power at CR= 250X, 500X and 1000X and PV temperature of 25°C.

Figure 6.5 shows the electrical efficiency comparison between the manufacturer data and the developed mathematical model at concentration ratios of 250X, 500X and 1000X with PV surface temperature of 25^{o}C. The maximum electrical efficiency is at CR=250X with electrical efficiency of about 41% and minimum at CR=1000X with electrical efficiency of 39%.

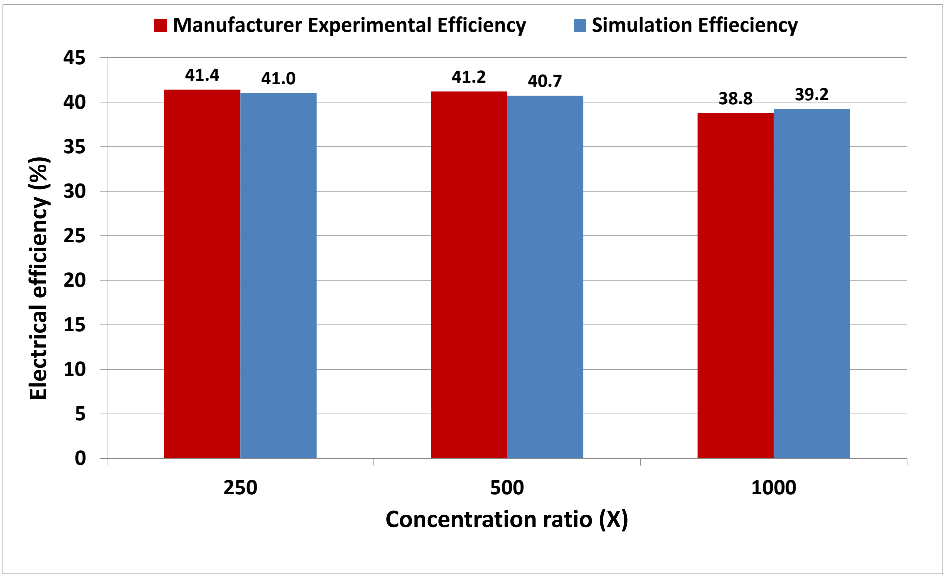

Figure 6.5: Electrical efficiency at CR= 250X, 500X and 1000X and PV temperature 25^{o}C.

The maximum difference between the experimental and the developed model in terms of electrical efficiency is at CR=500X where the predicted value is 1.2% less than experimental output. Table 6.1 compares the experimental and modelled I-V curve parameters: I_{SC}, V_{OC}, I_m, V_m and FF for the concentration ratios of 250X, 500X and 1000X and at PV surface temperature of 25^{o}C.

Table 6.1: I-V curve parameters of experimental and developed model at different CR.

	I_{SC} (A)		V_{OC} (V)		I_m (A)		V_m (V)		FF (%)	
	Exp.	**Model**	**Exp.**	**Model**	**Exp.**	**Model**	**Exp.**	**Model**	**Exp.**	**Model**
250X	3.79	3.79	3.07	3.08	3.71	3.70	2.80	2.77	89.28	87.80
500X	7.58	7.58	3.12	3.13	7.42	7.40	2.79	2.75	87.54	85.77
1000X	15.07	15.07	3.16	3.17	14.77	14.66	2.64	2.67	81.88	81.94

The Table shows that the model is able to accurately predict the I_{SC} and V_{OC} at different concentration ratios. But, there is a small deviation in predicting I_m and V_m leading to a maximum variation in predicting the *FF* of about 2% at CR=500X. The *FF* of the multi-junction solar cell decreased with increasing the applied concentration ratio. For example, the experimental *FF* of the solar cell under concentration ratio of 250X and 1000X are about 88% and 82% respectively.

After testing the capability of the developed model to respond to different input radiation concentration ratios, it was examined under different PV surface temperature and compared against the indoor experimental output data provided by the manufacturer. Figure 6.6 compares the predicted and experimental electrical power in the range of 25^oC-110^oC and at concentration ratio of 500X. It can be noticed that the electrical power decreased as the PV surface temperature increased. The maximum power is at PV surface temperature of 25^oC and the minimum output power is at PV surface temperature of 110^oC. The model is able to predict the electrical power of the solar cell with maximum difference of 1.6% at PV surface temperature of 25^oC i.e. 20.36 W compared to the experimental output power of 20.71 W. In comparison to the conventional crystalline silicon solar cells, the electrical power temperature coefficients of the multi-junction solar cells are much lower i.e. less sensitive to high temperature [202]. For example, the experimental output power at PV surface temperature of 25^oC is 20.71 W while at PV surface temperature of 110^oC is 18.70 W with power reduction of only 2 W i.e. a reduction of about 0.02 $W/^oC$.

Figure 6.7 shows the electrical efficiency of the manufacturer experimental data and the developed model at the same conditions. Similar to the output power, the electrical efficiency also decreases as the PV temperature increases.

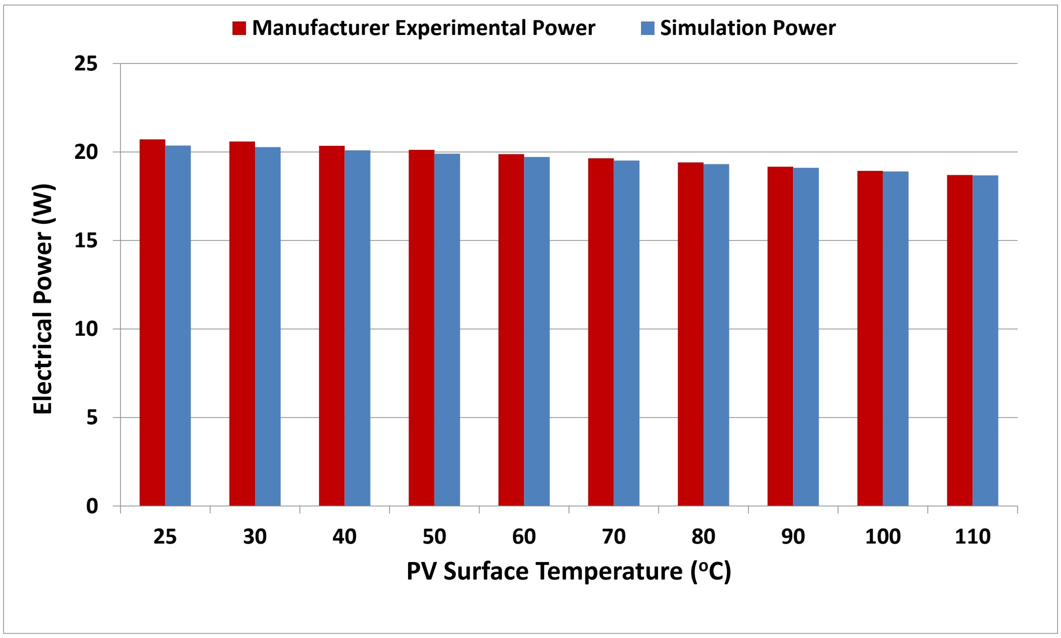

Figure 6.6: Electrical power at CR= 500X and PV temperature 25-110°C.

The maximum difference between the experimental and the developed model in terms of electrical efficiency is at PV temperature of 25°C where the predicted value is about 1.2% less than experimental output.

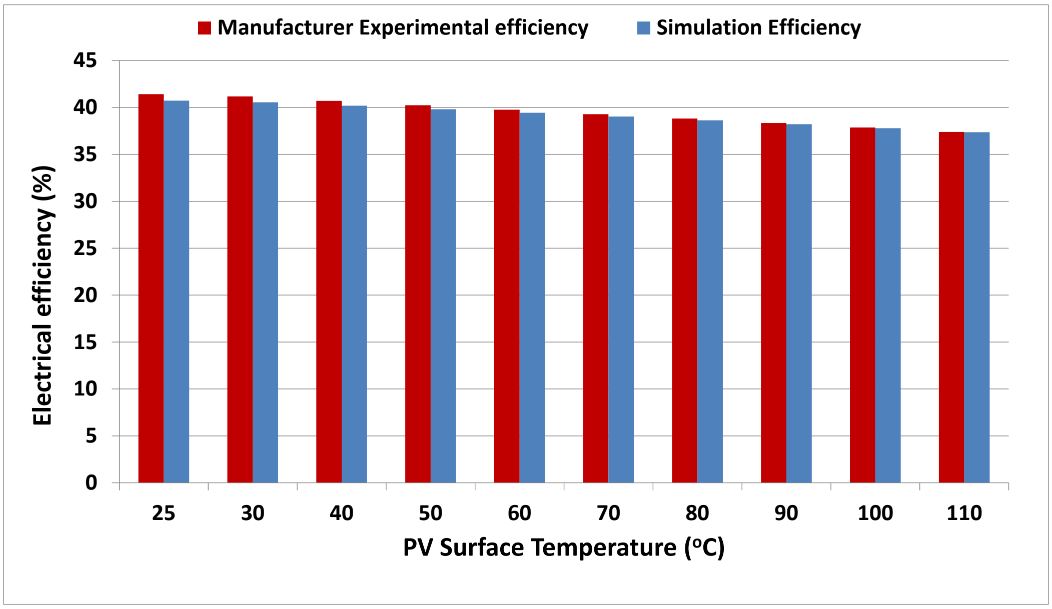

Figure 6.7: Electrical efficiency at CR= 500X and PV temperature 25-110°C.

Figure 6.8 shows the developed model I-V curve responses at different PV temperature i.e. 25-110°C and concentration ratio of 500X. As previously stated, the open circuit voltage decreases as the PV temperature increases which ultimately reduces the cell efficiency. On the other hand, the short circuit current increases with PV surface temperature.

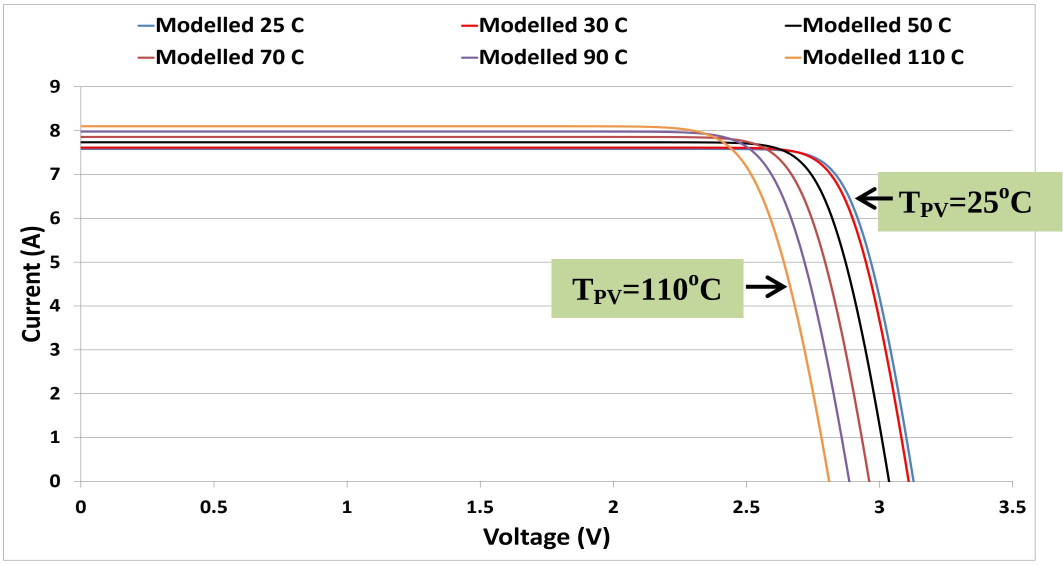

Figure 6.8: Modelled I-V curves at CR= 500X and PV temperature 25-110°C.

Figure 6.9 below demonstrates the negative influence of increasing the PV temperature from 25°C to 110°C on the electrical power output. The maximum power is at PV temperature of 25°C which exceeds 20 W and the minimum power output is at PV surface temperature of 110°C which is around 18 W.

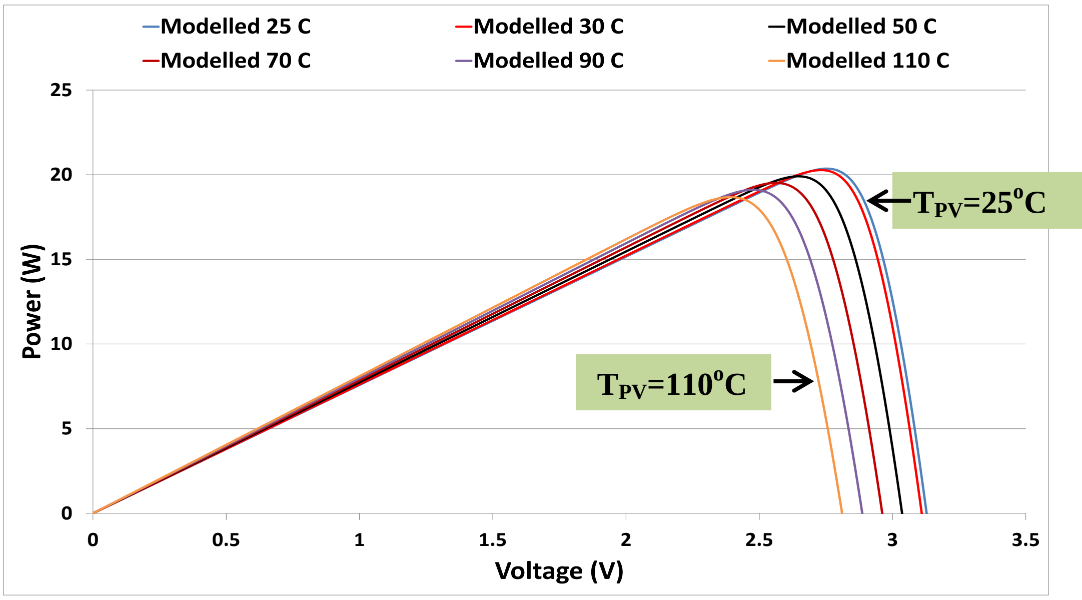

Figure 6.9: Modelled power curves at CR= 500X and PV temperature 25-110°C.

I-V curve parameters are extracted for PV temperature of 25°C, 70°C and 110°C at concentration ratio of 500X to be compared with the manufacturer experimental output as shown in Table 6.2.

Table 6.2: I-V curve parameters of experimental and developed model data at different PV temperature.

	I_{SC} (A)		V_{OC} (V)		P_m (W)		FF (%)	
	Exp.	**Model**	**Exp.**	**Model**	**Exp.**	**Model**	**Exp.**	**Model**
25°C	7.58	7.58	3.12	3.13	20.70	20.35	87.54	85.77
70°C	7.85	7.86	2.93	2.97	19.64	19.52	85.39	83.62
110°C	8.10	8.10	2.76	2.82	18.70	18.68	83.65	81.78

The Table above shows the ability of the model to predict the short circuit current (I_{SC}) and open circuit voltage (V_{OC}) at different PV surface temperature with a small variation. Also, there is a small deviation in predicting the maximum power P_m leading to a maximum variation in predicting the Fill Factor (*FF*) of about 2% at PV surface temperature of 110°C. The Fill Factor of the multi-junction solar cell decreased with increasing the PV surface temperature due to the reduction in output power. For example, the experimental *FF* of the solar cell at PV surface temperature of 25°C and 110°C are about 88% and 84% respectively. Calibration of the developed lumped diode model against the manufacturer experimental data under different PV surface temperature and concentration ratios was implemented to ensure its accuracy. Electrical I-V curve model is a valuable tool to predict the performance of the solar cell which will be used to evaluate the outdoor HCPV electrical output.

6.4. Outdoor experimental electrical characterisation of the developed HCPV system

A single HCPV experimental set-up integrating a multi-junction solar cell was installed and tested outdoor where Solmetric I-V tracer was used to measure the I-V and power curves for electrical performance analysis. The HCPV system was examined under different input solar irradiation and PV surface temperature. Moreover, as the influence of solar cell incident rays illumination uniformity on the electrical efficiency was investigated previously in chapter 4 it will be useful to examine its influence on the I-V curve electrical parameters such as open circuit voltage and maximum power before and after placing the SOE.

6.4.1. Influence of increasing the incident radiation

Figure 6.10 shows the outdoor experimental I-V curves for the multi-junction solar cell under concentration ratios of 43X, 63X, 80X and 114X and at PV surface temperature of 25°C. It can be observed that the short circuit current (I_{SC}) and the maximum power (P_m) increased noticeably by increasing the incident concentration ratio which ultimately increases the electrical efficiency (η_{elect}) of the solar cell. On the other hand, there is a slight increment in open circuit voltage (V_{OC}) as the concentration ratio increases.

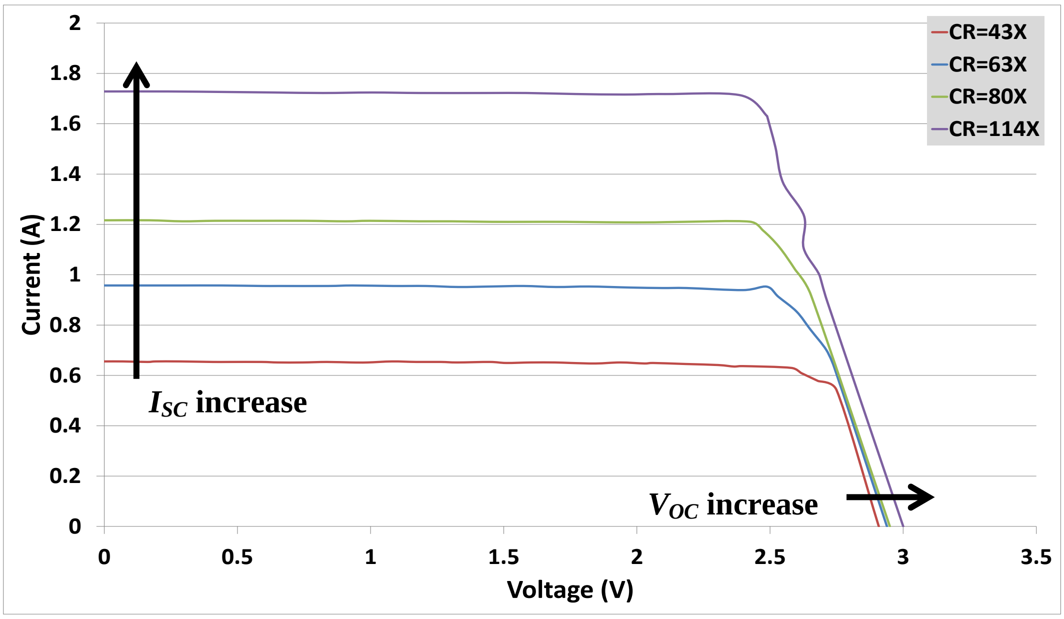

Figure 6.10: Outdoor I-V curves at CR=43X, 63X, 80X and 114X and at PV temperature of 25°C.

Figure 6.11 shows the power curves under concentration ratios of 43X, 63X, 80X and 114X and at PV surface temperature of 25°C. This Figure also shows the increment of the maximum power (P_m) and the open circuit voltage (V_{OC}) as the concentration ratio increases.

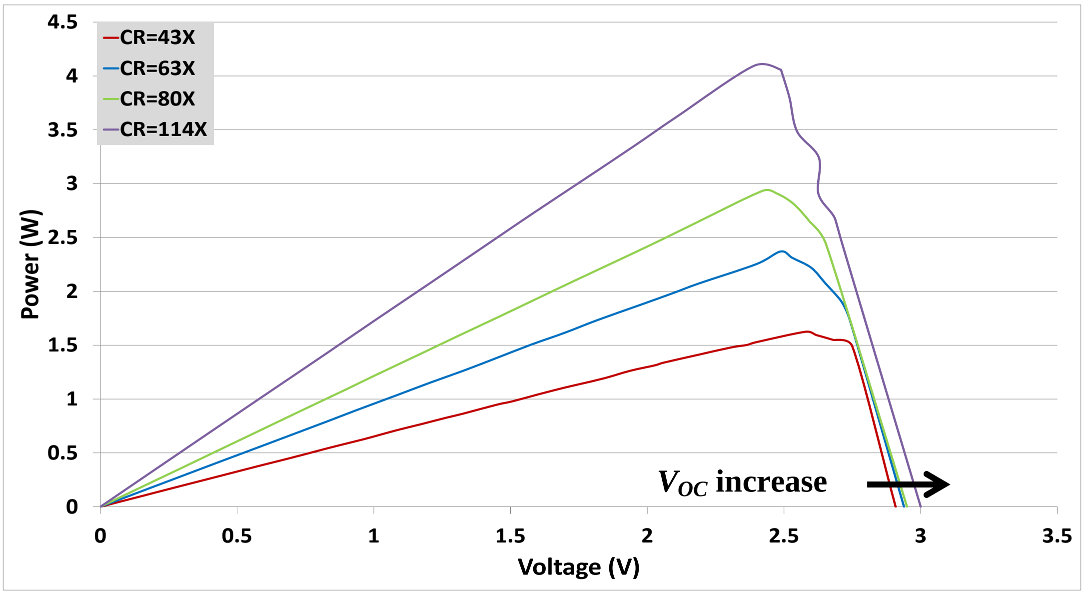

Figure 6.11: Outdoor power curves at CR=43X, 63X, 80X and 114X and at PV temperature of 25°C.

From the above two Figures, the increase in the short circuit current (I_{SC}), open circuit voltage (V_{OC}) and electrical maximum power (P_m) as the concentration ratio increases can be calculated. These I-V curve parameters are compared at different concentration ratios in Table 6.3. It can be noticed that the short circuit current (I_{SC}) increased linearly by increasing the concentration ratio where $I_{SC} \approx 0.01516$ A at CR=1X. On the other hand, open circuit voltage (V_{OC}) increased slightly from 2.91 V at CR=43X to 3.00 at CR=114X. The maximum power increased from 1.6 W at CR=43X to about 4.1 W at CR=114X with increment of more than 150%.

Table 6.3: I-V curve parameters of experimental output at different concentration ratios.

	I_{SC} **(A)**	V_{OC} **(V)**	P_m **(W)**
43X	0.6556	2.9085	1.6249
63X	0.9574	2.9391	2.3700
80X	1.2164	2.9500	2.9347
114X	1.7283	3.0002	4.0938

6.4.2. Influence of increasing the PV surface temperature

Figure 6.12 shows the outdoor experimental I-V curves for the multi-junction solar cell under concentration ratio of 114X and at different PV surface temperature from 25°C to 50°C with a temperature step of 5°C. As shown in the electrical model, the short circuit current (I_{SC}) increased with increasing the PV surface temperature while the open circuit voltage (V_{OC}) and the maximum power (P_m) decreased.

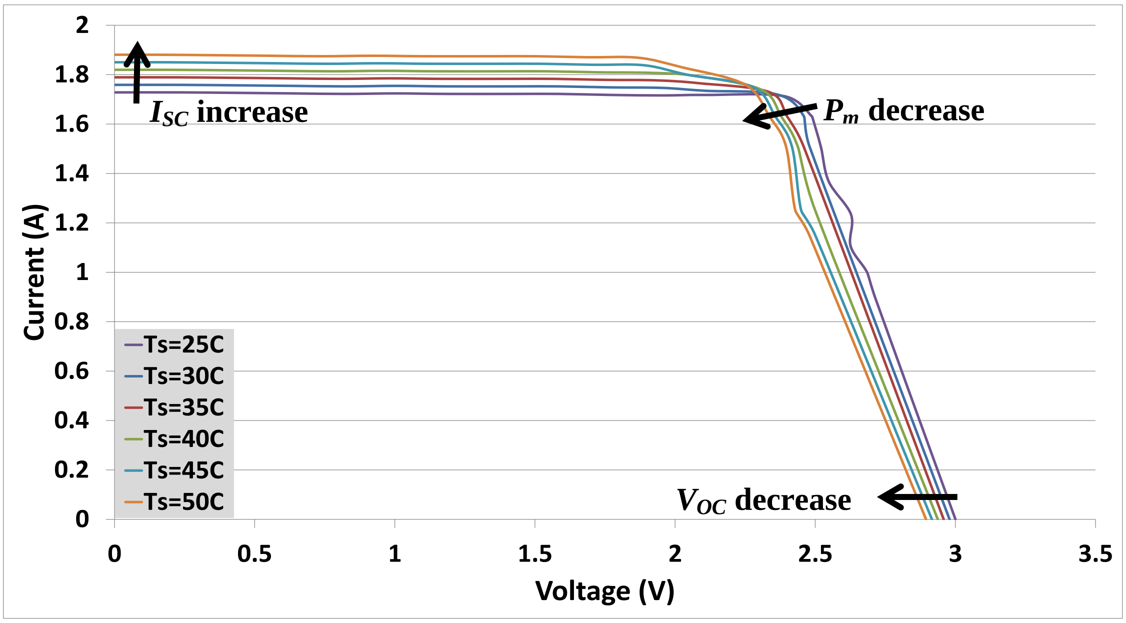

Figure 6.12: Outdoor I-V curves at CR= 114X and PV temperature 25-50°C.

From this Figure, the increase or decrease in the short circuit current (I_{SC}), open circuit voltage (V_{OC}) and electrical efficiency (η_{elect}) for every 1°C increase in the PV surface temperature can be calculated which is called temperature coefficients. These I-V curve parameters at different PV surface temperatures are compared in Table 6.4 and the average temperature coefficients of these parameters are calculated and listed in Table 6.5.

Table 6.4: I-V curve parameters of experimental data at different PV surface Temperature.

	I_{SC} (A)	V_{OC} (V)	η_{elect} (%)
25°C	1.7283	3.0002	35.91
30°C	1.7588	2.9792	35.67
35°C	1.7893	2.9582	35.43
40°C	1.8198	2.9372	35.20
45°C	1.8503	2.9162	34.97
50°C	1.8807	2.8952	34.73

The average temperature coefficient of the electrical efficiency is only -0.047%/°C, which is much lower than silicon PV cells about -0.5%/°C [161,203]. Therefore, the degradation in the electrical efficiency caused by the elevated cell temperature for HCPV integrating triple-junction solar cell is not as significant as that in silicon PV systems. This is an advantage if these solar cells are used in high ambient temperature regions.

Table 6.5: Experimental average temperature coefficients.

	I_{SC} (A/°C)	V_{OC} (V/°C)	η_{elect} (%/°C)
Average temperature coefficient	0.0061	-0.0042	-0.047

Figure 6.13 shows the outdoor experimental power curves for the multi-junction solar cell under concentration ratio of 114X and at different PV surface temperature from 25°C to 50°C with a temperature step of 5°C. It can be seen that the open circuit voltage (V_{OC}) and the maximum power (P_m) decreased with increasing the PV surface temperature which has the same trend as shown in the electrical model. For example, the open circuit voltage (V_{OC}) and the maximum power (P_m) at PV surface temperature of 25°C are 3.00 V and 4.09 W while at PV surface temperature of 50°C they are 2.90 V and 3.96 W respectively.

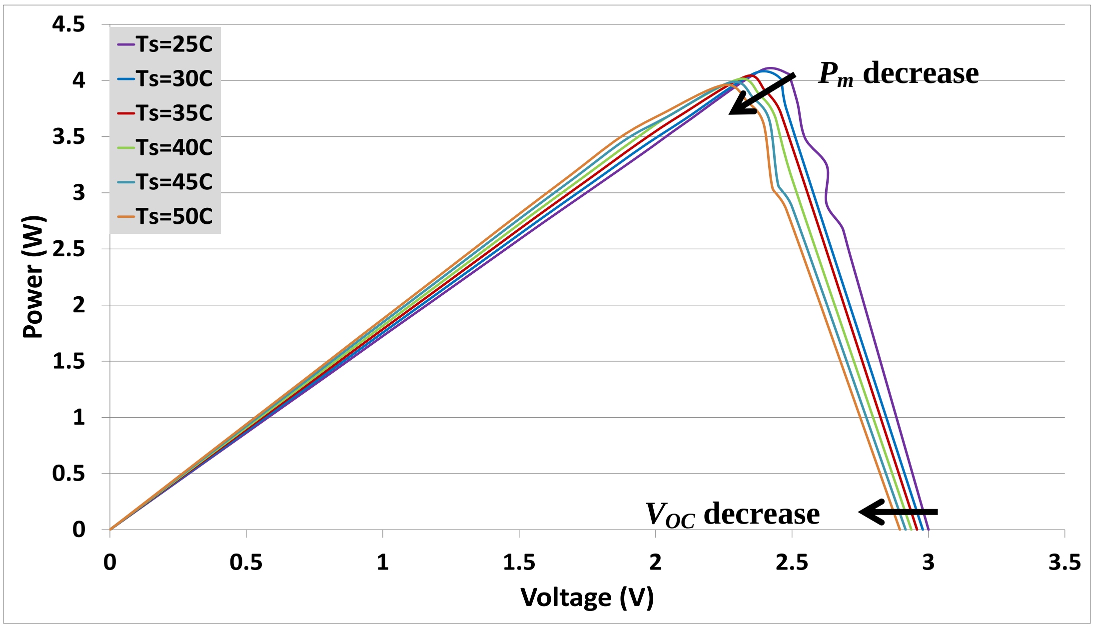

Figure 6.13: Outdoor power curves at CR= 114X and PV temperature 25-50°C.

The HCPV system was examined under different input solar irradiation and PV surface temperature. Increasing the incident radiation is an effective method to increase the power output of the multi-junction solar cell. But, to maintain its optimum electrical performance it is crucial to maintain its surface temperature. The electrical efficiency temperature coefficient is an important parameter that enables the prediction of the solar cell electrical efficiency even without the need to measure the electrical output if the PV surface temperature is known; this aspect will be covered in details in the next chapter.

6.4.3. Influence of non-uniform illumination

The influence of non-uniform incident rays on the I-V curve of the multi-junction solar cell is investigated using the same experimental HCPV set-up. Figure 6.14 shows the outdoor experimental I-V and power curves for the solar cell under concentration ratio of 119X and at PV surface temperature of 25°C with and without secondary optical element (SOE). It can be seen that the open circuit voltage (V_{OC}) and the maximum power (P_m) increased after introducing the SOE which increases the irradiation uniformity on the solar cell surface. The open circuit voltage increased from 2.94 V to 3.00 V while the output power increased from 3.31 W to 3.76 W.

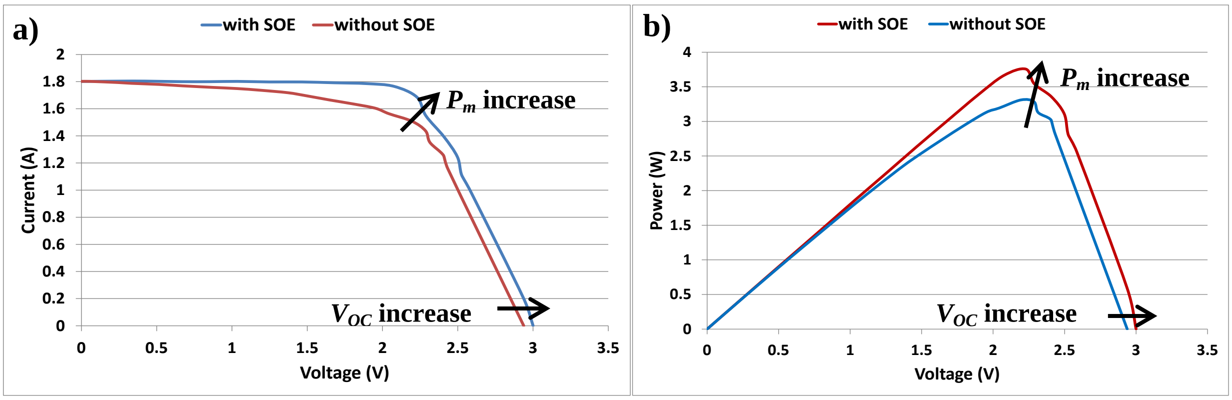

Figure 6.14: a) Outdoor I-V curves; b) power curves at CR=119X and PV temperature of 25°C.

Another case at lower concentration ratio (74X) is illustrated in Figure 6.15 which shows the outdoor experimental I-V curves for the solar cell at PV surface temperature of 25^{o}C with and without SOE.

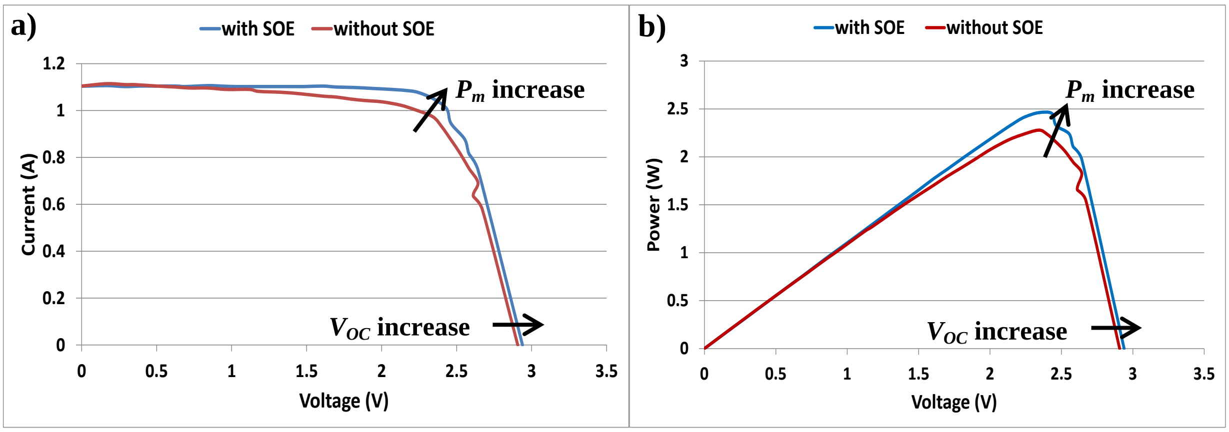

Figure 6.15: a) Outdoor I-V curves; b) power curves at CR=74X and PV temperature of 25^{o}C.

The open circuit voltage (V_{OC}) and the maximum power (P_m) increased after introducing the SOE. The open circuit voltage increased from 2.91 V to 2.94 V while the output power increased from 2.28 W to 2.46 W. Unlike the previous case i.e. at CR=119X the influence of placing the SOE here is smaller. It can be concluded that the positive influence of inserting the SOE on those parameters is more at high concentration ratios where the degree of non-uniformity is higher.

Table 6.6 summarises the influence of introducing the developed SOE to the HCPV in order to improve the incident illumination uniformity on the open circuit voltage (V_{OC}) and electrical maximum power (P_m) for the above two concentration ratios 119X and 74X.

Table 6.6: Influence of introducing SOE on the open circuit voltage and maximum power.

	Without SOE		**With SOE**		**Increment in Power**	**Increment in electrical efficiency**
	V_{OC} (V)	**P_m (W)**	**V_{OC} (V)**	**P_m (W)**	**P_m (%)**	**η_{elect} (%)**
119X	2.94	3.31	3.00	3.76	13.60	13.60
74X	2.91	2.28	2.94	2.46	7.90	7.90

This Table shows that placing the SOE at concentration ratio of 119X would enhance the incident rays uniformity and ultimately increase the output electrical power and efficiency by about 14%. Moreover, at lower concentration ratio i.e. 74X where the negative influence of degree of non-uniformity is less, the electrical power and efficiency was increased by about 8%.

6.4.4. Outdoor experimental and developed electrical model I-V curve comparison

In this section the predicted I-V curves of the developed electrical model and the outdoor experimental HCPV with SOE will be compared. Figure 6.16 shows the two I-V curves at concentration ratio of 43X, 63X, 80X and 114X at PV surface temperature of 25^{o}C. Although the SOE is introduced to the HCPV system, when compared against the mathematical I-V curve the effects of non-uniform illumination including reduction in open circuit voltage (V_{OC}) and maximum power (P_m) are observed. Those effects become clearer at higher concentration ratios where the degree of non-uniformity is higher especially reduction in maximum power (P_m). For example, the maximum power (P_m) difference between the model and experimental output at concentration ratio of 43X is 0.1 W while it is about 0.6 W at concentration ratio of 114X. It can be concluded that as the concentration ratio of the HCPV system increases, it becomes more and more difficult to maintain uniformity of the incident flux on the solar cell. Moreover, as the concentration ratio increases the series resistance increases which limits the amount of output current. The negative influence of the series resistance can be observed on the open circuit voltage (V_{OC}) where the I-V curve slope is increased by increasing the concentration ratio as shown in Figure 6.16d.

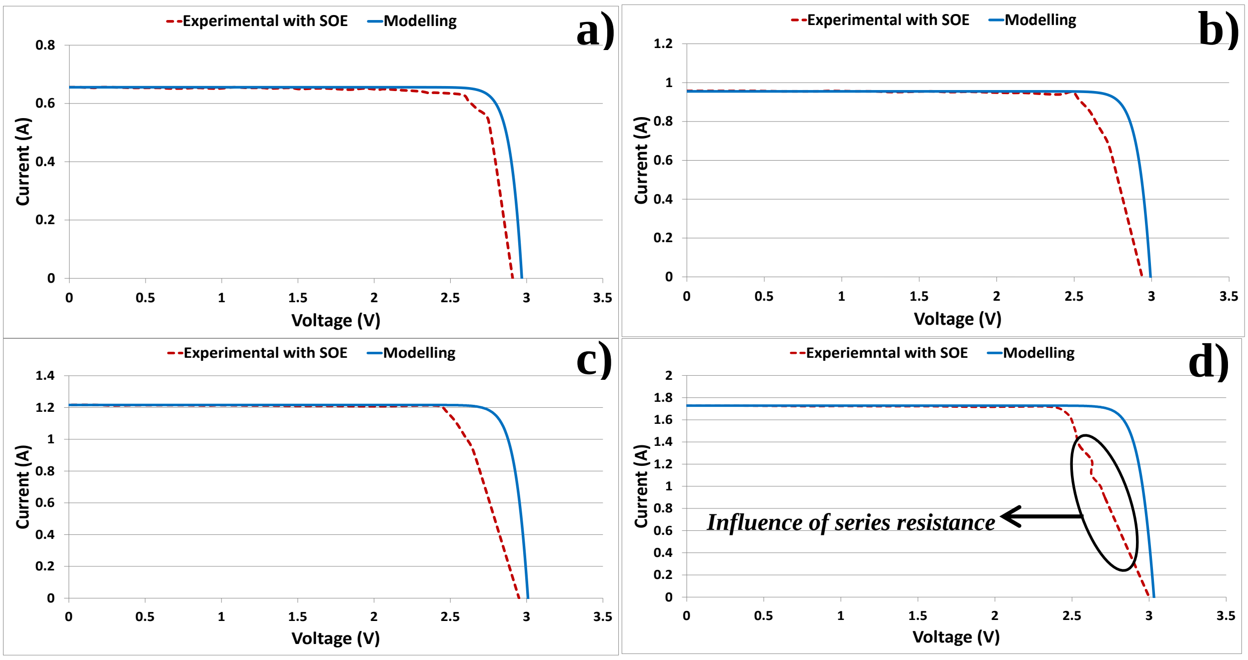

Figure 6.16: Experimental with SOE and modelled I-V curves comparison at a) CR=43X; b) 63X; c) 80X; and d) 114X and at PV temperature of 25^{o}C.

Figure 6.17 shows the developed model and the outdoor experimental HCPV with SOE power curves at concentration ratio of 43X, 63X, 80X and 114X and at PV surface temperature of 25^{o}C. The negative influence of non-uniform illumination on the output power is minimal at CR=43X while it increases with the concentration ratio.

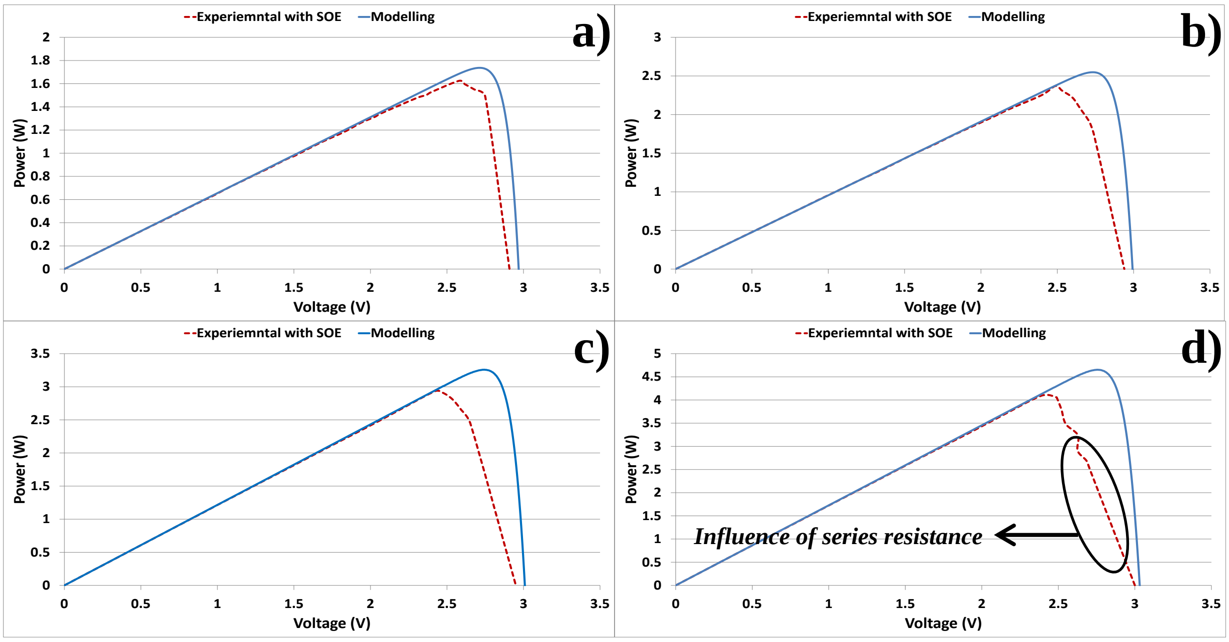

Figure 6.17: Experimental with SOE and modelled power curves comparison at a) CR=43X; b) 63X; c) 80X; and d) 114X and at PV temperature of 25^{o}C.

Table 6.7 compares the experimental and model open circuit voltage (V_{OC}), electrical maximum power (P_m) and electrical efficiency outputs at concentration ratio of 43X, 63X, 80X and 114X and PV surface temperature of 25°C. Both experimental and model outputs show that open circuit voltage (V_{OC}) increased slightly with the concentration ratios. Moreover, the maximum power (P_m) increases linearly with the applied concentration ratio. The experimental electrical efficiency decreased with increasing the concentration ratio from 37.79% at CR=43X to 35.91% at highest concentration ratio i.e. 114X. On the other hand, the predicted electrical efficiency using the model, which assumes uniform incident illumination, increases with the concentration ratio. It increases from 40.39% at CR=43X to 40.82% at CR=114X.

Table 6.7: Experimental and model V_{OC}, P_m and η_{elect} at concentration ratio of 43X, 63X, 80X and 114X and PV surface temperature of 25°C.

	Experimental		**Model**		**Experimental efficiency**	**Model efficiency**
	V_{OC} (V)	**P_m (W)**	**V_{OC} (V)**	**P_m (W)**	**η_{elect} (%)**	**η_{elect} (%)**
43X	2.9085	1.6249	2.9700	1.7370	37.79	40.39
63X	2.9391	2.3700	2.9950	2.5480	37.62	40.45
80X	2.9500	2.9347	3.0100	3.2580	36.68	40.73
114X	3.0002	4.0938	3.0350	4.6530	35.91	40.82

Figure 6.18 compares the electrical efficiency of the experimental and modelling under concentration ratio of 43X, 63X, 80X and 114X and at PV surface temperature of 25°C. The average experimental electrical efficiency of the four different concentration ratios is 37% while the average predicted efficiency is 40.60%. The experimental average efficiency is lower than that predicted by the model by less than 10%.

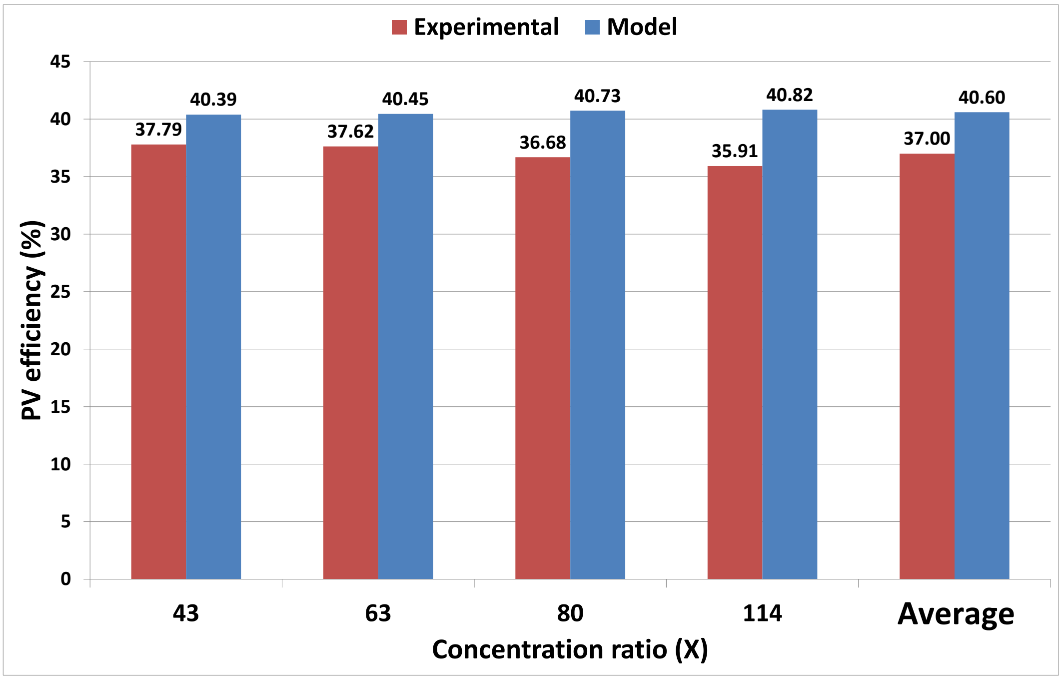

Figure 6.18: Experimental with SOE and modelled electrical efficiency comparison at CR of 43X, 63X, 80X and 114X and at PV temperature of 25°C.

6.5. Summary

This chapter described the development of a mathematical model able to predict the electrical performance of the solar cell by generating I-V curve under different solar concentration ratios and PV surface temperatures. The model was calibrated against the manufacturer indoor experimental data and the needed empirical parameters were evaluated. It was able to respond to the variation of the concentration ratio with maximum difference in electrical power of 1.7% and respond to the variation of the PV surface temperature with maximum difference in electrical power of 1.6%.

The I-V curve parameters of the MJ solar cell were examined experimentally under different concentration ratios and PV temperatures. It was found that input irradiance is the most influencing parameter where the electrical power increased more than 150% when the concentration ratio increased from 43X to 114X. Moreover, the influence of non-uniform incident rays on the multi-junction solar cell output was investigated. It was found that maximum power (P_m) and open circuit voltage (V_{OC}) are both improved after placing the SOE with electrical efficiency increment of about 14% and 8% at concentration ratio of 119X and 74X respectively.

The outdoor measured I-V curve of the HCPV with SOE was compared with the developed model output at different concentration ratios. The experimental average efficiency was about 10% lower than the model average efficiency.

A technique was established in this chapter able to predict the multi-junction solar cell performance using I-V curve electrical model. Moreover, another technique using electrical efficiency temperature coefficient was introduced here but will be covered in more details in the next chapter. Both techniques need to have the PV temperature as an input parameter. Therefore, in the next chapter a thermal model will be developed using Finite Element analysis (FEA) and Computational Fluid Dynamic (CFD) to evaluate the PV surface temperature under different solar irradiation and ambient conditions.

CHAPTER 7

Thermal modelling of a multi-junction solar cell based HCPV/T and indoor/outdoor characterisation

7.1. Introduction

This chapter describes the development of a 3-D thermal model using Finite element analysis (FEA) able to predict the PV temperature under different concentration ratios taking into account the ambient conditions such as temperature and wind speed. Moreover, passive and active cooling systems will be developed to study the capability of these methods to maintain the 1 cm^2 multi-junction (MJ) solar cell temperature within the operational limit in harsh environment like Saudi Arabia where the ambient temperature reaches up to 50 ^oC in summer time. Furthermore, the feasibility of utilising the output thermal energy absorbed by the coolant in case of water active cooling for different thermal applications will be analysed. Also, the annual yield total power i.e. electrical and thermal of the HCPV/T system will be calculated for the case of Saudi Arabia. Finally, indoor and outdoor thermal characterisation of the HCPV/T will be undertaken for validation purpose.

7.2. High concentrator PV cooling methods

High concentration will elevate PV cell surface temperature which reduces the electrical efficiency and power output from the cell and ultimately degrades its life [25]. Therefore, effective cooling is necessary to dissipate the heat from the solar cell and maintain the highest performance at all conditions.

Passive and active cooling are the two main methods for removing heat from high-illumination photovoltaic cells. Active cooling is more effective in reducing the PV surface temperature and can enable utilisation of the removed heat by the cooling fluid for different thermal applications [39].

Various passive and active cooling methods incorporated with a single HCPV system have been described in the literature to maintain the electrical performance and keep the cell temperature below the operational limit. According to Royne et al. passive cooling can be adequate for single cell geometries for concentration ratio up to 1000 suns since there is a large area available behind the cell for a heat sink [38]. However, more than one high concentration study concluded that passive cooling is not dissipating enough heat from the cell even when a very large heat sink is used especially in high ambient temperatures [162,173,204]. Therefore, more investigation has to be undertaken to find the optimum solution for each case of HCPV system.

7.3. Thermal model development of a high concentrator multi-junction PV

Thermal simulation using FEA is a valuable tool to predict the solar cell's operating temperature and cooling requirements for a range of parameters such as ambient temperature, wind speed, solar irradiation, inlet fluid temperature and inlet fluid volume flow rate. It improves the prediction accuracy of the electrical and thermal behaviour of multi-junction solar cells and the output data can be utilised to optimise the HCPV/T systems. A brief literature review on thermal modelling of high concentrator multi-junction PV can be found in Appendix F. In the current study, the focus was on studying the thermal behaviour of the triple-junction solar cell based HCPV/T system at high ambient temperature regions where it can reach 50 ^{o}C using COMSOL multi-physics software.

7.3.1. Thermal model methodology

AZURSPACE III-V multi-junction PV cell type 3C42A made of GaInP-GaInAs-Ge and area of 0.01 x 0.01 m^2 (0.0001 m^2) with electrical efficiency of 41.2% under concentration ratio of 500X (X = 1000 W/m^2) and temperature of 25 ^{o}C [90] was used in this work. Figure 7.1 shows a schematic diagram of the multi-junction solar cell assembly (0.0316x0.0296m^2)

which consists of the solar cell, two copper layers, a ceramic layer, two by-pass diodes, two electrical terminals and two side solders.

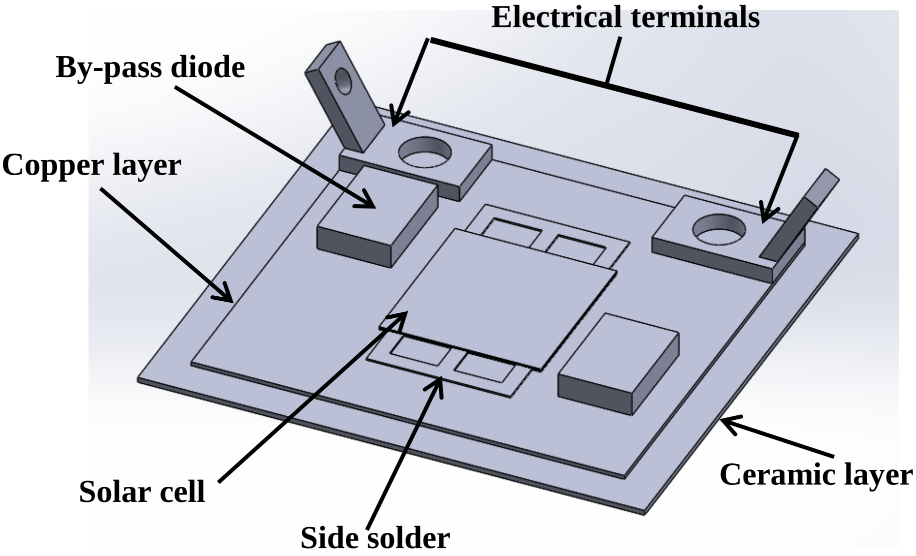

Figure 7.1: Schematic diagram of CPV assembly.

The input solar irradiation flux (q_{in}) on the surface of the PV cell can be calculated using the following equation:

$$q_{in} = q_{irra} \times GCR \times \eta_{opt} \tag{7.1}$$

where q_{irra} is the solar irradiation flux above the Fresnel lens in (W/m^2), GCR is the geometrical concentration ratio of the HCPV optical system and η_{opt} is the optical efficiency. The product of GCR and η_{opt} is the applied concentration ratio (CR).

Although the maximum operation temperature of this solar cell is 110 ^{o}C [90], the typical operational temperature range is between 25 ^{o}C and 80 °C which has to be maintained under very high concentration ratios. The solar radiation energy received by the PV cell is partially used to generate electricity and the rest is converted to heat. The amount of input energy that is converted to heat (q_{heat}) can be calculated using equation 7.2 [41,155,161,176,205]:

$$q_{heat} = q_{in} \times (1 - \eta_{elect}) \tag{7.2}$$

where q_{in} is solar radiation flux on the surface of the PV cell in (W/m^2) and η_{elect} is the cell electrical efficiency given as a function of thermal coefficient ($\beta_{thermal}$ = 0.047%), efficiency at reference temperature (η_{Tref} = 41.2%), average PV temperature (T_{PV}) and reference temperature (T_{ref}=298.15K) as shown in equation 7.3 [41,155]:

$$\eta_{elect} = \eta_{Tref} - \left[\beta_{thermal}\left(T_{PV} - T_{ref}\right)\right] \tag{7.3}$$

At each iteration in the thermal simulation, the PV cell efficiency (η_{elect}) is calculated by equation 7.3 with the user input values for $\beta_{thermal}$, η_{Tref}, T_{ref} and from COMSOL solved value for the cell temperature, T_{PV}.

7.3.2. Theory and governing equations

All three modes of heat transfer conduction, convection and radiation are needed when analysing the thermal performance of HCPV assembly. Conjugate heat transfer physical model in COMSOL has the advantage of combining both heat transfer in solids and fluids at the same time. Heat is transferred within the multi-junction solar cell solid layers by conduction while some heat is transferred to the surroundings by both natural and forced convection. Also, some heat is lost to the environment from the assembly surfaces by radiation.

Steady state heat conduction within the PV assembly to the top surface of the cooling channel is given by the Fourier’s law of heat conduction [155,173,203,206]:

$$Q_{cond} = -k \cdot A \cdot \frac{dT}{dx} \tag{7.4}$$

Where Q_{cond} is the conduction heat-transfer rate (W), A is cross-sectional area (m^2), k is the thermal conductivity of the material (W/ (m.K)) and dT/dx is the temperature gradient.

The solar energy that is converted to heat will be dissipated from the HCPV assembly to the environment or collected by the cooling system to be used in another application. The heat which is transferred either by natural or forced convection is given by [155,173,203,206]:

$$Q_{conv} = h \cdot A \cdot \Delta T \tag{7.5}$$

Where Q_{conv} is the convection heat-transfer rate (W), h is convection (natural or forced) heat transfer coefficient (W/m^2.K), A is cross-sectional area (m^2) and ΔT is temperature difference between fluid and surface (K).

The heat lost to the environment due to radiation is given by [155,173,203,206]:

$$Q_{radi} = \varepsilon \cdot \sigma \cdot A \cdot (T_{surf}^4 - T_{amb}^4) \tag{7.6}$$

Where Q_{rad} is the radiation heat-transfer rate (W), ε is the emissivity of the material, σ is Stefan Boltzmann constant and A is area of the object (m^2), T_{surf} is the surface temperature (K) and T_{amb} is the ambient temperature (K).

The Conjugate heat transfer physical model also solves numerically the heat transfer equations together with Navier-Stokes equations. For incompressible flow, the continuity (7.7) and momentum (7.8) equations are listed below [155]:

$$\nabla \cdot (\rho u) = 0 \tag{7.7}$$

$$\rho u \cdot \nabla u = -\nabla p + \nabla \cdot (\mu(\nabla u + (\nabla u)^T)) \tag{7.8}$$

The conduction-convection equation is also solved for the heat transfer in the flowing cooling water, which is shown in equation 7.9 [155,203,206]:

$$\rho \cdot C_p \cdot u \cdot \nabla T = \nabla \cdot (k \nabla T) \tag{7.9}$$

Where ρ is the density of the fluid, u is the velocity of the fluid, p is the pressure, μ is the dynamic viscosity, C_p is the heat capacity of the fluid at constant pressure and T is the fluid temperature. Turbulent flow may dissipate heat more effectively than laminar flow but it causes pressure drop in the cooling channel which ultimately leads to high power consumption to run the pump i.e. more costly cooling system [38,155,173]. This aspect is crucial during the design and selection of the cooling system as it is not feasible to consume high amounts of power produced by the HCPV system for cooling. In the current study, the fully developed water flow is laminar i.e. Reynolds number (*Re*) < 2300; therefore conjugate heat transfer laminar flow model was chosen for the simulation. Reynolds number here was calculated based on the hydraulic diameter of the rectangular cooling channel.

7.3.3. Development of heat sinks and cooling channel for HCPV

A single HCPV under high concentration ratios system is thermally modelled under passive and active cooling. For passive cooling analysis, four Aluminium heat sink geometries were designed using SolidWorks and then exported to COMSOL for thermal simulation. These designs were inspired by CPVs and electronic component heat sinks in the literature and the market which need to be compact, low cost and light weight [207,208]. For active cooling analysis, Aluminium cooling channel was developed for water to flow in one direction to cool the PV. The criteria for assessing those developed heat sinks and active water cooling channel will be based on the ability to maintain the 1cm^2 PV average temperature within the operating limit specified by the manufacturer i.e. 25-80^{o}C and the ability to maintain high electrical efficiency under the worst climate scenario in Saudi Arabia i.e. ambient temperature of 50^{o}C, direct normal irradiance of 1000 W/m^2 and wind speed of 0 m/s [10,22,209].

7.3.3.1. Passive cooling heat sink geometries

Passive cooling can be a better cooling option for HCPV especially in remote areas where water resources are limited and periodic maintenance for the cooling system is costly. In this work, four heat sinks namely Angular Fins Heat Sink (AFHS), Round Pins Heat Sink (RPHS), Straight Fins Heat Sink (SFHS) and Extended Straight Fins Heat Sink (ESFHS) were developed to be investigated for cooling CPV cells at high concentration ratio and at different ambient temperatures.

Angular Fins Heat Sink (AFHS)

AFHS made of Aluminium is attached to the bottom of PV assembly to dissipate the heat load. AFHS consists of 0.09x0.09m^2 base with 0.002m thickness and 9 angular fins as shown in Figure 7.2a. Each fin is 0.09m long and 0.001m thick with 20^o spacing angle between the angular fins. The length of the fins from the base is varied from maximum of 0.035m to minimum of 0.025m.

Round Pins Heat Sink (RPHS)

Aluminium RPHS is attached underneath the solar cell (see Figure 7.2b) to dissipate heat consisting of 0.09x0.09m^2 base with 0.002m thickness and 144 round pins. Each round pin is 0.05m high and 0.005m diameter with 0.0025m spacing distance between all the round pins in all directions.

Straight Fins Heat Sink (SFHS)

Aluminium SFHS consists of 0.09x0.09m^2 base with 0.002m thickness and 30 straight fins. Each fin is 0.09m long, 0.05m high and 0.001m thick with 0.002m spacing distance between each straight fin as shown in Figure 7.2c.

Extended Straight Fins Heat Sink (ESFHS)

ESFHS has the same geometry as SFHS but the fins height is extended to 0.1m and the number of the fins increased to 44. Each fin is 0.001m thick with 0.001m spacing distance between each straight fin as shown in Figure 7.2d.

7.3.3.2. Active cooling channel geometry

Figure 7.3 shows the solar cell and the cooling channel assembly with the dimensions in m which was described in details in chapter 3. The calculated hydraulic diameter of this cooling channel is 1.11x10^{-2} m i.e. 1.1 cm.

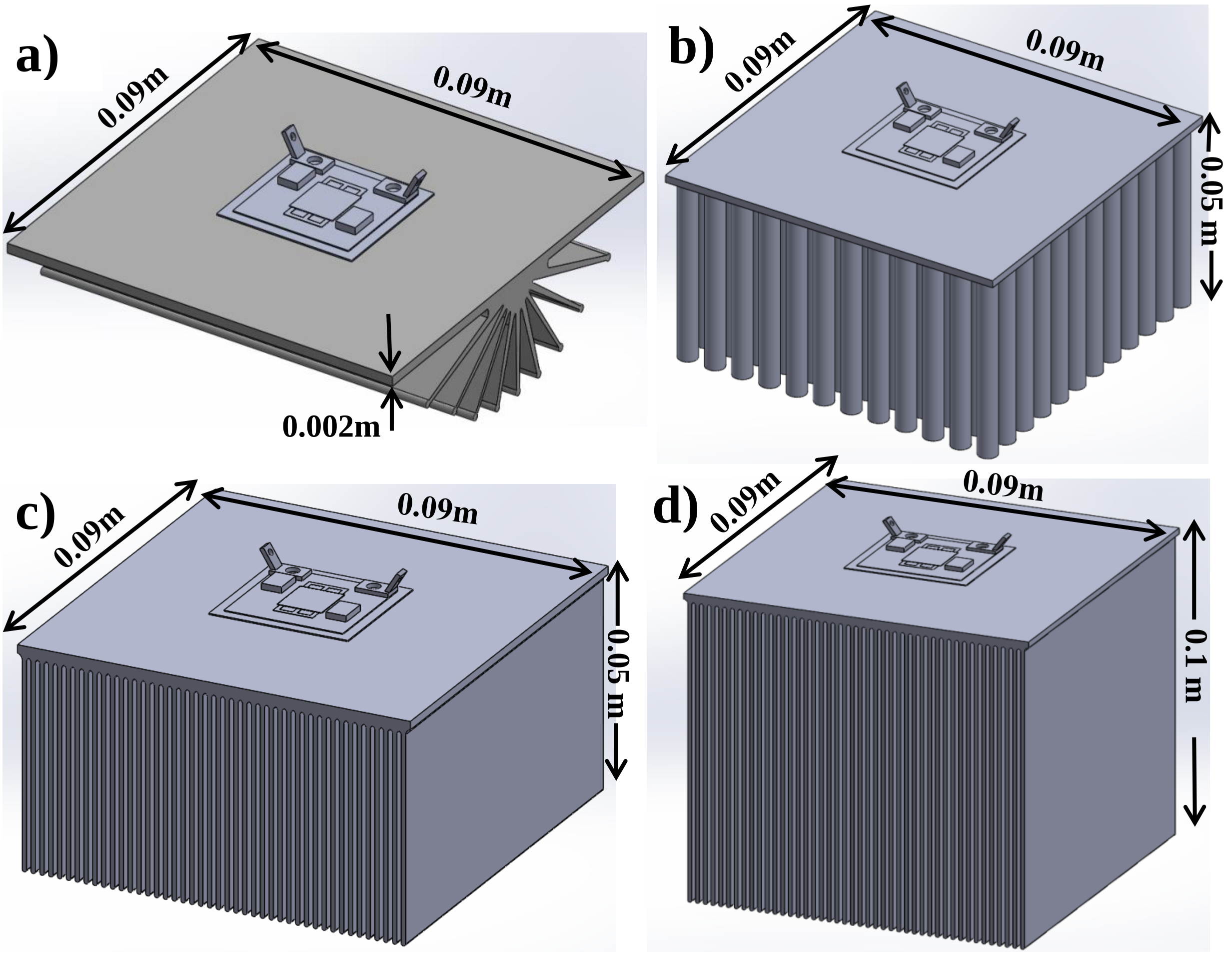

Figure 7.2: Schematic diagram of a) AFHS; b) RPHS; c) SFHS; d) ESFH.

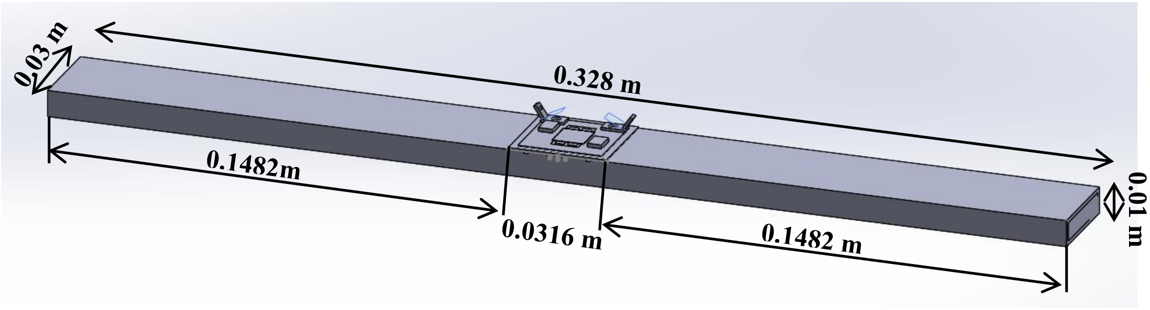

Figure 7.3: PV assembly attached to the water cooling channel.

Figure 7.4a shows the component drawing of a single HCPV/T system including the Fresnel lens, solar cell and cooling channel while 7.4b shows the schematic diagram of the cooling channel where water with an inlet temperature and inlet mass flow rate is passed through a tube with a rectangular cross-section where a constant heat flux was applied. The heat flux is used to represent the heat transferred from the concentrated PV cell [176].

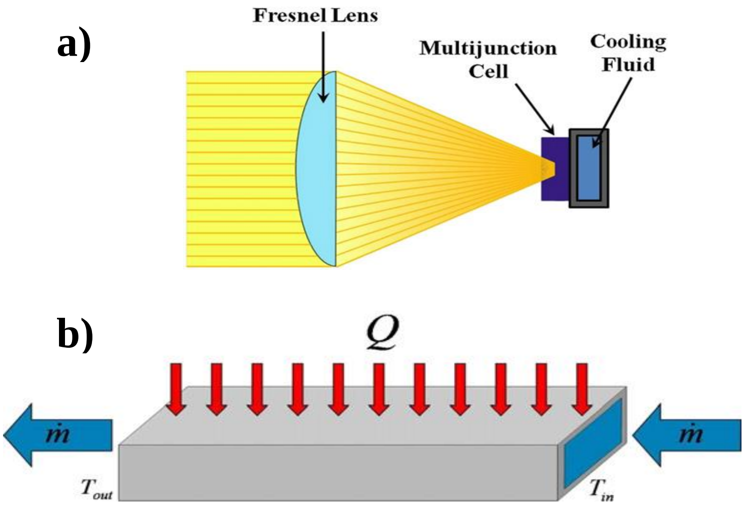

Figure 7.4: a) Component drawing of a single HCPV/T system; b) cooling simulation schematic [176].

7.3.4. Thermal model boundary conditions and assumptions

Figure 7.5 shows a front view of the PV assembly including the solar cell and Al_2O_3 Ceramic sandwiched between two layers of Copper and beneath that there is a thermal paste bonding the heat sink/cooling channel to the PV assembly. Moreover, the PV assembly includes two electrical terminals, two by-pass diodes and two side-solders which were considered in the thermal model. According to Chou et al. [210] and Theristis et al. [206] the triple-junction solar cell can be modelled as one homogeneous entity Germanium cell (Ge) since the top (GaInP) and middle (GaInAs) subcells are much thinner than the bottom (Ge) subcell and hence they would not affect the thermal model.

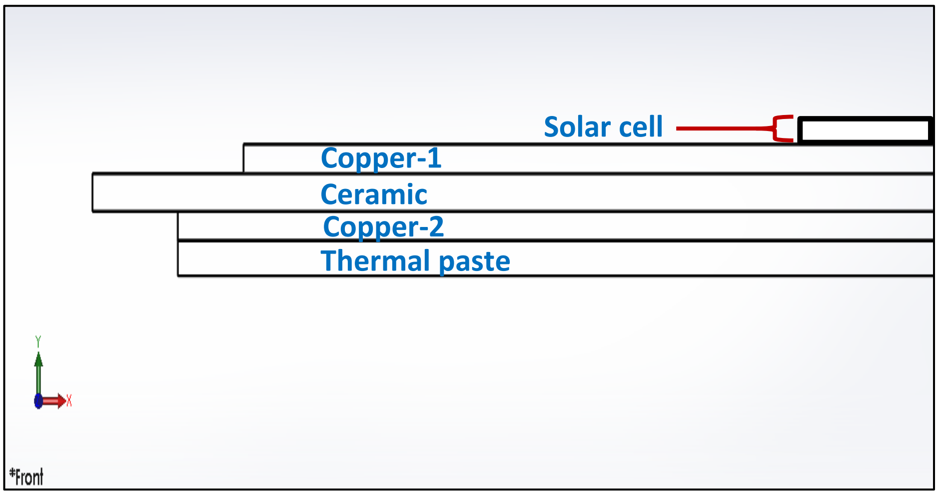

Figure 7.5: Schematic diagram of PV assembly layers.

The mechanical dimensions of each layer of the PV assembly [155,206] and the thermo-physical properties of the PV assembly components [155,173,206,211] are presented in Table 7.1 and 7.2 respectively.

Table 7.1: PV assembly dimensions.

Layer	**Length (m)**	**Width (m)**	**Thickness (m)**
Solar cell	0.01	0.01	0.000190
Copper-1	0.027	0.025	0.000250
Al_2O_3 Ceramic	0.0316	0.0296	0.000320
Copper-2	0.029	0.027	0.000250
Thermal paste	0.029	0.027	0.0003

Table 7.2: Thermo-physical properties of PV assembly components.

Material	**Thermal Conductivity** [W/mK]	**Heat Capacity** [J/kgK]	**Density** [kg/m^3]	**Emissivity (ε)**
Germanium	60	320	5323	0.90
Copper	400	385	8700	0.05
Al_2O_3 Ceramic	30	900	3900	0.75
Thermal paste	3	700	3000	0.00
Aluminium	160	900	2700	0.09
Terminal Brass	151	380	8800	0.03
Side Solder	50	150	9000	0.03
By-pass diode	130	700	2329	0.60

In order to model the above 3-D thermal cases, several assumptions, boundary conditions and settings were used [155,203,206] as follows:

1. The direct solar radiation (q_{irra}) intensity is considered to be 1000 W/m^2 and it was applied uniformly on the Fresnel lens top surface.
2. The geometrical concentration ratio (GCR) of the Fresnel lens is 625X and the optical efficiency (η_{opt}) is 80% i.e. the applied concentration ratio CR is 500X.
3. Therefore, the heat flux (q_{in}) is 500,000 W/m^2 and the input power (Q_{in}) in W is the product of the heat flux (q_{in}) and the receiver area A_r = 0.0001 m^2 which equals to 50 W.

4. All solar irradiation power that is not converted to electricity will be developed into heat as per equation 7.2.
5. Range of ambient temperature to be examined: 25°C, 30°C, 35°C, 40°C, 45°C, 50°C.
6. The wind speed is assumed to be 0 m/s.
7. The inlet cooling water temperature for active cooling case is uniform and assumed to be 25°C. Also, the water velocity inside the cooling channel is set to 0.01 m/s which is equivalent to the volume flow rate of about $1.88x10^{-6}$ m^{3}/s and mass flow rate of about 0.00189 kg/s.
8. The inlet cooling water flow is fully developed, laminar and steady flow (Figure 7.6).
9. No slip boundary condition is applied for the internal surfaces of the cooling water channel (Figure 7.6).
10. The cooling channel is not inclined i.e. in horizontal position.
11. The buoyancy force of the cooling water is considered in this CFD model by adding volume force in y-axis to the water domain.
12. Natural convection was applied to all free surfaces i.e. top, sides and bottom.
13. Surface to ambient radiation was also applied to all free surfaces.
14. The initial temperature of all surfaces is set to 25°C.

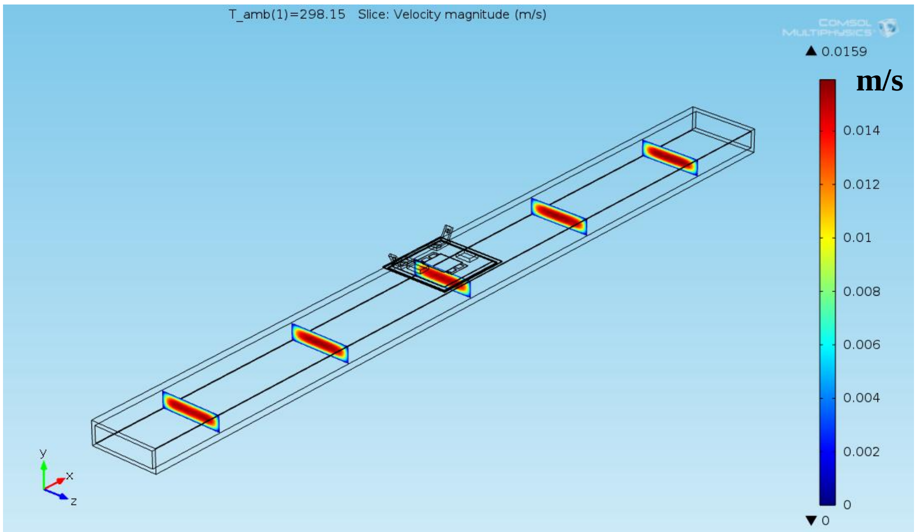

Figure 7.6: Water profile in the cooling channel (m/s).

7.3.5. Thermal model meshing and solver

For the four heat sink geometries i.e. passive cooling cases (AFHS, RPHS, SFHS and ESFH), the assembly (heat sink and the PV) was meshed using the physics controlled mesh sequence in COMSOL. A fine mesh setting with 207,130 elements over the whole assembly was used with minimum and maximum element sizes of 0.0009 and 0.0072 m respectively. A mesh independency study was conducted by gradually increasing the number of elements starting with coarse mesh with 59,820 elements until the PV temperature difference was minimised to less than 1 ^{o}C. Moreover, the relative tolerance of the solver was decreased from 0.001 as a default setting to 0.00001 to examine any difference in the final solution but no change was noticed. The average computational time that is taken to solve each CPV assembly thermal simulation at different ambient temperature was about 2.5 hours including the mesh generation time.

For the cooling channel i.e. active cooling case, three different meshing sizes were chosen for the assembly. The internal wall of the cooling channel where the no slip boundary condition was applied, finer fluid dynamics mesh was selected with minimum and maximum element sizes of 0.00012 and 0.00108m respectively. In addition, the water domain was meshed using fine fluid dynamics mesh where the minimum and maximum element sizes were 0.00029 and 0.00155 m correspondingly. Finally, the remaining geometry including the cooling channel and the PV assembly were meshed utilising finer general physics mesh as the minimum and maximum sizes are 0.00131 and 0.018 m respectively. A mesh independency study was also conducted here using the same technique above by gradually increasing the number of elements starting with coarse mesh until the PV temperature difference was minimised to less than 1 ^{o}C. Moreover, the influence of relative tolerance of the solver was also examined by decreasing its value. The average computational time that is taken to solve the thermal simulation at different ambient temperature is about 4 hours including the mesh generation time.

The simulation ran using GMRES (Generalized Minimum Residual) which is an iterative solver to solve general linear systems. Unlike direct solvers, iterative methods approach the solution gradually rather than in one large computational step. Consequently, when solving a problem with an iterative method, the error estimate in the solution decrease with the number of iterations which can be observed [212].

7.4. Thermal and electrical results of the thermal simulation

In order to evaluate the level of challenge, the scenario of the PV assembly (0.0316x0.0296 m^2) with no cooling was simulated. Figure 7.7 shows that the maximum cell temperature can reach 750 °C at ambient temperature of 50 °C if no cooling is applied.

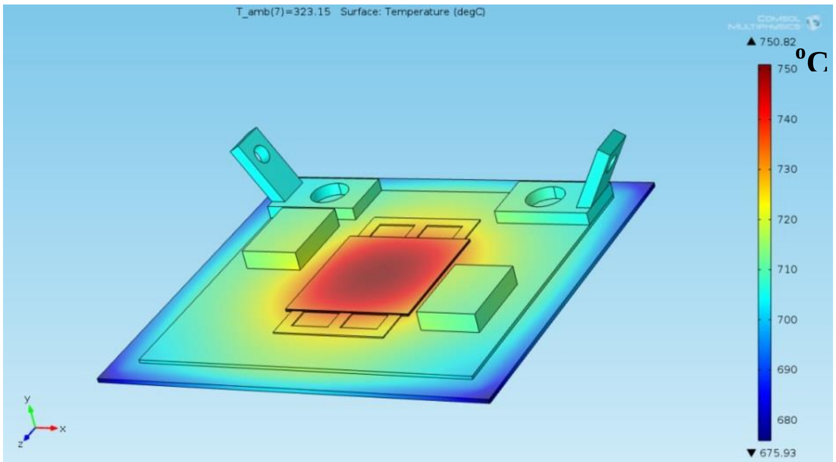

Figure 7.7: PV assembly temperature distribution for solar cell without heat sink at 50°C ambient temperature.

Figure 7.8 shows the variation in cell surface average temperature with time at tested ambient temperature of 50 °C. It can be observed that the cell temperature increased from the initial temperature i.e. ambient temperature to 700 °C in only about 60 seconds and reached steady state i.e. temperature of 742 °C in about 120 seconds.

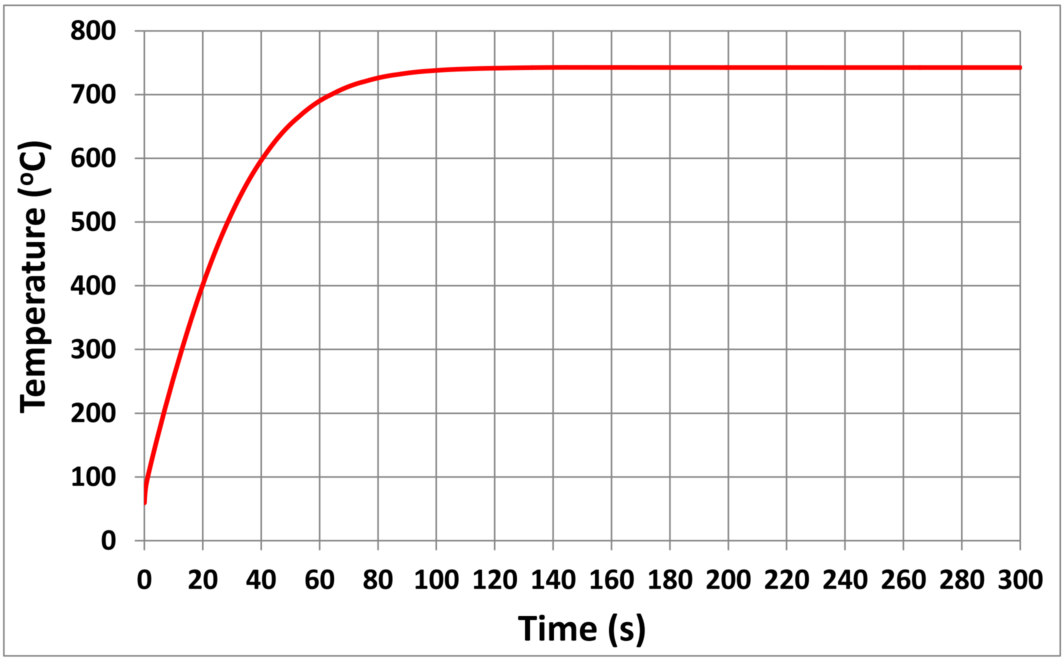

Figure 7.8: Variation in cell temperature with time at ambient temperature of 50 °C.

In case of passive cooling, the generated heat is transferred through the PV cell solid layers by conduction to the heat sink where it is dissipated to the surrounding by natural convection and radiation. Figure 7.9a shows the temperature contours of the solar cell assembly attached to the AFHS under CR of 500X. The maximum temperature on the PV surface reached 210^{o}C at ambient temperature of 50^{o}C. Compared to the case of no cooling above, it is clear that AFHS heat sink is able to significantly reduce the PV volumetric average temperature from about 742 ^{o}C to about 206 ^{o}C. However, it is not efficient enough to keep the PV average temperature within the recommended operating temperature limit (25-80 ^{o}C). Figure 7.9b shows the temperature contours of the solar cell assembly attached to the RPHS which performs better than AFHS; the maximum temperature on the PV surface reaches 117 °C at ambient temperature of 50 °C and the solar cell volumetric average temperature is about 112 ^{o}C. On the other hand, Figure 7.9c shows the temperature profile of the PV assembly attached to SFHS; the maximum temperature is 96 °C at the same ambient temperature and the solar cell volumetric average temperature is 92 ^{o}C. Although RPHS and SFHS are tested at the same surrounding conditions, SFHS is performing better than RPHS in dissipating heat load with PV average temperature difference between the two heat sinks of 21 K in all tested ambient temperatures. Finally, Figure 7.9d shows the temperature distribution of the solar cell assembly attached to the ESFHS where the maximum temperature on the PV surface reaches 85 °C at ambient temperature of 50 °C but the volumetric solar cell average temperature is about 80 °C. ESFHS is the only heat sink which keeps the PV average temperature within the safe operating temperature. It can be concluded that design of the heat sink play a major role in heat dissipation performance.

In case of active cooling, the generated heat is transferred through the PV cell solid layers by conduction to the water channel where it is dissipated mainly by forced convection. Figure 7.10 shows the temperature plot of the PV assembly above the cooling channel at 0.01m/s inlet water velocity corresponding to Reynolds number of around 122; the maximum temperature on the PV surface is 67 °C and the volumetric average PV temperature is about 63 °C at ambient temperature of 50 °C. Clearly, there is a drop in the PV average temperature of about 17 K compared to ESFHS and about 143 K compared to AFHS at the high ambient temperature of 50°C.

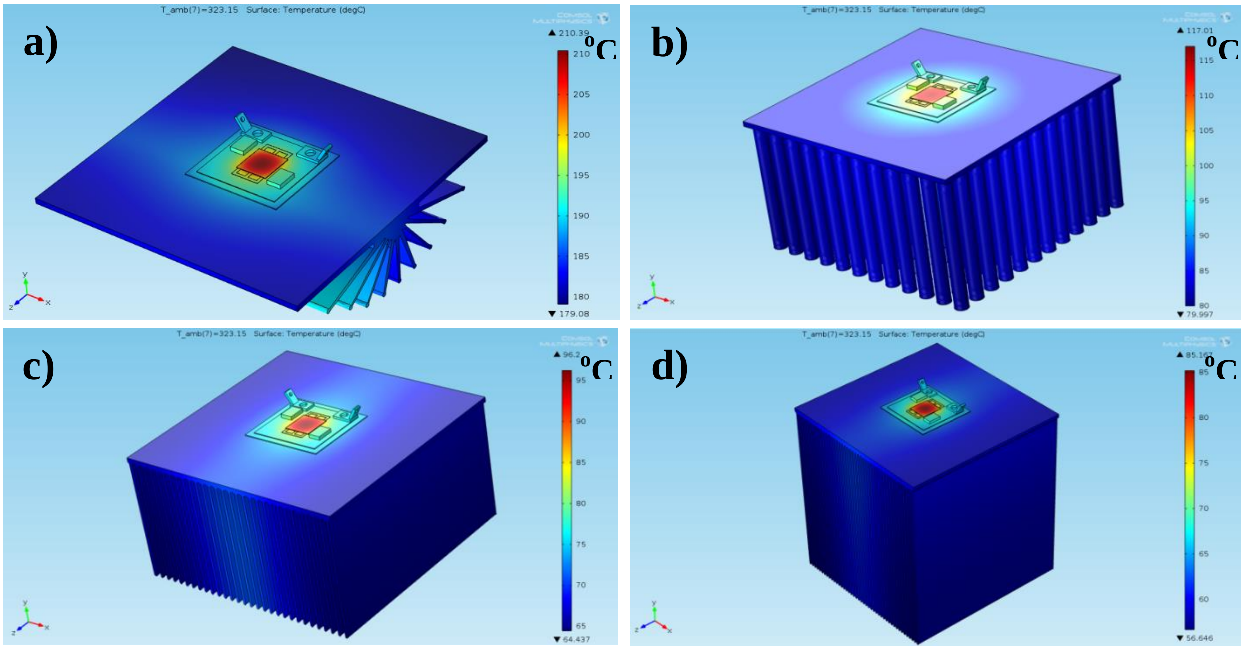

Figure 7.9: HCPV assembly temperature profile for a) AFHS; b) RPHS; c) SFHS; and d) ESFHS at 50°C ambient temperature.

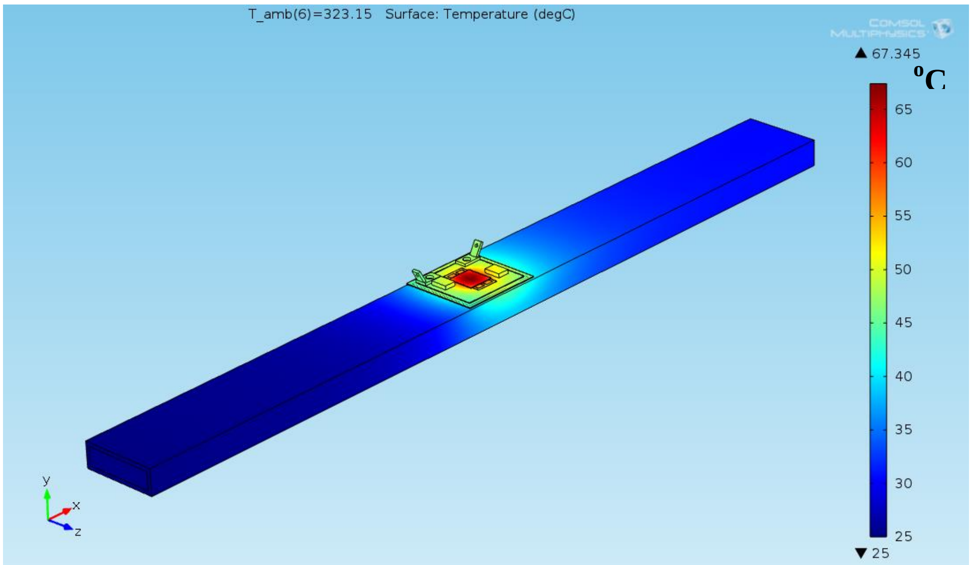

Figure 7.10: HCPV assembly temperature profile for water active cooling case at 50 °C ambient temperature.

Figure 7.11 demonstrates the performance of the four passive cooling heat sinks and the active water cooling in maintaining the PV average temperature at different ambient temperatures. It can be noticed that the heat sink dissipation performance is negatively influenced by the increase in the ambient temperature. For example, at ambient temperature of 25 °C the average temperature of the solar cell attached to SFHS is about 66 ^{o}C while at ambient temperature of 50 ^{o}C the average temperature is about 92 ^{o}C. AFHS shows the worst heat dissipation performance compared to the other heat sinks as the PV average temperature exceeded the maximum operating temperature (110 ^{o}C) in all tested cases. Also, RPHS is not able to maintain the PV average temperature below 110 ^{o}C at ambient temperature of 50 ^{o}C as it reached to more than 112 ^{o}C. On the other hand, SFHS is able to keep the PV average temperature within the operating limits (25-80 ^{o}C) at all ambient temperatures except at 45^{o}C and 50^{o}C. ESFHS is the only heat sink geometry design that is efficient enough to maintain the PV average temperature within the operating temperature limit even at ambient temperature of 50 ^{o}C. Unlike passive cooling method which is strongly influenced by the surrounding conditions, water cooling at moderate velocity (0.01 m/s) that can be supplied directly from the domestic tap water has the ability to keep the PV average temperature almost steady i.e. 60 °C regardless of the ambient temperature.

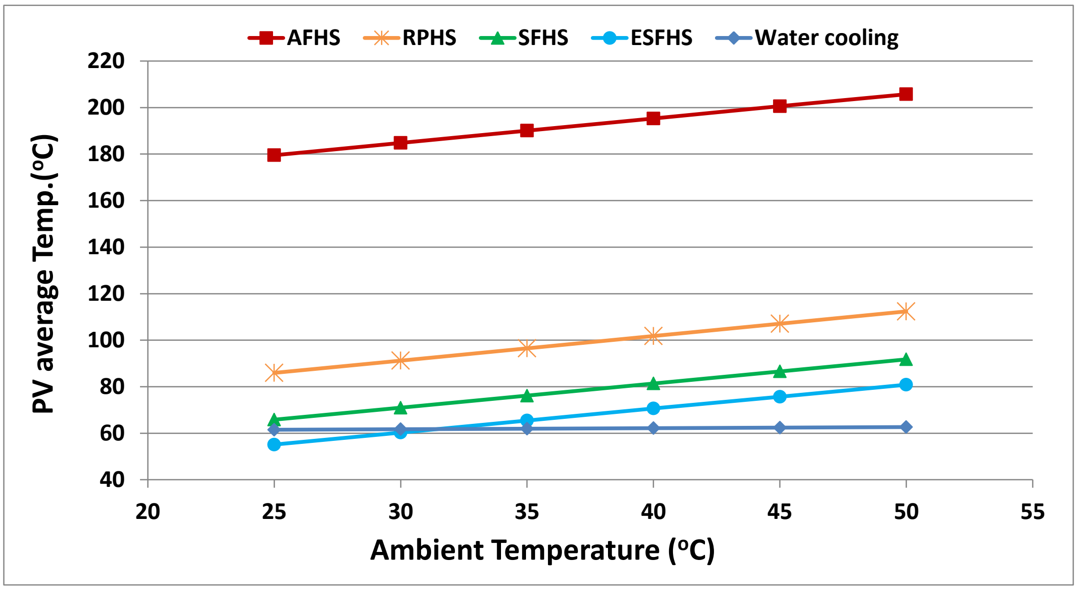

Figure 7.11: PV average temperature at different ambient temperatures.

As a result of increasing the PV average temperature in case of AFHS, RPHS, SFHS and ESFHS when ambient temperature increases, the PV electrical efficiency decreases accordingly as illustrated in Figure 7.12. Due to the high PV average temperature of the AFHS assembly the electrical efficiency are about 33.9% and 32.7% at 25°C and 50°C ambient temperature respectively. Also, the PV electrical efficiency of the ESFHS at ambient temperature of 25°C and 50°C are 39.8% and 38.6%. On the other hand, active water cooling is capable of maintaining the output electrical efficiency at about 39.5% at the range of different ambient temperatures used. It can be noticed that the performance sensitivity of this type of solar cell (triple-junction) to the temperature is low compared to the conventional silicon solar cells.

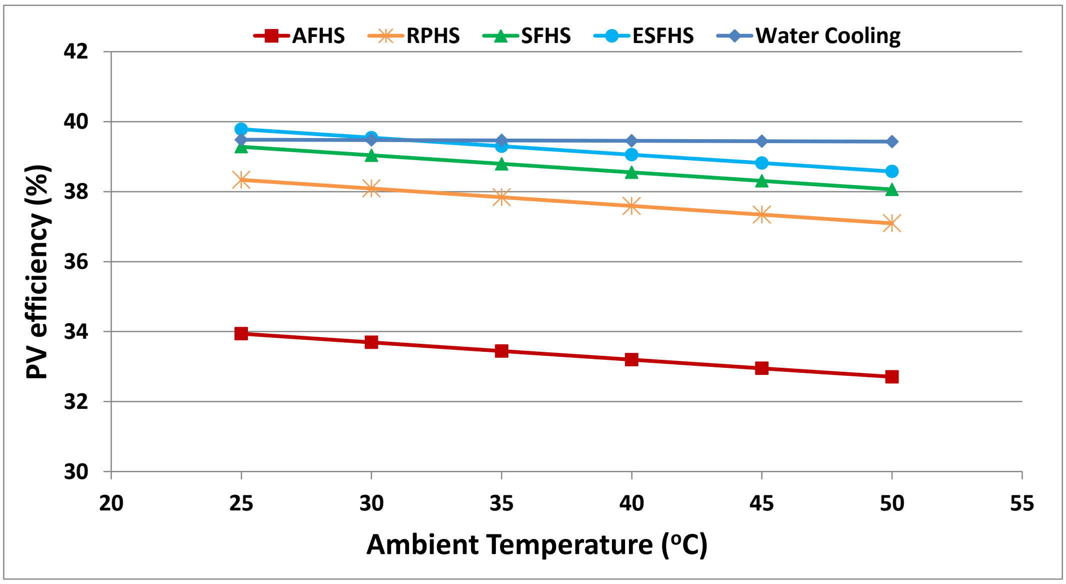

Figure 7.12: PV electrical efficiency at different ambient temperatures for the different cooling methods.

Based on energy conservation principle at steady state, the following relations must be satisfied:

$$Q_{in} = Q_{therm} + Q_{elec} \tag{7.10}$$

or

$$Q_{in} = Q_{radi} + Q_{conv} + Q_{cool} + Q_{elec} \tag{7.11}$$

Where Q_{in} is the input solar energy, Q_{therm} is the thermal energy generated by the system, Q_{elec} is the electrical energy generated by the PV, Q_{radi} is the surface to ambient radiation energy, Q_{conv} is the natural/forced convection heat transfer to the atmosphere and Q_{cool} is the thermal energy removed by the cooling system. In passive cooling systems, the thermal energy carried by the coolant is equal to zero i.e. $Q_{cool} = 0$ while surface to ambient radiation (Q_{radi}) and natural convection (Q_{conv}) are dominant. On the other hand, in active cooling systems radiation (Q_{radi}) and natural convection (Q_{conv}) mechanisms are very small compared to the thermal energy removed by the cooling fluid (Q_{cool}). The thermal energy extracted by the water (Q_{cool}) per second can be calculated using the following equation:

$$Q_{cool} = \dot{m} C_p (T_{out} - T_{in}) \tag{7.12}$$

Where $\dot{m}$ is the mass flow rate of the water in (kg/s), C_p is the heat capacity of the water at constant pressure in (J/(kg·K)), T_{out} is the water outlet temperature in (°C) and T_{in} is the water inlet temperature in (°C). The mass flow rate of the water passing through the cooling channel can be calculated using the following equation:

$$\dot{m} = \rho UA \tag{7.13}$$

Where ρ is the density of the water in (kg/m^3), U is the mean velocity of the water in (m/s) and A is the cooling channel cross sectional area in (m^2).

The electrical energy generated by the PV (Q_{elec}) is calculated using the following equation:

$$Q_{elec} = Q_{in} \cdot \eta_{elec} \tag{7.14}$$

Table 7.3 presents the produced electrical and thermal energy for PV attached to ESFHS at different ambient temperatures and with Q_{in}= 50 W.

Table 7.3: Thermal and electrical energy generated by the HCPV system attached to ESFHS.

Ambient Temp. (°C)	**Q_{therm} (W)**	**Q_{radi} (W)**	**Q_{conv} (W)**	**Q_{cool} (W)**	**Q_{elec} (W)**	**Utilised energy (W)**
25	30.108	0.165	29.943	0.000	19.892	19.892
30	30.229	0.175	30.054	0.000	19.771	19.771
35	30.351	0.185	30.166	0.000	19.649	19.649
40	30.473	0.197	30.276	0.000	19.527	19.527
45	30.591	0.205	30.386	0.000	19.409	19.409
50	30.713	0.217	30.496	0.000	19.287	19.287

It can be observed that the thermal radiation and natural convection energies are increased as the ambient temperature increases while the electrical output is decreased. Moreover, the surface to ambient radiation is relatively small compared to the natural convection. Also, most of the input energy into the HCPV system is wasted to the atmosphere in the form of thermal energy. For example, at ambient temperature of 25°C more than 60% of the input energy is converted to heat and this percentage increases as the ambient temperature increases. This heat can be utilised using HCPV/T system which generates both electrical and thermal energies as illustrated below.

Table 7.4 presents the produced electrical and thermal energy for HCPV attached to the water cooling channel at different ambient temperatures.

Table 7.4: Thermal and electrical energy generated by the HCPV/T system attached to a water cooling channel.

Ambient Temp. (^{o}C)	**Q_{therm} (W)**	**Q_{radi} (W)**	**Q_{conv} (W)**	**Q_{cool} (W)**	**Q_{elec} (W)**	**Utilised energy (W)**
25	30.258	0.131	1.224	28.903	19.742	48.645
30	30.263	0.050	0.383	29.830	19.737	49.567
35	30.268	-0.034	-0.509	30.811	19.732	50.543
40	30.274	-0.122	-1.532	31.928	19.726	51.654
45	30.280	-0.214	-2.654	33.148	19.720	52.868
50	30.285	-0.311	-3.841	34.437	19.715	54.152

It can be observed that the system gains heat through thermal radiation and natural convection (negative sign) at ambient temperature of 35^{o}C and above which means that the average temperature of the whole assembly i.e. PV and the cooling channel is less than the temperature of the ambient. For instance, at ambient temperature of 50^{o}C the system is gaining more than 4 W through thermal radiation and natural convection. This will enhance the thermal and total energy output of the system since the electrical performance of the multi-junction PV is almost steady at all ambient temperatures. Therefore, it can be concluded that high ambient temperature for such a system is an advantage if the thermal energy output is utilised. Moreover, the surface to ambient radiation and natural convection here are relatively small compared to the water forced convection. For example, at ambient temperature of 25^{o}C the sum of the radiation and natural convection energy losses is less than 1.4 W i.e. less than 3% of the energy input while the other 97% of the energy is utilised as Q_{elec} and Q_{cool}.

The thermal efficiency of the HCPV/T system is given by the following equation:

$$\eta_{therm} = \frac{Q_{cool}}{Q_{in}} \tag{7.15}$$

Figure 7.13 shows the electrical (η_{elec}) and thermal efficiencies (η_{therm}) generated by the HCPV/T system at different ambient temperature. The small reduction in the electrical efficiency (η_{elec}) which is less than 1% i.e. from about 39.48% to 39.43% is compensated since the thermal efficiency (η_{therm}) is increased from 58% at ambient temperature of 25^{o}C to about 69% at ambient temperature of 50^{o}C with about 19% increase. It can be concluded that the electrically worst case scenario for the HCPV/T i.e. at ambient temperature of 50°C is the best case scenario for the thermal output.

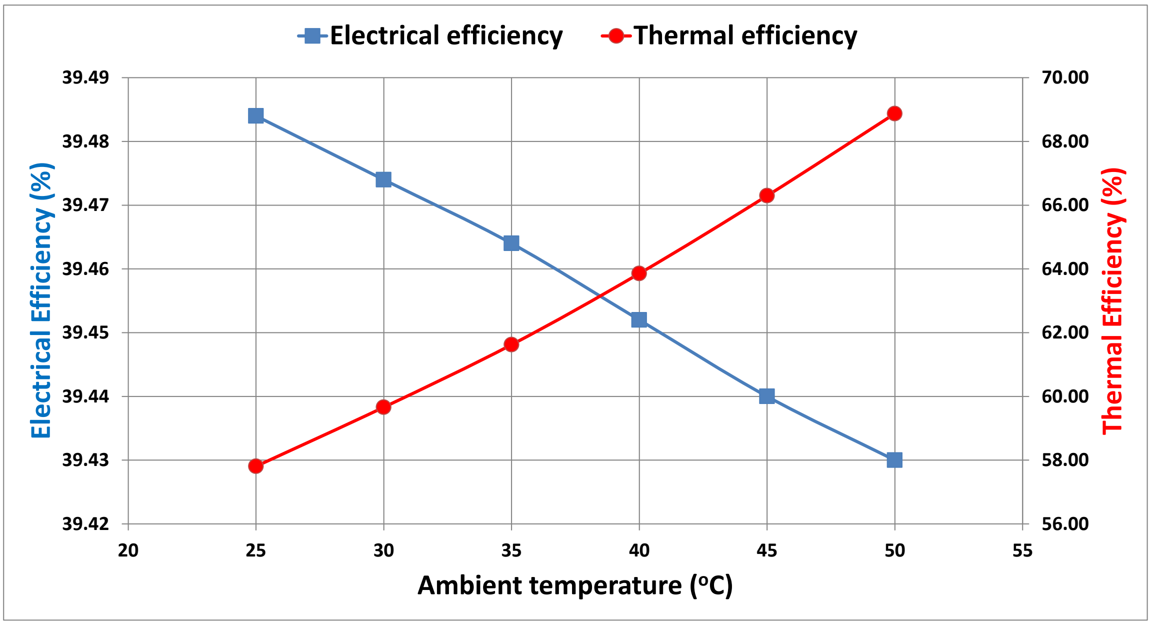

Figure 7.13: HCPV/T electrical and thermal efficiency at different ambient temperatures.

The optical loss is not considered in the calculated electrical and thermal efficiencies presented above. Therefore, the total efficiency of the HCPV/T system including the optical, electrical and thermal losses can be calculated using the following equation:

$$\eta_{tot} = \frac{Q_{elec} + Q_{cool}}{q_{irra} \times GCR \times A_r} \qquad (7.16)$$

Figure 7.14 shows the total efficiency (η_{tot}) generated by the HCPV/T system at different ambient temperature taking into account all the losses in the system. Due to the increase in the thermal efficiency as the ambient temperature increases and the stable electrical performance of the system, the total efficiency is increased with increasing the ambient temperature. For instance, the total efficiency of the HCPV/T at 25°C ambient temperature is about 78% while at ambient temperature of 50°C the total efficiency is more than 86% with percentage increase of around 11%.

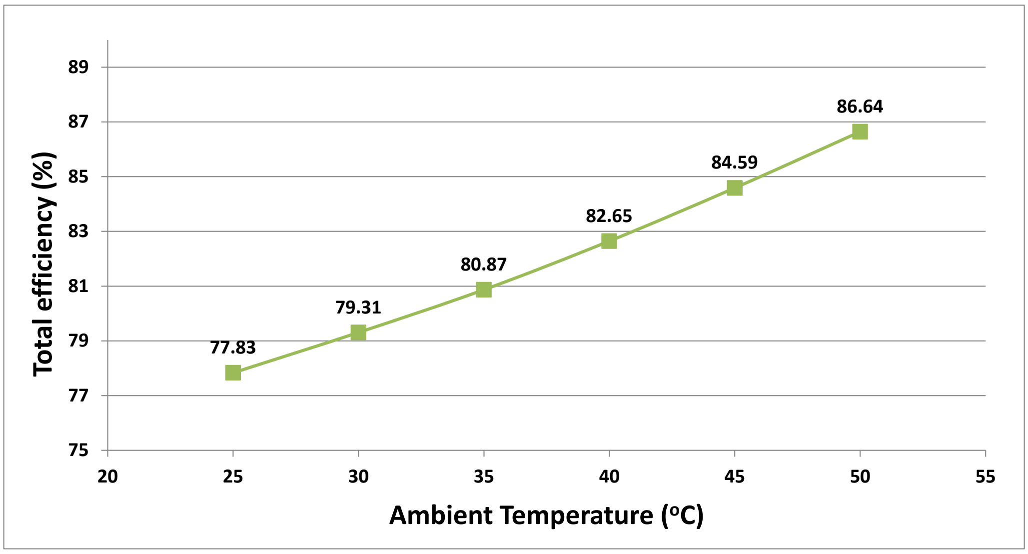

Figure 7.14: HCPV/T total efficiency at different ambient temperatures.

7.5. Feasibility of utilising HCPV/T outlet water temperature in different thermal applications

Figure 7.15 shows the water temperature along the cooling channel for a single HCPV/T at different ambient temperatures captured from COMSOL. At ambient temperature of 50^{o}C, the output cooling water average temperature was raised from the input temperature of 25^{o}C to about 30^{o}C while at 25^{o}C ambient temperature the outlet water temperature is increased to about 29^{o}C. Moreover, three CPV assemblies were placed in series on the same cooling channel, as shown in Figure 7.16, where the heat flux is applied uniformly on each PV top surface and thermally simulated applying the same assumptions and boundary conditions described in section 7.4.4 to predict the outlet water temperature. As demonstrated in the Figure, the spacing distance between two solar cells is the same spacing distance between the inlet of the cooling channel and solar cell 1 and the distance between the outlet of the cooling channel and solar cell 3 i.e. 0.0583 m.

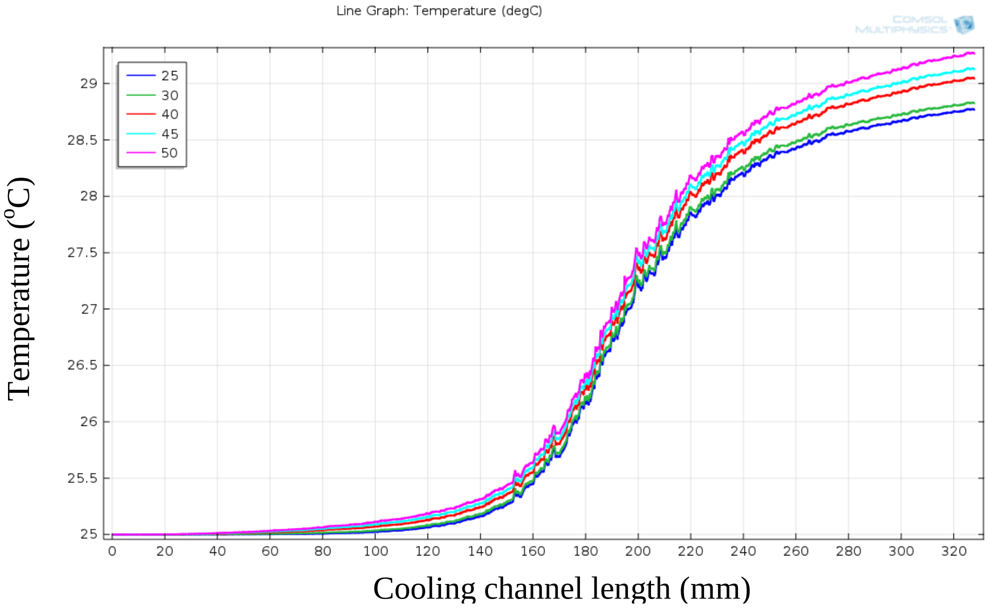

Figure 7.15: One HCPV water temperature along the cooling channel at different ambient temperature.

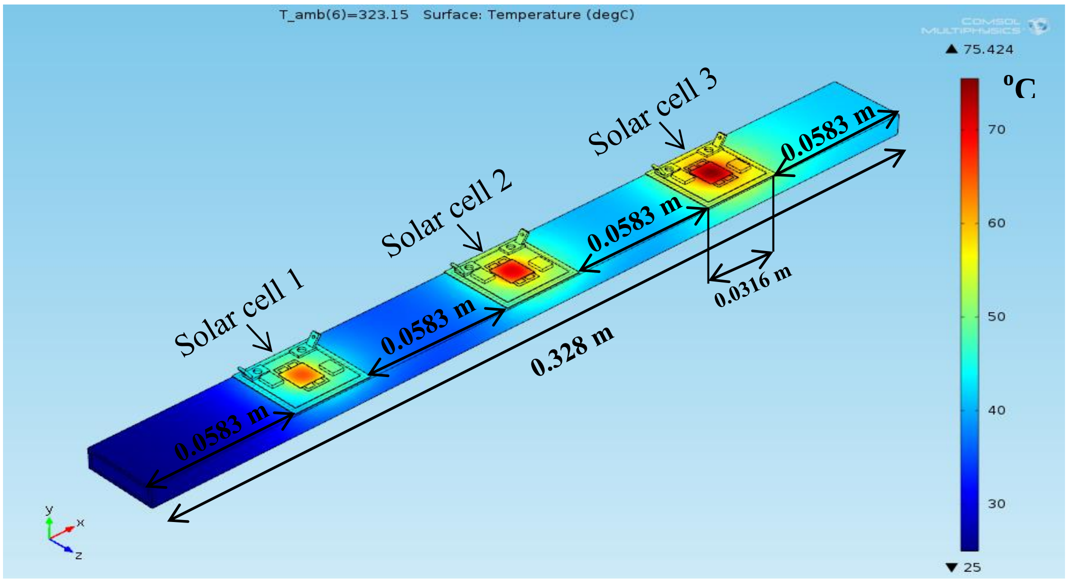

Figure 7.16: Three HCPVs temperature profile for water cooling at 50 °C ambient temperature.

Due to the increase in the water temperature along the cooling channel, the PV performance differs; the first solar cell close to the water entrance has the highest performance where the water temperature is 25°C while the last solar cell close to the water channel exit has the lowest performance as shown in Figure 7.17. For example, at ambient temperature of 50 °C the electrical efficiency of the solar cell number 1 is about 39.5% while cell number 3 is about 39.0%.

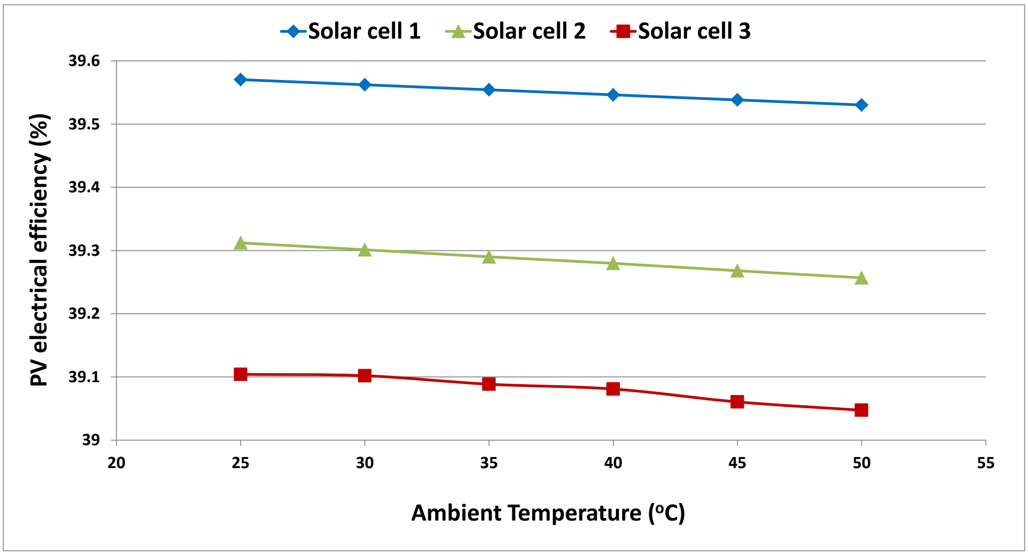

Figure 7.17: PV electrical efficiency of each solar cell in series at different ambient temperatures.

The average outlet water temperature at ambient temperature of 50 °C is increased from 25 °C before the first cell to about 38 °C after the third cell as shown in Figure 7.18. In other words, a single PV assembly increases the coolant water temperature by about 5 °C.

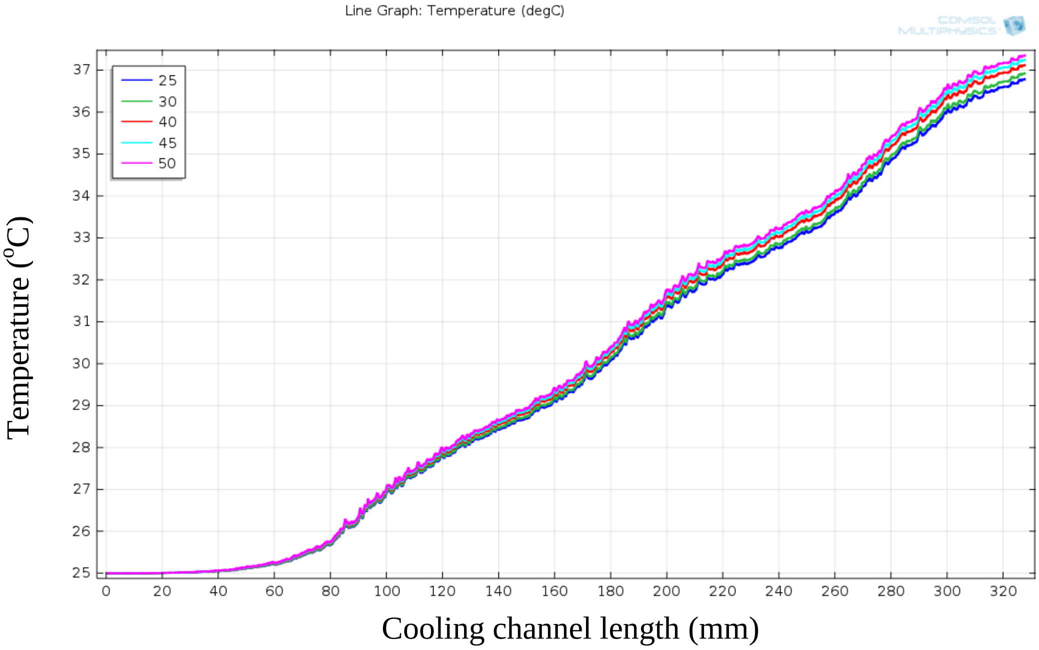

Figure 7.18: Three HCPVs water temperature along the cooling channel at different ambient temperature.

By extrapolating these data, Figure 7.19 shows that placing 14 HCPVs in series on the cooling channel will increase the outlet water average temperature to 90°C even at the lowest tested ambient temperature of 25°C which makes the coupling to different thermal applications such as a single stage absorption cooling system feasible [158].

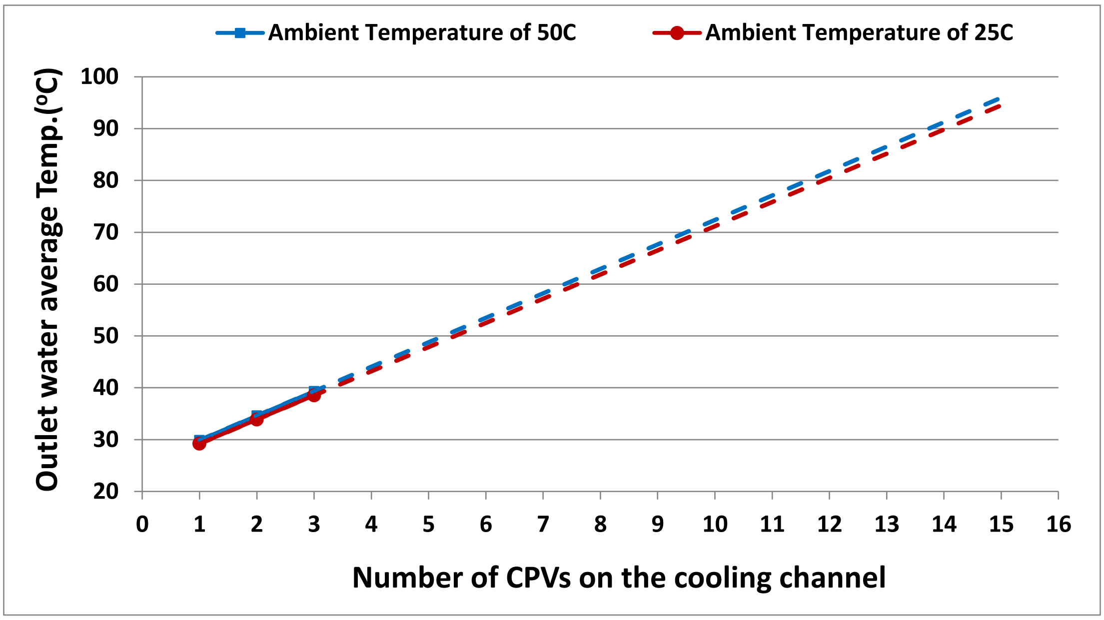

Figure 7.19: Increasing of outlet water temperature with number of HCPVs.

Table 7.5 shows the produced electrical (Q_{elec}), thermal (Q_{therm}) and total utilised energy for the three HCPVs attached to the water cooling channel at different ambient temperatures. The heat absorbed by the cooling water increased from about 86 W to 93 W when the ambient temperature increased from 25°C to 50°C while the electrical output of the three solar cells is almost stable at around 58 W. The increase in the thermal energy gained by the coolant is due to the gained heat from the ambient by natural convection and radiation. Therefore, the total output including the thermal and electrical power increased by about 5% when the ambient temperature increased from 25°C to 50°C i.e. from 145 W to about 152 W. Moreover, the Table below shows that the thermal efficiency increased from about 58% to about 62% while the electrical efficiency is almost steady at 39%. The total efficiency of the HCPV/T using three solar cells system considering the optical, thermal and electrical losses is demonstrated in the Table as well. The total efficiency increased with increasing the ambient temperature.

For instance, the total efficiency of the HCPV/T at 25°C ambient temperature is about 78% while at ambient temperature of 50°C the total efficiency is more than 81% with percentage increase of more than 5%.

Table 7.5: Output power and efficiency of 3 HCPVs attached to the water cooling channel.

Ambient Temp. (°C)	Q_{cool} **(W)**	Q_{elec} **(W)**	**Utilised energy (W)**	η_{therm}**(%)**	η_{elec}**(%)**	η_{tot}**(%)**
25	86.444	58.993	145.437	57.629	39.329	77.566
30	87.874	58.983	146.857	58.583	39.322	78.324
35	89.205	58.966	148.171	59.470	39.311	79.024
40	90.485	58.953	149.438	60.323	39.302	79.700
45	91.743	58.933	150.677	61.162	39.289	80.361
50	93.106	58.917	152.023	62.070	39.278	81.079

7.6. Effect of varying input parameters on the HCPV/T performance

In this section, the influence of varying the input solar irradiation, the cooling water volume flow rate and cooling water inlet temperature on the HCPV/T thermal and electrical performance was examined.

7.6.1. Effect of the input solar irradiation on the HCPV/T performance

A thermal simulation was undertaken to examine the influence of varying the input solar irradiation (q_{irra}) on the electrical (Q_{elec}) and thermal (Q_{therm}) outputs of a single HCPV/T at ambient temperature of 50°C applying the same assumptions and boundary conditions described in section 7.4.4. The input irradiances to be tested are: 500, 600, 700, 800, 900 and 1000 W/m^2. Although the average temperature of the PV increased with the input irradiation, Figure 7.20 shows that when the solar irradiance increased from 500 to 1000 W/m^2 the electrical output increased 100% from 10 to 20 W. On the other hand, the thermal power increased from about 20 W at solar irradiance of 500 W/m^2 to 35 W at 1000 W/m^2 with increase of 75%. It can be concluded, that the input irradiance has a noticeable influence on the HCPV/T thermal and electrical performance.

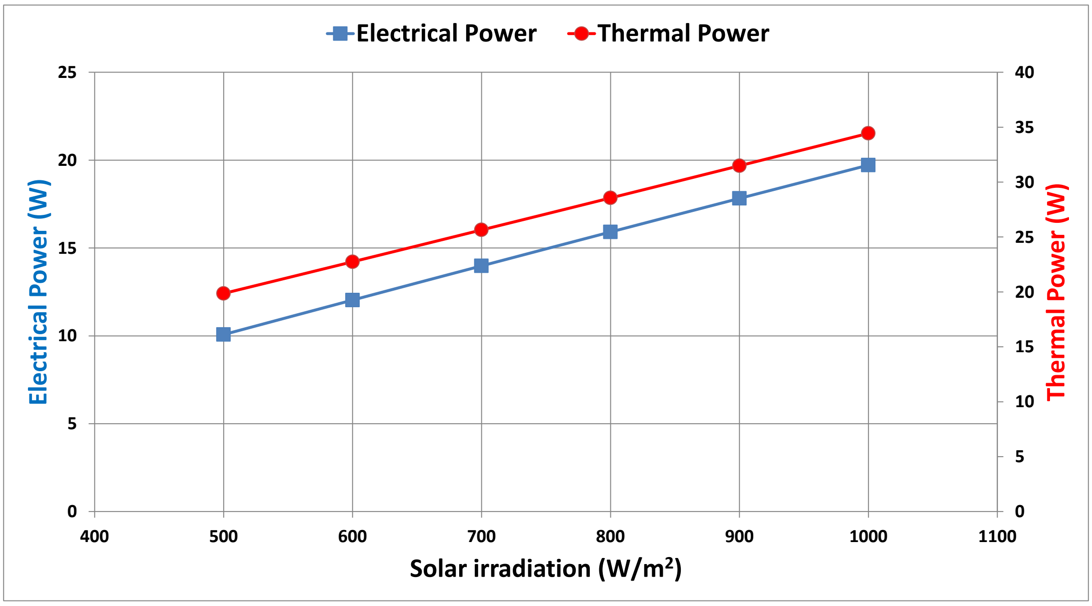

Figure 7.20: Electrical and thermal outputs of a single HCPV at different irradiance.

7.6.2. Effect of the cooling water volume flow rate on the HCPV/T performance

The effect of varying the input cooling water volume flow rate on the electrical (Q_{elec}) and thermal outputs (Q_{therm}) of a single HCPV/T at ambient temperature of 50°C applying the same assumptions and boundary conditions described in section 7.4.4 was examined. This was carried out by varying the input water velocity (U) into the cooling channel. The input velocities tested were: 0.01, 0.03, 0.05, 0.07 and 0.09 m/s. This is equivalent to volume flow rates of $1.89\text{x}10^{-6}$, $5.67\text{x}10^{-6}$, $9.45\text{x}10^{-6}$, $1.32\text{x}10^{-5}$ and $1.70\text{x}10^{-5}$ m^3/s with corresponding Reynolds number of 121.6, 364.92, 608.2, 851.5 and 1094.8. Figure 7.21 shows the PV average temperature as the inlet water velocity increases from 0.01 to 0.09 m/s. The PV temperature decreased by more than 10 K when the inlet water velocity increased from 0.01 m/s to 0.09 m/s i.e. from about 63°C to about 52°C.

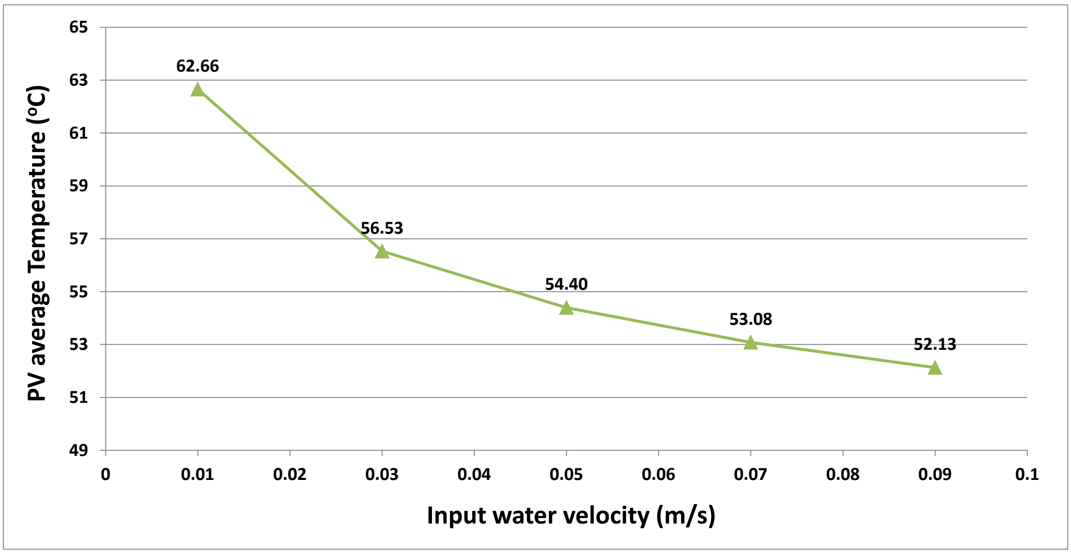

Figure 7.21: PV average temperature of a single HCPV at different inlet water velocity.

Figure 7.22 shows that due to the reduction in the PV temperature when the inlet cooling water velocity increased from 0.01 to 0.09 m/s the electrical output increased from 19.72 to 19.96 W with increment of only 1.2%. Moreover, the thermal power increased from about 34.44 W at water velocity of 0.01 m/s to 35.37 W at 0.09 m/s with increment of 2.7%.

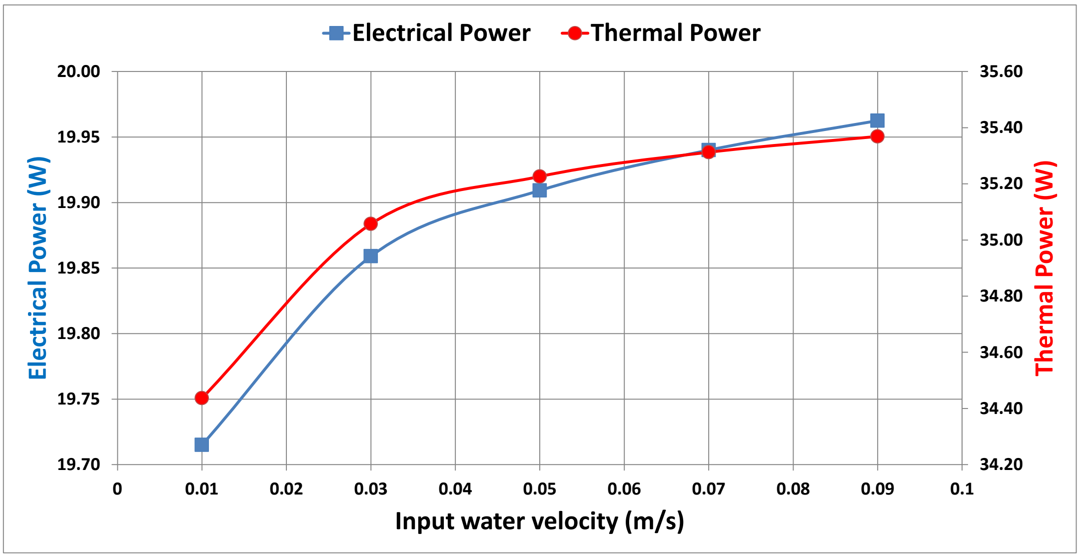

Figure 7.22: Electrical and thermal outputs of a single HCPV at different inlet water velocity.

The small increase in the thermal efficiency can be referred to the reduction in the natural convection and radiation to ambient as ΔT decreases. The positive influence of increasing the volume flow rate by increasing the inlet water velocity more than 0.01 m/s on the HCPV/T performance is not significant due to the low sensitivity of the MJ solar cell to the elevated temperature which has limited effect on the electrical output. Therefore, it can be concluded that the extra power required for increasing the cooling water flow rate may not be economically feasible in this case.

7.6.3. Effect of cooling water inlet temperature on the HCPV/T performance

A thermal modelling is undertaken to examine the influence of varying the inlet cooling water temperature (T_{in}) on the electrical (Q_{elec}) and thermal power output (Q_{therm}) of a single HCPV/T at ambient temperature of 50 °C applying the same assumptions and boundary conditions described in section 7.4.4. The inlet water temperatures to be tested are: 25, 30, 35, 40 and 45°C. Figure 7.23 shows that when the (T_{in}) increased from 25 to 45 °C the electrical output decreased from about 19.70 W to about 19.25 W with reduction of 2.3%. This can be referred to the decrease in the cooling effect as (ΔT) between the coolant and the PV decreases. Moreover, the thermal power decreased from about 34.5 W at cooling water inlet temperature of 25 °C to 30.5 W at cooling water inlet temperature of 45 °C with reduction of 11.6%. The reduction in the thermal power as T_{in} increases can be referred to the reduction in the ΔT as well.

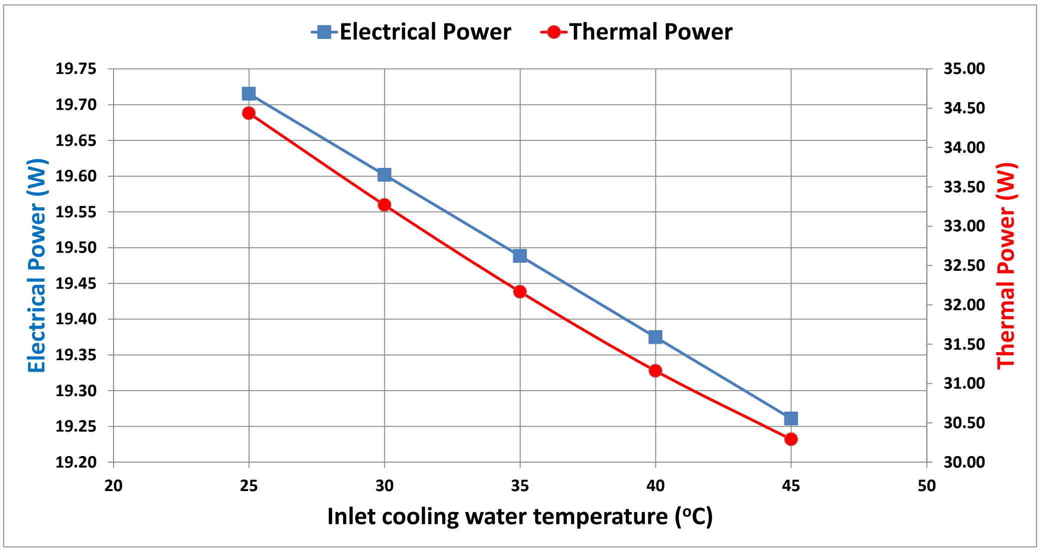

Figure 7.23: Electrical and thermal outputs of a single HCPV at different inlet cooling water temperature.

Figure 7.24 shows that the PV average temperature has exceeded the recommended operating temperature i.e. 80°C at inlet water cooling temperature of 45°C. Therefore, the inlet cooling water average temperature should be 43°C and less to maintain the PV within the safe operation limit.

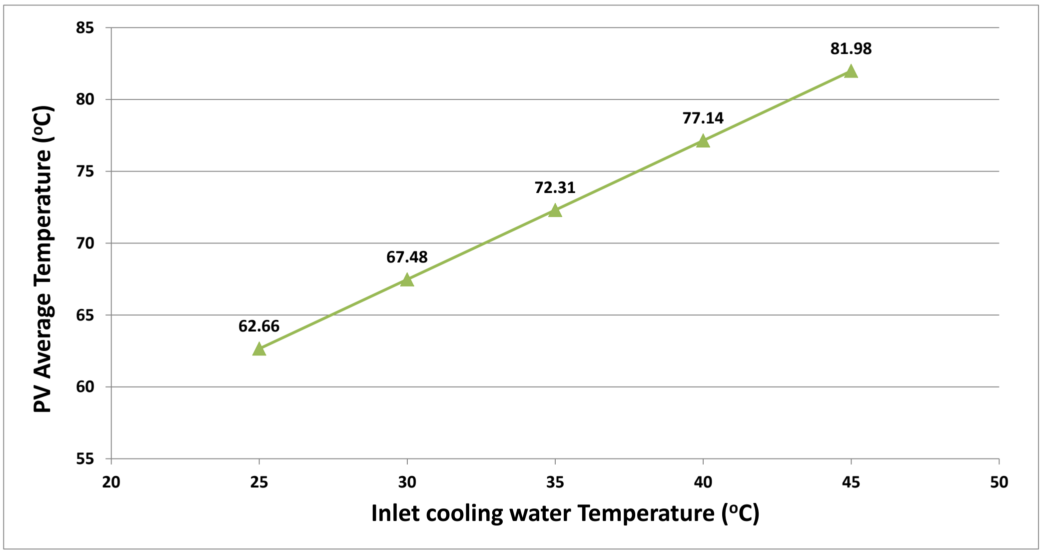

Figure 7.24: Average PV temperature at different inlet cooling water temperature.

7.7. HCPV/T outdoor performance based on Saudi Arabia solar irradiation and ambient conditions

In this section, analysis will be carried out to estimate the maximum and average power output that can be collected from a single HCPV/T in one year based on Saudi Arabia solar irradiation and ambient conditions. The thermal modelling assumptions are the same as in section 7.4.4 except the following:

1. From chapter 6, the outdoor electrical efficiency of the solar cell at high concentration i.e. >100X and surface temperature of 25 °C (reference temperature) is about 36%.
2. The maximum daily total DNI is 10,157 Wh/m^2 while the average daily total DNI is 6047 Wh/m^2 [22]. Therefore, if the annual average value of sunshine duration is about 12 hours [213] then the maximum hourly DNI is about 850 W/m^2 while the average hourly DNI is about 500 W/m^2.

3. The applied *CR* is 500X where X = 850 and 500 W/m^2. Therefore, the applied heat fluxes (q_{in}) are 425,000 and 250,000 W/m^2 and the input power (Q_{in}) in W are equal to 42.5 and 25.0 W respectively.
4. The annual day average ambient temperature is 33 °C [214].
5. The annual average wind speed is 3.7 m/s [213].

The resulting HCPV/T electrical and thermal efficiency for the maximum input power is 34.4% and 68.3% respectively and the total efficiency is 82.2%. Moreover, the resulting HCPV/T electrical and thermal efficiency for the average input power is 35.0% and 74.3% respectively and the total efficiency is 87.5%. The ambient temperature is higher than the overall HCPV/T system temperature leading to a heat gain from the surrounding which increases the thermal efficiency especially in the case of average input power. Figure 7.25 shows the yearly average and maximum electrical, thermal and total power yield of a single HCPV/T based on Saudi Arabia average and maximum hourly DNI and ambient conditions.

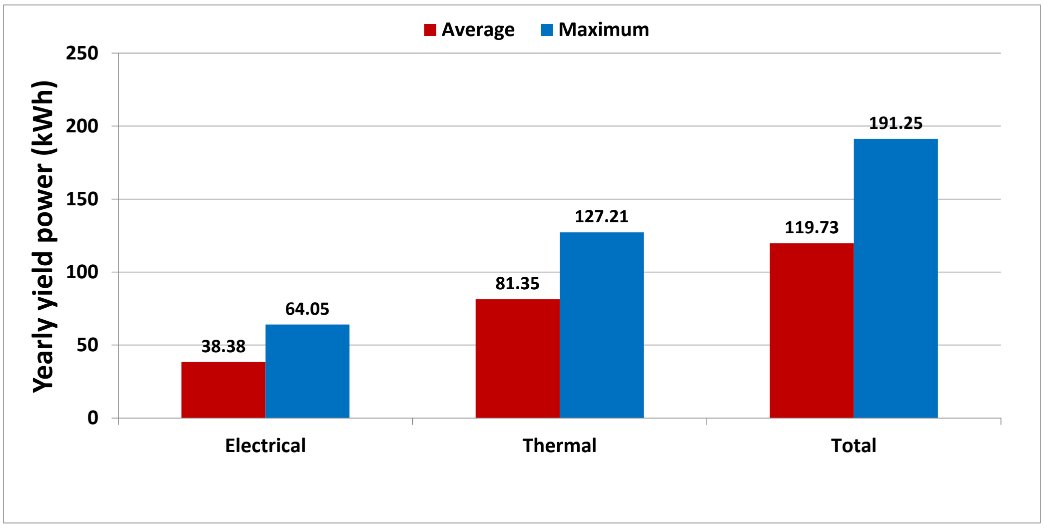

Figure 7.25: Thermal, electrical and total yearly yield average and maximum power of a single HCPV/T.

The average and maximum electrical power that can be generated in a year are up to 38.4 and 64.1 kWh respectively. Moreover, the average and maximum thermal power that can be collected in a year are about 81.4 and 127.2 kWh respectively. Finally, the average and maximum total power (i.e. electrical plus thermal) that can be collected in a year are up to

119.7 and 191.3 kWh respectively. Table 7.6 summarises the average and maximum power yield of a single HCPV/T based on daily, monthly and yearly periods. This Table can be used as a reference to calculate the expected power output if more than one HCPV/T system is installed. For example, if 10 HCPV/T systems are installed then the maximum and average yearly yield total powers are up to 1912.5 kWh and 1197.3 kWh respectively.

Table 7.6: Electrical, thermal and total yield power of a single HCPV/T at different periods of time.

	Period	Electrical Power (kWh)		Thermal Power (kWh)		Total Power (kWh)	
		Average	Maximum	Average	Maximum	Average	Maximum
Single HCPV/T	Daily	0.11	0.18	0.22	0.35	0.33	0.53
	Monthly	3.15	5.26	6.69	10.46	9.84	15.72
	Yearly	38.38	64.05	81.35	127.21	119.73	191.25

The annual electrical energy demand of a typical house in Saudi Arabia is 35,120 kWh including the heavy energy consumption by air conditioning and water heating [215]. Therefore, the annual total power yield of 184 units of 0.25x0.25 m^2 HCPV/T which only occupy 11.5 m^2 can respond to more than this demand. In comparison to 1.2x0.8 m^2 flat plate silicon PV module with electrical efficiency of 20%, more than 47 m^2 area is needed to respond to the same annual demand; therefore HCPV/T system can save about 76% of the area needed. Besides the energy and monetary savings, there is one more benefit which is the amount of pollution to be displaced through the use of renewable energy. The Global Warming Potential (GWP) can be used as a pollution indicator due to its popularity in the literature [176,216]. One average kWh of electricity equates to a GWP of 0.0006428 tons of CO_2; therefore 184 HCPV/T units can displace about 23 tons of CO_2 every year.

7.8. Thermal model validation

Indoor and outdoor experimental tests can be undertaken to study the thermal performance of the HCPV/T system. The advantage of carrying out the outdoor testing is that the thermal and electrical output can be measured simultaneously under real conditions. But, the disadvantage of this method is the uncontrollable atmospheric parameters that may affect the results such as wind speed. The indoor thermal and electrical testing can be implemented using a pulsed or continuous solar simulator. However, unlike conventional silicon based system the HCPV system integrating Fresnel lens and multi-junction solar cell is very demanding in terms of incident light collimation, uniformity and spectral match which makes HCPV solar simulator very expensive for this project. Therefore, alternative method is followed for indoor thermal testing which is based on simulating the heat load on the PV surface using Electrical Resistance Heater (ERH) as demonstrated below [155,205].

7.8.1. Indoor thermal model validation

The heat load on the solar cell was calculated through the PV thermal modelling which follows the same assumptions described in section 7.4.4 except that the ambient and cooling water input temperatures were 17.45 °C and 17.50 °C respectively as measured during the experimental test. Moreover, the inlet water volume flow rate was varied from: 8.33×10^{-7}, 1.67×10^{-6}, 2.50×10^{-6}, 3.33×10^{-6} and 4.17×10^{-6} m^3/s which are equivalent to the following water velocity: 0.004, 0.009, 0.013, 0.018 and 0.022 m/s respectively. Table 7.7 below shows the modelling results including the thermal power generated to be applied as a heat load on the CPV system.

Table 7.7: Thermal and electrical outputs of the thermal modelling at different water flow rate.

Water flow rate (m^3/s)	Received power by PV (W)	PV average Temp. (^oC)	Electrical efficiency (%)	Electrical power output (W)	Thermal power generated (W)
8.33×10^{-7}	50	60.59	39.53	19.76	30.24
1.67×10^{-6}	50	54.57	39.81	19.91	30.09
2.50×10^{-6}	50	52.37	39.91	19.96	30.04
3.33×10^{-6}	50	50.64	40.00	20.00	30.00
4.17×10^{-6}	50	49.67	40.04	20.02	29.98

It can be noticed that the PV electrical power increases with the water flow rate which ultimately reduces the heat load i.e. the generated thermal power. For example, at water flow rate of 8.33×10^{-7} m^3/s the heat load is 30.24 W while at 4.17×10^{-6} m^3/s the heat load is 29.98

W. In the experimental set-up, a 35 W 15 Ω ERH with dimensions of 0.011m x 0.0105m x 0.0045m was used to simulate the heat load at the top of the PV assembly as shown in Figure 7.26.

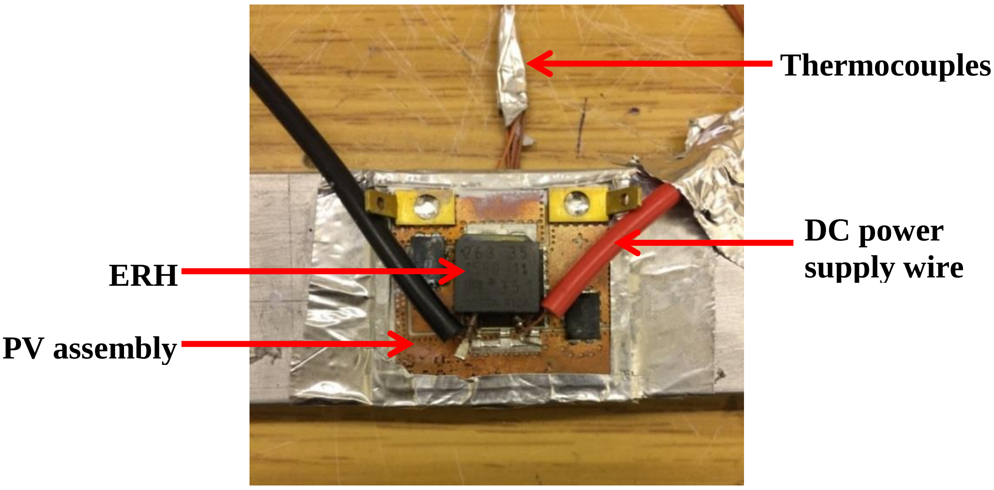

Figure 7.26: ERH at the top of the PV assembly.

Variable DC power supply was used to set the power input into the resistance heater. Moreover, a flow meter was used to control the water volume flow rate and a data logger to collect the temperature data including the two high precision Resistance Temperature Detectors (RTD) data at the inlet and outlet of the cooling channel as shown in Figure 7.27.

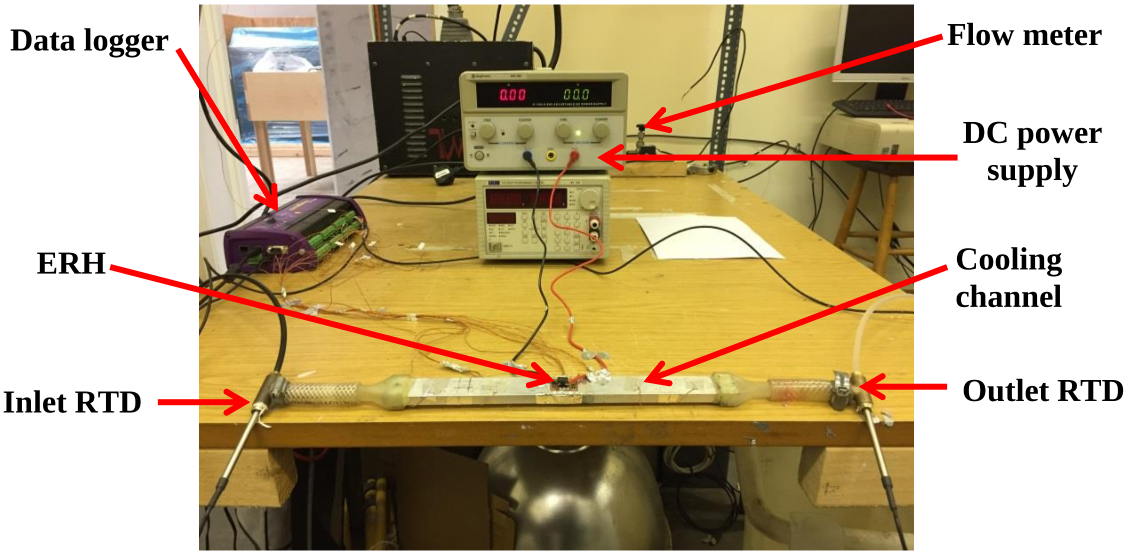

Figure 7.27: Indoor thermal modelling validation experimental set-up.

Five u-shape grooves on the cooling channel (Figure 7.28a) with dimensions of 0.0015m× 0.00075m were made to insert three 0.00013m diameter thermocouples just underneath the

PV and two at opposite corners of the PV assembly as shown in Figure 7.28b. Thirteen thermocouples in total were distributed on the CPV system as shown in Figure 7.28 to measure the PV surface temperature, PV assembly, top and side of the cooling channel.

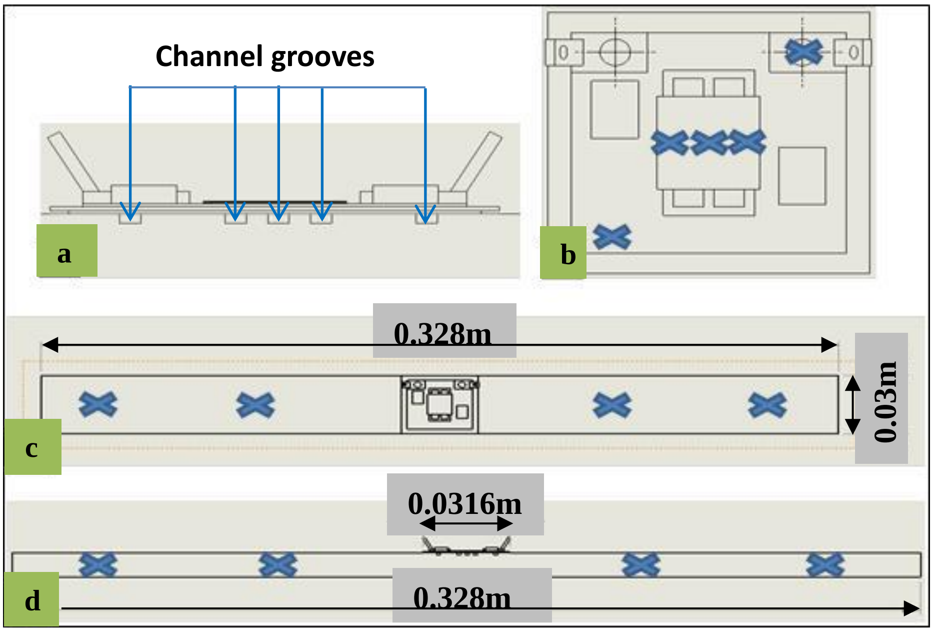

Figure 7.28: a) Side view of the cooling channel grooves; b) thermocouples locations on the PV assembly; c) & d): thermocouples locations at the top and side of the cooling channel.

Figure 7.29 shows the close agreement between the experimental and the simulation average temperature at different locations at flow rate of $8.33\text{x}10^{-7}$ m^3/s. For example, the simulation PV temperature is only 3.6% higher than the experimental while the coolant outlet temperature of the simulation is 2.8% higher than experimental value.

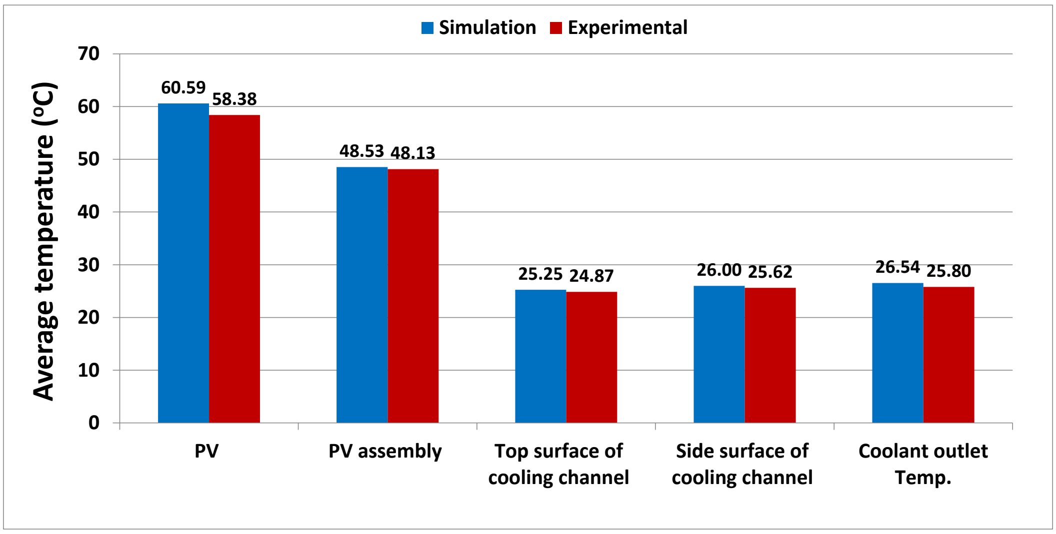

Figure 7.29: Temperature comparison at flow rate of $8.33\text{x}10^{-7}$ m^3/s.

The experimental thermal efficiency of the system was calculated and compared against the simulation one as shown in Figure 7.30. It can be observed that the thermal efficiency increases as the inlet cooling water flow rate increases. For example, the simulation thermal efficiency at flow rate of 8.33×10^{-7} m^3/s is about 56% while at flow rate of 4.17×10^{-6} m^3/s the thermal efficiency is about 58% with increment of about 3.6%. Also, the Figure shows the close agreement between the experimental and the simulation thermal efficiency with maximum deviation of about 8% at flow rate of 8.33×10^{-7} m^3/s. The difference between the simulation and experimental thermal efficiency can be referred to the small deviation in inlet cooling water temperature (T_{in}) and mean velocity (U) which influence the ΔT (T_{out} -T_{in}) and mass flow rate ($\dot{m}$) respectively since water is directly supplied from the tap water.

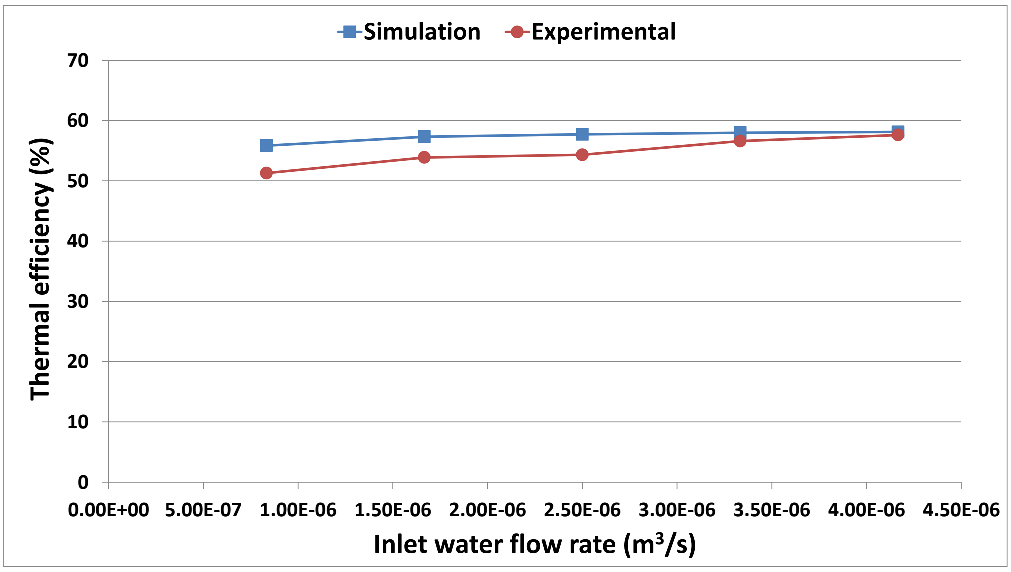

Figure 7.30: Simulation and indoor experimental thermal efficiency at different water flow rates.

7.8.2. Outdoor thermal model validation

Outdoor HCPV/T experimental set-up that was used for optical and electrical performance analysis was also used to study the thermal performance of the system. The thermal modelling assumptions are the same as in section 7.4.4 except the following:

1. From chapter 6, the outdoor electrical efficiency of the solar cell at high concentration i.e. >100X and at reference temperature is about 36%.

2. The applied concentration ratio is 114X. Therefore, the applied heat flux (q_{in}) is 114,000 W/m^2 and the input power (Q_{in}) in W are equal to 11.4 W.
3. The cooling channel is inclined at 42^o from normal.
4. The wind speed is assumed to be 4 m/s [217].
5. The ambient and cooling water input temperatures are 24.54 °C and 25.00 °C respectively as measured during the experimental test.
6. The inlet water volume flow rate is varied from: 8.33x10^{-7}, 1.67x10^{-6}, 2.50x10^{-6}, 3.33x10^{-6} and 4.17x10^{-6} m^3/s which are equivalent to the following water velocity: 0.004, 0.009, 0.013, 0.018 and 0.022 m/s respectively.

For both simulation and experimental results, Figure 7.31 shows that the PV average temperature decreases as the cooling water flow rate increases. Also, the Figure shows the close agreement between the experimental and the predicted PV average temperature at different water flow rate with maximum deviation of less than 3 ^{o}C i.e. 10% at flow rate of 4.17x10^{-6} m^3/s.

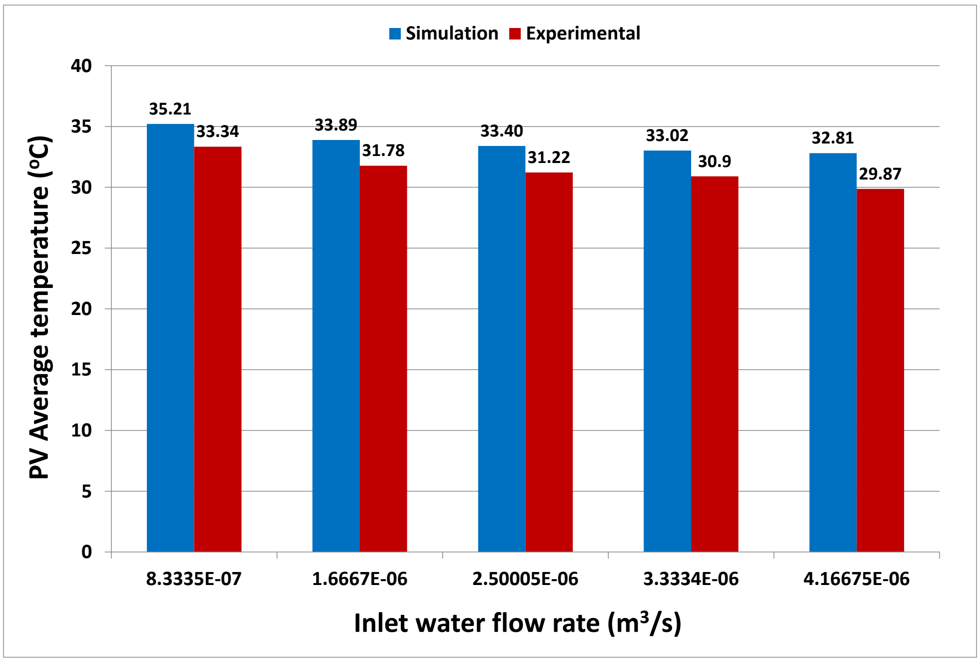

Figure 7.31: Simulation and experimental temperature comparison at different flow rates.

The experimental thermal efficiency of the system is calculated and compared against the simulation one as shown in Figure 7.32. The maximum thermal efficiency deviation between the two results is about 10% at flow rate of 2.50x10^{-6} m^3/s. The difference between the simulation and experimental thermal efficiency can be due to the small deviation in the inlet water temperature (T_{in}) and mean velocity (U) especially in outdoors testing where long supply hose was used to feed the system by cooling water.

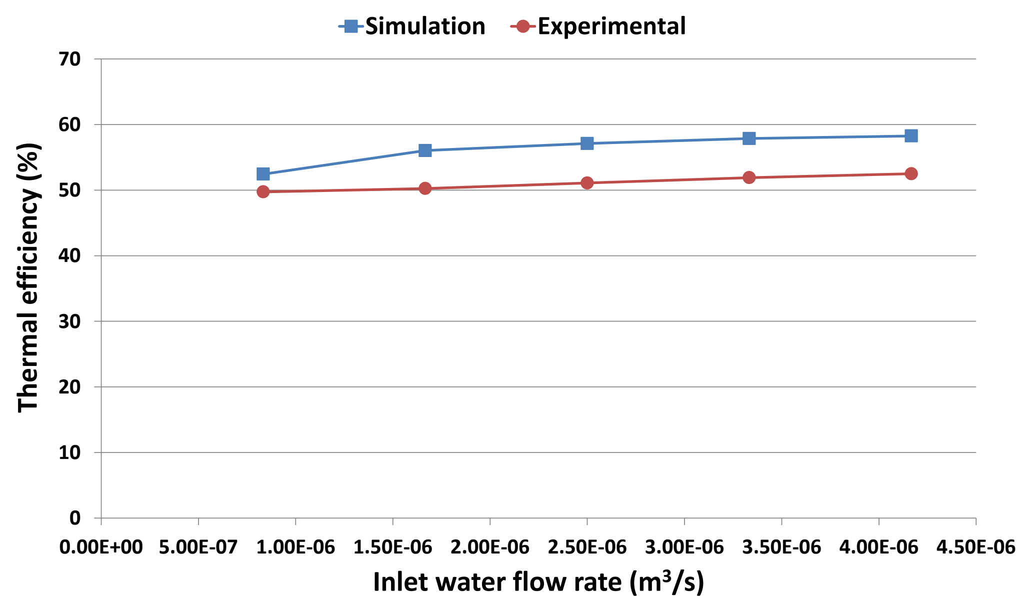

Figure 7.32: Simulation and outdoor experimental thermal efficiency at different water flow rates.

The experimental electrical efficiency of the system is calculated and compared against the simulation one as shown in Figure 7.33. The electrical efficiency increased by increasing the volume flow rate of the water. Due to the close agreement in the average PV temperature and low sensitivity of the solar cell to the temperature there is also close agreement in the electrical efficiency between the experimental and the simulation with maximum difference of about 0.4%. The difference between the simulation and experimental electrical efficiency can be referred to the small deviation in solar cell average temperature. As shown in Figure 7.31, the resulting simulation PV cell temperature is higher than the experimental PV cell temperature in all inlet water flow rates. Consequently, the resulting electrical efficiency of the simulation is lower than the experimental one as demonstrated in figure 7.33.

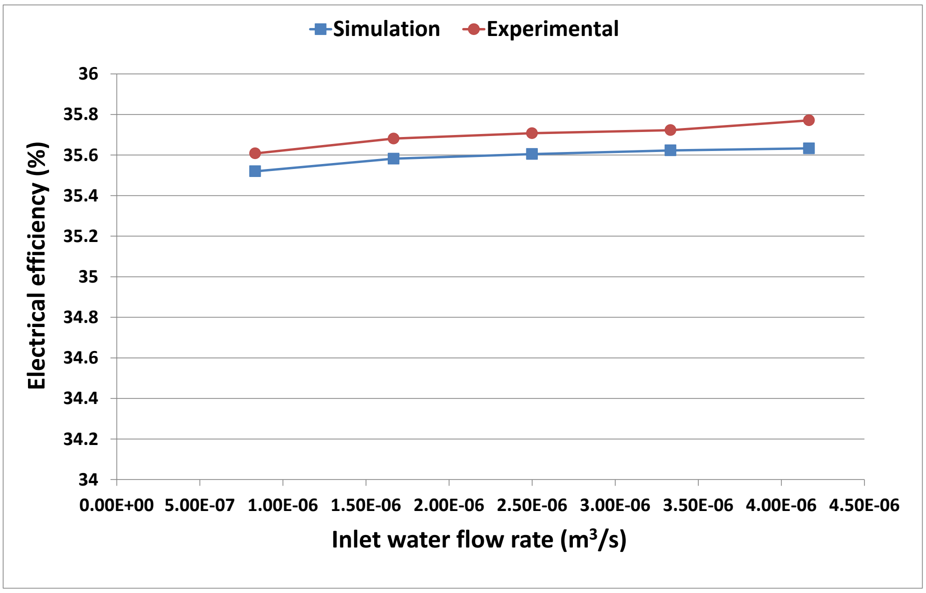

Figure 7.33: Simulation and outdoor experimental electrical efficiency at different water flow rates.

7.9. Summary

Four heat sinks geometries were developed and tested thermally to keep the solar cell within the safe operating temperature. Only ESFHS with thinner and longer fins was able to maintain the PV temperature ≤ 80 °C at concentration ratio of 500X and at ambient temperature of 50 °C. It can be concluded that design of the heat sink play a major role in heat dissipation performance.

Passive cooling can be a better choice for HCPV in remote areas where water resources are limited and periodic maintenance for the cooling system is costly. However, to make HCPV more cost effective HCPV/T principle is applied where both electrical and thermal energy can be utilised. Water cooling at moderate velocity i.e. 0.01 m/s ($Re \approx 122$), which can be supplied directly from the domestic tap water, has the ability to keep the PV temperature almost steady regardless of the ambient temperature. Due to stable PV temperature, the electrical efficiency is almost constant.

The influence of varying the input solar irradiation, the cooling water volume flow rate and cooling water inlet temperature on the HCPV/T performance was examined. It was found that the input irradiance is the most influencing parameter as the electrical and thermal output increased 100% and 75% respectively when the input solar irradiance increased from 500 to 1000 W/m^2.

HCPV/T outdoor performance analysis based on Saudi Arabia solar irradiation and ambient conditions was undertaken to estimate the power output that can be collected in one year. Based on the annual electrical energy demand of a typical house in Saudi Arabia including the heavy energy consumption by air conditioning and water heating, 184 units of the developed 0.25x0.25 m^2 HCPV/T which only occupy 11.5 m^2 can respond to more than the this demand. Also, in comparison to the flat plate silicon PV module with electrical efficiency of 20% and 1.2x0.8 m^2 area, HCPV/T system can save about 76% of the area needed. Moreover, in terms of pollution these units can displace about 23 tons of CO_2 every year.

Indoor and outdoor experimental tests were undertaken for thermal characterisation of the HCPV/T and for validation purpose. Close agreement between the experimental and the predicted PV average temperature was found with maximum deviation of less than 3 ^oC i.e. 10%. Also, maximum difference of 10% was found between the experimental and simulation thermal output.

CHAPTER 8

Conclusions and Recommendations for future works

8.1. Introduction

Due to the energy issues experienced all over the world and the problems associated with the use of conventional fossil fuel, interest in harnessing renewable energy sources is increasing. Developed countries are facing global warming problems while developing countries suffer from inadequate generation and supply of energy.

Solar PV power has been one of the fastest growing solar energy technologies that can be successful alternative to the fossil fuel and potential contributor to the energy but it suffers from low efficiency which leads to high initial cost. One method to reduce the PV technology cost is to replace the expensive PV material with cheaper optical concentrators such as lenses and mirrors; this technology is called CPV. Point-focus Fresnel lens concentrator can be integrated to CPV systems to achieve high concentration ratios exceeding 100 suns hence called high concentrator PV (HCPV). To make HCPV systems more cost effective, the thermal energy absorbed by the coolant can be utilised for different thermal applications therefore called HCPV/T. HCPV/T technology has attracted more attention especially after introducing multi-junction solar cells for terrestrial applications as those cells keep achieving new conversion efficiency records. However, as the research in this area is at its early stages there are certain issues still arise during operations that need further studies including non-uniform illumination, hot spot, small acceptance angle and high PV temperature. Moreover, there are some challenges related to the environment like high ambient temperature and dust.

The present study involves the development and performance characterisation including optical, electrical and thermal of MJ based HCPV/T for residential application that can generates electricity and heat simultaneously. Detailed modelling is important to predict the performance and helps to overcome the HCPV/T related challenges for cost effective systems.

8.2. Theoretical and experimental investigations

The performance of the HCPV/T system was characterised both theoretically and experimentally. It was characterised optically by examining the optical efficiency, the incident irradiation uniformity on the receiver and the acceptance angle. Also, it was characterised electrically by examining the influence of the concentration ratios, PV surface temperature and irradiation uniformity on the triple-junction solar cell output. Moreover, it was characterised thermally by predicting the PV temperature and the thermal energy absorbed by the coolant.

8.2.1. Optical performance investigation

A ray tracing software was used for optical theoretical characterisation. It was found that the Fresnel lens optical efficiency was inversely proportional to its size. Also, the degree of non-uniformity is directly proportional to the geometrical concentration ratio. Outdoor investigation revealed that non-uniform illumination on the solar cell can reduce the MJ electrical output by more than 40% when compared to the case with improved uniformity after placing the SOE at the optimum distance l and by 45% when compared to the efficiency of the solar cell obtained at standard controlled lab conditions. The distance between the concentrator and the receiver (l) was increased to reduce the non-uniformity of illumination. The measured electrical efficiency under point-focus profile (non-uniformity >692) is about 22% and after increasing the distance (l) the illumination uniformity over the PV improved (non-uniformity <1) and the electrical efficiency increased to about 37% with increase of 68%. Although, non-uniform illumination was improved by increasing the distance (l), the optical efficiency was reduced significantly. In order to increase the optical efficiency and maintain the same level of irradiation uniformity, the first technique of increasing the distance (*l*) was combined with introducing a SOE above the receiver. It was found that optical efficiency increased more than 250% from 13% to about 46% with almost the same degree of uniformity and electrical efficiency. There was a close agreement between the simulated optical efficiency and the experimental work with maximum difference of about 9%. The hot spot initiated by the non-uniform illumination was assessed experimentally by measuring the centre, side and corner surface temperature of the PV. A difference of about 13 ^{o}C was found between the centre and the side (0.005m distance) of the PV surface. Whereas, after enhancing the incident illumination uniformity a difference of about 1^{o}C was measured.

Although the electrical performance of the HCPV was enhanced after improving the irradiation uniformity on the receiver, the total optical efficiency was reduced by about 29% after inserting the SOE. Methods to enhance the HCPV optical performance by optimising the primary optical element were examined. A parametric study including focal length, thickness, groove pitch and transmissivity of the Fresnel lens was implemented. The optical efficiency of the system was enhanced with average increase of about 21%. The HCPV optimised optical system was also examined after introducing the SOE and compared with the HCPV optical system before optimisation. It was found that the total optical efficiency was increased from 46.2% to 60.0% with increment of about 30%.

The acceptance angle of the HCPV optical system with and without SOE was also examined. It was found that the acceptance angle increases after placing the developed SOE almost twice from 0.8^{o} to 1.5^{o}, 0.8^{o} to 1.6^{o} and 0.8^{o} to 1.9^{o} for 0.25x0.25m^{2}, 0.18x0.18m^{2} and 0.13x0.13m^{2} Fresnel lenses respectively. Increasing the acceptance angle can reduce the overall cost of the HCPV system as the demand for high precision tracking system will be reduced.

Space and cost analysis before and after the optical optimisation were implemented. It was found that about 20% of the area required can be saved after the optical optimisation if 16

HCPV units are connected with more electrical power i.e. 112 W compared to 86 W with increment of about 30%, which consequently reduces the cost of the system.

Densely packed receiver configuration including 4 PVs was compared to the single PV configuration. It was found that densely packed configuration can increase the optical and electrical power by about 18% due to the larger receiver area and acceptance angle with area saving of 75%.

8.2.2. Electrical performance investigation

Unlike crystalline-silicon technology, multi-junction solar cell is an emerging technology and research in this area is at its early stages. There are only few reports on its electrical and thermal performance characterisation under high concentration and even less in harsh environment like Saudi Arabia. Electrical modelling for a single multi-junction solar cell using lumped diode circuit model has been used to evaluate the PV electrical performance under different concentration ratios and temperatures. The model was calibrated against the manufacturer indoor experimental output data and it was able to respond to the variation of the concentration ratio with maximum difference in electrical power of 1.7% and respond to the variation of the PV surface temperature with maximum difference in electrical power of 1.6%.

A single HCPV unit was installed outdoor and I-V tracer was used to measure the output I-V curve under PV surface temperature of 25^{o}C-50^{o}C with a temperature step of 5^{o}C and different concentration ratios: 43X, 63X, 80X and 114X. It was found that the electrical efficiency is mainly influenced by the incident irradiation not the PV average temperature as the electrical power increased more than 150% when the concentration ratio increased from 43X to 114X. Compared to silicon PV cells, triple-junction solar cell has low temperature coefficient i.e. less sensitive to the elevated temperature which makes it a suitable candidate at high ambient temperature regions.

The I-V curve parameters before and after inserting the SOE were studied to examine the influence of non-uniform incident rays on the electrical output. It was found that maximum power (P_m) and open circuit voltage (V_{OC}) are both improved after placing the SOE with electrical efficiency (η_{elect}) increment of about 14% and 8% at concentration ratio of 119X and 74X respectively.

8.2.3. Thermal performance investigation

A 3D thermal model using FEA and CFD was developed to examine the performance of the HCPV/T system at high concentration under passive and active cooling in harsh environment where ambient temperature can be up to 50 ^{o}C in summer time.

Passive cooling can be a better choice for HCPV in remote areas where water resources are limited and periodic maintenance for the cooling system is costly. Four heat sinks geometries were developed and tested at different ambient temperatures (25-50 ^{o}C) to keep the solar cell within the safe operating temperature recommended by the manufacturer. Only one heat sink (ESFHS) with optimised fins was able to maintain the operating temperature $\leq$80 ^{o}C under high concentration ratio i.e. 500X. The average electrical efficiency of the solar cell attached to this heat sink was 39.2% i.e. about 5% less than efficiency at reference temperature of 25 ^{o}C.

To make the HCPV more cost effective by utilising both electricity and thermal energy, the bottom side of the solar cell was attached to 0.011 m hydraulic diameter Aluminium rectangular channel for water cooling. Unlike passive cooling method, which is strongly influenced by the surrounding conditions, water cooling at moderate velocity i.e. 0.01 m/s ($Re \approx 122$) which can be supplied directly from the domestic tap water has the ability to keep the PV average temperature almost steady i.e. 60 ^{o}C regardless of the ambient temperature. Due to stable PV temperature, the electrical efficiency is almost constant at 39.5% at different ambient temperatures. Moreover, it was found that HCPV/T system performs better at higher ambient temperature due to the increase in the generated thermal energy and the low electrical sensitivity of the MJ solar cell to the elevated temperature. The total efficiency of the HCPV/T system at 25 and 50 ^{o}C ambient temperatures are about 78% and 87% respectively with increase of about 11%.

The outlet water average temperature of the HCPV/T was examined at different ambient temperature. It was found that placing 14 CPVs on the cooling channel is enough to raise the outlet temperature to 90^{o}C which would make the coupling to a single stage absorption cooling system feasible.

The influence of varying the input solar irradiation, the cooling water volume flow rate and cooling water inlet temperature on the HCPV/T thermal and electrical performance was examined. It was found that input irradiance is the most influencing parameter where the electrical and thermal output increased 100% and 75% when the solar irradiance increased from 500 to 1000 W/m^2 respectively.

A 0.25x0.25 m^2 HCPV/T performance analysis under concentration ratio of 425X and 250X based on Saudi Arabia solar irradiation and ambient conditions was undertaken to estimate the maximum and average power output that can be collected in one year. It was found that the annual maximum and average electrical power yields are up to 64.1 kWh and 38.4 kWh respectively. Whereas, the yearly maximum and average thermal power yields are 127.2 kWh and 81.4 kWh correspondingly. Therefore, the yearly maximum and average total power yields can be up to 191.3 kWh and 119.7 kWh respectively. It can be concluded that 184 units of 0.25x0.25 m^2 HCPV/T, which occupy 11.5 m^2, can respond to more than the annual electrical energy demand of a typical house in Saudi Arabia. Also, in comparison to the flat plate silicon PV module with electrical efficiency of 20% and 1.2x0.8 m^2 area, HCPV/T system can save about 76% of the area needed. Moreover, in terms of pollution these units can displace about 23 tons of CO_2 every year.

Indoor and outdoor experimental tests were undertaken for thermal characterisation of the HCPV/T and for validation purpose. Maximum deviation of 10% was found between the experimental and simulation thermal output. Also, there is a close agreement between the experimental and the predicted PV average temperature with maximum difference of less than 3 ^{o}C i.e. 10%.

8.3. Future works

This work shows that MJ based HCPV/T system tested under real ambient conditions of Saudi Arabia can achieve 35% and 74% electrical and thermal efficiency respectively with total efficiency of about 88%. Also, 184 units of 0.25x0.25m^2 HCPV/T which occupy only 11.5 m^2 can respond to more than the annual electrical energy demand of a typical house in Saudi Arabia and displace about 23 tons of CO_2 every year. However, the present study suggests steps for further work in enhancing the performance of the HCPV/T. The following recommendations are put forward:

- Although the electrical efficiency of the HCPV/T was improved after using the in-house developed reflective SOE, signs of non-uniform illumination were observed in the measured I-V curve especially at high concentration. Therefore, it can be useful if different types of SOE such as refractive optics are tested to examine any improvement in the optical and electrical outputs.
- Integrate an automated tracking system and thermal storage to the existing HCPV/T will allow performing a long term electrical and thermal analysis.
- Expand the present study on a module of HCPV/T where number of these systems are connected electrically and examine its performance experimentally outdoor.
- Couple the HCPV/T module to a thermal system to utilise the thermal energy and examine its performance experimentally outdoor.

REFERENCES

[1] International Energy Agency. World Energy Oulook 2014. OECD/ IEA: CORLET Paris Cedex France: 2014.

[2] International Energy Agency. World Energy Outlook 2011. OECD/ IEA: CORLET Paris Cedex France: 2011. doi:10.1787/weo-2011-en.

[3] Boyle G. Renewable energy. OXFORD university press; 2004.

[4] Longo A. Energy Generation Cost Assessment for Europe (EG-CAE). Renewable Energy Technologies and Socio-Economic Tools Info Day 2004. http://ec.europa.eu/research/energy/pdf/socio_eco01_longo.pdf. (accessed January 1, 2015).

[5] Sims R. Renewable energy: A response to climate change. Solar Energy 2004;76:9–17.

[6] Schimmelpfenning D. The option value of renewable energy The case of climate change. Energy Economics 1995;17:311–7. doi:10.1016/0140-9883(95)00034-R.

[7] Hankins M. Stand-alone Solar Electric Systems: The Earthscan Expert Handbook for Planning, Design and Installation. Taylor & Francis; 2012.

[8] King R, Law D, Edmondson K, Fetzer C, Kinsey G, Yoon H, et al. 40% efficient metamorphic GaInPGaInAsGe multijunction solar cells. Applied Physics Letters 2007;90:98–100. doi:10.1063/1.2734507.

[9] Mah O. Fundamentals of photovoltaic materials. National Solar Power Research Institute 1998:1–10.

[10] Environmental Protection and Control Department. Jubail Industrial City Solar Irradiation 2000-2012 data 2013.

[11] World Bank IBRD-IDA. Data on Country population (million). World Bank Group: 2015.

[12] BP. Statistical Review of World Energy. 2015.

[13] Alawaji SH. Evaluation of solar energy research and its applications in Saudi Arabia-20 years of experience. Renewable and Sustainable Energy Reviews 2001;5:59–77.

[14] BP. Statistical Review of World Energy. 2004.

[15] International Energy Agency. World Energy Outlook 2010. OECD/ IEA: CORLET Paris Cedex France: 2010.

[16] Nachet S, Aoun M. The Saudi electricity sector : pressing issues and challenges. Centre for Energy at Ifri Paris: 2015.

[17] Electricity and Cogeneration Regulatory Authority. Activities and Acheivements of the Autority in 2014. Kingdom of Saudi Arabia: 2014.

[18] Electricity and Cogeneration Regulatory Authority. Activities and Achievements of the Authority in 2012. Kingdom of Saudi Arabia: 2012.

[19] Anonymous. Energy Sustainability for Future Generations. King Abdullah City of Atomic and Renewable Energy (KACARE) 2015.

http://www.kacare.gov.sa/en/?page_id=84.

[20] Lahn G, Stevens P. Burning Oil to Keep Cool: the Hidden Energy Crisis in Saudi Arabia 2011:49.

[21] World Bank IBRD-IDA. Data on CO2 emissions (metric tons per capita). World Bank Group: 2015.

[22] Zell E, Gasim S, Wilcox S, Katamoura S, Stoffel T, Shibli H, et al. Assessment of solar radiation resources in Saudi Arabia. Solar Energy 2015;119:422–38. doi:10.1016/j.solener.2015.06.031.

[23] Hepbasli A, Alsuhaibani Z. A key review on present status and future directions of solar energy studies and applications in Saudi Arabia. Renewable and Sustainable Energy Reviews 2011;15:5021–50.

[24] Salim A, Eugenio N. A comprehensive report on the performance of the longest operating 350 kW concentrator photovoltaic power system 1990;29:1–24.

[25] Baig H, Heasman K, Mallick T. Non-uniform illumination in concentrating solar cells. Renewable and Sustainable Energy Reviews 2012;16:5890–909.

[26] Alawaji S, Hasnain H, Mahmood S. Role of solar energy research in transferring of technology to Saudi Arabia. Energy Sources 1999;21:923–34.

[27] Adinoy J, Said M. Effect of dust accumulation on the power outputs of solar photovoltaic modules. Renewable Energy 2013;60:633–6.

[28] Aldihani A, Aldossary A, Mahmoud S, Al-dadah R. The Effect of Cooling on the Performance of Photovoltaic Cells under Dusty Environmental Conditions. Energy Procedia 2014;0:6–9. doi:10.1016/j.egypro.2014.12.010.

[29] Harbi Y, Eugenio N, Zahrani S. photovoltaic-thermal solar energy experiment in saudi arabia 1998;5:5–8.

[30] Rehman S. Saudi Arabian geothermal energy resources- An update. World Geothermal Congress 2010, Proceedings World Geothermal Congress 25-29: Proceedings World Geothermal Congress 25-29; 2010, p. 1–6.

[31] Anonymous. Royal Embassy of Saudi Arabia. Saudi Arabia Launches Solar Energy Program. Energy Business 2010.

[32] Anonymous. IBM, KACST Unveil Research Initiative to Desalinate Seawater Using Solar Power. Nanotechnology Weekly 2010:34.

[33] Lovegrove K, Stein W. Concentrating Solar Power Technology: principles, developments and applications. 1st ed. Cambridge, UK: Woodhead Publishing Limited; 2012. doi:10.1533/9780857096173.1.16.

[34] Viana T, Rüther R, Martins F, Pereira E. Assessing the potential of concentrating solar photovoltaic generation in Brazil with satellite-derived direct normal irradiation. Solar Energy 2011;85:486–95. doi:10.1016/j.solener.2010.12.015.

[35] Twidell J, Weir AD. Renewable energy resources. Taylor & Francis; 2006.

[36] Garboushian V, Roubideaux D, Yoon S. Integrated high-concentration PV near-term alternative for low-cost large-scale solar electric power. Solar Energy Materials and Solar Cells 1997;47:315–23. doi:10.1016/S0927-0248(97)00056-1.

[37] Micheli L, Sarmah N, Luo X, Reddy K, Mallick T. Opportunities and challenges in micro- and nano-technologies for concentrating photovoltaic cooling: A review. Renewable and Sustainable Energy Reviews 2013;20:595–610.

[38] Royne A, Dey C, Mills D. Cooling of photovoltaic cells under concentrated illumination: a critical review. Solar Energy Materials and Solar Cells 2005;86:451–83. doi:10.1016/j.solmat.2004.09.003.

[39] Al-Amri F, Mallick T. Alleviating operating temperature of concentration solar cell by air active cooling and surface radiation. Applied Thermal Engineering 2013;59:348–54. doi:10.1016/j.applthermaleng.2013.05.045.

[40] Xu N, Ji J, Sun W, Han L, Chen H, Jin Z. Outdoor performance analysis of a 1090× point-focus Fresnel high concentrator photovoltaic/thermal system with triple-junction solar cells. Energy Conversion and Management 2015;100:191–200.

[41] Aldossary A, Algarue A, Mahmoud S, Al-dadah R. Performance of Multi Junction Photovoltaic Cells with High Concentration Ratio in Saudi Arabia. Energy Procedia 2014;0:6–9. doi:10.1016/j.egypro.2014.12.252.

[42] Anonymous. CONCENTRATING SOLAR | bigdishsolar on WordPress.com n.d. http://bigdishsolar.com/the-csp-context/ (accessed November 23, 2015).

[43] Mousazadeh H, Keyhani A, Javadi A, Mobli H, Abrinia K, Sharifi A. A review of principle and sun-tracking methods for maximizing solar systems output. Renewable and Sustainable Energy Reviews 2009;13:1800–18. doi:10.1016/j.rser.2009.01.022.

[44] Verlinden P, Terao A, Daroczi S, Crane R. One year comparison of a concentrator module with silicon point-contact solar cell to a fixed flat plate in northern California. The 16th European Photovoltaic solar energy conference, Glasgow, UK: 2000.

[45] Sciences N. Development and study of a dense array concentration Photovoltaic (CPV) system. University of Trento, 2013.

[46] Luque A, Andreev V. Concentrator Photovoltaics. vol. 130. Berlin, Heidelberg: Springer Berlin Heidelberg; 2007. doi:10.1007/978-3-540-68798-6.

[47] Swanson R. Photovoltaic Concentrators. In: Luque A, Hegedus S, editors. Handbook of Photovoltaic Science and Engineering, Chichester, UK: John Wiley & Sons, Ltd; 2003, p. 449–503.

[48] Sala G, Antón I. Photovoltaic Concentrators. In: A. Luque, S. Hegedus, editors. Handbook of Photovoltaic Science and Engineering, Chichester, UK: John Wiley & Sons Ltd; 2011, p. 402–51.

[49] Swanson R. The Promise of Concentrators 2000;111.

[50] Philipps SP, Bett AW, Horowitz K, Kurtz S. Current Status of Concentrator Photovoltaic (CPV) Technology. 2015. doi:http://www.ise.fraunhofer.de/en/publications/veroeffentlichungen-pdf-dateien-en/studien-und-konzeptpapiere/current-status-of-concentrator-photovoltaic-cpv-technology.pdf.

[51] Chemisana D. Building integrated concentrating photovoltaics: A review. Renewable and Sustainable Energy Reviews 2011;15:603–11. doi:10.1016/j.rser.2010.07.017.

[52] Soitec - Four-junction solar cell developped using Soitec’s expertise in semiconductor

materials sets new efficiency record of 38.9% for CPV module n.d. http://www.soitec.com/en/news/press-releases/article-1737/ (accessed February 17, 2016).

[53] Pérez P, Muñoz E, Almonacid G, Vidal P. High Concentrator PhotoVoltaics efficiencies: Present status and forecast. Renewable and Sustainable Energy Reviews 2011;15:1810–5.

[54] Melia J. CPV – State and Future of the Industry. 2012.

[55] National Center for Photovoltaics (NCPV). Best Research-Cell Efficiencies. National Renewable Energy Laboratory (NREL) 2016. http://www.nrel.gov/ncpv/images/efficiency_chart.jpg (accessed March 6, 2016).

[56] Green M, Emery K, Hishikawa Y, Warta W, Dunlop E. Solar cell efficiency tables (version 47). Progress in Photovoltaics: Research and Applications 2015;24.

[57] Fraunhofer ISE. New world record for solar cell efficiency at 46% 2014. https://www.ise.fraunhofer.de/en/press-and-media/press-releases/press-releases-2014/new-world-record-for-solar-cell-efficiency-at-46-percent (accessed March 6, 2016).

[58] Wesoff E. Sharp Hits Record 44.4% Efficiency for Triple-Junction Solar Cell 2013. http://www.greentechmedia.com/articles/read/Sharp-Hits-Record-44.4-Efficiency-For-Triple-Junction-Solar-Cell (accessed October 10, 2014).

[59] Sarmah N. Design and Performance Evaluation of a Low Concentrating Line-axis Dielectric Photovoltaic System. Heriot-Watt University, 2012.

[60] Selimoglu O. Design and Realisation of a new Concentrating Photovoltaic Solar Energy Module based on Lossless Horizontally Staggered Light Guide. Middle East Technical University, 2013.

[61] Markvart T. Solar Electricity. Second edi. Chichester, UK: John Wiley & Sons Ltd; 2000.

[62] International Renewable Energy Agency. Renewable Energy Technologies: Cost Analysis Series. 2012.

[63] Green M. Solar cells: operating principles, technology, and system applications. United States: Prentice-Hall, Inc.,Englewood Cliffs, NJ; 1982.

[64] Fonash S. Solar cell device physics. Second edi. Elsevier Science; 2010.

[65] Jeffery G. The physics of the solar cell. In: Luque A, Hegedus S, editors. Handbook of Photovoltaic Science and Engineering, Chichester, UK: John Wiley & Sons Ltd; 2011, p. 82–129.

[66] Chapin D, Fuller C, Pearson G. A new silicon p-n junction photocell for converting solar radiation into electrical power [3]. Journal of Applied Physics 1954;25:676–7. doi:10.1063/1.1721711.

[67] Basore P. Optimum grid-line patterns for concentrator solar cells under nonuniform illumination. Solar Cells 1985;14:249–60. doi:10.1016/0379-6787(85)90061-4.

[68] Wolf M, Rauschenbach H. Series resistance effects on solar cell measurements. Advanced Energy Conversion 1963;3:455–79. doi:10.1016/0365-1789(63)90063-8.

[69] Pasquinelli M, Barakel D. Serial resistance effect on p-type and n-type silicon concentrated solar cells. 2011 International Conference on Clean Electrical Power (ICCEP), IEEE; 2011, p. 161–3. doi:10.1109/ICCEP.2011.6036370.

[70] Castro M, Anton I, Sala G. Pilot production of concentrator silicon solar cells: Approaching industrialization. Solar Energy Materials and Solar Cells 2008;92:1697–705. doi:10.1016/j.solmat.2008.08.001.

[71] Mallick T, Eames P. Design and fabrication of low concentrating second generation PRIDE concentrator. Solar Energy Materials and Solar Cells 2007;91:597–608. doi:10.1016/j.solmat.2006.11.016.

[72] Mallick T, Eames P, Norton B. Non-concentrating and asymmetric compound parabolic concentrating building façade integrated photovoltaics: An experimental comparison. Solar Energy 2006;80:834–49. doi:10.1016/j.solener.2005.05.011.

[73] Garner C, Nasby R. Effects of nonuniform illumination on the performance of silicon concentrator solar cells. 1979 International Electron Devices Meeting, vol. 25, IRE; 1979, p. 312–3. doi:10.1109/IEDM.1979.189611.

[74] Huang H, Su Y, Gao Y, Riffat S. Design analysis of a Fresnel lens concentrating PV cell. International Journal of Low-Carbon Technologies 2011;6:165–70. doi:10.1093/ijlct/ctr002.

[75] Vivar M, Morilla C, Antón I, Fernández J, Sala G. Laser grooved buried contact cells optimised for linear concentration systems. Solar Energy Materials and Solar Cells 2010;94:187–93. doi:10.1016/j.solmat.2009.08.022.

[76] French R, Rodríguez J, Yang M, Derryberry R, Pfeiffenberger N. Optical properties of polymeric materials for concentrator photovoltaic systems. Solar Energy Materials and Solar Cells 2011;95:2077–86. doi:10.1016/j.solmat.2011.02.025.

[77] Kurtz S, Geisz J. Multijunction solar cells for conversion of concentrated sunlight to electricity. Optics Express 2010;18 Suppl 1:A73-8. doi:10.1364/OE.18.000A73.

[78] Benitez P, Cvetkovic A, Winston R, Diaz G, Reed L, Cisneros J, et al. High-concentration mirror-based kohler integrating system for tandem solar cells. Conference Record of the 2006 IEEE 4th World Conference on Photovoltaic Energy Conversion, WCPEC-4 2007;1:690–3. doi:10.1109/WCPEC.2006.279549.

[79] Rumyantsev V. Solar concentrator modules with silicone-on- glass Fresnel lens panels and multijunction cells. Optics Express 2010;18:277–80.

[80] Wolf M. Limitations and Possibilities for Improvement of Photovoltaic Solar Energy Converters: Part I: Considerations for Earth’s Surface Operation. Proceedings of the IRE 1960;48:1246–63. doi:10.1109/JRPROC.1960.287647.

[81] Yastrebova N. High-efficiency multi-junction solar cells : Current status and future potential. University of Ottawa: 2007.

[82] Bailey S, Raffaelle R. Space Solar Cells and Arrays. In: Hegedus S, Luque A, editors. Handbook of Photovoltaic Science and Engineering, Chichester, UK: John Wiley & Sons Ltd; 2003, p. 413–48.

[83] Friedman D, Kurtz S, Bertness K, Kibbler A, Kramer C, Olson J, et al. Accelerated publication 30.2% efficient GaInP/GaAs monolithic two-terminal tandem concentrator cell. Progress in Photovoltaics: Research and Applications 1995;3:47–50.

doi:10.1002/pip.4670030105.

[84] Olson J, Friedman D, Kurtz S. High-efficiency III-V multijunction solar cells. In: Luque A, Hegedus S, editors. Handbook of Photovoltaic Science and Engineering, Chichester, UK: John Wiley & Sons, Ltd; 2003.

[85] Miles R, Hynes K, Forbes I. Photovoltaic solar cells: An overview of state-of-the-art cell development and environmental issues. Progress in Crystal Growth and Characterization of Materials 2005;51:1–42. doi:10.1016/j.pcrysgrow.2005.10.002.

[86] Cotal H, Fetzer C, Boisvert J, Kinsey G, King R, Hebert P, et al. III–V multijunction solar cells for concentrating photovoltaics. Energy & Environmental Science 2009;2:174. doi:10.1039/b809257e.

[87] Henry C. Limiting efficiencies of ideal single and multiple energy gap terrestrial solar cells. Journal of Applied Physics 1980;51:4494. doi:10.1063/1.328272.

[88] Sellami N. Design and characterisation of a novel translucent solar concentrator. Heriot-Watt University, 2013.

[89] Zahedi A. Review of modelling details in relation to low-concentration solar concentrating photovoltaic. Renewable and Sustainable Energy Reviews 2011;15:1609–14. doi:10.1016/j.rser.2010.11.051.

[90] AZURSPACE. Enhanced Fresnel Assembly - EFA Type: 3C42A – with 10x10mm^2 CPV TJ Solar Cell Application: Concentrating Photovoltaic (CPV) Modules 2014:0–3. http://www.azurspace.com/images/products/DB_3987-00-00_3C42_AzurDesign_EFA_10x10_2014-03-27.pdf.

[91] Spectrolab. CDO-030-C3MJ Concentrator Solar Cell. Spectrolab, Inc 2009:2. http://www.spectrolab.com/DataSheets/PV/CPV/PV CDO-030-C3MJ.pdf (accessed August 16, 2016).

[92] Emery K. Measurement and Characterization of Solar Cells and Modules. In: Hegedus S, Luque A, editors. Handbook of Photovoltaic Science and Engineering, Chichester, UK: John Wiley & Sons Ltd; 2003, p. 701–52.

[93] Osterwald C, Wanlass M, Moriarty T. Effects of spectral error in efficiency measurements of GaInAs-based concentrator solar cells. 2014.

[94] Nishioka K, Takamoto T, Agui T, Kaneiwa M, Uraoka Y, Fuyuki T. Annual output estimation of concentrator photovoltaic systems using high-efficiency InGaP/InGaAs/Ge triple-junction solar cells based on experimental solar cell’s characteristics and field-test meteorological data. Solar Energy Materials and Solar Cells 2006;90:57–67. doi:10.1016/j.solmat.2005.01.011.

[95] Giannuzzi A. Enhancing the Efficiency of solar concentrators by controlled optical aberrations. University of Bologna, 2014.

[96] Domínguez C, Antón I, Sala G. Multijunction solar cell model for translating I-V characteristics as a function of irradiance, spectrum, and cell temperature. Progress in Photovoltaics: Research and Applications 2010:n/a-n/a. doi:10.1002/pip.965.

[97] Kinsey G, Hebert P, Barbour K, Krut D, Cotal H, Sherif R. Concentrator Multijunction Solar Cell Characteristics Under Variable Intensity and Temperature 2008:503–8. doi:10.1002/pip.

[98] Miller D, Kurtz S. Durability of Fresnel lenses: A review specific to the concentrating photovoltaic application. Solar Energy Materials and Solar Cells 2011;95:2037–68. doi:10.1016/j.solmat.2011.01.031.

[99] Chemisana D, Ibáñez M, Barrau J. Comparison of Fresnel concentrators for building integrated photovoltaics. Energy Conversion and Management 2009;50:1079–84. doi:10.1016/j.enconman.2008.12.002.

[100] Xie W, Dai Y, Wang R, Sumathy K. Concentrated solar energy applications using Fresnel lenses: A review. Renewable and Sustainable Energy Reviews 2011;15:2588–606. doi:10.1016/j.rser.2011.03.031.

[101] Herrero R, Victoria M, Domínguez C, Askins S, Antón I, Sala G. Concentration photovoltaic optical system irradiance distribution measurements and its effect on multi - junction solar cells 2012:423–30. doi:10.1002/pip.

[102] Leutz R, Suzuki A, Akisawa A, Kashiwagi T. Design of a Nonimaging Fresnel Lens for Solar Concentrators 1999;65:379–87.

[103] Chong K, Lau S, Yew T, Tan P. Design and development in optics of concentrator photovoltaic system. Renewable and Sustainable Energy Reviews 2013;19:598–612. doi:10.1016/j.rser.2012.11.005.

[104] Wallhead I, Jiménez T, Ortiz J, Toledo I, Toledo C. Design of an efficient Fresnel-type lens utilizing double total internal reflection for solar energy collection. Optics Express 2012;20:A1005-10.

[105] Jing L, Liu H, Zhao H, Lu Z, Wu H, Wang H, et al. Design of novel compound fresnel lens for high-performance photovoltaic concentrator. International Journal of Photoenergy 2012;2012. doi:10.1155/2012/630692.

[106] Hiramatsue M, Miyazaki Y, Egami T, Akisawa A, Miruta Y. Development of non-imaging fresnel lens and sun-tracking device 2003:2383–5.

[107] Miñano J, Benítez P, Zamora P, Buljan M, Mohedano R, Santamaría A. Free-form optics for Fresnel-lens-based photovoltaic concentrators 2013;21:494–502. doi:10.1117/12.620240.J.

[108] Pan J, Huang J, Wang C, Hong H, Liang Y. High concentration and homogenized Fresnel lens without secondary optics element. Optics Communications 2011;284:4283–8. doi:10.1016/j.optcom.2011.06.019.

[109] Benítez P, Miñano J, Zamora P, Mohedano R, Cvetkovic A, Buljan M, et al. High performance Fresnel-based photovoltaic concentrator. Optics Express 2010;18:A25-40.

[110] Sierra C, Azquez A. High solar energy concentration with a Fresnel lens 2005;0:1339–43.

[111] Madhugiri G. High solar energy concentration with a Fresnel lens : A Review. International Journal of Modern Engineering Research 2012;2.

[112] Hernández M, Cvetkovic A, Benítez P, Miñano JC. High-performance Kohler concentrators with uniform irradiance on solar cell. Optical Engineering+ Applications, 2008, p. 705908.

[113] Li D, Sawhney M, Kurtz R, Solomon L, Collette J. Impact of the Location of a Solar Cell in Relationship to the Focal Length of a Fresnel Lens on Power Production

2014;4:1–6. doi:10.5923/j.ep.20140401.01.

[114] Krüger D, Pandian Y, Hennecke K, Schmitz M. Parabolic trough collector testing in the frame of the REACt project. Desalination 2008;220:612–8. doi:10.1016/j.desal.2007.04.062.

[115] Tao T, Zheng H, Su Y, Riffat S. A novel combined solar concentration/wind augmentation system: Constructions and preliminary testing of a prototype. Applied Thermal Engineering 2011;31:3664–8. doi:10.1016/j.applthermaleng.2011.01.015.

[116] Mittelman G, Kribus A, Mouchtar O, Dayan A. Water desalination with concentrating photovoltaic/thermal (CPVT) systems. Solar Energy 2009;83:1322–34. doi:10.1016/j.solener.2009.04.003.

[117] Mallick T, Eames P, Hyde T, Norton B. The design and experimental characterisation of an asymmetric compound parabolic photovoltaic concentrator for building fa??ade integration in the UK. Solar Energy 2004;77:319–27. doi:10.1016/j.solener.2004.05.015.

[118] Mallick T, Eames P, Norton B. Non-concentrating and asymmetric compound parabolic concentrating building façade integrated photovoltaics: An experimental comparison. Solar Energy 2006;80:834–49. doi:10.1016/j.solener.2005.05.011.

[119] Mallick T, Eames P, Norton B. Using air flow to alleviate temperature elevation in solar cells within asymmetric compound parabolic concentrators. Solar Energy 2007;81:173–84. doi:10.1016/j.solener.2006.04.003.

[120] Mallick T, Eames P, Norton B. Power losses in an asymmetric compound parabolic photovoltaic concentrator. Solar Energy Materials and Solar Cells 2007;91:1137–46. doi:10.1016/j.solmat.2007.03.020.

[121] Fraidenraich N, Tiba C, Brandão B, Vilela O. Analytic solutions for the geometric and optical properties of stationary compound parabolic concentrators with fully illuminated inverted V receiver. Solar Energy 2008;82:132–43. doi:10.1016/j.solener.2007.06.012.

[122] Lovegrove K, Stein W. Concentrating solar power technology. vol. 21. 2012.

[123] Luque A, Sala G, Luque-Heredia I. Photovoltaic concentration at the onset of its commercial deployment. Progress in Photovoltaics: Research and Applications 2006;14:413–28. doi:10.1002/pip.705.

[124] Reis F. Development of photovoltaic systems with concentration. University of Lisbon, 2013.

[125] Swanson R. BASIC TYPES OF CONCENTRATORS. In: Hegedus S, Luque A, editors. Handbook of Photovoltaic Science and Engineering, Chichester, UK: John Wiley & Sons Ltd; 2003, p. 449–503.

[126] Swanson R. Photovoltaic Concentrators. In: Hegedus S, Luque A, editors. Handbook of Photovoltaic Science and Engineering, Chichester, UK: John Wiley & Sons Ltd; 2003, p. 449–503.

[127] Kurtz S. Opportunities and Challenges for Development of a Mature Concentrating Photovoltaic Power Industry. Denver, Colorado: 2012.

[128] Chen Y, Chiang H. Design of the Secondary Optical Elements for Concentrated

Photovoltaic Units with Fresnel Lenses. Applied Sciences 2015;5:770–86. doi:10.3390/app5040770.

[129] Chaves J. Introduction to Nonimaging Optics, Second Edition. CRC Press; 2015.

[130] Fartaria T. Tolerance study and optical optimization of a concentrated photovoltaic module. The University of Lisbon, 2011.

[131] Victoria M, Herrero R, Domínguez C, Antón I, Askins S, Sala G. Characterization of the spatial distribution of irradiance and spectrum in concentrating photovoltaic systems and their effect on multi-junction solar cells. Progress in Photovoltaics: Research and Applications 2013;21:308–18. doi:10.1002/pip.1183.

[132] Buljan M, Mendes J, Benítez P, Miñano J. Recent trends in concentrated photovoltaics concentrators architecture. Journal of Photonics for Energy 2014;4:40995. doi:10.1117/1.JPE.4.040995.

[133] Zubi G, Bernal J, Fracastoro G. High concentration photovoltaic systems applying III–V cells. Renewable and Sustainable Energy Reviews 2009;13:2645–52. doi:10.1016/j.rser.2009.07.002.

[134] Leutz R, Suzuki A. Nonimaging Fresnel lenses: design and performance of solar concentrators. vol. 83. Springer; 2001.

[135] Welford WT, Winston R. The optics of nonimaging concentrators: light and solar energy. Academic Press; 1978.

[136] Anonymous. Concentrating Photovoltaics Solar Power n.d. http://www.greenrhinoenergy.com/solar/technologies/pv_concentration.php (accessed November 26, 2015).

[137] Verlinden PJ, Lewandowski A, Kendall H, Carter S, Cheah K, Varfolomeev I, et al. Update on two-year performance of 120 kWp concentrator PV systems using multi-junction III–V solar cells and parabolic dish reflective optics. 2008 33rd IEEE Photovolatic Specialists Conference, IEEE; 2008, p. 1–6. doi:10.1109/PVSC.2008.4922734.

[138] Oshida I. Step lenses and step prisms for utilization of solar energy. New Sources of Energy, Proceedings of the Conference, Rome: 1961, p. 598–603.

[139] Harmon S. Solar-optical analyses of a mass-produced plastic circular Fresnel lens. Solar Energy 1977;19:105–8. doi:10.1016/0038-092X(77)90096-2.

[140] James L, Williams J. Fresnel optics for solar concentration on photovoltaic cells. Proceedings of the 13th IEEE Photovoltaic Specialists Conference, Washington D.C.: 1978, p. 673–9.

[141] Nakata Y, Shibuya N, Kobe T, Okamoto K, Suzuki A, Tsuji T. Performance of Circular Fresnel Lens Photovoltaic Concentrator. Japanese Journal of Applied Physics 1980;19:75. doi:10.7567/JJAPS.19S2.75.

[142] Franklin E, Coventry J. Effects of highly non-uniform illumination distribution on electrical performance of solar cells. Solar Australian and New Zealand Solar Energy Society, 2003.

[143] Katz E, Gordon J, Feuermann D. Effects of ultra-high flux and intensity distribution in multi-junction solar cells. Progress in Photovoltaics: Research and Applications

2006;14:297–303. doi:10.1002/pip.670.

[144] Jebens R. Fresnel lens concentrator. Patent No. 4,799,778, 1989.

[145] Kurtz S, Friedman D, Olson J. The effect of chromatic aberrations on two-junction, two-terminal, devices on a concentrator system [solar cells]. Proceedings of 1994 IEEE 1st World Conference on Photovoltaic Energy Conversion - WCPEC (A Joint Conference of PVSC, PVSEC and PSEC), vol. 2, IEEE; n.d., p. 1791–4. doi:10.1109/WCPEC.1994.520650.

[146] Grilikhes V, Rumyantsev V, Shvarts M. Indoor and outdoor testing of space concentrator AlGaAs/GaAs photovoltaic modules with Fresnel lenses. Conference Record of the Twenty Fifth IEEE Photovoltaic Specialists Conference - 1996, IEEE; 1996, p. 345–8. doi:10.1109/PVSC.1996.564016.

[147] Rumyantsev V, Chosta O, Grilikhes V, Sadchikov N, Soluyanov A, Shvarts M, et al. Terrestrial and space concentrator PV modules with composite (glass-silicone) Fresnel lenses. Conference Record of the Twenty-Ninth IEEE Photovoltaic Specialists Conference, 2002., IEEE; n.d., p. 1596–9. doi:10.1109/PVSC.2002.1190920.

[148] Kemmoku Y, Sakakibara T, Hiramatsu M, Miyazaki Y, Egami T. Field test of a concentrator photovoltaic system with flat Fresnel lens n.d.;3:2379–2382 Vol.3.

[149] Davies P. Design of single-surface spherical lenses as secondary concentrators for photovoltaic cells. Pure and Applied Optics: Journal of the European Optical Society Part A 1993;2:315–24. doi:10.1088/0963-9659/2/4/004.

[150] Whitfield G, Bentley R, Weatherby C, Hunt A, Mohring H, Klotz F, et al. The development and testing of small concentrating PV systems. Solar Energy 1999;67:23–34. doi:10.1016/S0038-092X(00)00045-1.

[151] Andreev V, Grilikhes V, Khvostikov V, Khvostikova O, Rumyantsev V, Sadchikov N, et al. Concentrator PV modules and solar cells for TPV systems. Solar Energy Materials and Solar Cells 2004;84:3–17. doi:10.1016/j.solmat.2004.02.037.

[152] Ryu K, Rhee J, Park K, Kim J. Concept and design of modular Fresnel lenses for concentration solar PV system. Solar Energy 2006;80:1580–7. doi:10.1016/j.solener.2005.12.006.

[153] Shanks K, Senthilarasu S, Mallick T. Optics for concentrating photovoltaics: Trends, limits and opportunities for materials and design. Renewable and Sustainable Energy Reviews 2016;60:394–407. doi:10.1016/j.rser.2016.01.089.

[154] Zhuang Z, Yu F. Optimization design of hybrid Fresnel-based concentrator for generating uniformity irradiance with the broad solar spectrum. Optics & Laser Technology 2014;60:27–33. doi:10.1016/j.optlastec.2013.12.021.

[155] Aldossary A, Mahmoud S, AL-Dadah R. Technical feasibility study of passive and active cooling for concentrator PV in harsh environment. Applied Thermal Engineering 2016;100:490–500. doi:10.1016/j.applthermaleng.2016.02.023.

[156] Segev G, Mittelman G, Kribus A. Equivalent circuit models for triple-junction concentrator solar cells. Solar Energy Materials and Solar Cells 2012;98:57–65. doi:10.1016/j.solmat.2011.10.013.

[157] Luque A, Sala G, Arboiro J. Electric and thermal model for non-uniformly illuminated concentration cells. Solar Energy Materials and Solar Cells 1998;51:269–90.

doi:10.1016/S0927-0248(97)00228-6.

[158] Renno C, Petito F. Design and modeling of a concentrating photovoltaic thermal (CPV/T) system for a domestic application. Energy and Buildings 2013;62:392–402. doi:10.1016/j.enbuild.2013.02.040.

[159] Mittelman G, Kribus A, Dayan A. Solar cooling with concentrating photovoltaic/thermal (CPVT) systems. Energy Conversion and Management 2007;48:2481–90. doi:10.1016/j.enconman.2007.04.004.

[160] Kribus A, Kaftori D, Mittelman G, Hirshfeld A, Flitsanov Y, Dayan A. A miniature concentrating photovoltaic and thermal system. Energy Conversion and Management 2006;47:3582–90. doi:10.1016/j.enconman.2006.01.013.

[161] Xu N, Ji J, Sun W, Huang W, Li J, Jin Z. Numerical simulation and experimental validation of a high concentration photovoltaic / thermal module based on point-focus Fresnel lens. APPLIED ENERGY 2016;168:269–81. doi:10.1016/j.apenergy.2016.01.077.

[162] Edenburn M. Active and passive cooling for concentrating photovoltaic arrays. 14th Photovoltaic Specialists Conference, vol. 1, 1980, p. 771–6.

[163] Mifiano J, Zanesco I. Flat high concentration devices 1994:1123–6.

[164] Araki K, Uozumi H, Yamaguchi M. A simple passive cooling structure and its heat analysis for 500 concentrator PV module. 29th IEEE PVSC, Conference record; 2002, p. 1568–1571.

[165] Mo S, Chen Z, Hu P. Performance of a Passively Cooled Fresnel Lens Concentrating Photovoltaic Module. 2011 Asia-Pacific Power and Energy Engineering Conference, IEEE; 2011, p. 1–4. doi:10.1109/APPEEC.2011.5747676.

[166] Tan L. Passive Cooling of Concentrated Solar Cells Using Phase Change Material Thermal Storage. RMIT University, 2013.

[167] Anderson W, Dussinger P, Sarraf D, Tamanna S. Heat pipe cooling of concentrating photovoltaic cells. 2008 33rd IEEE Photovolatic Specialists Conference 2008:1–6. doi:10.1109/PVSC.2008.4922577.

[168] Du B, Hu E, Kolhe M. Performance analysis of water cooled concentrated photovoltaic (CPV) system. Renewable and Sustainable Energy Reviews 2012;16:6732–6. doi:10.1016/j.rser.2012.09.007.

[169] Akbarzadeh A, Wadowski T. Heat pipe-based cooling systems for photovoltaic cells under concentrated solar radiation. Applied Thermal Engineering 1996;16:81–7. doi:10.1016/1359-4311(95)00012-3.

[170] Farahat M. Improvement the thermal electric performance of a photovoltaic cells by cooling and concentration techniques. IEEE 39th international universities power engineeringconference, 2004, p. 623–8.

[171] Tuckerman D, Pease R. High-performance heat sinking for VLSI. IEEE Electron Device Letters 1981;2:126–9. doi:10.1109/EDL.1981.25367.

[172] Van Kessel T, Abduljabar A, Khonkar H, Moumen N, Sandstrom R, Al-Saaedi Y, et al. Concentrator photovoltaic reliability testing at extreme concentrations up to 2000 suns. 2009 34th IEEE Photovoltaic Specialists Conference (PVSC), IEEE; 2009, p. 001020–

3. doi:10.1109/PVSC.2009.5411195.

[173] Theristis M, Sarmah N, Mallick T, O’Donovan T. Design and numerical analysis of enhanced cooling techniques for a high concentration photovoltaic (HCPV) system. 27th European Photovoltaic Solar Energy Conference and Exhibition, 2012, p. 260–5. doi:10.4229/27thEUPVSEC2012-1AV.3.35.

[174] Helmers H, Schachtner M, Bett A. Influence of temperature and irradiance on triple-junction solar subcells. Solar Energy Materials and Solar Cells 2013;116:144–52. doi:10.1016/j.solmat.2013.03.039.

[175] Coventry J. Performance of a concentrating photovoltaic/thermal solar collector. Solar Energy 2005;78:211–22. doi:10.1016/j.solener.2004.03.014.

[176] Kerzmann T, Schaefer L. System simulation of a linear concentrating photovoltaic system with an active cooling system. Renewable Energy 2012;41:254–61. doi:10.1016/j.renene.2011.11.004.

[177] DiYPRO company 2016. http://diypro.en.ec21.com/ (accessed July 11, 2016).

[178] HTSP Silicone Heat Transfer Compound Plus 2016. http://www.electrolube.com/core/components/products/tds/044/HTSP.pdf (accessed December 28, 2016).

[179] BuildParts - Materials - FullCure 720 2016. http://www.buildparts.com/materials/fullcure720 (accessed November 2, 2016).

[180] Peltier Thermo-Electric Cooler Module 2016. https://www.adafruit.com/products/1335 (accessed November 4, 2016).

[181] Technical information of alanod solar relective material. Alanod-Solar 2016. http://www.bluetec.eu/en/Reflection/Technical_Informations (accessed July 4, 2016).

[182] PVA-1000S PV Analyzer Kit. Solmetric 2016. http://www.solmetric.com/pvanalyzermatrix.html (accessed November 5, 2016).

[183] I-V Curve Tracer Wireless PV Reference Sensor. Solmetric 2016. http://www.solmetric.net/get/Solmetric_PVA_Brochure_single-page_081314.pdf (accessed November 5, 2016).

[184] Light heat flux sensor. Captec Enterprise 2005. http://www.captecenterprise.com/news.htm (accessed November 5, 2016).

[185] DataTaker Intelligent Data Loggers - DT85 General Purpose Data Logger. Datataker 2016. http://www.datataker.com/DT85.php.

[186] Abdullahi B. Development and Optimization of heat pipe based Compound Parabolic Collector. University Of Birmingham, 2015.

[187] Glass Variable Area Flowmeters. CT Platon 2016. http://www.ctplaton.com/uploads/pdf/En/deb_ng_lg.pdf (accessed November 8, 2016).

[188] SMP10 pyranometer, the smartest way to measure solar radiation - Kipp & Zonen. Kipp & Zonen 2016. http://www.kippzonen.com/Product/281/SMP10-Pyranometer#.WCIVCS2LSpp (accessed November 8, 2016).

[189] El-Nashar A. Seasonal effect of dust deposition on a field of evacuated tube collectors on the performance of a solar desalination plant. Desalination 2009;239:66–81.

doi:10.1016/j.desal.2008.03.007.

[190] Cheatle K. Fundamentals of test measurement instrumentation. ISA--Instrumentation, Systems, and Automation Society; 2006.

[191] Elsayed A. Heat Transfer in Helically Coiled Small Diameter Tubes for Miniature Cooling Systems. University of Birmingham, 2011.

[192] Mallick T. Optics and Heat Transfer for Asymmetric Compound Parabolic Photovoltaic Concentrators for Building Integrated Photovoltaics. University of Ulster, 2003.

[193] Ramirez-Iniguez R, Idrus SM, Sun Z. Optical wireless communications : IR for wireless connectivity. CRC Press; 2008.

[194] Saleh I, O'Donovan T, Reddy K, Mallick T. An optical analysis of a static 3-D solar concentrator. Solar Energy 2013;88:57–70. doi:10.1016/j.solener.2012.11.004.

[195] Rodrigo P, Velázquez R, Fernández E, Almonacid F, Pérez-Higueras P. Analysis of electrical mismatches in high-concentrator photovoltaic power plants with distributed inverter configurations. Energy 2016;107:374–87. doi:10.1016/j.energy.2016.04.039.

[196] Amonix. Amonix claims new PV module efficiency record 2014.

[197] Davis A, Kühnlenz F. Optical Design using Fresnel Lenses Basic Principles and some Practical Examples. Optik and Photonik, Wiley 2007:52–5. doi:10.1002/opph.201190287.

[198] Schulz U, Munzert P, Rickelt F, Kaiser N. Breakthroughs in Photonics 2013: Organic Nanostructures for Antireflection. IEEE Photonics Journal 2014;6:1–5. doi:10.1109/JPHOT.2014.2311432.

[199] Schulz U, Kaiser N, Munzert P, Scheler M, Uhlig H. Method for reducing boundary surface reflection of plastic substrates and substrate modified in such a manner and use thereof. US20050233083 A1, 2005.

[200] Kumar V, Shrivastava R, Untawale S. Fresnel lens: A promising alternative of reflectors in concentrated solar power. Renewable and Sustainable Energy Reviews 2015;44:376–90. doi:10.1016/j.rser.2014.12.006.

[201] Singh G. Solar power generation by PV (photovoltaic) technology: A review. Energy 2013;53:1–13. doi:10.1016/j.energy.2013.02.057.

[202] Kinsey G, Edmondson K. Spectral Response and Energy Output of Concentrator Multijunction Solar Cells 2009:279–88. doi:10.1002/pip.

[203] Fontenault B, Gutierrez E. Modeling a Combined Photovoltaic-Thermal Solar Panel. Comsol conference, Boston: 2012.

[204] Eveloy V, Rodgers P, Bojanampati S. Enhancement of photovoltaic solar module performance for power generation in the Middle East. 2012 28th Annual IEEE Semiconductor Thermal Measurement and Management Symposium (SEMI-THERM) 2012:87–97.

[205] Wu Y, Eames P, Mallick T, Sabry M. Experimental characterisation of a Fresnel lens photovoltaic concentrating system. Solar Energy 2012;86:430–40. doi:10.1016/j.solener.2011.10.032.

[206] Theristis M, O’Donovan T. Electrical-thermal analysis of III-V triple-junction solar cells under variable spectra and ambient temperatures. Solar Energy 2015;118:533–46. doi:10.1016/j.solener.2015.06.003.

[207] Blumenfeld P, Foresi J, Lang Y. Thermal Management and Engineering Economics in CPV Design 2010:20. http://www.meptec.org/Resources/16 - EMCORE - BLUMENFELD.pdf (accessed September 20, 2016).

[208] Arias A, Barrera J, Osorio G, Mejía R. Designing a concentrating photovoltaic (CPV) system in adjunct with a silicon photovoltaic panel for a solar competition car. In: Dhar NK, Balaya P, Dutta AK, editors., International Society for Optics and Photonics; 2014, p. 91150W. doi:10.1117/12.2050830.

[209] Anonymous. Solar Energy Renewable Energy Atlas. KACARE 2016. https://rratlas.kacare.gov.sa/RRMMPublicPortal/?q=en/Solar (accessed May 1, 2016).

[210] Chou T, Shih Z, Hong H, Han C, Chiang K. Thermal Performance Assessment and Validation of High-Concentration Photovoltaic Solar Cell Module. IEEE Transactions on Components, Packaging and Manufacturing Technology 2012;2:578–86. doi:10.1109/TCPMT.2011.2181165.

[211] Goldberg Y. Handbook Series on Semiconductor Parameters. In: Levinshtein M, Rumyantsev S, Shur M, editors. 2, World Scientific Pub. Co., Inc.; 1999, p. 62–88.

[212] Frei W. Solutions to Linear Systems of Equations: Direct and Iterative Solvers. COMSOL 2013. https://www.comsol.com/blogs/solutions-linear-systems-equations-direct-iterative-solvers/ (accessed January 11, 2016).

[213] King Abdullah City for Atomic and Renewable Energy. Solar resource hourly data. Riyadh: 2016.

[214] Baras A, Bamhair W, Alkhoshi Y, Alodan M. Opportunities and challenges of solar energy in Saudi Arabia. World Renewable Energy Forum, Denver, Colorado: 2012, p. 4721.

[215] Shaahid S, Elhadidy M. Economic analysis of hybrid photovoltaic-diesel-battery power systems for residential loads in hot regions-A step to clean future. Renewable and Sustainable Energy Reviews 2008;12:488–503.

[216] U.S. Environmental Protection Agency. Greenhouse gas equivalencies calculator 2010. http://www.epa.gov/cleanenergy/energy-resources/calculator.html (accessed October 25, 2016).

[217] Average Weather For Birmingham, United Kingdom 2016. https://weatherspark.com/averages/28699/Birmingham-England-United-Kingdom (accessed October 16, 2016).

[218] MIRO-SUN test report 2010. http://www.bluetec.eu/sites/default/files/pictures/MIRO_SUN_engl_101112_1.pdf.

[219] 3M Double Sided Tape 2017. http://solutions.3m.co.uk/wps/portal/3M/en_GB/tapes-adhesives/-/tapes/double-sided-tape/ (accessed January 1, 2017).

[220] Zheng H, Tao T, Dai J, Kang H. Light tracing analysis of a new kind of trough solar concentrator. Energy Conversion and Management 2011;52:2373–7. doi:10.1016/j.enconman.2010.12.042.

[221] Colina-Marquez J, Lopez-Vasquez A, Machuca-Martinez F. Modelling of direct solar radiation in a compound parabolic collector (CPC) with the ray tracing technique. Dyna-Columbia 2010;163:132–40.

[222] Groulx D, Sponagle B. Ray-tracing analysis of a two-stage solar concentrator. Transactions of the Canadian Society for Mechanical Engineering 2010.

[223] Wu Y. Thermal Management of Concentrator Photovoltaics. University of Warwick, 2009.

[224] Leutz R, Suzuki A, Akisawa T, Kashiwagi T. Flux Uniformity and Spectral Reproduction in Solar Concentrators Using Secondary Optics 2001:775–84.

[225] Reinhardt K, Mayberry C, Lewis B, Kreifels T. Multijunction solar cell iso-junction dark current study. Conference Record of the Twenty-Eighth IEEE Photovoltaic Specialists Conference - 2000 (Cat. No.00CH37036), IEEE; 2000, p. 1118–21. doi:10.1109/PVSC.2000.916083.

[226] Nishioka K, Takamoto T, Agui T, Kaneiwa M, Uraoka Y, Fuyuki T. Evaluation of InGaP/InGaAs/Ge Triple-Junction Solar Cell under Concentrated Light by Simulation Program with Integrated Circuit Emphasis. Japanese Journal of Applied Physics 2004;43:882–9. doi:10.1143/JJAP.43.882.

[227] Nishioka K, Sueto T, Uchida M, Ota Y. Detailed Analysis of Temperature Characteristics of an InGaP/InGaAs/Ge Triple-Junction Solar Cell. Journal of Electronic Materials 2010;39:704–8. doi:10.1007/s11664-010-1171-y.

[228] Steiner M, Phillips S, Hermle M, Bett A, Dimorth F. Front contact grid optimization of III–V solar cells with SPICE network simulation. 24th European Solar Energy Conference and Exhibition, Hamburg: 2009.

[229] Emelyanov V, Kalyuzhnyy N. Distributed resistance effects simulation in concentrator MJ SCS using 3D-network model. 25th European Photovoltaic Solar Energy Conference and Exhibition/ 5th World Conference on Photovoltaic Energy Conversion 2010.

[230] Min C, Nuofu C, Xiaoli Y, Yu W, Yiming B, Xingwang Z. Thermal analysis and test for single concentrator solar cells. Journal of Semiconductors 2009;30:44011. doi:10.1088/1674-4926/30/4/044011.

[231] Cotal H, Frost J. Heat transfer modeling of concentrator multijunction solar cell assemblies using finite difference techniques. 2010 35th IEEE Photovoltaic Specialists Conference 2010:000213–8. doi:10.1109/PVSC.2010.5614514.

[232] Al-Amri F, Mallick T. Alleviating Operating Temperature of High Concentration Solar Cell by Active Cooling. World Renewable Energy Forum, Denver, Colorado: 2012, p. 70–4.

APPENDIX A

Optical and mechanical properties of the reflective material used in the SOE.

Parameter	**Value**
Material	Aluminium
Total solar reflectance (%)	90
Total light reflectance (%)	≥ 87
Thickness (m)	0.0003
Density (kg/m^3)	2700
Heat conductivity W/(m*K)	≥ 220

Table A.1: Optical and mechanical properties of the SOE reflective material [218].

Total spectral reflectance of the SOE material

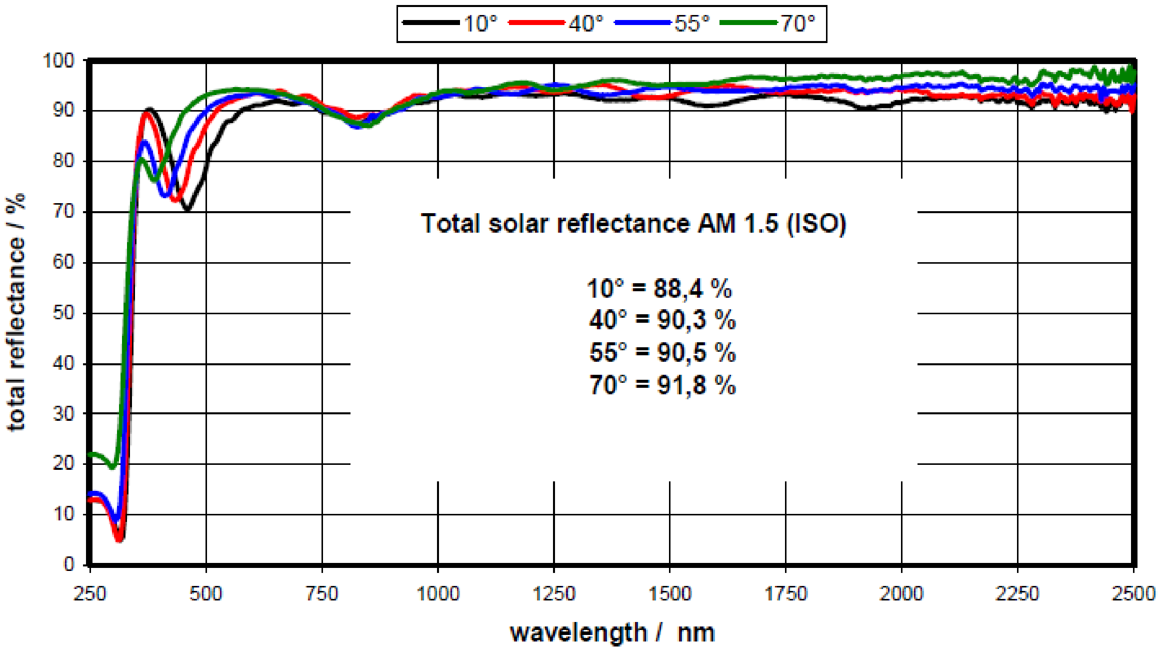

Figure A.1: Spectral reflectance of the SOE reflective material [218].

Technical details of the 3M double face tape.

Parameter	**Value**
Brand	3M 9088
Type	Double sided tape
Thickness (m)	0.0001
Width (m)	0.012
Temperature range (^{o}C)	≤120

Table A.2: Technical details of the 3M double face tape [219].

APPENDIX B

Calibration curve Figures of the used surface thermocouples

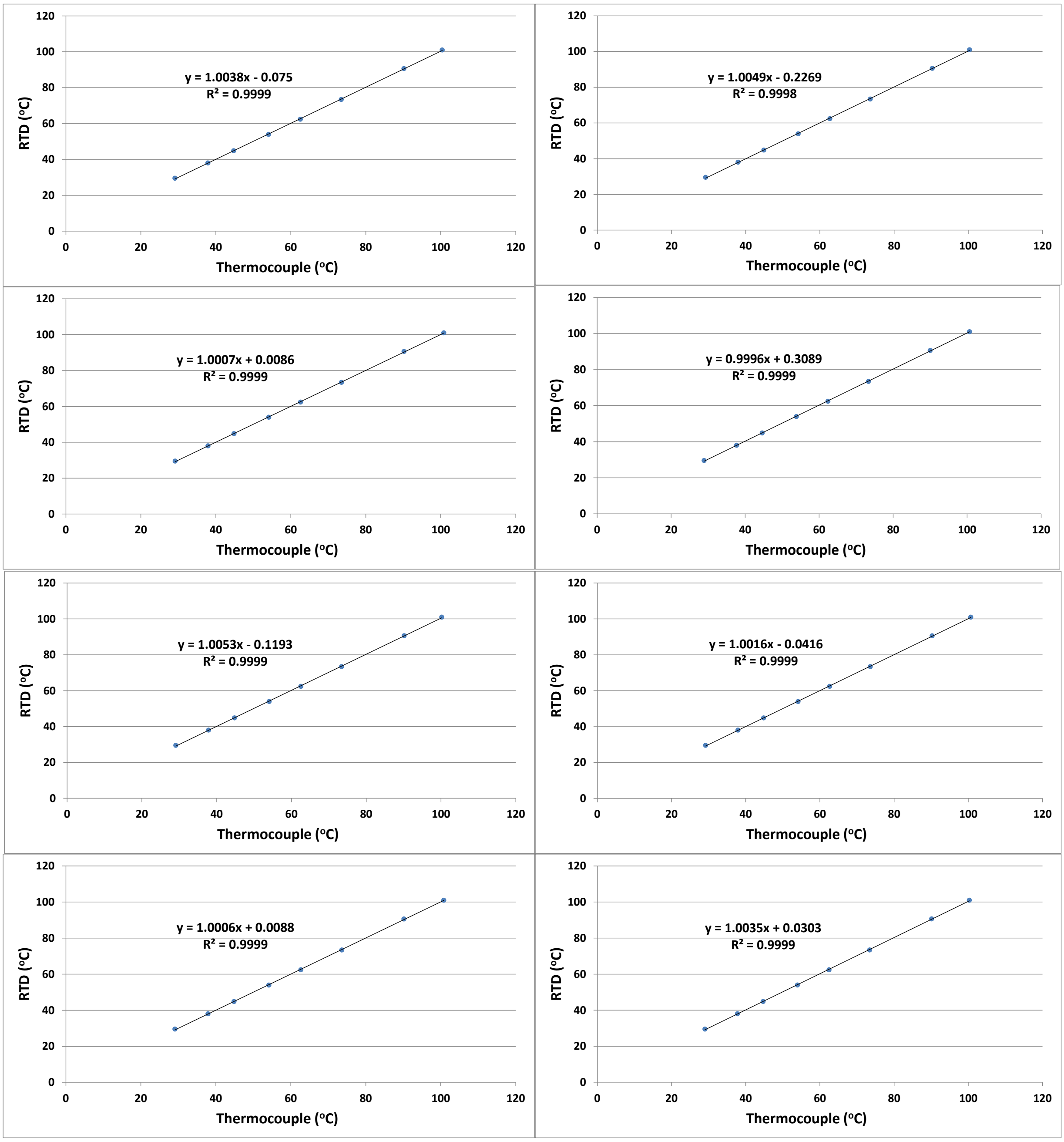

Figure B.1: Temperature relations between RTD and surface thermocouples 1 to 8.

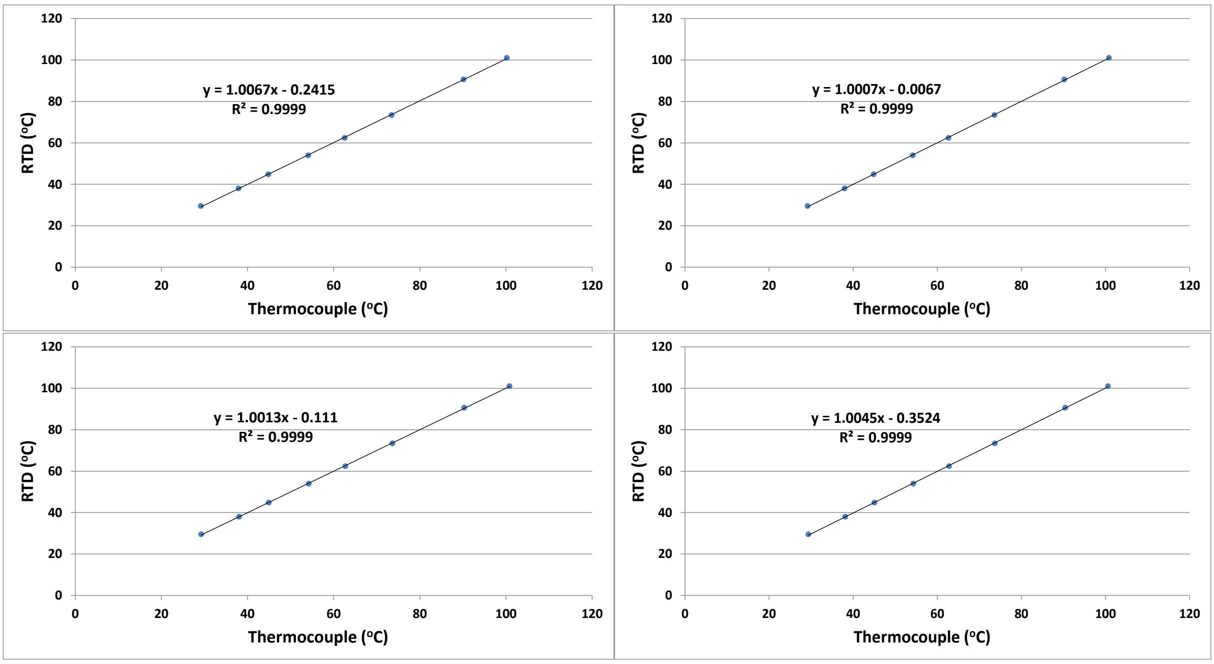

Figure B.2: Temperature relations between RTD and surface thermocouples 9 to 12.

APPENDIX C

Brief literature review on ray tracing method for optical modelling of solar concentrators

Ray tracing method is a well-known technique used to develop several solar concentrators and optical devices such as lenses and reflectors used in different applications. The use of the ray tracing technique dates back to early times before the advent of the computer as the calculations were implemented using hand drawings, trigonometry and logarithmic Tables [88]. The ray tracing calculations are now performed using algorithms or commercial software.

Zheng et al. used ray tracing to study the influence of the incident angle of the light rays on the efficiency and concentration ability of a new kind of trough solar collector [220]. The concentrator system was drawn by the commercial package UG and then exported to optical software. The light beam used in the tracing software had a fixed wavelength of 550nm which can work to evaluate reflective concentrators but it cannot be considered for refractive lenses as the absorbance and refractive index of the lens material vary as a function of the wavelength [88].

Colina-Marquez et al. developed a mathematical model based on ray tracing technique to simulate the reflection of direct solar radiation on a CPC [221]. Results showed that the energy distribution at the absorber depends on the surface reflectivity; it is more uniform when the reflective surfaces of the CPC have higher reflectivity.

Groulx and Sponagle presented a ray tracing analysis which was conducted on a 2-stage solar concentrator made of two parabolic mirrors [222]. The effects of the secondary mirror's focal length, the distance between the secondary mirror and the target and the misalignment with the sun were studied. It was found that the solar concentrator system is very sensitive to misalignments with respect to the sun and small misalignments in the order of ±0.2^o would bring the concentration efficiency to zero.

Wu used a two-dimensional ray tracing method to predict the optical performance and the angular acceptance of an Asymmetric Compound Parabolic Photovoltaic Concentrator (ACPPVC) under the solar inclination angles in the UK [223]. The predicted highest optical efficiency was 88.67% for the ACPPVC system.

Sarmah also utilised ray tracing method to examine the optical performance, acceptance half angle and radiation intensity distribution on the receiver of a truncated dielectric asymmetric compound parabolic concentrator (DiACPC) [59]. The maximum optical efficiency of the DiACPC was found to be 83% and the designed dielectric concentrator was capable of collecting 68% of the diffuse radiation.

Sellami designed and optimised a novel static non-imaging transparent 3-D concentrator via ray-tracing technique [88]. A preliminary optical efficiency investigation was carried out on 160 concentrators of different geometries and 20 of them were chosen for further study. It was found that the concentrators are capable of saving more than 60% of the solar cells used in conventional flat PV systems.

Abdullahi used OptisWorks to investigate the effects of acceptance angle, receiver radius, truncation, collector length and orientation on a compound parabolic collector (CPC) performance [186]. Results showed that CPC can achieve daily average optical efficiencies of 76.5% and 64.4% for acceptance angles of 60^o and 40^o respectively.

Ray tracing method was also applied to study the irradiation uniformity. For example, Leutz et al. proposed a cone shape secondary optical element to achieve a uniform flux distribution on the receiver following the edge-ray principle and using ray tracing method [224].

APPENDIX D

Brief literature review on electrical modelling of a multi-junction solar cell

Characterising the performance of terrestrial multi-junction solar cells is crucial for designing high concentration Photovoltaic (HCPV) systems. These cells may operate over a range of incident flux typical between 100 up to 1000 suns and a range of operating temperatures up to about 100^{o}C [156]. The dependence of the cell's performance on these two operating parameters should then be well defined. There are a number of methods used in the literature to predict the I-V characteristics of the multi-junction solar cell such as two diodes equivalent circuit model for each subcell, single diode equivalent circuit model for each subcell, lumped diode model and network cell model [156].

Two diode equivalent circuit models were proposed by Reinhardt et al. [225] and Nishioka et al. [226] to predict the influence of temperature and irradiation on the solar cell performance but the combined effects of temperature and high incident radiation flux were not studied. The Reinhardt et al. model was caliberated against InGaP/InGaAs/Ge cell data only at room temperature and 1 sun = 1000 W/m^2 [225]. While, the Nishioka et al. model was caliberated against measurements at room temperature and for the concentration ratio range of 1-1000X [226]. In other work, Nishioka et al. successfully compared the temperature sensitivity predictions of the developed model in [226] to the Sharp solar cell data at 1 sun and temperature below 120 ^{o}C [227].

Kirbus et al. presented a single diode equivalent circuit model caliberated for both high concentration and temperature levels [156]. The model included a separate I-V relationship for each subcell of the triple-junction solar cell. The outputs of the model were calibirated against the Sharp solar cell and coefficients were optimised to fit the I-V curves measured data. The results showed that at high concentrations, the open circuit voltage and efficiency temperature coefficients predictions deviate from the measured data.

Segev et al. presented single and two diode equivalent circuit models for InGaP/InGaAs/Ge triple-junction cells caliberated against available emperical data published by two manufacturers Sharp and Spectrolab [156]. The two models have added the band gap dependance on the cell temperature and alloy composition which was not fully addressed in previous models. Results showed that both models have produced total root-mean-square (RMS) errors lower than 2.5%, indicating that even the single diode model may be adequate for practical applications. Although two diodes model is more complicated, it has shown only slightly better results compared to the single diode model.

Kinsey et al. proposed a single diode model caliberated against the Spectrolab multi-junction cell (C1MJ) experimental data at elevated temperature and intensity where a lumped cell I-V relationship was considered with a single ideality factor [97]. A qualitative comparison between the model outputs and measured open circuit temperature coefficients at different concentration levels was presented. A lumped diode model was also suggested by Dominguez et al. and calibrated against commercial triple-junction cell empirical data at temperature below 120 ^{o}C and concentration level up to 700X [96]. In order to extract the model coefficients, a fitting procedure with respect to the RMS errors in the I-V predictions was carried out. The validity of the method has been demonstrated by its application to a set of commercial triple-junction receivers with a mean prediction RMS errors of 0.85% i.e. low prediction errors.

More sophisticated, distributed (network) cell models were recently suggested [228,229]. In this method, the cell is divided into many small elementary cells (hundreds or thousands) to increase accuracy. The advantage of the distributed model is reported only in the case of non-uniform illumination over the cell. However, this approach is complex to implement and requires high computational resources, making it unsuitable at the engineering level [156].

APPENDIX E

Engineering Equation Solver (EES) code of I-V curve model for multi-junction solar cell including the empirical parameters

```
{Photo-generated current, Iscr here is Iscr at 1x * CR}
Iscr_1=0.01516
X=500
Iscr_Xx=Iscr_1*X
Ki=0.0061
Tc=298.15
T=335.81
IL=(Iscr_Xx+Ki*(T-Tc))

{Saturation current}

T=335.81
gamma=-0.312
Eg=1.6
Kb=8.62e-5
Isat=(T^(3+(gamma/2)))*exp(-Eg/(Kb*T))

{IV curve MJ as a whole manufacturer input}
IL=7.81
Isat=1.510E-17
Rs=0.018
n=2.53
q=1.6e-19
KB=1.38e-23
T=335.81
I=IL-Isat*(exp(((q*(V+(I*Rs))/(n*KB*T))))-1)
```

Ideality factor (n) =2.53, Series resistance (R_S) =0.018Ω,, E_g=1.6eV and temperature dependence of the saturation current(γ) =0.312.

APPENDIX F

Brief literature review on thermal modelling of high concentrator multi-junction PV

Thermal modelling using FEA has been utilised to predict the thermal behaviour of the HCPV systems under high concentration ratios. Min et al. designed a thermal model for concentrator solar cells based on energy conservation principles [230]. It was found that 0.000009 m^2 triple-junction solar cell surface temperature under 400X concentration with no cooling can reach 1200 ^oC. Metal plates were used as heat sinks for cooling the system and the surface temperature was remarkably reduced. It was found that in order to keep the cell at a constant temperature the heat sink area needs to increase linearly with the concentration ratio. The thermal model was validated by outdoor experiment with cell temperature deviation of 8%.

Cotal and Frost developed a steady-state heat transfer modelling to examine the various parts of concentrator cell assembly (CCA) temperature under different packaging scenarios by varying the adhesive thermal conductivity and thickness [231]. In the absence of forced convection, it was found that conduction heat transfer is the main method of removing heat away from the solar cell which makes the thermal resistance between the layers more crucial. The accuracy of the heat transfer rate flowing through the different layers of the CCA model was validated by using energy conservation principles.

Chou et al. used a three-dimensional FEA to establish a detailed model of the HCPV solar cell package able to calculate the dissipated power of the solar cell [210]. Outdoor experiments using IR thermography measurement were also performed to validate the thermal model and the estimation of dissipated power. Simulation results showed that the geometry of the heat sink plate play an important role in the thermal management of the HCPV solar cell module.

Al-Amri and Mallick presented a heat transfer model using a finite difference technique for multi-junction concentrating solar cell system [232]. The model includes GaInP/GaAs/Ge triple-junction solar cell with water flow in ducts behind the solar cell assembly. Results showed that the maximum cell temperature was strongly dependent on the coolant inlet velocity and channel width.

In 2015, Theristis and Donovan presented a three-dimensional finite element analysis using COMSOL Multiphysics to predict the multi-junction solar cell’s operating temperature and cooling requirements at a range of ambient temperatures [206]. The convective heat transfer coefficient between the back-plate and ambient air was identified to be an important parameter in achieving high electrical efficiency. The results showed that a single cell configuration with area of $1cm^2$ can be cooled passively for concentration ratios of up to 500X with a heat sink thermal resistance below 1.63 K/W, but for ambient temperature above 40 ^oC, a thermal resistance less than 1.4 K/W is required to keep the solar cell operating within safe operating conditions. In other work, Theristis et al. developed a thermal model using COMSOL Multiphysics to predict the heat output of a 0.01x0.01 m^2 PV cell, in order to examine the most efficient and cost effective cooling system for a 500X concentrating PV cell [173]. Different geometries and materials of heat sinks were designed and examined for passively cooling purposes. It was shown that passive cooling of a HCPV system with concentration ratio of 500X is insufficient to maintain the solar cell below the operating temperature limit set by the manufacturer (80 ^oC) especially at high ambient temperatures. More investigation is needed to be undertaken to find the optimum solution for cooling the HCPV system in hot climates.